THE DISCOVERY AND CHARACTERIZATION OF THE MOST DISTANT QUASARS

Eduardo Bañados Torres
Max-Planck-Institut für Astronomie

Heidelberg 2015

Dissertation in Astronomy
submitted to the
Combined Faculties of the Natural Sciences and Mathematics
of the Ruperto-Carola-University of Heidelberg, Germany
for the degree of
Doctor of Natural Sciences

put forward by

Eduardo Bañados Torres
born in Santiago, Chile

Oral examination: 30 June 2015

THE DISCOVERY AND CHARACTERIZATION OF THE MOST DISTANT QUASARS

Eduardo Bañados Torres
Max-Planck-Institut für Astronomie

Referees:	Prof. Dr. Hans-Walter Rix
	Prof. Dr. Jochen Heidt

Abstract

Luminous quasars at high redshift ($z > 5.5$) provide direct probes of the growth supermassive black holes and their host galaxies at the epoch of cosmic reionization, which is one of the current frontiers of astrophysical research. In this thesis, $z > 5.5$ quasars are studied from different angles. (1) The criteria to identify high-redshift quasars using the Panoramic Survey Telescope & Rapid Response System 1 (Pan-STARRS1, PS1) survey are presented. These selection criteria have resulted in 54 newly discovered quasars at $z > 5.5$. These new discoveries almost double the number of known $z > 5.5$ quasars and increase the number of quasars at $z > 6.5$ from four to eight. The quasar sample spans a factor of ~20 in luminosity and shows a diverse range of properties, including a number of weak-line and radio-loud quasars. (2) Using the available data in the literature, the radio-loud fraction (RLF) of quasars at $z \sim 6$ is constrained to $\mathrm{RLF} = 8.1^{+5.0}_{-3.2}\%$. This result is consistent with a non-evolving RLF of quasars up to $z = 6$. (3) High-redshift quasars are thought to reside in massive dark matter halos and should therefore be located in regions with an overdensity of galaxies. To find such overdensities, the first search for galaxies using narrow-band imaging in the field of a $z = 5.7$ quasar is performed. No overdensity of galaxies is found around the quasar, with the possible implication that high-redshift quasars may not reside in the center of the most massive dark matter halos. (4) A strong [C II] emission line (an effective cooling line of the interstellar medium) in the host galaxy of a PS1-discovered quasar at $z = 6.54$ is reported. This is the brightest quasar known at $z > 6.5$ and given its high rest-frame UV and [C II] luminosities, it has the potential of becoming an important laboratory for the study of star formation and of the interstellar medium only ~800 Myr after the Big Bang. As a final note, the number of quasars at $z > 5.5$ presented in this thesis marks the transition phase from studies of individual sources to statistical studies of the high-redshift quasar population, which was impossible with earlier, smaller samples.

Zusammenfassung

Quasare hoher Leuchtkraft bei hohen Rotverschiebungen ($z > 5,5$) ermöglichen eine direkte Überprüfung des Wachstums supermassiver Schwarzer Löcher und deren Heimat-Galaxien zur Zeit der kosmische Reionisation, eines der aktuellen Forschungsthemen im Bereich der Astrophysik. Diese Arbeit betrachtet Quasare mit Rotverschiebungen von $z > 5,5$ unter verschiedenen Gesichtspunkten. (1) Kriterien zur Identifikation hochgradig rotverschobener Quasare mittels der Panoramic Survey Telescope & Rapid Response System 1 (Pan-STARRS1, PS1) Durchmusterung werden vorgestellt. Diese Selektionskriterien haben zur Entdeckung von 54 neuen Quasaren mit $z > 5,5$ geführt. Diese Neuentdeckungen bedeuten eine annähernde Verdopplung der Anzahl der bekannten Quasare mit $z > 5,5$ und erhöhen die Anzahl der bekannten Quasare mit $z > 6,5$ von vier auf acht. Die Stichprobe der Quasare umfasst einen Faktor von ~20 in Leuchtkraft und weist eine Vielzahl von Eigenschaften auf, unter anderem sind Quasare mit schwachen Linien und radiolaute Quasare enthalten. (2) Unter Verwendung der aus der Literatur zur Verfügung stehenden Daten ist der Anteil der radiolauten Quasaren (radio-loud fraction, RLF) bei $z \sim 6$ eingegrenzt auf RLF $= 8,1^{+5,0}_{-3,2}\%$. Dieses Resultat ist konsistent mit einem konstanten RLF der Quasare bis hin zu $z = 6$. (3) Hochgradig rotverschobene Quasare werden als eingebettet in massive Halos aus dunkler Materie angenommen, und sollten deshalb in Regionen mit einer übergroßen Dichte an Galaxien anzutreffen sein. Es wird hier die erste Arbeit zur Auffindung solche Überdichten mittels Schmalbandaufnahmen in der Umgebung eines Quasars bei $z = 5,7$ präsentiert. In der Umgebung des Quasars wird keine Region übergroßer Galaxiendichte gefunden, was möglicherweise impliziert, dass sich hochgradig rotverschobene Quasare nicht zwingend in den Zentren der massivsten Halos aus dunkler Materie befinden. (4) Eine starke [C II]-Emissionslinie (eine effektive Linie aus Kühlung des interstellaren Mediums) in der Heimat-Galaxie eines mittels PS1 entdeckten Quasars bei $z = 6,54$ wird beschrieben. Hierbei handelt es sich um den leuchtkräftigsten Quasar bei $z > 6,5$. Seine hohe UV und [C II]-Leuchtkraft ermöglicht es, dieses Objekt für Studien der Sternentstehung und des insterstellaren Mediums zu Zeiten von nur ~800 Millionen Jahre nach dem Urknall zu erforschen. Abschließend ist zu sagen, dass die Anzahl der Quasare mit $z > 5,5$, die in dieser Arbeit vorgestellt werden, einen Übergang von Studien über individuelle Objekte hin zu Studien der Population hochgradig rotverschobener Quasare darstellen, was mit kleineren Stichproben bislang nicht möglich war.

Publications

Parts of the work presented in this thesis have previously appeared in the following articles:

- Bañados, E., Decarli, R., Walter, F., et al. 2015a;
  accepted for publication in the Astrophysical Journal Letters;
  Bright [C II] 158 μm emission in a quasar host galaxy at $z = 6.54$
- Bañados, E., Venemans, B., Morganson, E., et al. 2015b; ApJ, 804, 118;
  Constraining the radio-loud fraction of quasars at $z > 5.5$
- Venemans, B., Bañados, E., Decarli, R., et al. 2015; ApJ, 801, L11;
  The identification of z-dropouts in Pan-STARRS1: three quasars at $6.5 < z < 6.7$.
- Bañados, E., Venemans, B., Morganson, E., et al. 2014; AJ 148, 14;
  Discovery of eight $z \sim 6$ *quasars from Pan-STARRS1*
- Bañados, E., Venemans, B., Walter, et al. 2013; ApJ, 773, 178;
  The galaxy environment of a QSO at $z \sim 5.7$

A mis padres y a mis
abuelitas Flora y Sonia.

Contents

2 The Pan-STARRS1 distant quasar survey 21

List of Figures

List of Tables

Chapter 1

Introduction[†]

One of the main challenges in observational cosmology is to understand how the first luminous objects and large scale structures of the universe formed and evolved through cosmic time. Quasi-stellar radio sources or quasi-stellar objects (quasars or QSOs)[1] are super massive black holes accreting material at the center of galaxies. As the black holes pull in matter, they release enormous amounts of energy. In fact, quasars are the most luminous, powerful, and energetic non-transient sources known in the universe and can therefore be studied in detail at the earliest cosmic epochs[2].

As the title of the present thesis suggests, this work is focused on the discovery and characterization of the most *distant* quasars. In order to understand what is meant by *distant*, a brief review of cosmological concepts that will be used throughout this work, such as *redshift* and *distances*, will be provided. Next, in order to place this thesis into its broader context, an overview of the history of the universe is given, highlighting the phases where the majority of the present study is focused. Afterwards, more specific topics will be introduced that are crucial to understanding the chapters that follow.

[†] This chapter is partly based on sections of the following articles: Bañados et al. (2013, 2014, 2015a,b); Venemans et al. (2015).

[1] Originally the name quasars was employed because these objects were thought to be star-like sources with strong radio emission. Later on, it was discovered that not all quasars were strong radio-emitters and the name was therefore changed to QSOs. Nowadays, both terms are used indistinctly (see Section 1.4).

[2] Gamma-ray bursts are *transient* objects thought to be the end product of rare massive stars (Woosley & Bloom 2006) and pinpoint location of distant galaxies. They can be, for a short period of time, brighter than quasars (see e.g., Cucchiara et al. 2011; Salvaterra 2015).

1.1 Cosmology[3]

In this section some cosmological concepts that will provide the necessary background for the understanding of this thesis are introduced.

1.1.1 Cosmological redshift

The expansion of the universe causes the observed light coming from a distant object to be redshifted. The redshift, z, quantifies the ratio of the observed wavelength to the emitted wavelength of light. The measured redshift is related to the expansion factor of the universe at the time that the photons were emitted. This is expressed by the following relation:

$$1 + z = \frac{\lambda_{\rm obs}}{\lambda_{\rm em}} = \frac{1}{a(t_{\rm em})} \tag{1.1}$$

where $\lambda_{\rm obs}$ and $\lambda_{\rm em}$ are the observed and emitted wavelengths and $a(t)$ is the scale factor that describes the time evolution of our universe. For example, if we observe the light coming from a quasar at $z = 6$, it means that those photons were emitted when the universe was 1/7th of its current size.

1.1.2 The Friedmann-Lemaître equations

The Friedmann-Lemaître equations are a special case of Einstein's field equations for a homogeneous, isotropic universe. They describe the behavior of the scale factor $a(t)$ and therefore regulate the dynamics of the universe. These equations can be written in the following form:

$$H^2 = \left(\frac{\dot{a}}{a}\right)^2 = \frac{8\pi G}{3}\epsilon - \frac{\kappa c^2}{a^2} + \frac{\Lambda}{3} \tag{1.2}$$

$$\frac{\ddot{a}}{a} = -\frac{4\pi G}{3}\left(\epsilon + \frac{3P}{c^2}\right) + \frac{\Lambda}{3} \tag{1.3}$$

---

[3] A proper discussion of cosmology is beyond the scope of this section. For readers interested in further details, they are referred to the following books and articles: Peebles (1993), Hogg (1999), Ryden (2003), Bennett (2006), and Schneider (2015).

where H is known as the Hubble parameter, G is the gravitational constant, Λ is the cosmological constant, c is the speed of light, and κ is the curvature parameter. These equations of state relate the pressure (P) and energy density (ϵ) through the scale factor a.

Assuming $\Lambda = 0$ and $\kappa = 0$ in equation 1.2—which separates an eternally expanding universe ($\kappa \geq 0$) from one that will recollapse in the future ($\kappa < 0$)—we can determine the current critical density, ϵ_c, by setting $t = t_0$ and $H_0 = \dot{a}(t_0)/a(t_0) = \dot{a}(t_0)$:

$$\epsilon_c = \frac{3H_0^2}{8\pi G} = 1.88 \times 10^{-29}\, h^2\, \mathrm{g\,cm^{-3}} \tag{1.4}$$

where $h = H_0/100\,\mathrm{km\,s^{-1}\,Mpc^{-1}}$. We can then define the dimensionless quantity called *density parameter* as

$$\Omega_0 = \frac{\epsilon}{\epsilon_c} = \frac{8\pi G}{3H^2}\epsilon \tag{1.5}$$

where $\Omega_0 = 1$ implies a flat universe, $\Omega_0 < 1$ an open universe, and $\Omega_0 > 1$ a closed universe. Analogous to equation 1.5, we can define the dimensionless density parameters for matter, radiation, and vacuum as

$$\Omega_m = \frac{\epsilon_{m,0}}{\epsilon_c}; \qquad \Omega_r = \frac{\epsilon_{r,0}}{\epsilon_c}; \qquad \Omega_\Lambda = \frac{\epsilon_\Lambda}{\epsilon_c} = \frac{\Lambda}{3H_0^2} \tag{1.6}$$

and we can therefore write the density parameter as

$$\Omega_0 = \Omega_m + \Omega_\Lambda + \Omega_r. \tag{1.7}$$

The equation 1.2 can be represented in terms of the present values of the density parameters:

$$H^2 = \left(\frac{\dot{a}}{a}\right)^2 = H_0^2\left(\frac{\Omega_r}{a^4} + \frac{\Omega_m}{a^3} + \frac{(1-\Omega_0)}{a^2} + \Omega_\Lambda\right) \tag{1.8}$$

where $1 - \Omega_0$ is the spatial curvature density.

1.1.3 Redshift and age of the universe

The differential relation between time and the scale factor a is given by

$$dt = da\left(\frac{1}{\dot{a}}\right) = \frac{da}{aH}\,. \tag{1.9}$$

Integrating the last relation and using equation 1.8, we obtain the age of the universe at a given scale factor a

$$t(a) = \frac{1}{H_0}\int_0^a \left(\frac{\Omega_r}{x^2} + \frac{\Omega_m}{x} + (1-\Omega_0) + \Omega_\Lambda\, x^2\right)^{-1/2} dx. \tag{1.10}$$

Using equation 1.10 and the relation between redshift and the scale factor given by equation 1.1, we can directly calculate the age of the universe at a given redshift. Table 1.1 lists the age of the universe at specific redshifts for future references. The values were calculated using the most recent estimates of the cosmological parameters for a flat ΛCDM universe: $H_0 = 67.7\,\mathrm{km\,s^{-1}\,Mpc^{-1}}$, $\Omega_M = 0.307$, and $\Omega_\Lambda = 0.693$ (Planck Collaboration et al. 2015b).

1.1.4 Distances

If we observe two objects at z_1 and z_2 such that $z_2 > z_1$, it means that the light coming from the object at z_2 traveled for a longer time in order to reach us. We then conclude that the object at z_2 is more distant than the object at z_1. However, because the universe is expanding, the distance between two locations is also increasing, making it harder to have a standard meaning for *distance*. As a matter of fact, in cosmology there are several definitions of distance, which are mostly described in terms of the redshift—the only observable related to distances that we can measure directly.

1.1.4.1 Co-moving distance

The *proper distance* between two points is the distance that would be measured along a geodesic if the universe was frozen at a given time t with a fixed scale factor $a(t)$. The *co-moving distance*, D_C, is the distance between two points measured at the present time, i.e., the proper distance multiplied by $(1 + z)$. As a result, the co-moving distance does not change in time due to the expansion of the universe and can be calculated as

$$D_C(z) = c\int_0^z \frac{dx}{H(x)} \tag{1.11}$$

where $H(x)$ is given by equation 1.8.

Table 1.1. Age of the universe at given redshifts

Redshift	Age of the universe	Age (%)[a]
3500	48553 yr	0.0004
1100	367526 yr	0.003
50	47 Myr	0.3
15	270 Myr	2.0
10	474 Myr	3.4
9	547 Myr	4.0
8	641 Myr	4.6
7	765 Myr	5.5
6.5	843 Myr	6.1
6.0	936 Myr	6.8
5.5	1.0 Gyr	7.6
5	1.2 Gyr	8.5
4	1.5 Gyr	11.2
3	2.2 Gyr	15.6
2	3.3 Gyr	23.8
1	5.9 Gyr	42.5
0.5	8.6 Gyr	62.4
0	13.8 Gyr	100

Note. — Quantities calculated with equation 1.10, assuming a flat ΛCDM cosmology with $H_0 = 67.7\,\mathrm{km\,s^{-1}\,Mpc^{-1}}$, $\Omega_M = 0.307$, and $\Omega_\Lambda = 0.693$ (Planck Collaboration et al. 2015b).

[a] Percentage with respect to the universe's present age.

1.1.4.2 Luminosity distance

The *luminosity distance*, D_L, of an object is defined in terms of its bolometric luminosity, L, and its observed flux, F, as

$$D_L(z) = \sqrt{\frac{L}{4\pi F}}. \tag{1.12}$$

1.1.4.3 Angular diameter distance

The *angular diameter distance*, D_A, is defined as the ratio between the physical size of an object, D, and its angular size observed in the sky, θ, in radians:

$$D_A(z) = \frac{D}{\theta}. \tag{1.13}$$

In general, the angular diameter distance to an object at a redshift z can be expressed in terms of the comoving distance as

$$D_A(z) = \frac{f_K\left[D_C(z)\right]}{1+z} \tag{1.14}$$

where the function $f_K(x)$ is

$$f_K(x) = \begin{cases} 1/\sqrt{K}\,\sin(\sqrt{K}\,x) & K > 0 \\ x & K = 0 \\ 1/\sqrt{-K}\,\sinh(\sqrt{-K}\,x) & K < 0 \end{cases}$$

and K is the curvature scalar defined as

$$K = \left(\frac{H_0}{c}\right)^2 (\Omega_0 - 1) = \left(\frac{H_0}{c}\right)^2 (\Omega_m + \Omega_\Lambda + \Omega_r - 1). \tag{1.15}$$

The luminosity distance can then be calculated by using the general relation between angular diameter distance and luminosity distance given by

$$D_L(z) = (1+z)^2\, D_A(z). \tag{1.16}$$

1.2 A brief history of the universe

Figure 1.1 shows a schematic view of the history of the universe. Cosmic time began about 13,800,000,000 years ago (13.8 Gyr) with what is commonly known as the *Big Bang*. The universe was small and hot, and the energy density was dominated by radiation. As time went by, at $z \sim 3500$, the energy density was dominated by matter, but the universe was still hot enough that photons, electrons, and atomic nuclei moved together in a quantum photon-baryon plasma. The universe continued expanding and cooling down.

After approximately 370,000 years ($z \sim 1100$), the universe reached a temperature of about 3000 K. At this temperature photons decoupled from baryons, and protons and electrons combined to form neutral atoms, an era known as *recombination*[4]. The photons that last interacted with matter at $z \sim 1100$ traveled freely through the universe and they are now observed as the *Cosmic Microwave Background* (CMB; Penzias & Wilson 1965; Bennett et al. 1996, 2013; Planck Collaboration et al. 2015a). After the epoch of recombination, the universe remained in a largely neutral state, a period called the *dark ages*, which finished around $z \sim 15 - 50$ when the first stars, galaxies, and quasars formed and began to reionize the universe.

The current thesis is mainly focused on what happened during the *epoch of reionization* and the phases that followed right after it. Cosmic reionization is a major phase transition of the entire intergalactic medium and its understanding is of crucial importance. It will allow us to comprehend not only how the first sources of light in the universe formed but also how all the other structures were created, including the galaxies and galaxy clusters we see today. We still do not know exactly when and how cosmic reionization started but we do have some constraints (see Fan et al. 2006a, for a review). For example, the analysis of secondary CMB anisotropies can place some restrictions on the duration of cosmic reionization. The most recent analysis of such anisotropies is based on the study of the kinematic Sunyaev–Zeldovich effect, placing an upper limit for reionization of $\Delta z < 5.4$ (George et al. 2015). Additionally, the most up to date measurements of the Thomson optical depth from Planck Collaboration et al. (2015b) imply that if reionization was an instantaneous event it would have occurred at $z_{reion} = 8.8^{+1.3}_{-1.2}$. Furthermore, observations of Gunn–Peterson absorption troughs (Gunn & Peterson 1965) in the spectra of high-redshift quasars and gamma-ray bursts (e.g., Fan et al. 2006c; Chornock et al. 2013; McGreer et al. 2015) and the declining fraction of Lyα emission in high-redshift galaxies (e.g., Treu et al. 2013; Konno et al. 2014; Pentericci et al. 2014; Schenker et al. 2014) show that reionization ended around a redshift of $z \sim 6$.

---

[4] Note that the name *re*combination could be misleading since there was no ‘combination’ in the past. In fact, electrons and protons combined for the *first time* during the epoch of recombination.

After reionization was complete, structures in the universe continued forming and growing. At $z \sim 2$ the peak of quasar activity took place, where most of the black hole and galaxy growth is believed to occur. The present-day universe is at $z = 0$ in which matter and dark energy are its dominant components. In the future, the universe will be largely dark energy dominated.

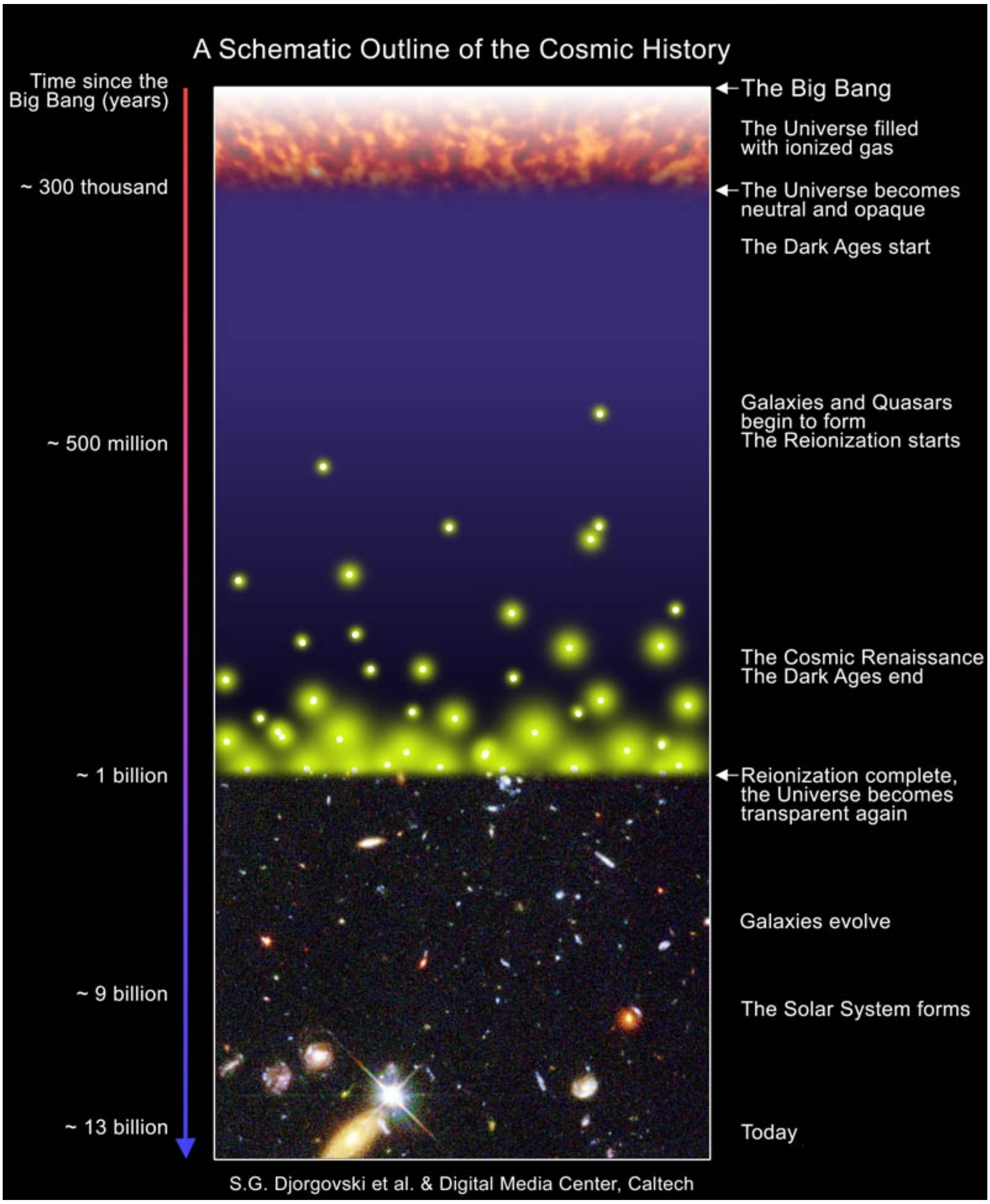

Figure 1.1: Schematic view of the history of the universe. Image courtesy of S.G. Djorgovski et al. & Digital Media Center, Caltech.

1.3 The most distant galaxies

One of the current frontiers in observational astronomy is to identify and characterize the first stars, galaxies, and black holes that formed during the epoch of reionization ($z > 6.5$). The motivation is to find answers to questions such as when and how did the first stars, galaxies, and black holes form? What are the first galaxies? Were their physical properties different from the galaxies seen in the present universe? When did cosmic reionization occur? How did reionization proceed? What are the main sources responsible for the reionization of the universe? The reviews by Robertson et al. (2010); Fan (2012); Dunlop (2013); Ellis (2014) discuss in more detail the motivations to study the first luminous sources in the universe and the techniques currently used to find them.

Nowadays, it is broadly believed that the dominant sources of reionization are star-forming galaxies (see e.g., Loeb & Barkana 2001; Dressler et al. 2014; Bouwens et al. 2015a; Robertson et al. 2015). However, the contribution of quasars (or more generally, active galactic nuclei; AGNs[5]) to the cosmic ionizing background is still uncertain and could be significant. Especially because the luminosity function of high-redshift AGNs is not well constrained (neither at the bright-end nor at the faint-end) and the formation process of massive black holes is not yet understood (e.g., Glikman et al. 2011; Haardt & Salvaterra 2015; Giallongo et al. 2015).

The *Hubble Space Telescope* (*HST*) has been pushed to its limits in order to try to identify the first galaxies, which is also one of the main drivers to build ambitious facilities such as the *James Webb Space Telescope* (*JWST*). Hundreds of $z > 8$ galaxy candidates have been reported (e.g., Bouwens et al. 2015b; Schmidt et al. 2014; Ishigaki et al. 2015), including a number of very good candidates at redshifts as high as $z \sim 10-11$ (e.g., Zheng et al. 2012; Coe et al. 2013; Oesch et al. 2014; Zitrin et al. 2014; Pirzkal et al. 2015). Even though all these objects are promising galaxy candidates, their redshifts are based solely on photometry. Spectroscopic confirmation of them has, thus far, proven to be impossible with the current facilities. To confirm these candidates and constrain the physics of formation and evolution of normal galaxies in this crucial epoch of the universe, we will probably have to wait for the launch of the *JWST* or the new generation of 30-m class telescopes.

The spectroscopic confirmation of astronomical objects at $z \sim 7-8$ is challenging with the current facilities (see e.g., Vanzella et al. 2014), yet not impossible. The current most distant object with a secure redshift is the gamma-ray burst GRB 090423 at $z = 8.2$ (Salvaterra et al. 2009; Tanvir et al. 2009), although its host galaxy remains undetected even with *HST*, *Spitzer*,

---

[5] Quasars are the most luminous members of a class of objects known as active galactic nuclei (AGN, Antonucci 1993). Quasars are commonly defined to have an absolute magnitude brighter than $M_B < -23$ (Schmidt & Green 1983).

and Atacama Large Millimiter Array (ALMA) observations (Tanvir et al. 2012; Berger et al. 2014). The most distant confirmed galaxy is at $z = 7.7$ (Oesch et al. 2015), while the most distant quasar is at $z = 7.1$ (Mortlock et al. 2011). Figures 1.2, 1.3, and 1.4 show the spectra for these three objects. The difference in terms of quality and information that can be obtained from these spectra is remarkable, the quasar spectrum being the only one with a signal high enough to allow for a detailed characterization with the current generation of telescopes.

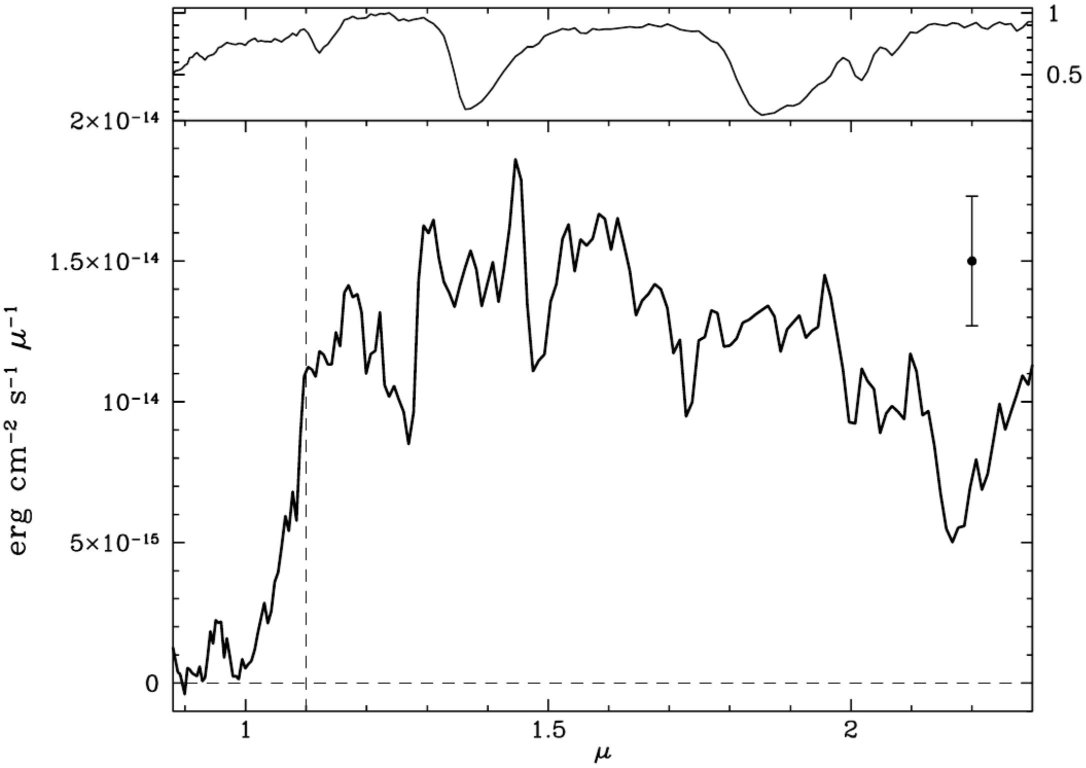

Figure 1.2: Spectrum of the most distant spectroscopically-confirmed cosmic object to date, the gamma-ray burst GRB 090423 at $z = 8.2$. This object was independently discovered by Salvaterra et al. (2009) and Tanvir et al. (2009). The figure is taken from Salvaterra et al. (2009). The bottom panel shows the spectrum of GRB 090423, while the top panel shows the atmospheric transparency convolved with the instrumental response.

Another alternative to studying and characterizing these distant galaxies is through (sub-)millimeter and radio observations. Several groups have tried to identify the [C II] 158 μm fine-structure transition line (hereafter [C II]) in the first spectroscopically identified galaxies in the epoch of reionization. The [C II] line is the dominant coolant of interstellar neutral gas and is one of the brightest lines in the spectrum of star-forming galaxies, accounting for up to 1% of the total far-infrared (FIR) luminosity in $z \sim 0$ main sequence galaxies. Studies of the [C II] line may also provide key insights into galaxy kinematics at the highest redshifts (see Carilli & Walter 2013 for a review). However, thus far, there are no convincing detections of [C II] emission from

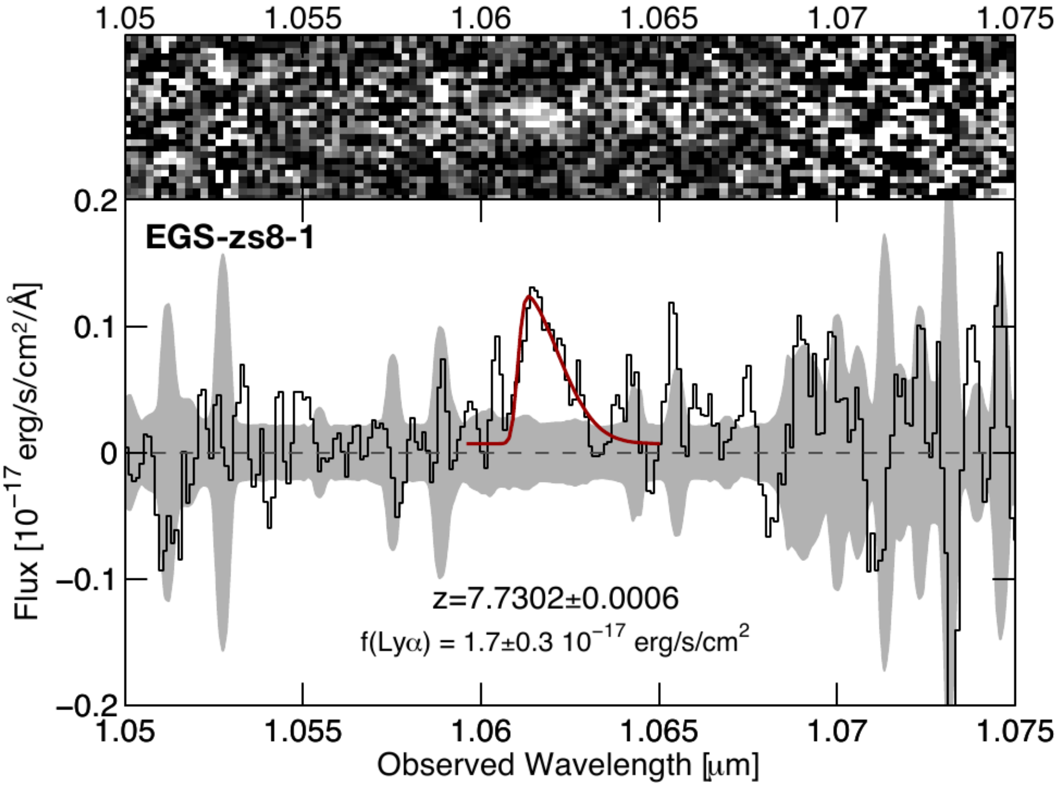

Figure 1.3: Spectra of the most distant spectroscopically-confirmed galaxy to date at $z = 7.7302 \pm 0.0006$ Figure taken from Oesch et al. (2015).

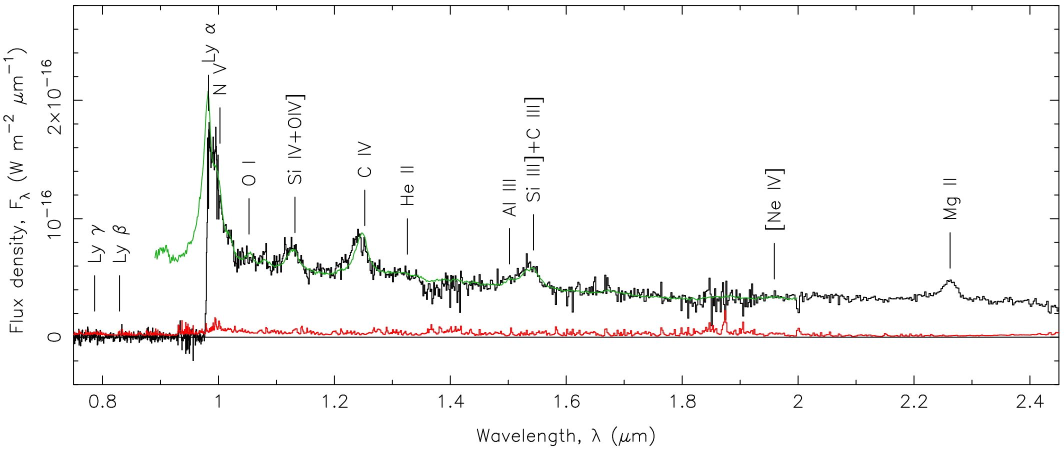

Figure 1.4: Spectrum of the most distant spectroscopically-confirmed quasar to date, ULAS J1120+0641 at $z = 7.1$. Figure adapted from Mortlock et al. (2011).

star-forming galaxies during the epoch of reionization (Walter et al. 2012a; Ouchi et al. 2013; Kanekar et al. 2013; González-López et al. 2014; Ota et al. 2014; Schaerer et al. 2015; Watson et al. 2015; but see also the recent work of Maiolino et al. 2015).

On the other hand, the [C II] line has been identified in a number of more extreme objects such as submillimeter galaxies and quasar host galaxies at $z \sim 6$ (Maiolino et al. 2005; Walter et al. 2009a; Riechers 2013; Wang et al. 2013; Willott et al. 2013, 2015). These objects are most likely the progenitors of massive early-type galaxies seen in the present universe (Volonteri 2010). Thus, luminous quasars are thought to be important tools to pinpoint the locations of these extreme galaxies in the early universe. Indeed, the [C II] line has even been detected in the host galaxy of the currently most distant known quasar at $z = 7.1$ (Venemans et al. 2012). Figure 1.5 shows a compilation of some of the results from observations of [C II] emission from $z \geq 6$ quasars. In Chapter 5, a bright [C II] emission from the $z = 6.54$ host galaxy of one of the brightest quasars discovered in this thesis will be presented. This quasar has the potential of becoming an important laboratory for the study of star formation and of the interstellar medium only ~ 800 Myr after the Big Bang.

1.4 The discovery of quasars[6]

During the 1950s and early 1960s the techniques in radio astronomy were developing fast. Astronomers were able to find the location of some radio sources that were accurate enough to allow for identification of their optical counterparts. Hazard et al. (1963) was able to identify an accurate position of the strong radio source 3C 273 (the object number 273 in the third Cambridge catalog of radio sources; Edge et al. 1959) through the method of lunar occultations. This measurement allowed Maarten Schmidt (1963) to identify an optical counterpart to 3C 273: a 13th magnitude star. However, Schmidt noted that this ‘star’ had a peculiar spectrum with very broad emission lines. To his surprise, Schmidt realized that the Hydrogen Balmer emission lines in the spectrum of this ‘radio-star’ were redshifted by 16% (see Figure 1.6). This implied a source with a huge energy at an extragalactic distance of ~ 770 Mpc ($z = 0.16$). With this interpretation in mind, the same year, Greenstein & Matthews (1963) recognized that the object 3C 48 (already thought to have a peculiar spectrum and previously classified as a ‘radio-star’) had an extragalactic nature as well. The emission lines in 3C 48 were redshifted by 36.7%, i.e., at a redshift of $z = 0.37$. In 1964, astronomers were already referring to these objects as *quasi-stellar radio objects* (Greenstein & Schmidt 1964), given their star-like appearance in visible light. However, just one year later, Sandage (1965) found that several other celestial ob-

---

[6] For readers interested in further details and anecdotes related to the discovery of quasars, they are referred to the following articles: Kellermann (2013, 2015), and Hazard et al. (2015)

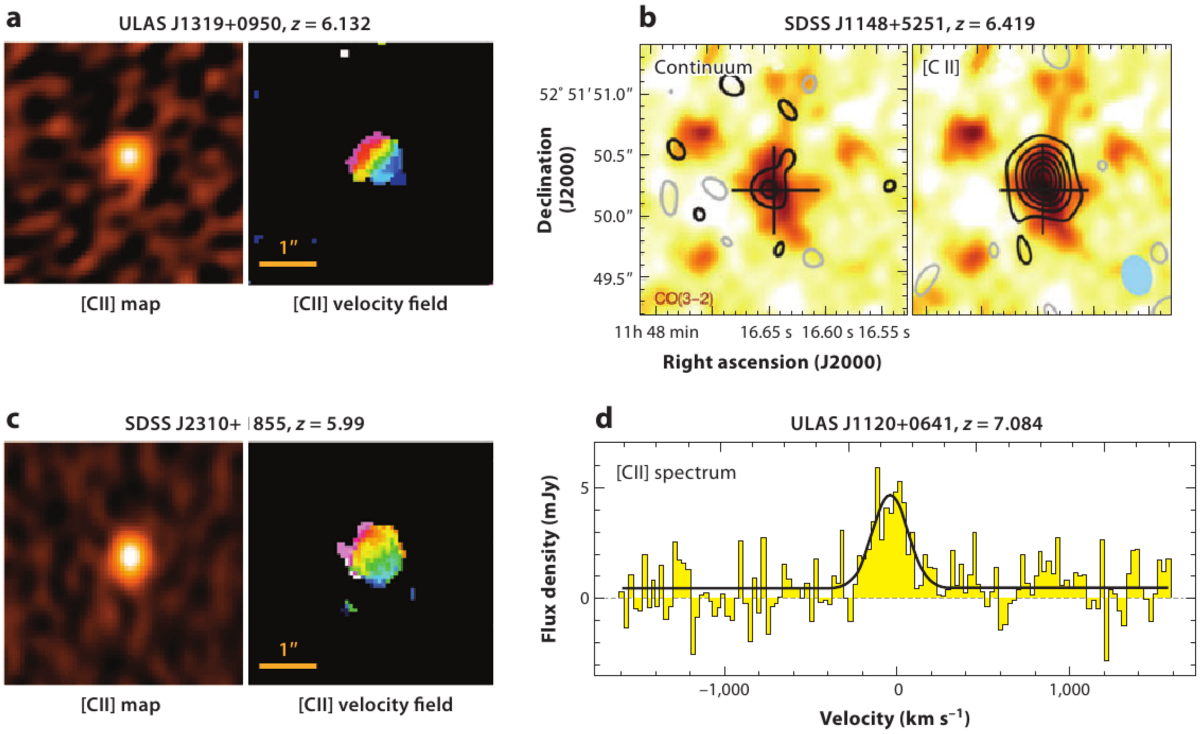

Figure 1.5: Examples of [C II] emission from $z \geq 6$ quasars. *a*, *c*) ALMA images for two $z \sim 6$ quasars (Wang et al. 2013). *b*) Very Large Array (VLA) CO maps and Plateu de Bure interferometer (PdBI) [C II] observations of the $z = 6.42$ quasar J1148+5251 (Walter et al. 2009b). *d*) PdBI [C II] spectrum of the most distant quasar currently know at $z = 7.1$ (Venemans et al. 2012). Figure taken from Carilli & Walter (2013).

jects had similar characteristics to these quasars but without the radio emission. Sandage called these objects quasi-stellar galaxies and described them as a ‘major new constituent of the universe’. Later on, radio-emission was no longer part of the definition of quasars and the name was eventually revised to quasi-stellar object (QSO). Nevertheless, in the literature and in the present thesis, the terms quasar and QSO are used indistinctly. These discoveries revolutionized the view of extragalactic astronomy. Even though 3C 273 and 3C 48 were not the most distant objects known at that time (Minkowski 1960 had already reported a redshift of $z = 0.46$ for the radio-galaxy 3C 295), within only a few years of their initial discovery in 1963, quasars with values of redshifts as high as $z \sim 2$ were being identified (e.g., Schmidt 1965; Arp et al. 1967).

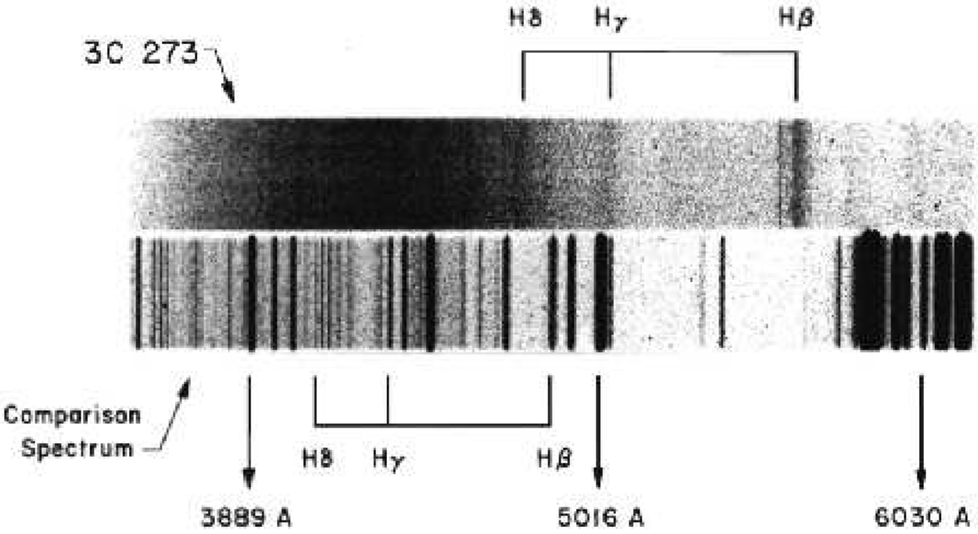

Figure 1.6: Discovery spectrum of 3C 273 by Maarten Schmidt, the first discovered quasar. The Balmer lines at a redshift of 0.16 are labeled. Figure from Hazard et al. (2015).

1.5 Quasars at $z > 5.5$

In this thesis, high-redshift means $z > 5.5$ and quasars at $z > 5.5$ are considered *distant*. This is an arbitrary definition, but is motivated by the fact that these quasars provide diagnostic tools to measure the universe's properties far back into the epoch of reionization (i.e., when the universe was less than 1 Gyr old; see Table 1.1 and Figure 1.1).

The first quasar at $z > 5.5$ was discovered by Fan et al. (2000b), and since then tremendous observational efforts have been made to find more of these objects. Over the years prior to this thesis (2000 – 2011), numerous studies established a sample of 60 quasars at $5.5 < z < 7.1$, mostly discovered using optical surveys such as the Sloan Digital Sky Survey (SDSS; Fan et al. 2001, 2003, 2004, 2006b) and the Canada-France High-z Quasar Survey (CFHQS; Willott et al. 2005a, 2007, 2009, 2010b,a). The left panel of Figure 1.7 shows the distribution of these 60 quasars color coded by their discovery surveys.

These high-redshift quasars have been extensively studied, and the main results include *a*) massive black holes ($> 10^8\,M_\odot$) are already in place less than a Gyr after the Big Bang (e.g., Willott et al. 2003; Kurk et al. 2007; Jiang et al. 2007b); *b*) quasar host galaxies are massive and intensely forming stars (up to $1000\,M_\odot\,\mathrm{yr}^{-1}$; see e.g., Walter et al. 2009a); and *c*) the neutral fraction of Hydrogen in the intergalactic medium increases rapidly above $z > 6$, providing strong constraints on the end of the epoch of reionization (e.g., Fan et al. 2006c). These findings strongly suggest that fundamental changes are happening at $z \sim 6-7$. In addition, the initial formation and growth of these supermassive black holes are still controversial and highly debated (e.g., Volonteri 2012; Volonteri & Bellovary 2012; Becerra et al. 2015; Glover 2015). Therefore, the discovery and characterization of a statistically significant sample of quasars in this redshift range is crucial to further study this important era in the history of the universe.

In this thesis 54 quasars at $z > 5.5$ were discovered and they are presented in Chapters 2 and 3. This includes the discovery of the first luminous $z > 5.5$ quasars in the southern sky, which constitutes the ideal ground for follow-up investigations using facilities such as ALMA, the Very Large Telescope (VLT), and the Magellan telescopes. This sample increases the number of $z > 5.5$ quasars known prior to this thesis by almost 100%, and spans about two decades in absolute luminosity. This is a much-needed increase in source number and luminosity range in order to characterize the typical $z \sim 6$ quasar population and therefore not just the 'tip of the iceberg'. The right panel of Figure 1.7 shows the status of the field by the end of this thesis, with a total of 135 quasars known at $z > 5.5$.

1.6 Radio-loud and radio-quiet quasars

As discussed in Section 1.4, quasars were originally considered radio-emitter objects (Schmidt 1963), however it was rapidly found that most quasars do not emit in radio or are weak radio emitters (Sandage 1965). More than 50 years after their discovery, the reasons behind the existence of quasars with strong and weak radio emission remain unknown. Kellermann et al. (1989) introduced the radio-loudness parameter, R, defined as the ratio between the radio and optical flux densities: $R = f_{\nu,5\,\mathrm{GHz}}/f_{\nu,4400\,\text{Å}}$. They found that quasars are drawn from a bimodal distribution and classify a quasar as radio-loud if $R > 10$. Figure 1.8 shows an example of this distribution showing the observed bimodality.

The existence of this radio-quiet/radio-loud bimodality is still a matter of debate. However, at low redshifts, it is now well established that roughly 10–20% of all quasars are radio-loud. It has been suggested that the radio-loud fraction (RLF) of quasars is a function of both optical luminosity and redshift (e.g., Padovani 1993; La Franca et al. 1994; Hooper et al. 1995). If a differential evolution between radio-quiet and radio-loud quasars exists, it could indicate changes in properties of black holes such as accretion modes, black hole masses, or spin (Rees et al. 1982; Wilson & Colbert 1995; Laor 2000). This could provide insights into why some quasars show a strong radio emission, while the majority of them are found to be radio-quiet sources.

Some studies have found evidence of such evolution. In particular, Jiang et al. (2007a) find that the RLF decreases strongly with increasing redshift at a given luminosity. For example, they

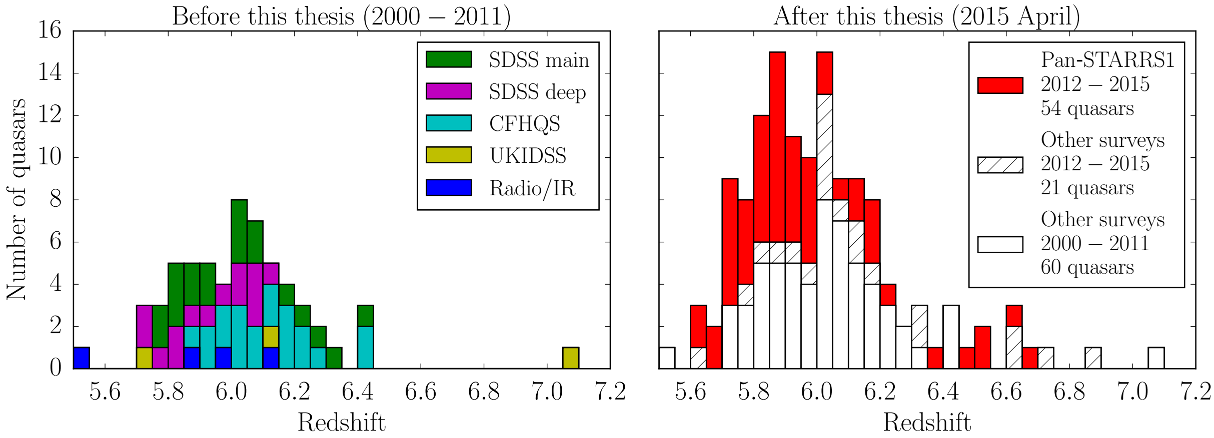

Figure 1.7: Redshift distribution of the $z > 5.5$ quasars known before and after this thesis. The discovery surveys are color coded.
Left: 60 quasars at $z > 5.5$ discovered before starting this thesis. SDSS main includes the quasars in Fan et al. (2000b, 2001, 2003, 2004, 2006b). SDSS deep includes the quasars in Mahabal et al. (2005); Goto (2006); Jiang et al. (2008); Wang et al. (2008); Jiang et al. (2009); De Rosa et al. (2011). CFHQS includes the quasars in Willott et al. (2007, 2009, 2010a,b). UKIDSS includes the quasars in Venemans et al. (2007a); Mortlock et al. (2009, 2011). Radio/IR includes quasars selected by their radio or infrared properties by Cool et al. (2006); McGreer et al. (2006); Stern et al. (2007); Zeimann et al. (2011).
Right: 135 quasars at $z > 5.5$ discovered by the end of this thesis. Pan-STARRS1 includes the quasars discovered in this thesis, which are also presented in Morganson et al. (2012); Bañados et al. (2014, 2015b); Venemans et al. (2015); and E. Bañados et al. in prep. Other surveys (2012 – 2015) includes the quasars in McGreer et al. (2013); Venemans et al. (2013); Wang et al. (2013); Carnall et al. (2015); Jiang et al. (2015); Kashikawa et al. (2015); Reed et al. (2015); Wu et al. (2015); B. P. Venemans et al. in prep; F. Wang et al. in prep; and S. J. Warren et al. in prep. Other surveys (2000 – 2011) are the same quasars of the left panel.

find that the RLF at $M_{2500} = -26$ declines from 24% to 4% as redshift increases from 0.5 to 3. Kratzer & Richards (2014) find a behavior in agreement with these findings in a similar redshift range ($z \sim 0.5 - 2.5$), but they also point out that the evolution of the RLF closely tracks the apparent magnitudes, which suggests a possible bias in the results. However, these results are in stark contrast to other studies finding little or no evidence of such evolution (e.g., Goldschmidt et al. 1999; Stern et al. 2000; Ivezić et al. 2002; Cirasuolo et al. 2003).

If an evolution of the RLF of quasars with redshift exists it should be most evident at the highest redshifts. In Chapter 3, four new radio-loud $z \sim 6$ quasars are identified—doubling the number of radio-loud quasars at these redshifts—and, using the available data in the literature, the RLF of quasars at $z \sim 6$, is restricted to $8.1^{+5.0}_{-3.2}\%$. This result is consistent with there being no evolution of the RLF with redshift, in contrast to what has been suggested by some studies at lower redshifts.

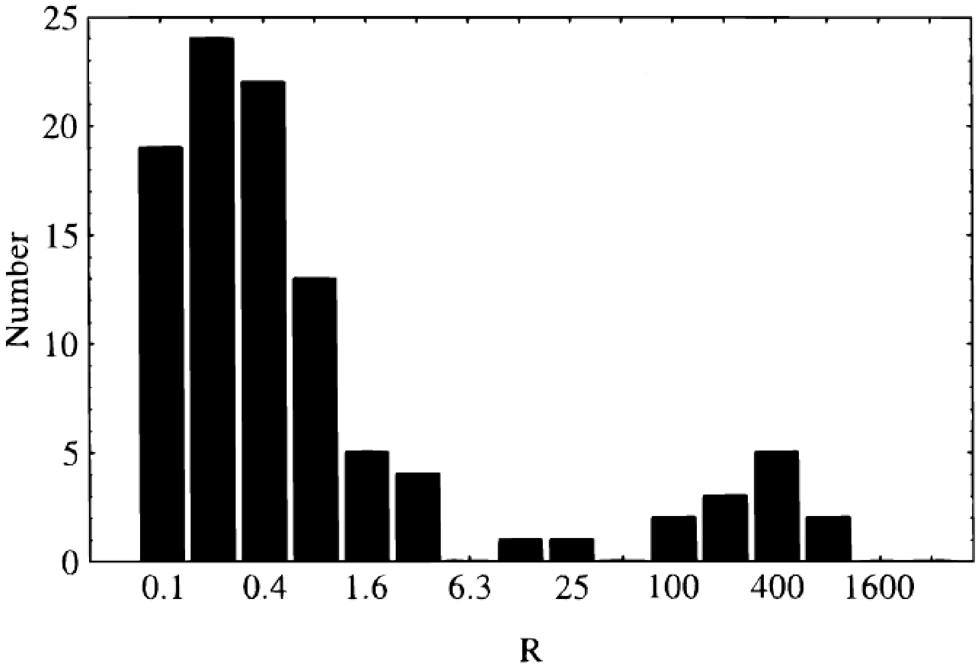

Figure 1.8: Example of the distribution of the radio-loudness parameter, $R = f_{\nu,5\,\mathrm{GHz}}/f_{\nu,4400\,\text{Å}}$, for the Palomar-Green quasar sample. An apparent bimodal distribution is evident. Figure taken from Falcke et al. (1996).

1.7 The environments of high-redshift quasars

The detection of black holes with masses $> 10^9\,M_\odot$ less than 1 Gyr after the Big Bang (e.g., De Rosa et al. 2014) is challenging for structure-formation models. Some models propose that supermassive black holes are hosted in high-density peak dark matter halos (e.g., Volonteri & Rees 2006; Costa et al. 2014). Numerical models predict that the most massive dark matter halos at $z \sim 6$ will evolve into massive $> 10^{14} - 10^{15}\,M_\odot$ clusters in the local Universe (e.g., Springel et al. 2005).

At redshifts of $2 < z < 5$, significant galaxy overdensities or protoclusters have been found around more than half a dozen luminous radio galaxies, confirming the idea that luminous AGNs pinpoint dense regions in the early universe (see, e.g., Venemans et al. 2007b and references therein). Nevertheless, the environments associated with other classes of AGNs, such as the optically selected quasars, are currently less well constrained.

Recently, there have been a number of studies which have found contradictory results regarding the galaxy environment of quasars at $z \sim 2$–5. In a narrow-band imaging survey around a quasar at $z = 2.4$, Cantalupo et al. (2012) found a much larger number of Lyman alpha emitters (LAEs) than in blank-field Lyα surveys. They suggest that this overdensity may be fully explained by quasar fluorescence, which boosts gas-rich but intrinsically faint LAEs, thereby increasing the number of detectable objects. Francis & Bland-Hawthorn (2004) carried out deep narrow-band observations centered on a $z = 2.168$ quasar. They were expecting to see 6–25 Lyα-fluorescent clouds and tens of normal LAEs, based on similar surveys. However, they did not detect any Lyα emission. In light of this result, Bruns et al. (2012) developed a semi-analytical model to interpret the observations. They concluded that the intense ultraviolet emission of the quasar may be suppressing the star formation in galaxies that are situated close to the quasar. This is consistent with the findings of Kashikawa et al. (2007), in which they found that LAEs are clustered around a quasar at $z = 4.87$ but avoid it in its immediate vicinity ($\sim$ 4.5 comoving Mpc). Swinbank et al. (2012), on the other hand, reported a galaxy overdensity an order of magnitude higher than what it would be expected in the field within 8.2 comoving Mpc of a quasar at $z = 4.528$. The same authors did not find clear evidence of overdensities in the fields of two quasars at $z \sim 2.2$. Very recently, Husband et al. (2013) noted that the luminous quasars in their sample at $z \sim 5$ were typically found in overdense regions. Nevertheless, they mentioned that even the richest quasar environment they studied was no richer than other structures identified in blank fields.

Since the discovery of $z \sim 6$ quasars, several groups have tried to identify galaxy overdensities associated with them. The results are as puzzling as those at lower redshifts. No unambiguous relation has been found between galaxy overdensities and $z \sim 6$ quasars, mainly due to the difficulty of finding galaxies with accurate redshifts at $z \sim 6$. So far, these efforts have mainly been based on studies of continuum i-dropout galaxies, characterized by a large magnitude difference between the i and z bands (i.e., using the same technique that was used to detect the quasars). This technique probes a redshift range of approximately $\Delta z \approx 1$, which is large enough to identify galaxies that are not physically related to the quasar. Willott et al. (2005b) carried out a survey with Gemini of three $z > 6.2$ quasars. They found no evidence of an overdensity of i-dropouts in the 27 arcmin^2 field surrounding the quasars. Stiavelli et al. (2005), however, came to a different conclusion for one of these fields. They observed a small field around SDSS J1030 + 0524 at $z = 6.28$ with the Advanced Camera for Surveys (ACS) of the *HST* and found more than twice the number of dropouts with $i_{775} - z_{850} > 1.5$ expected from statistics obtained by the Great Observatories Origins Deep Survey (GOODS). The ACS field used in this study only surveys the region close to the quasar, but the observations are more sensitive to fainter galaxies. Stiavelli et al. (2005) explain that the difference is that their data set is deeper and the majority of the excess sources are fainter than the limiting magnitude of Willott et al. (2005b). Using ACS observations, Zheng et al. (2006) found an overdensity in the field of a radio-loud quasar at $z = 5.8$: the surface density of $1.3 < i - z < 2.0$ sources was about six times higher than the number expected from ACS deep fields. Furthermore, Ajiki et al. (2006) presented corroborative evidence of the overdensity reported by Zheng et al. (2006). Kim et al. (2009) studied i-dropout galaxies in five fields centered on $z \sim 6$ quasars using ACS and reported that regions near quasars are sometimes overdense and sometimes underdense. From a theoretical perspective, Overzier et al. (2009), using semi-analytic galaxy models in combination with the dark matter Millennium simulation (Springel et al. 2005; De Lucia & Blaizot 2007), showed that the lack of neighboring galaxies as found by Willott et al. (2005b) and Kim et al. (2009) was not inconsistent with quasars occupying massive halos due to a combination of depth, field-of-view, and projection effects. However, the same simulations also predicted that there should be regions much more overdense than those seen around any $z \sim 6$ quasar observed to date. Utsumi et al. (2010) found an overdensity of i-dropout galaxies around a quasar at $z = 6.43$, but at the same time these objects avoided the center near the quasar (∼ 15 comoving Mpc), similar to what Kashikawa et al. (2007) reported at lower redshift. At high redshift, it is very hard to obtain spectra of faint galaxies, but there are a few cases at $z \sim 5$, based on available spectroscopy, where quasars are located in regions with an overdensity of galaxies (Capak et al. 2011; Walter et al. 2012b; Husband et al. 2013). It is worth noting that in some of these cases, the quasars do not reside in the center of the overdensities but at distances of ∼ 5–15 comoving Mpc. It is important to note that a few galaxy overdensities or protoclusters have been discovered serendipitously in random fields (e.g., Ouchi et al. 2005 at $z \sim 5.7$; Toshikawa et al. 2012 at $z \sim 6$; Trenti et al. 2012 at $z \sim 8$), suggesting that not all overdensities host AGNs. However, this could also be explained by the duty cycle of AGN activity.

In summary, current dropout studies at $z \sim 6$ give partly contradictory results. An efficient alternative is to search for LAEs in a narrow redshift range near the quasar using narrow-band filters. However, mainly due to the extremely low density of $z \sim 6$ quasars of $\sim 6 \times 10^{-10}$ Mpc^{-3} (Fan et al. 2004), until recently no high-redshift quasars were known to have a redshift that shifts the Lyα line into a region of the optical spectrum that is devoid of bright sky emission lines. These atmospheric windows, for example around 8160 Å and 9120 Å, have successfully been used by blank field Lyα surveys to search for galaxies at $z = 5.7$ and $z = 6.6$ (e.g., Hu et al. 1999, 2002; Ouchi et al. 2005, 2008). The first study using narrow-band imaging to detect the Lyα-emitting halo and possibly companions around quasars at $z > 6$ was carried out using the *HST* by Decarli et al. (2012). Even though the goal of these observations was to detect the Lyα halo around the quasars, they did not find any companions in the immediate vicinity of two $z > 6$ quasars. This latter result was not unexpected because of the small field-of-view covered by their study (∼ 1 arcmin^2). In Chapter 4, the first ground-based study to search for LAEs around a $z \sim 6$ quasar using wide (∼ 50 arcmin^2) and deep (mag∼ 26) narrow- and broad-band photometry is presented.

Chapter 2

The Pan-STARRS1 distant quasar survey: 92 quasars within the 1st Gyr of the universe †

2.1 Context

High-redshift quasars provide us with unique information about the evolution of supermassive black holes (SMBHs), their host galaxies, and the intergalactic medium (IGM) at early cosmic time. Since distant ($z \gtrsim 5.5$) luminous quasars are rare, with an estimated source density of $\sim 1\,\mathrm{Gpc}^{-3}$ (e.g., Fan et al. 2004; Willott et al. 2010b), surveys covering a large area of the sky are required to uncover the distant quasar population. Over the last 15 years more than 60 quasars with redshifts between $5.5 < z < 6.5$ have been discovered in various surveys (e.g., Fan et al. 2006c; Jiang et al. 2008; Mortlock et al. 2009; Willott et al. 2010b; Carnall et al. 2015; Jiang et al. 2015; Reed et al. 2015). Most of these quasars have been found in optical surveys such as the Sloan Digital Sky Survey (SDSS) and the Canda-France High-z Quasar Survey (CFHQS) by looking for sources with a large break between the optical i and z bands, the so-called i-band dropouts or i-dropouts. To find quasars beyond $z \sim 6.5$, wide-field surveys with coverage beyond $\sim 1\,\mu$m are needed.

Recently, a handful of quasars above $z > 6.5$ have been discovered in near-infrared (NIR) surveys. Mortlock et al. (2011) presented a quasar at $z = 7.1$ discovered in the UK infrared Telescope Infrared Deep Sky Survey (UKIDSS; Lawrence et al. 2007), while Venemans et al. (2013) reported three quasars at $6.6 < z < 6.9$ from the Visible and Infrared Survey Tele-

---

† This chapter is based on the following papers: Bañados et al. (2014); Venemans et al. (2015), and Bañados et al. in prep.

scope Kilo-Degree Infrared Galaxy (VIKING) survey. Detailed studies of these four $z > 6.5$ quasars have provided insights into the properties of the universe when it was $\sim$ 800 Myr old. For example, the optical spectrum of the $z = 7.1$ quasar places constraints on the fraction of neutral hydrogen (Mortlock et al. 2011; Bolton et al. 2011), while Simcoe et al. (2012) use near-infrared spectroscopy to put limits on the metal enrichment of the IGM up to $z \sim 7$. Furthermore, these quasars set a lower limit to the number density of SMBHs at $z > 6.5$: $\rho(M_{\rm BH} > 10^9\,M_\odot) > 1.1 \times 10^{-9}\,{\rm Mpc}^{-3}$ (Venemans et al. 2013; De Rosa et al. 2014). The main limitation of both UKIDSS and VIKING surveys to find a statistical number of $z > 6.5$ quasars is that they cover only a small fraction of the extragalactic sky: UKIDSS has imaged $\sim 4000\,{\rm deg}^2$, while VIKING will cover an area of $1500\,{\rm deg}^2$.

The Panoramic Survey Telescope & Rapid Response System 1 (Pan-STARRS1, PS1; Kaiser et al. 2002, 2010) 3π has surveyed all the sky above declination $-30°$ in the filters $g_{\rm P1}$, $r_{\rm P1}$, $i_{\rm P1}$, $z_{\rm P1}$, and $y_{\rm P1}$ (Stubbs et al. 2010; Tonry et al. 2012). The PS1 3π survey mapped each region of the sky in two sets of pairs per filter yearly. Each pair is taken during the same night. The second pair for $g_{\rm P1}$, $r_{\rm P1}$, and $i_{\rm P1}$ is obtained during the same lunation, whereas $z_{\rm P1}$ and $y_{\rm P1}$ are observed approximately 5–6 months later. There are some regions of the sky that are not covered or have less coverage (i.e., 0 or 2 exposures per year) than the average survey. This is mostly due to weather restrictions (especially for $g_{\rm P1}$, $r_{\rm P1}$, and $i_{\rm P1}$ bands because their observation pairs are taken within the same month) or areas falling into the camera chip gaps.

PS1 presents an excellent opportunity to perform high-redshift quasar searches for three reasons: (1) it covers a larger area than previous high-redshift quasar surveys, especially in the southern hemisphere; (2) it goes more than one mag deeper than SDSS in the reddest bands where $z \sim 6$ quasars are visible; and (3) the additional y-band ($\lambda_{\rm eff} = 9620\,$Å; FWHM= 890 Å; Tonry et al. 2012) enables the search for luminous quasars beyond the SDSS limit ($z > 6.5$) over more than $20,000\,{\rm deg}^2$ of extragalactic sky by selecting sources with a red $z_{\rm P1} - y_{\rm P1}$ color (z-dropouts). In mid-2014, PS1 produced its second internal release of the 3π stacked catalog (PV2), which is based on the co-added PS1 exposures (see Metcalfe et al. 2013). This is the catalog used for the present work, which includes data obtained primarily during the period 2010 May–2014 March. The PS1 magnitudes presented in this chapter supersede the magnitudes reported in Bañados et al. (2014, 2015b) and Venemans et al. (2015), which were based on the PS1 PV1 catalog.

This chapter is organized as follows. In Section 2.2, we introduce our final color selection procedures for i-dropout and z-dropout quasars from the PS1 stacked catalog. The imaging and spectroscopic follow-up observations are presented in Section 2.4. In Section 2.5, we present the spectra of the 54 PS1 discovered quasars at $z > 5.6$ and discuss some individual objects. In Section 2.6, we introduce the PS1 distant quasar sample, which consists of 92 quasars at $z > 5.6$ that were discovered by PS1 or that satisfy the selection criteria presented in this thesis. We finally summarize our results in Section 2.7.

The International Astronomical Union (IAU) naming convention for non-transient objects discovered using the Pan-STARRS1 survey is "PSO JRRR.rrrr+DD.dddd" where RRR.rrrr and +DD.dddd are the right ascension and declination in decimal degrees (J2000), respectively. For PS1 discovered quasars we will use abbreviated names of the form "PRRR+DD", while quasars discovered by other surveys will be named as "Jhhmm+ddmm".

For future references, Figure 2.1 shows the photometric filters most used in this chapter as well as a composite quasar spectrum redshifted to $z = 6$ in which key spectral emission lines are labeled. Table A.1 in the Appendix A lists the coordinates and redshifts of all the $z > 5.5$ quasars known by the end of this thesis.

All magnitudes throughout this chapter are given in the AB system, and we adopt a flat ΛCDM cosmology with $H_0 = 67.7\,\mathrm{km\,s^{-1}\,Mpc^{-1}}$, $\Omega_M = 0.307$, and $\Omega_\Lambda = 0.693$ (Planck Collaboration et al. 2015b).

2.2 Candidate selection

Quasars at redshifts $z \gtrsim 5.7$ are observationally characterized by their blue continuum (i.e., blue $y - J$ color). In addition, $5.7 \lesssim z \lesssim 6.5$ and $z \gtrsim 6.5$ are distinguished by their very red $i - z$ (i-dropout) and $z - y$ (z-dropout) colors, respectively. They are very faint or completely undetected in the i or z bands due to the optically thick Lyα forest at these redshifts, causing most of the light coming from wavelengths $\lambda_{\mathrm{rest}} < 1216\,\text{Å}$ to be absorbed.

To determine our initial selection criteria, we have taken the composite quasar spectrum from Decarli et al. (2010), which consists of 96 bright quasars at $0 < z < 3$. We chose this template because at red wavelengths it is less affected by host galaxy contamination than other composite spectra in the literature (e.g., Francis et al. 1991; Vanden Berk et al. 2001) and it samples the rest frame wavelengths of $5.7 < z < 7.2$ quasars in the PS1 filters. For $\lambda_{\mathrm{rest}} < 1010\,\text{Å}$, we replaced the template with a flat f_λ, normalized to the UV continuum blueward of Lyα. We then applied the intergalactic attenuation correction from Meiksin (2006), tuning the optical depth, τ_{IGM}, to match the transmitted flux blueward of Lyα in the $z \sim 6$ SDSS composite spectrum from Fan et al. (2006b). Figure 2.2 shows the expected track of our quasar template through the $i_{\mathrm{P1}} - z_{\mathrm{P1}}$ and $z_{\mathrm{P1}} - y_{\mathrm{P1}}$ colors as the redshift is increased from $z = 5.0$ to $z = 6.5$. We are also interested in the location of our potential contaminants in this diagram. Since the observational color scatter for brown dwarfs is significant, we compared with real PS1 colors of known brown dwarfs. We cross-matched our compilation of 1697 L, T, and Y dwarfs with the PS1 stacked catalog, taking the closest match within a 2″ radius. There are 850 matches[1] (657 and 193 L and T dwarfs, respectively) with measurements in the $i_{\rm P1}$, $z_{\rm P1}$, and $y_{\rm P1}$ bands, and with a signal-to-noise ratio (S/N) $>$ 5 in the $z_{\rm P1}$ and $y_{\rm P1}$ bands. The PS1 colors of brown dwarfs are represented by small circles in Figure 2.2.

Since high-redshift quasars are very rare and because of the high number of other sources (or artifacts) that mimic high-redshift quasar colors, we cleaned our sample in several steps:

1. We selected initial high-redshift quasar candidates from the PS1 stacked database (see Section 2.2.1).
2. At the position of each candidate, we applied forced aperture photometry in the stacked images in order to corroborate the catalog colors (see Section 2.2.2).
3. This was followed by forced photometry in all the detection-band (i.e., $z_{\rm P1}$ and/or $y_{\rm P1}$) single-epoch images to remove artifacts (see Section 2.2.3).
4. We then matched the candidate list to public infrared surveys to eliminate or prioritize candidates using the extra information provided by these surveys (see Section 2.3).
5. Before following-up the candidates, we visually inspected their PS1 stacked and single-epoch images (and infrared images when available) to ensure that they were real astrophysical objects.
6. We then obtained optical and NIR follow-up photometry (see Section 2.4.1).

---

[1] The discovery papers for these L and T dwarfs are: Kirkpatrick et al. (1997); Martín et al. (1998); Kirkpatrick et al. (1999); Martín et al. (1999); Zapatero Osorio et al. (1999); Fan et al. (2000a); Kirkpatrick et al. (2000); Zapatero Osorio et al. (2000); Gizis et al. (2001); Barrado y Navascués et al. (2002); Burgasser et al. (2002); Geballe et al. (2002); Hawley et al. (2002); Liu et al. (2002); Schneider et al. (2002); Cruz et al. (2003); Kendall et al. (2003); Lépine et al. (2003); Wilson et al. (2003); Kendall et al. (2004); Knapp et al. (2004); Tinney et al. (2005); Artigau et al. (2006); Chiu et al. (2006); Liebert & Gizis (2006); McElwain & Burgasser (2006); Cruz et al. (2007); Kendall et al. (2007a,b); Lodieu et al. (2007); Stern et al. (2007); Chiu et al. (2008); Metchev et al. (2008); Phan-Bao et al. (2008); Pinfield et al. (2008); Reid et al. (2008); Bouvier et al. (2009); Scholz et al. (2009); Sheppard & Cushing (2009); Zhang et al. (2009); Bowler et al. (2010); Burningham et al. (2010); Kirkpatrick et al. (2010); Lucas et al. (2010); Martín et al. (2010); Schmidt et al. (2010); Scholz (2010a,b); Aberasturi et al. (2011); Albert et al. (2011); Artigau et al. (2011); Deacon et al. (2011); Geißler et al. (2011); Gizis et al. (2011b,a); Kirkpatrick et al. (2011); Mainzer et al. (2011b); Matsuoka et al. (2011); Scholz et al. (2011); Deacon et al. (2012); Gizis et al. (2012); Lodieu et al. (2012b,a); Luhman et al. (2012); Scholz et al. (2012); Beamín et al. (2013); Best et al. (2013); Bihain et al. (2013); Boudreault & Lodieu (2013); Burningham et al. (2013); Castro et al. (2013); Day-Jones et al. (2013); Gomes et al. (2013); Liu et al. (2013); Mace et al. (2013); Marocco et al. (2013); Thompson et al. (2013); Cushing et al. (2014); Kirkpatrick et al. (2014); Marocco et al. (2014); Reylé et al. (2014); Lodieu et al. (2014); Marocco et al. (2015)

7. Finally, we obtained spectra to confirm the nature and redshifts of the remaining candidates (see Section 2.4.2).

2.2.1 The Pan-STARRS1 catalog

We excluded candidates in the Galactic plane ($|b| < 20°$), and in M31 ($7° <$R.A.$< 14°$; $37° <$ Decl.$< 43°$) from our search. We also excluded those measurements for which the Image Processing Pipeline (IPP; Magnier 2006, 2007) flagged the result as suspicious (see Table B.1 in Appendix B for details). We required than more than 85% of the expected point-spread function (PSF)-weighted flux in the $i_{\rm P1}z_{\rm P1}y_{\rm P1}$ ($z_{\rm P1}y_{\rm P1}$) bands was located in valid pixels (i.e., that the PS1 catalog entry has `PSF_QF` > 0.85) for i-dropout (z-dropout) criteria. Quasars at $z > 5.5$ are expected to be unresolved. To avoid extended sources we required the differences between the PSF and aperture magnitudes (${\rm mag}_{\rm P1,ext}$) to be consistent with each other (see below). When referring to limiting magnitudes (${\rm mag}_{\rm P1,lim}$) throughout the text, these correspond to 3σ-limiting magnitudes.

2.2.1.1 *i*-dropout search ($5.7 \lesssim z \lesssim 6.2$)

This is the selection on which we initially focused and therefore the one with the most comprehensive follow-up. Our initial search (Bañados et al. 2014) explored this color region, given that quasars on the redshift range $5.7 \lesssim z \lesssim 6.2$ are best differentiated from brown dwarfs in PS1 color space (see upper left region in Figure 2.2). The selection criteria can be summarized as follows:

$$
\begin{aligned}
{\rm S/N}(z_{\rm P1}) > 10 && (2.1a)\\
{\rm S/N}(y_{\rm P1}) > 5 && (2.1b)\\
(({\rm S/N}(i_{\rm P1}) \geq 3)\ {\rm AND}\ (i_{\rm P1} - z_{\rm P1} > 2.2))\ {\rm OR} && \\
(({\rm S/N}(i_{\rm P1}) < 3)\ {\rm AND}\ (i_{\rm P1,lim} - z_{\rm P1} > 2.0)) && (2.1c)\\
z_{\rm P1} - y_{\rm P1} < 0.5 && (2.1d)\\
({\rm S/N}(r_{\rm P1}) < 3)\ {\rm OR}\ (r_{\rm P1} - z_{\rm P1} > 2.2) && (2.1e)\\
{\rm S/N}(g_{\rm P1}) < 3) && (2.1f)\\
(z_{\rm P1,ext} < 0.3)\ {\rm OR}\ (y_{\rm P1,ext} < 0.3) && (2.1g)
\end{aligned}
$$

2.2.1.2 *i*-dropout search ($6.2 \lesssim z \lesssim 6.5$)

The color region explored by these PS1 selection criteria is highly contaminated, especially by L and T dwarfs (see upper right region in Figure 2.2). Our selection criteria can be described as:

$$\mathrm{S/N}(z_{\mathrm{P1}}) > 7 \tag{2.2a}$$
$$\mathrm{S/N}(y_{\mathrm{P1}}) > 7 \tag{2.2b}$$
$$\begin{aligned}&((\mathrm{S/N}(i_{\mathrm{P1}}) \geq 3)\ \mathrm{AND}\ (i_{\mathrm{P1}} - z_{\mathrm{P1}} > 2.2))\ \mathrm{OR}\\ &((\mathrm{S/N}(i_{\mathrm{P1}}) < 3)\ \mathrm{AND}\ (i_{\mathrm{P1,lim}} - z_{\mathrm{P1}} > 2.2))\end{aligned} \tag{2.2c}$$
$$z_{\mathrm{P1}} - y_{\mathrm{P1}} \geq 0.5 \tag{2.2d}$$
$$(\mathrm{S/N}(r_{\mathrm{P1}}) < 3) \tag{2.2e}$$
$$\mathrm{S/N}(g_{\mathrm{P1}}) < 3) \tag{2.2f}$$
$$(z_{\mathrm{P1,ext}} < 0.3)\ \mathrm{OR}\ (y_{\mathrm{P1,ext}} < 0.3) \tag{2.2g}$$

2.2.1.3 *z*-dropout search ($z \gtrsim 6.5$)

The PS1 selection for *z*-dropout candidates is:

$$\mathrm{S/N}(y_{\mathrm{P1}}) > 7 \tag{2.3a}$$
$$\begin{aligned}&((\mathrm{S/N}(z_{\mathrm{P1}}) \geq 3)\ \mathrm{AND}\ (z_{\mathrm{P1}} - y_{\mathrm{P1}} > 1.4))\ \mathrm{OR}\\ &((\mathrm{S/N}(z_{\mathrm{P1}}) < 3)\ \mathrm{AND}\ (z_{\mathrm{P1,lim}} - y_{\mathrm{P1}} > 1.4))\end{aligned} \tag{2.3b}$$
$$(\mathrm{S/N}(i_{\mathrm{P1}}) < 3) \tag{2.3c}$$
$$(\mathrm{S/N}(r_{\mathrm{P1}}) < 3) \tag{2.3d}$$
$$\mathrm{S/N}(g_{\mathrm{P1}}) < 3) \tag{2.3e}$$
$$y_{\mathrm{P1,ext}} < 0.3 \tag{2.3f}$$

For bright sources ($y_{\mathrm{P1}} < 19.5$), we applied the same criteria, but we relaxed our limits in the g_{P1}, r_{P1}, and i_{P1} bands, requiring S/N < 5.

However, the total number of *z*-dropouts selected from the PS1 catalog wass much larger than for the *i*-dropout searches. This is expected, given that these candidates are basically detected only in one band (y_{P1}) and therefore many of them are probably spurious objects. Hence, in order to clean and reduce the number of *z*-dropouts, in contrast to the procedure followed for

i-dropouts, we first required the z-dropout candidates to have a counterpart in public infrared surveys (Section 2.3). Then, we performed forced photometry on the images (Sections 2.2.2 and 2.2.3).

2.2.2 Forced photometry on stacked images

In order to confirm and check the PS1 catalog colors, we implemented an algorithm to compute aperture photometry on the stacked images. This algorithm retrieves $5' \times 5'$ stacked postage stamps images centered on the candidates and their respective stacked catalogs. We then computed the aperture that maximizes the S/N of bright stars in the field and used it to obtain the aperture photometry of the respective candidate in the image. Since the aperture photometry is noisier than the PSF photometry, we relaxed the color criteria, requiring them to be consistent within 2σ with our own measurements from the stacked images. This step mainly eliminated candidates that had bad $i_{\rm P1}$ or $z_{\rm P1}$ photometry in the catalog for i-dropouts and z-dropouts, respectively. This was not surprising since our candidates were very faint or not detected in the $i_{\rm P1}$ or $z_{\rm P1}$ bands, and large photometric errors were expected.

We found empirically that when the diameter of our computed optimal apertures (aper_diameter) was smaller than $0\overset{''}{.}75$ or greater than $3\overset{''}{.}75$, the images had evident problems mostly related to background subtraction, causing unreliable catalog magnitudes. Thus, we only considered candidates whose optimal apertures in the $i_{\rm P1}$, $z_{\rm P1}$, and $y_{\rm P1}$ bands were $0\overset{''}{.}75 <$ aper_diameter $< 3\overset{''}{.}75$.

2.2.3 Single epoch forced photometry

It is possible that a fraction of our candidates are moving objects, spurious objects, or artifacts that appear as very bright sources in some of the individual exposures but do not appear in others. After stacking the images, such objects could still look like reasonable quasar candidates. For candidates selected using the criteria in Section 2.2.1.1, we performed forced aperture photometry on all *individual* single epoch z band images (the detection band with the highest S/N) by using the optimal aperture determined in Section 2.2.2. We flagged the images in which the S/N at the position of the candidate was S/N < 3 while, based on the magnitude of the candidate measured on the stacked image, a S/N > 5 was expected. We retained candidates that had less than 40% flagged images and in which the standard deviation of the single epoch magnitudes was less than 1 mag. These criteria were determined based on tests performed with known quasars and objects that had a counterpart in SDSS and in the *Wide-field Infrared Survey Explorer* (*WISE*; Wright et al. 2010). The same strategy was applied to the candidates selected according to the criteria of Sections 2.2.1.2 and 2.2.1.3. For the former (i-dropouts at $6.2 \lesssim z \lesssim 6.5$), forced photometry was performed in the z and y images, while for the latter (z-dropouts at $z \gtrsim 6.5$) it was only performed in the y images.

2.3 Public infrared surveys

We matched our sources with several public infrared surveys to extend and verify the photometry of the quasar candidates. The extra information was used to either remove foreground interlopers or to prioritize the subsequent follow-up. Note that a counterpart in at least one of the following surveys is a requirement for our current selection of z-dropout candidates.

2MASS: The PS1 candidates were matched within $3''$ with the Two Micron All Sky Survey (2MASS; Skrutskie et al. 2006). This is a rather shallow all-sky survey in the J, H, and K bands. Nevertheless, given its large area coverage, it is ideal to eliminate bright foreground interlopers and even find extremely bright high-redshift quasars (Wu et al. 2015). In order to remove bright cool dwarfs, we required our candidates to be undetected in 2MASS or that their $y_{\rm P1} - J$ color to be $y_{\rm P1} - J < 1$ (see Figure 2.3).

UKIDSS: All of our objects were matched with the NIR data of the UKIDSS survey (Lawrence et al. 2007) using a $2''$ matching radius. The UKIDSS Large Area Survey (LAS) provides Y, J, H, and K imaging over $\sim$4000 deg^2. We kept the candidates that had $Y - J < 0.6$ or $y_{\rm P1} - J < 1$ and removed the rest from our candidate lists (see Figure 2.3).

UHS: The UKIRT Hemisphere Survey (UHS)[2] provides J band imaging over $\sim$12000 deg^2 to a 5σ depth of $J \approx 20.5$. Our candidates were matched to objects in the UHS survey within $2''$. We applied the same color criteria as for our 2MASS matched list.

VHS: For z-dropout candidates in the area $150° <$ R.A. $< 240°$ and $-20° <$ Decl. $< 0°$, aperture photometry was performed on the Y, J, H, and K_s images of the VISTA Hemisphere Survey (VHS; McMahon et al. 2013). We applied the same color criteria as for our UKIDSS matched list.

WISE: WISE (Wright et al. 2010) surveyed the entire mid-infrared sky in four bands centered at 3.4, 4.6, 12, and 22 μm (hereafter W_1, W_2, W_3, and W_4). The NEOWISE observations (Mainzer et al. 2011a) surveyed 70% of the sky in W_1 and W_2. Both surveys were combined to produce the ALLWISE catalog[3]. Even though more than 60% of the known $z > 6$ quasars are detected in the ALLWISE catalog, a selection of high-redshift quasars purely based on *WISE* is extremely

---

[2] `http://casu.ast.cam.ac.uk/wfcamsp/uhs`

[3] `http://wise2.ipac.caltech.edu/docs/release/allwise`

difficult owing to their *WISE* colors, which are hard to distinguish from the much more numerous active galactic nuclei (AGNs) and star-forming galaxies at lower redshifts (Blain et al. 2013). Nevertheless, the combination of *WISE* and optical surveys is a powerful tool to remove or avoid a large amount of the main foreground contaminants of optical surveys, i.e., cool dwarfs (see Figure 2.4). We cross-matched our quasar candidates with the ALLWISE catalog within 3″. At this stage, we only used the *WISE* information to prioritize some candidates for follow-up observations. Objects with S/N > 3 in W_1 and W_2 were assigned a higher priority if their colors fulfilled the additional criteria:

$$\begin{aligned} -0.2 < W_1 - W_2 < 0.85 \\ W_1 - W_2 > -1.45 \times (y_{\rm P1} - W_1) - 0.455. \end{aligned}$$

For the few objects with S/N > 3 in W_3, a higher priority was assigned if

$$W_2 - W_3 > 0$$

Recently, in part motivated by the quasar selection criteria presented in Carnall et al. (2015), we added an additional prioritization for *i*-dropout candidates:

$$z_{\rm P1} - W_2 < 2.5.$$

The dashed lines in Figure 2.4 show our prioritization criteria. Objects undetected in the ALLWISE catalog or with S/N < 3 in W_1 or W_2 were assigned an intermediate priority, while the remaining candidates were given a low priority. Note that we have not rejected candidates because of their *WISE* colors and we have even discovered quasars that do not fulfill our prioritization criteria.

2.4 Follow-up observations

2.4.1 Photometry

Obtaining deeper optical and NIR photometry is essential for confirming the reality and colors of our candidates and removing lower-redshift interlopers with similar optical colors to quasars or contaminants that could have scattered into our color selection. The photometric follow-up observations were carried out over different observing runs and different instruments. We obtained optical and NIR images with the MPG 2.2 m/GROND (Greiner et al. 2008), NTT/EFOSC2 (Buzzoni et al. 1984), NTT/SofI (Moorwood et al. 1998), the Calar Alto (CAHA) 3.5 m/Omega2000 (Bizenberger et al. 1998; Bailer-Jones et al. 2000), and the CAHA 2.2 m/CAFOS[4]; see Table 2.1 for the details of the observations.

The data reduction was carried out using standard reduction steps, consisting of bias subtraction, flat fielding, sky subtraction, image alignment, and finally stacking. The photometric zero points of the stacked images were calculated by using at least 5 stellar sources ($\mathrm{mag}_{\mathrm{P1,ext}} < 0.2$) in the images with magnitudes and colors from the PV1 catalog. Since all the filter curves are not exactly the same, conversions between PS1 and GROND/EFOSC2/Omega2000/CAFOS magnitudes were computed as follows: first, we computed spectral synthetic magnitudes of template stars of various spectral classes (O – K) in each photometric system. We then produced color–color diagrams for various filters (e.g., $i_{\mathrm{G}} - i_{\mathrm{P1}}$ vs $i_{\mathrm{P1}} - z_{\mathrm{P1}}$). Through these plots we have inferred the photometric system correction terms via linear fits of the stellar loci. The color conversions are:

$$\begin{aligned}
g_{\mathrm{G}} &= g_{\mathrm{P1}} + 0.332 \times (g_{\mathrm{P1}} - r_{\mathrm{P1}}) + 0.055 \\
r_{\mathrm{G}} &= r_{\mathrm{P1}} + 0.044 \times (r_{\mathrm{P1}} - i_{\mathrm{P1}}) - 0.001 \\
i_{\mathrm{G}} &= i_{\mathrm{P1}} - 0.089 \times (r_{\mathrm{P1}} - i_{\mathrm{P1}}) + 0.001 \\
z_{\mathrm{G}} &= z_{\mathrm{P1}} - 0.214 \times (z_{\mathrm{P1}} - y_{\mathrm{P1}}) \\
J_{\mathrm{G}} &= J_{\mathrm{2M}} - 0.012 \times (J_{\mathrm{2M}} - H_{\mathrm{2M}}) + 0.004 \\
H_{\mathrm{G}} &= H_{\mathrm{2M}} + 0.030 \times (H_{\mathrm{2M}} - K_{\mathrm{2M}}) + 0.009 \\
I_{\mathrm{N}} &= i_{\mathrm{P1}} - 0.149 \times (i_{\mathrm{P1}} - z_{\mathrm{P1}}) - 0.001 \\
Z_{\mathrm{N}} &= z_{\mathrm{P1}} - 0.265 \times (z_{\mathrm{P1}} - y_{\mathrm{P1}}) \\
z_{\mathrm{O2K}} &= z_{\mathrm{P1}} - 0.245 \times (z_{\mathrm{P1}} - y_{\mathrm{P1}}) \\
Y_{\mathrm{O2K}} &= y_{\mathrm{P1}} - 0.413 \times (z_{\mathrm{P1}} - y_{\mathrm{P1}}) + 0.012 \\
J_{\mathrm{O2K}} &= J_{\mathrm{2M}} + 0.093 \times (J_{\mathrm{2M}} - H_{\mathrm{2M}}) \\
I_{\mathrm{C}} &= i_{\mathrm{P1}} - 0.098 \times (i_{\mathrm{P1}} - z_{\mathrm{P1}})
\end{aligned}$$

where J_{2M}, H_{2M}, and K_{2M} are 2MASS magnitudes in the AB system. J_{N}, H_{O2K}, and K_{G} are calibrated against 2MASS. The accuracy of the photometric zero points was typically 0.01 – 0.04 mag and are included in the magnitude errors presented in this work.

Candidates were considered foreground interlopers if they had $Y - J > 0.6$ or $y_{\mathrm{P1}} - J > 1$ (see Section 2.3 and Figure 2.3). Sources with a $y_{\mathrm{P1}} - J < -1$ or undetected in J were rejected on the basis that they could be moving, varying, or a spurious object in the PS1 catalog.

---

[4] `https://www.caha.es/CAHA/Instruments/CAFOS/index.html`

The NTT/EFOSC2 filters I_{N} (#705) and Z_{N} (#623) are significantly different from the PS1 i_{P1} and z_{P1} filters (see Figure 2.1). We considered foreground interlopers objects with $I_{\mathrm{N}} - Z_{\mathrm{N}} < 0.75$ for candidates selected by the criteria in Section 2.2.1.1 (i-dropouts; $5.7 \lesssim z \lesssim 6.2$), while we rejected objects with $I_{\mathrm{N}} - Z_{\mathrm{N}} < 2.0$ for candidates selected by the criteria of Section 2.2.1.2 (i-dropouts; $6.2 \lesssim z \lesssim 6.5$) or Section 2.2.1.3 ($z$-dropouts; $z \gtrsim 6.5$).

Tables 2.2, 2.3, and 2.4 present the imaging follow-up of the PS1 discovered quasars selected with the criteria of Sections 2.2.1.1, 2.2.1.2, and 2.2.1.3, respectively. Table 2.5 lists the imaging follow-up of three PS1 discovered quasars that were selected using a more relaxed selection criteria in terms of their optical colors. These three objects are situated at the low redshift end of our sample and they are discussed further in Section 2.5.1.

Table 2.1. Imaging observations of quasar candidates

Date	Telescope/Instrument	Filters	Exposure Time
2012 May 21–24	MPG 2.2 m/GROND	$g_\mathrm{G},r_\mathrm{G},i_\mathrm{G},z_\mathrm{G},J_\mathrm{G},H_\mathrm{G},K_\mathrm{G}$	460–1440 s
2013 Jan 14–18	MPG 2.2 m/GROND	$g_\mathrm{G},r_\mathrm{G},i_\mathrm{G},z_\mathrm{G},J_\mathrm{G},H_\mathrm{G},K_\mathrm{G}$	460–1440 s
2013 Jan 26	CAHA 3.5 m/Omega2000	$z_\mathrm{O2K},Y_\mathrm{O2K},J_\mathrm{O2K}$	900 s
2013 Mar 13–16	NTT/EFOSC2	I_N, Z_N	300 s
2013 Mar 23–29	CAHA 3.5 m/Omega2000	$z_\mathrm{O2K},Y_\mathrm{O2K},J_\mathrm{O2K}$	300 s
2013 Apr 16–18	CAHA 2.2 m/CAFOS	I_C	1000 s
2013 Apr 26–27	CAHA 3.5 m/Omega2000	$z_\mathrm{O2K},Y_\mathrm{O2K},J_\mathrm{O2K}$	300–600 s
2013 Aug 18–19	CAHA 3.5 m/Omega2000	$z_\mathrm{O2K},Y_\mathrm{O2K},J_\mathrm{O2K}$	300–600 s
2013 Sep 7–10	MPG 2.2 m/GROND	$g_\mathrm{G},r_\mathrm{G},i_\mathrm{G},z_\mathrm{G},J_\mathrm{G},H_\mathrm{G},K_\mathrm{G}$	460–1440 s
2013 Sep 27–Oct 1	NTT/EFOSC2	I_N, Z_N	600 s
2013 Oct 16–21	CAHA 3.5 m/Omega2000	$z_\mathrm{O2K},Y_\mathrm{O2K},J_\mathrm{O2K},H_\mathrm{O2K}$	300 s
2013 Nov 9–12	CAHA 2.2 m/CAFOS	I_C	1250 s
2013 Nov 15–17	CAHA 3.5 m/Omega2000	$z_\mathrm{O2K},Y_\mathrm{O2K},J_\mathrm{O2K}$	300 s
2013 Dec 14–15	CAHA 2.2 m/CAFOS	I_C	1500 s
2014 Jan 24–Feb 5	MPG 2.2 m/GROND	$g_\mathrm{G},r_\mathrm{G},i_\mathrm{G},z_\mathrm{G},J_\mathrm{G},H_\mathrm{G},K_\mathrm{G}$	460–1440 s
2014 Mar 2–6	NTT/EFOSC2	I_N, Z_N	600 s
2014 Mar 2 and 5	NTT/SofI	J_N	300 s
2014 Mar 16–19	CAHA 3.5 m/Omega2000	$z_\mathrm{O2K},Y_\mathrm{O2K},J_\mathrm{O2K}$	300 s
2014 Apr 22–24	CAHA 2.2 m/CAFOS	I_C	2400 s
2014 May 9	CAHA 3.5 m/Omega2000	$z_\mathrm{O2K},Y_\mathrm{O2K},J_\mathrm{O2K}$	300 s
2014 Jul 23–27	NTT/EFOSC2	I_N, Z_N	600 s
2014 Jul 25	NTT/SofI	J_N	600 s
2014 Aug 7 and 11–13	CAHA 3.5 m/Omega2000	$Y_\mathrm{O2K},J_\mathrm{O2K}$	600 s
2014 Aug 22–24	CAHA 2.2 m/CAFOS	I_C	1800 s
2014 Sep 12 and 14	CAHA 3.5 m/Omega2000	$Y_\mathrm{O2K},J_\mathrm{O2K}$	600 s
2014 Se[16–17	CAHA 2.2 m/CAFOS	I_C	1800 s
2014 Sep 17–25	MPG 2.2 m/GROND	$g_\mathrm{G},r_\mathrm{G},i_\mathrm{G},z_\mathrm{G},J_\mathrm{G},H_\mathrm{G},K_\mathrm{G}$	460–1440 s
2014 Dec 13–21	MPG 2.2 m/GROND	$g_\mathrm{G},r_\mathrm{G},i_\mathrm{G},z_\mathrm{G},J_\mathrm{G},H_\mathrm{G},K_\mathrm{G}$	460–1440 s
2015 Feb 7 and 28	CAHA 3.5 m/Omega2000	$z_\mathrm{O2K},Y_\mathrm{O2K},J_\mathrm{O2K}$	600–900 s
2015 Feb 19–23	NTT/EFOSC2	I_N, Z_N	600 s
2015 Feb 22	NTT/SofI	J_N	300 s
2015 Mar 1 and 11-12	CAHA 3.5 m/Omega2000	$z_\mathrm{O2K},Y_\mathrm{O2K},J_\mathrm{O2K},H_\mathrm{O2K}$	600–900 s

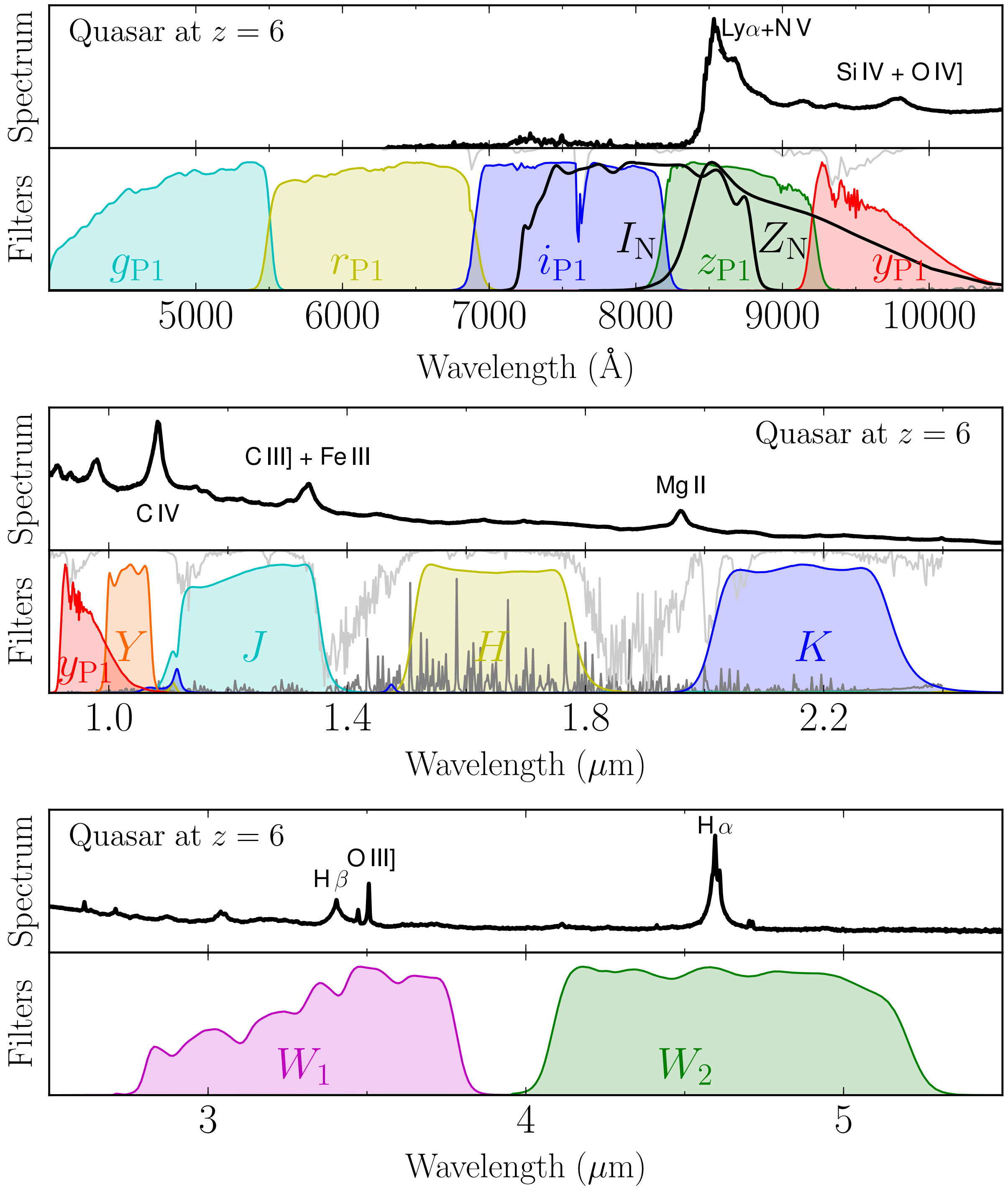

Figure 2.1: Composite quasar spectrum redshifted to $z = 6$ with key spectral lines labeled. The $z \sim 6$ composite spectrum from Fan et al. (2006b) is used for rest-frame wavelengths < 1225 Å, while for larger wavelengths the SDSS composite spectrum from Vanden Berk et al. (2001) is used. Transmission curves of filters used in the work presented in this chapter are shown. In the two upper panels, the relative strength of the sky emission (gray) and the telluric absorption spectrum (dark gray) are shown.

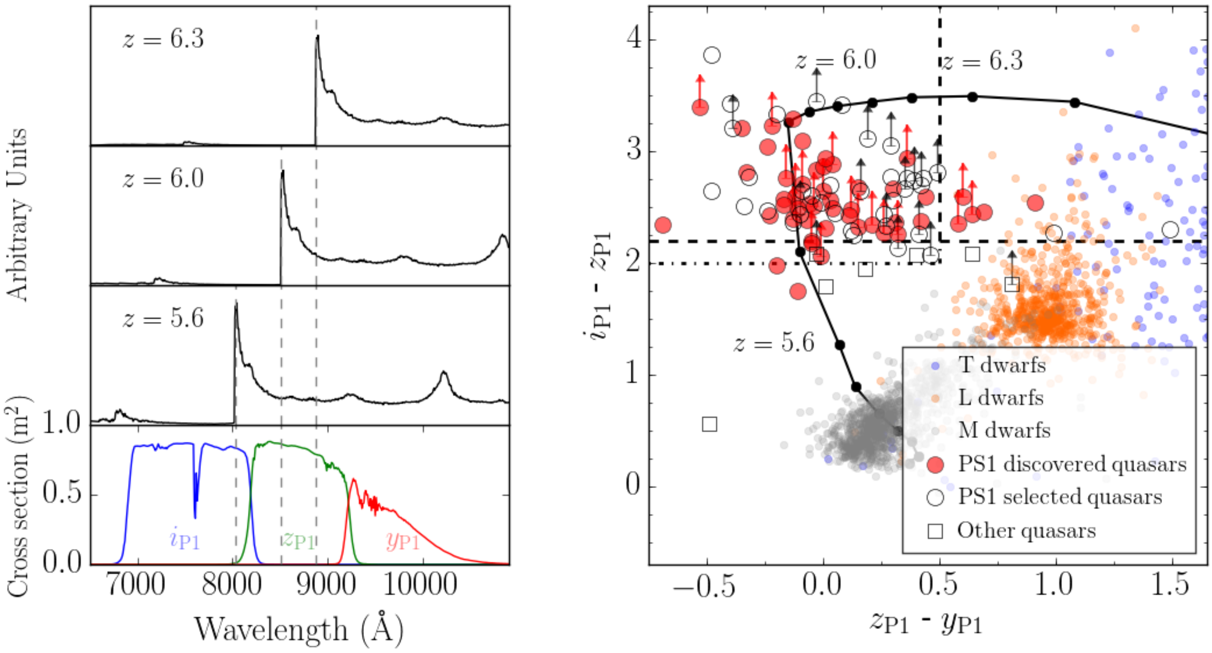

Figure 2.2: PS1 color selection criteria. *Left*: the bottom panel shows the PS1 capture cross section in units of m^2 e^{-1} photon^{-1} for the i_{P1}, z_{P1}, and y_{P1} bands (Tonry et al. 2012). The three upper panels show the composite quasar spectrum from Decarli et al. (2010) (with the intergalactic medium correction from Meiksin 2006) redshifted to $z = 5.6$, $z = 6.0$, and $z = 6.3$, from bottom to top. The gray dashed lines show the wavelength of the Lyα line at each redshift. *Right*: color–color diagram showing the criteria used to select quasar candidates (dashed and dot-dashed lines, see text). The thick black line shows the expected color of the quasar template from Decarli et al. (2010) redshifted from $z = 5.0$ to $z = 6.5$ in steps of $\Delta z = 0.1$ (see left panel). The L/T dwarfs that have a PS1 counterpart are shown with (orange/blue) small circles. A subsample of the M dwarfs from West et al. (2011) are represented by gray small circles. Upper limits for brown dwarfs are not plotted to enhance the clarity of the figure. Red filled circles are quasars discovered with Pan-STARRS1 in this work. Empty circles represent known quasars discovered by other surveys that satisfy the Pan-STARRS1 selection criteria presented in this thesis. Empty squares show known quasars discovered by other surveys that do not comply with the PS1 selection criteria of this thesis.

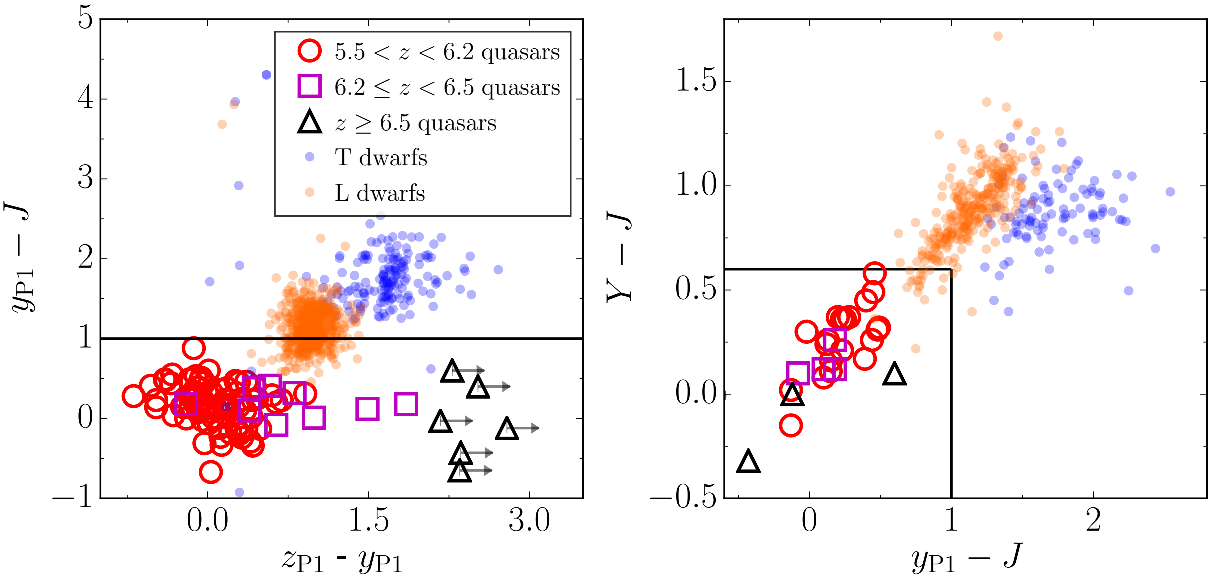

Figure 2.3: Selection criteria when the Y and/or J bands are available (black solid lines). Empty red circles, magenta squares, and black triangles represent the colors of known quasars at $5.5 < z < 6.2$, $6.2 \leq z < 6.5$, and $z \geq 6.5$, respectively. L and T dwarfs are shown with orange and blue small circles, respectively. Upper limits for brown dwarfs are not displayed to enhance the clarity of the figure. *Left*: $z_{P1} - y_{P1}$ vs. $y_{P1} - J$ color–color diagram. *Right*: $y_{P1} - J$ vs. $Y - J$ color–color diagram.

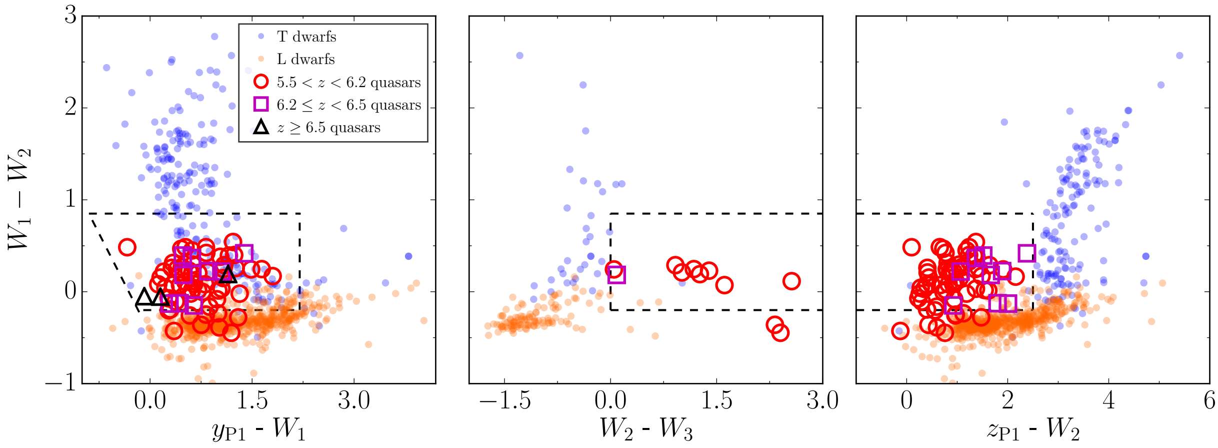

Figure 2.4: Prioritization criteria for candidates detected in *WISE* with S/N > 3 (black dashed lines). Empty red circles, magenta squares, and black triangles represent the colors of known quasars at $5.5 < z < 6.2$, $6.2 \leq z < 6.5$, and $z \geq 6.5$, respectively. L and T dwarfs are shown with orange and blue small circles, respectively. Upper limits for brown dwarfs are not displayed to enhance the clarity of the figure. *Left*: $y_{P1} - W_1$ vs. $W_1 - W_2$ color–color diagram. *Middle*: $W_2 - W_3$ vs. $W_1 - W_2$ color–color diagram. *Right*: $z_{P1} - W_2$ vs. $W_1 - W_2$ color–color diagram, this criteria is only used for *i*-dropout candidates.

Table 2.2. Follow-up photometry of the PS1 discovered quasars selected as *i*-dropouts ($5.7 \lesssim z \lesssim 6.2$)

Quasar	z	$i_{\rm G}$ mag	$z_{\rm G}$ mag	$J_{\rm G}$ mag	$H_{\rm G}$ mag	$I_{\rm N}$ mag	$Z_{\rm N}$ mag	$J_{\rm N}$ mag	$I_{\rm C}$ mag	$z_{\rm O2K}$ mag	$Y_{\rm O2K}$ mag	$J_{\rm O2K}$ mag	$H_{\rm O2K}$ mag
P002–06	5.93	> 23.01	20.55 ± 0.05	19.86 ± 0.14	19.92 ± 0.20	21.72 ± 0.09	–	–	–	–	–	–	–
P002+32	6.08	–	–	–	–	–	–	–	> 23.30	21.65 ± 0.09	–	21.38 ± 0.19	–
P004–24	5.69	22.09 ± 0.15	19.66 ± 0.03	19.30 ± 0.08	18.97 ± 0.08	20.81 ± 0.03	19.56 ± 0.04	–	–	–	–	–	–
P007+04	5.99	22.74 ± 0.24	20.39 ± 0.04	19.77 ± 0.11	19.71 ± 0.15	–	–	–	–	–	–	–	–
P021–25	5.77	22.83 ± 0.17	19.84 ± 0.01	19.21 ± 0.05	19.40 ± 0.08	–	–	–	–	–	–	–	–
P023–02	5.89	23.32 ± 0.20	20.38 ± 0.02	19.78 ± 0.10	19.44 ± 0.11	21.57 ± 0.05	–	–	–	–	–	–	–
P025–11	5.81	22.49 ± 0.11	20.25 ± 0.03	19.65 ± 0.06	19.37 ± 0.07	–	–	–	–	–	–	–	–
P029–29	5.96	21.84 ± 0.06	19.44 ± 0.02	19.07 ± 0.04	19.09 ± 0.05	20.54 ± 0.01	19.29 ± 0.02	–	–	–	–	–	–
P037–28	5.99	23.19 ± 0.15	20.78 ± 0.04	20.41 ± 0.14	20.59 ± 0.26	–	–	–	–	–	–	–	–
P040+17	5.63	–	–	–	–	–	–	–	22.43 ± 0.39	20.83 ± 0.06	–	20.43 ± 0.10	–
P042–02	5.88	23.20 ± 0.20	20.63 ± 0.03	20.41 ± 0.10	20.42 ± 0.14	21.53 ± 0.04	–	–	–	–	–	–	–
P045–22	5.7	22.78 ± 0.10	20.35 ± 0.03	19.65 ± 0.08	19.42 ± 0.08	–	–	–	–	–	–	–	–
P056–16	5.99	–	–	–	–	21.20 ± 0.03	19.86 ± 0.07	–	–	–	–	20.25 ± 0.10	19.72 ± 0.09
P060+24	6.18	> 23.44	20.48 ± 0.03	19.68 ± 0.09	19.68 ± 0.15	–	–	–	22.96 ± 0.29	20.40 ± 0.05	19.75 ± 0.40	19.71 ± 0.05	–
P065–19	6.11	> 23.30	19.93 ± 0.03	19.90 ± 0.15	19.34 ± 0.15	–	–	–	–	–	–	–	–
P071–02	5.7	–	–	–	–	20.23 ± 0.02	19.26 ± 0.02	–	–	–	–	19.02 ± 0.03	19.00 ± 0.03
P075–07	5.85	–	–	–	–	21.87 ± 0.06	20.60 ± 0.03	–	–	–	–	20.52 ± 0.12	20.45 ± 0.21
P127+03	5.82	> 23.27	20.98 ± 0.06	20.80 ± 0.21	20.43 ± 0.29	–	–	–	–	–	–	–	–
P135–13	5.86	23.34 ± 0.21	20.50 ± 0.02	20.80 ± 0.14	20.52 ± 0.20	–	–	–	–	–	–	–	–
P157–02	5.92	–	–	–	–	21.22 ± 0.03	–	20.20 ± 0.10	–	–	–	–	–
P167+56	5.92	–	–	–	–	–	–	–	23.40 ± 0.24	20.91 ± 0.04	–	20.31 ± 0.14	–
P172+26	5.8	–	–	–	–	–	–	–	22.89 ± 0.14	20.84 ± 0.09	–	20.44 ± 0.14	–
P183–12	5.86	–	–	–	–	20.69 ± 0.03	19.31 ± 0.02	–	–	–	–	–	–
P187–02	5.78	23.08 ± 0.24	21.18 ± 0.06	20.73 ± 0.13	20.48 ± 0.21	–	–	–	–	–	–	–	–
P187+04	5.89	–	–	–	–	21.85 ± 0.04	21.00 ± 0.04	–	–	–	–	–	–
P209–26	5.73	21.86 ± 0.07	19.56 ± 0.01	19.35 ± 0.05	19.11 ± 0.06	20.33 ± 0.01	19.57 ± 0.01	–	–	–	–	–	–
P210+40	6.01	–	–	–	–	–	–	–	> 23.25	–	–	–	–
P210+09	5.84	–	–	–	–	21.51 ± 0.05	–	–	–	20.66 ± 0.05	–	21.03 ± 0.23	–
P210–12	5.84	> 21.99	> 21.07	> 20.13	> 19.72	22.35 ± 0.06	21.00 ± 0.03	–	–	–	–	–	–
P213–22	5.88	–	–	–	–	20.70 ± 0.02	19.77 ± 0.01	–	–	–	–	–	–
P215–16	5.73	21.72 ± 0.17	19.66 ± 0.05	19.06 ± 0.08	19.34 ± 0.14	20.09 ± 0.02	19.15 ± 0.02	–	22.29 ± 0.10	–	–	–	–
P228+21	5.9	–	–	–	–	–	–	–	> 23.99	21.12 ± 0.13	–	20.89 ± 0.18	–
P235+17	5.79	–	–	–	–	–	–	–	–	19.28 ± 0.16	–	19.92 ± 0.08	–
P236+16	5.86	–	–	–	–	22.18 ± 0.07	–	–	22.42 ± 0.14	20.87 ± 0.10	–	20.73 ± 0.12	–
P242–12	5.81	22.64 ± 0.17	20.10 ± 0.02	19.59 ± 0.08	19.66 ± 0.15	–	–	–	–	–	–	–	–
P267+22	5.93	–	–	–	–	–	–	–	23.32 ± 0.17	21.14 ± 0.15	–	21.02 ± 0.22	–
P308–27	5.78	21.97 ± 0.09	19.82 ± 0.02	19.46 ± 0.06	19.62 ± 0.09	–	–	–	–	–	–	–	–
P319–10	5.85	22.55 ± 0.09	20.27 ± 0.02	20.02 ± 0.05	19.79 ± 0.08	21.21 ± 0.03	–	–	–	–	–	–	–
P320–24	5.73	22.84 ± 0.21	20.59 ± 0.04	20.26 ± 0.10	19.34 ± 0.07	–	–	–	–	–	–	–	–
P340–18	6.0	23.32 ± 0.17	20.11 ± 0.04	20.28 ± 0.08	19.90 ± 0.11	–	–	–	–	–	–	–	–
P359–06	6.17	> 22.99	20.14 ± 0.04	19.85 ± 0.10	19.47 ± 0.13	–	–	–	–	–	–	–	–

Note. — Quasars sorted by right ascension. Their complete names and coordinates are given in Table A.1. Their PS1 magnitudes are listed in Table A.2. These quasars were selected by the criteria in Section 2.2.1.1

Table 2.3. Follow-up photometry of the PS1 discovered quasars selected as *i*-dropouts $(6.2 \lesssim z \lesssim 6.5)$

Quasar	z	i_{G} mag	z_{G} mag	J_{G} mag	H_{G} mag	I_{N} mag	Z_{N} mag	J_{N} mag	I_{C} mag	Y_{O2K} mag	J_{O2K} mag
P009–10	5.96	> 23.39	21.11 ± 0.06	19.93 ± 0.07	19.72 ± 0.11	–	–	–	–	–	–
P065–26	6.16	22.70 ± 0.17	20.30 ± 0.03	19.32 ± 0.06	19.39 ± 0.18	22.24 ± 0.07	–	–	–	–	–
P159–02	6.35	–	–	–	–	> 23.74	–	20.00 ± 0.10	–	–	–
P217–16	6.13	–	–	–	–	22.53 ± 0.06	20.44 ± 0.03	–	–	> 18.43	19.69 ± 0.07
P308–21	6.22	> 23.60	20.98 ± 0.05	20.17 ± 0.11	–	–	–	–	–	–	–

Note. — Quasars sorted by right ascension. Their complete names and coordinates are given in Table A.1. Their PS1 magnitudes are listed in Table A.2. These quasars were selected by the criteria in Section 2.2.1.2. Note, however, that some quasars have a lower redshift than expected.

Table 2.4. Follow-up photometry of the PS1 discovered quasars selected as z-dropouts ($z \gtrsim 6.5$)

Quasar	z	I_N mag	Z_N mag	J_N mag	Y_{O2K} mag	J_{O2K} mag
P036+03	6.5412	23.62 ± 0.18	20.46 ± 0.04	19.51 ± 0.03	–	–
P167–13	6.508	> 24.86	22.08 ± 0.09	21.21 ± 0.09	–	–
P183+05	6.45	23.51 ± 0.21	20.93 ± 0.09	19.77 ± 0.08	–	–
P231–20	6.6	> 23.81	–	19.66 ± 0.05	–	–
P338+29	6.658	> 24.37	21.92 ± 0.09	20.73 ± 0.14	20.42 ± 0.10	20.74 ± 0.09

Note. — Quasars sorted by right ascension. Their complete names and coordinates are given in Table A.1. Their PS1 magnitudes are listed in Table A.2. These quasars were selected by the criteria in Section 2.2.1.3. Note, however, that some quasars have a lower redshift than expected.

2.4.2 Spectroscopy

In order to confirm the nature and redshifts of the candidates, we have carried out an optical and NIR spectroscopic campaign using the following instruments: EFOSC2 at the NTT telescope in La Silla, the FOcal Reducer/low dispersion Spectrograph 2 (FORS2; Appenzeller & Rupprecht 1992) at the Very Large Telescope (VLT), the Folded-port InfraRed Echellette (FIRE; Simcoe et al. 2008, 2013) spectrometer in the Baade Telescope at Las Campanas Observatory, the Low Resolution Imaging Spectrometer (LRIS; Oke et al. 1995) at the Keck I 10 m telescope on Mauna Kea, the Double Spectrograph (DBSP; Oke & Gunn 1982) on the 200-inch (5 m) Hale telescope at Palomar Observatory (P200), the Red Channel Spectrograph on the 6.5 m MMT Telescope, the Cassegrain TWIN spectrograph at the 3.5 m Calar Alto telescope (CAHA3.5 m), the Multi-Object Double Spectrograph (MODS; Pogge et al. 2010) and the LUCI spectograph (Seifert et al. 2003) at the Large Binocular Telescope (LBT).

The details of the spectroscopic observations of the PS1 discovered quasars are shown in Table 2.6. The data reduction included bias subtraction, flat fielding using lamp flats and sky subtraction. For the wavelength calibration exposures of He, HgCd and Ne arc lamps were obtained. The wavelength calibration was checked using sky emission lines. The typical rms of the wavelength calibration was better than 0.5 Å. For the flux calibrations, we used observations of the spectrophotometric standard stars G158-100, GD50, LTT7379, HD49798, EG274, and G191-B2B (Oke 1990; Hamuy et al. 1992, 1994).

Table 2.5. Follow-up photometry of the PS1 discovered quasars that do not satisfy all our selection criteria

Quasar	z	i_G mag	z_G mag	J_G mag	H_G mag	z_{O2K} mag	J_{O2K} mag
P000+26	5.71	–	–	–	–	19.49 ± 0.01	19.53 ± 0.02
P055–00	5.68	22.16 ± 0.18	20.58 ± 0.05	20.08 ± 0.16	20.03 ± 0.22	–	–
P135+16	5.63	22.70 ± 0.18	20.85 ± 0.04	20.30 ± 0.12	20.91 ± 0.33	–	–

Note. — Quasars sorted by right ascension. Their complete names and coordinates are given in Table A.1. Their PS1 magnitudes are listed in Table A.2. These quasars were selected by extended PS1 criteria and they are discussed in Section 2.5.1.

Table 2.6. Spectroscopic observations of the new PS1 quasars

Quasar	Date	Telescope/Instrument	Exposure Time	Slit Width
PSO J000.3401+26.8358	2014 Oct 19	MMT/Red Channel	300 s	1.″0
PSO J002.1073–06.4345	2013 Oct 24	VLT/FORS2	1482 s	1.″3
PSO J002.3786+32.8702	2014 Dec 23	P200/DBSP	1800 s	1.″5
PSO J004.8140–24.2991	2013 Aug 10	Magellan/FIRE	2409 s	0.″6
	2014 Oct 12	VLT/FORS2	1936 s	1.″3
PSO J007.0273+04.9571	2013 Jul 9	VLT/FORS2	1782 s	1.″3
PSO J009.7355–10.4316	2014 Oct 28	VLT/FORS2	1362 s	1.″3
PSO J021.4213–25.8822	2014 Nov 16	VLT/FORS2	1370 s	1.″3
PSO J023.0071–02.2675	2013 Oct 25	MMT/Red Channel	600 s	1.″25
PSO J025.2376–11.6831	2013 Oct 26	MMT/Red Channel	1800 s	1.″25
PSO J029.5172–29.0886	2013 Nov 27	VLT/FORS2	1482 s	1.″3
	2013 Dec 15	Magellan/FIRE	4501 s	0.″6
PSO J036.5078+03.0498	2014 Jul 25	NTT/EFOSC2	7200 s	1.″2
	2014 Sep 4–6	Magellan/FIRE	8433 s	0.″6
	2014 Oct 20	Keck I/LRIS	1800 s	1.″0
PSO J037.9706–28.8389	2013 Mar 4–5	VLT/FORS2	3600 s	1.″3
PSO J040.0159+17.5458	2014 Oct 19	MMT/Red Channel	1200 s	1.″0
PSO J042.6690–02.9174	2013 Oct 25	MMT/Red Channel	1800 s	1.″25
PSO J045.1840–22.5408	2013 Aug 9	VLT/FORS2	1782 s	1.″3
PSO J055.4244–00.8035[a]	2014 Feb 22	P200/DBSP	2400 s	1.″5
	2014 Aug 4	VLT/FORS2	1467 s	1.″3
PSO J056.7168–16.4769	2013 Oct 25	MMT/Red Channel	1800 s	1.″25
PSO J060.5529+24.8567	2015 Feb 17	P200/DBSP	2700 s	1.″5
PSO J065.4085–26.9543	2014 Mar 6	NTT/EFOSC2	3600 s	1.″5
	2014 Aug 4	VLT/FORS2	1467 s	1.″3
	2014 Oct 5	Magellan/FIRE	6742 s	1.″0
	2014 Dec 5	Magellan/FIRE	7228 s	0.″6
	2015 Mar 12	Magellan/FIRE	3001 s	0.″6
PSO J065.5041–19.4579	2014 Dec 23	P200/DBSP	1800 s	1.″5
PSO J071.4507–02.3332	2013 Oct 4	Magellan/FIRE	1818 s	0.″6
	2013 Oct 12	CAHA3.5m/TWIN	7200 s	1.″2
PSO J075.9356–07.5061	2013 Oct 26	MMT/Red Channel	2400 s	1.″25
PSO J127.2817+03.0657	2014 Dec 23	P200/DBSP	2700 s	1.″5
PSO J135.3860+16.2518[a]	2014 Mar 3	NTT/EFOSC2	3600 s	1.″5
	2014 Apr 5	LBT/MODS	2400 s	1.″2
	2014 Apr 26	VLT/FORS2	1467 s	1.″3
PSO J135.8704–13.8336	2014 Dec 23	P200/DBSP	1800 s	1.″5
PSO J157.9070–02.6599	2015 Mar 14	MMT/Red Channel	900 s	1.″0
PSO J159.2257–02.5438	2015 Mar 14	MMT/Red Channel	900 s	1.″0
PSO J167.4726+56.9521	2015 Mar 16	MMT/Red Channel	1200 s	1.″0
PSO J167.6415–13.4960	2014 Apr 26	VLT/FORS2	2630 s	1.″3
	2014 May 30–Jun 2	Magellan/FIRE	12004 s	0.″6
PSO J172.1770+26.8866	2015 Mar 16	MMT/Red Channel	2400 s	1.″0
PSO J174.7920–12.2845	2015 May 10	MMT/Red Channel	? s	?
PSO J183.1124+05.0926	2015 Mar 14–16	MMT/Red Channel	3000 s	1.″0
PSO J183.2991–12.7676	2013 Apr 13	VLT/FORS2	1782 s	1.″3
	2013 Apr 19	Magellan/FIRE	6000 s	0.″6
PSO J187.1047–02.5609	2014 Mar 9	MMT/Red Channel	1800 s	1.″0
PSO J187.3050+04.3243	2013 Apr 12	VLT/FORS2	2682 s	1.″3
PSO J201.9222+57.5440	2015 May 10	MMT/Red Channel	? s	?

2.5 54 new quasars at $z > 5.6$

We have discovered 54 quasars at $5.6 < z < 6.7$. Details of their spectroscopic observations are listed in Table 2.6 and their spectra are shown in Figure 2.5. The majority of these quasars were selected by the criteria of Section 2.2.1.1. This is because we focused our initial search on these criteria as they separate more efficiently high-redshift quasars from cool dwarfs (see Figure 2.2). This selection has yielded 41 new quasars so far. Once we had a better understanding of our data, we extended our search to find quasars at even higher redshifts. The criteria of Section 2.2.1.2 selected five of the new quasars, while another five were selected using the criteria of Section 2.2.1.3. We discovered three additional quasars that did not completely satisfy any of the previous selection criteria but were targeted because of their brightness or their radio properties (discussed individually in Section 2.5.1). The names, redshifts, and coordinates of these newly discovered quasars are listed in Table A.1 and their PS1 magnitudes are given in Table A.2.

The quasar redshifts were estimated by the peak of a single-Gaussian fit of emission lines—when prominent lines were available. The peak of the low-ionization Mg II line is thought to be a good proxy of the quasar systemic redshift (see Richards et al. 2002a; De Rosa et al. 2014, and references therein). Thus, for quasars with NIR spectra covering Mg II, the fit to this line was preferred for redshift estimation. Other lines used to determine redshifts were the N V, λ1240 (hereafter N V), [O I] λ1305 (hereafter [O I]), and/or $\mathrm{Si}_{\mathrm{IV}}$ + O IV] λ1398 (hereafter $\mathrm{Si}_{\mathrm{IV}}$ + O IV]). The observed wavelengths in the composite spectra from Vanden Berk et al. (2001) were taken as reference. The uncertainties in our line fittings were negligible compared to the intrinsic shifts known to exist with respect to the quasar systemic redshift (Richards et al. 2002a).

However, the discovery spectra of several of our quasars show a bright continuum almost devoid of bright emission lines (see Figure 2.5). In the absence of strong lines, an accurate redshift estimate for these quasars is challenging. We estimated their redshift by matching their continuum to the composite $z \sim 6$ quasar spectra from Fan et al. (2006b). We assumed the redshift that minimized the χ^2 between the observed spectrum and the template. However, it should be noted that due to the lack of strong features, the uncertainties of these redshift estimates can reach values as high as 0.05.

Once the redshifts had been estimated, we calculated the magnitude of the continuum rest-frame 1450 Å (m_{1450}) for each quasar, by fitting a power law of the form $f_\lambda = C \times \lambda^\beta$ to regions of the continuum that are generally uncontaminated by emission lines (1285–1295, 1315–1325, 1340–1375, 1425–1470, 1680–1710, 1975–2050, and 2150–2250 Å) and that were not affected by significant errors or absorption features. In cases where only a low S/N optical spectrum was available, a reliable continuum fitting was not possible and their y_{P1} or follow-up J magnitudes were used as a proxy for m_{1450}. The m_{1450} values are listed in Table A.1.

Table 2.6 (cont'd)

Quasar	Date	Telescope/Instrument	Exposure Time	Slit Width
PSO J209.2058–26.7083	2015 Mar 12	Magellan/FIRE	4819 s	0.″6
	2014 Apr 22	VLT/FORS2	1482 s	1.″3
PSO J210.7277+40.4008	2015 Feb 17	P200/DBSP	1800 s	1.″5
PSO J210.8296+09.0475	2015 Mar 14	MMT/Red Channel	1800 s	1.″0
PSO J210.8722–12.0094	2013 May 9	VLT/FORS2	2682 s	1.″3
PSO J213.3629–22.5617	2013 May 3	VLT/FORS2	1782 s	1.″3
	2013 May 15	Magellan/FIRE	15006 s	0.″6
PSO J215.1514–16.0417[b]	2011 Mar 12–13	MMT/Red Channel	2700 s	1.″0
	2011 Apr 9–12	CAHA3.5m/TWINS	4800 s	1.″5
	2011 May 28	LBT/LUCI	4800 s	1.″0
PSO J217.0891–16.0453	2014 Apr 22	VLT/FORS2	1467 s	1.″3
	2014 May 30	Magellan/FIRE	22509 s	0.″6
PSO J228.6871+21.2388	2015 Feb 17	P200/DBSP	1800 s	1.″5
PSOJ 231.6576–20.8335	2015 Mar 12	Magellan/FIRE	9638 s	0.″6
PSO J235.9450+17.0079	2014 Jul 21	P200/DBSP	1800 s	1.″5
PSO J236.2912+16.6088	2015 Mar 16	MMT/Red Channel	2400 s	1.″0
	2015 Mar 20	VLT/FORS2	1422 s	1.″3
PSO J242.4397–12.9816	2014 Mar 9	MMT/Red Channel	1800 s	1.″0
	2014 Jun 2	Magellan/FIRE	3001 s	0.″6
PSO J267.0021+22.7812	2015 Apr 13	VLT/FORS2	1500 s	1.″3
PSO J293.0317+71.6523	2015 May 10	MMT/Red Channel	? s	?
PSO J308.0416–21.2339	2014 Oct 10	VLT/FORS2	1362 s	1.″3
PSO J308.4829–27.6485	2013 Oct 1	Magellan/FIRE	3001 s	0.″6
PSO J319.6040–10.9326	2013 Oct 25	MMT/Red Channel	1800 s	1.″25
PSO J320.8703–24.3604	2013 Oct 21	VLT/FORS2	1482 s	1.″3
PSO J338.2298+29.5089	2014 Oct 19	MMT/Red Channel	1800 s	1.″0
	2014 Oct 30	Magellan/FIRE	7200 s	0.″6
	2014 Nov 27	LBT/MODS	2700 s	1.″2
	2014 Dec 6	LBT/LUCI	3360 s	1.″5
PSO J340.2041–18.6621	2012 Jun 21	NTT/EFOSC2	3600 s	1.″5
	2012 Nov 17	LBT/MODS	3000 s	1.″2
PSO J359.1352–06.3831	2014 Oct 19	MMT/Red Channel	600 s	1.″0

Note. — Quasars sorted by right ascension. For full coordinates and redshifts see Table A.1.

[a] Quasars discovered in Chapter 3 but included here for completeness.

[b] The first PS1 high-redshift quasar discovered by Morganson et al. (2012). Included here for completeness.

2.5.1 Notes on selected objects

Here we discuss some selected quasars, including three PS1 quasars that were not selected using the criteria of Section 2.2. The objects are sorted by descending redshift.

2.5.1.1 PSO J036.5078+03.0498 (z = 6.5412)

This is currently the brightest quasar at $z > 6.5$ (see Figure 2.6). We originally measured its redshift from the peak of the Mg II line ($z_{\mathrm{Mg\,II}} = 6.527 \pm 0.002$; Venemans et al. 2015). However, we also detected a bright [C II] 158 μm line on this quasar from which we estimated a systemic redshift of $z_{[\mathrm{C\,II}]} = 6.54122 \pm 0.0018$. For details on the [C II] detection see Chapter 5.

2.5.1.2 PSO J340.2041–18.6621 (z = 6.0)

We carried out 870 μm (345 GHz) observations of P340–18. The quasar remained undetected in the map with an rms of 1.6 mJy at the quasar position. However, we reported a tentative 4.7σ detection of a submillimeter source located at $\sim 2.'5$ from the quasar. Details of the submillimeter observations can be found in Appendix C.

2.5.1.3 PSO J007.0273+04.9571 (z = 5.99)

The discovery spectrum of this quasar does not clear emission lines from which the redshift could be determined. We estimated its redshift by matching the continuum to the composite spectrum of Fan et al. (2006b). This quasar was independently discovered by Jiang et al. (2015). They determined a slightly higher redshift for this object ($z = 6.04$), measured from the wavelength where the sharp flux drop occurs. They also note an interesting strong emission line at $\lambda = 7580$ Å. This feature exists in their three MMT spectra of this object and it also appears in our discovery spectrum (see Figure 2.5). Jiang et al. (2015) propose that this line could be due to a luminous Lyα emitter or an ionized IGM bubble at $z = 5.23$.

2.5.1.4 PSO J002.1073–06.4345 (z = 5.93)

This quasar was discovered independently by Jiang et al. (2015), and our redshift estimate is in good agreement with theirs ($z = 5.929$).

2.5.1.5 PSO J210.8296+09.0475 (z = 5.84)

The S/N of the discovery spectrum of this quasar is very low. At this S/N the spectrum did not show any strong lines and its redshift was determined by matching the continuum to the composite spectrum of Fan et al. (2006b). This quasar was independently discovered by Jiang et al. (2015) and they reported a slightly higher redshift ($z = 5.86$).

2.5.1.6 PSO J000.3401+26.8358 (z = 5.71)

This quasar has a color $i_{\rm P1} - z_{\rm P1} = 1.98$ and therefore it does not satisfy our selection criteria presented in Section 2.2. However, it was targeted for follow-up because it was relatively bright ($z_{\rm P1} = 19.33$) and it did satisfy all the other criteria including good *WISE* colors (see Section 2.3 and Figure 2.4). As expected from its somewhat blue $i_{\rm P1} - zps$ color, the redshift of this quasar lies at the lower end of our quasar sample. The confirmation of this quasar is encouraging for future searches of $z \sim 5.2 - 5.7$ quasars, which have similar $i - z$ colors to the much more numerous M dwarfs. The combination of PS1 and *WISE* may be a promising way forward to find these thus far elusive quasars.

2.5.1.7 PSO J045.1840–22.5408 (z = 5.70)

The discovery spectrum of this quasar looks very peculiar and seems to be significantly affected by absorption systems or intrinsic absorption from the host galaxy. The spectrum shows a weak-line emission quasar and the S/N does not allow us to identify emission lines in regions not affected by significant telluric absorption or sky emission to calculate the redshift from. The spectrum shows several absorption lines around 8300 Å (e.g., $\lambda = 8265.2$, 8281.3, 8306.8, and 8315.6 Å). Most of the lines are blended and, given the resolution of the spectrum, it is hard to unambiguously identify them. These lines could be due to a group of galaxies at $z \sim 1.96$ if we assume that all the lines are due to Mg II absorbers. We identify a Mg II $\lambda\lambda 2796, 2803$ doublet at $z = 2.0721 \pm 0.0005$ (observed at $\lambda = 8589.2$ Å and 8611.9 Å). The corresponding Mg I $\lambda 2853$ Å seems marginally detected at $\lambda = 8764.0$ Å.

2.5.1.8 PSO J055.4244–00.8035 (z = 5.68)

This quasar was discovered by the selection criteria presented in Chapter 3 Section 3.3.3. That selection was based on the PS1 PV1 catalog and further required a radio-counterpart in the Faint Images of the Radio Sky at Twenty cm survey (FIRST; Becker et al. 1995), which allowed us to relax the requirements on optical colors (for more details see Chapter 3). This is currently the radio loudest quasar known at $z > 5.5$ (see Figure 3.2 and Table 3.3). While the PV1 $i_{\rm P1} - z_{\rm P1}$ color for this quasar was a lower limit of $i_{\rm P1} - z_{\rm P1} > 1.3$, its PV2 $i_{\rm P1} - z_{\rm P1}$ color is a detection of $i_{\rm P1} - z_{\rm P1} = 2.2$. Although its PV2 color is significantly redder than the limit previously reported, its color is exactly on the boundary of our selection in Section 2.2.1.1. This quasar does not satisfy the selection criteria presented in this chapter and we would have missed it if it did not have a strong radio emission.

2.5.1.9 PSO J135.3860+16.2518 ($z = 5.63$)

As P055–00, this quasar was selected by the PS1/FIRST criteria presented in Chapter 3 Section 3.3.3. P135+16 is also among the radio loudest quasars at $z > 5.5$ (see Figure 3.2 and Table 3.3). Its PV1 and PV2 $i_{\rm P1} - z_{\rm P1}$ colors do not differ much: $i_{\rm P1} - z_{\rm P1} = 1.70$ vs. $i_{\rm P1} - z_{\rm P1} = 1.75$. This color is too blue for the color cuts typically applied in optical searches for high-redshift quasars (for instance, the color cuts presented in this chapter). Thus, this quasar would have been missed if it was not by its radio emission.

2.6 The PS1 distant quasar sample

At the end of this thesis (2015 April) there are 135 known quasars at $z > 5.5$. We provide their names, coordinates, and redshifts in Table A.1; and their PS1 PV2 and *WISE* magnitudes in Table A.2. The PS1 PV2 catalog has information in the $i_{\rm P1}$, $z_{\rm P1}$, $y_{\rm P1}$ bands (which are the PS1 bands that we used to identify high-redshift quasars) for 74% (100/135) of them. The selection criteria presented in this chapter select 89 of these quasars plus three PS1-discovered quasars that were selected by different criteria (see Section 2.5.1). Thus, the PS1 distant quasar sample currently consists of 92 quasars at $z > 5.6$.

Figure 2.6 shows the redshift and UV luminosity distribution of all known quasars at $z > 5.5$, highlighting the PS1 distant quasar sample in red. The large range of luminosities of this well defined sample of quasars is remarkable. As a comparison, Figure 2.7 shows the $z_{\rm P1}$ distribution of $5.6 < z < 6.5$ quasars with a S/N > 10 in the $z_{\rm P1}$ band from the PS1 sample and the SDSS main quasar sample (Fan et al. 2006c). With the current depth of PS1, we can identify quasars that are more than a mag fainter than the SDSS main quasar survey.

The sky distribution of all quasars at $z > 5.5$ is presented in Figure 2.8. We can see that most of the new discoveries presented this chapter are located in the southern sky. There are six known quasars at decl. $< -30°$, which could in principle also be part of the PS1 selected sample but they are outside of the PS1 footprint. The six quasars at decl. $< -30°$ were discovered by Venemans et al. (2013), Carnall et al. (2015), and Reed et al. (2015) using the VIKING, VST ATLAS, and DES surveys, respectively.

In the following, we briefly comment on the eight known quasars that have PS1 information but do *not* satisfy our current selection criteria. The objects are sorted by descending redshift.

ULAS J1120+0641 (z = 7.08): This is the most distant quasar currently known at $z = 7.0842$ (Mortlock et al. 2011; Venemans et al. 2012). This quasar satisfies all our color requirements (see Figures 2.3 and 2.4), however, its current S/N($y_{\rm P1}$) is only 5.6 below our S/N($y_{\rm P1}$)> 7 cut. It is therefore likely that this quasar will be selected in the next PS1 PV3 release.

CFHQS J0050+3445 (6.25): This quasar was discovered by Willott et al. (2010b). Its $i_{\rm P1} - z_{\rm P1} > 1.81$ limit prevents it from being selected by our criteria. It could eventually be selected by our criteria if the $i_{\rm P1}$ band goes deep enough in the PS1 PV3 release.

SDSS J0303–0019 (z = 6.08): It was discovered by Jiang et al. (2008) in the deep SDSS stripe 82. It has the right colors required by our criteria of Section 2.2.1.1, however, its current S/N($y_{\rm P1}$) is 4.9, i.e., just below our cut at S/N($y_{\rm P1}$)> 5. Thus, this quasar will likely be selected by PS1 PV3.

SDSS J1257+6349 (z = 6.02): Quasar recently reported by Jiang et al. (2015). With colors of $i_{\rm P1} - z_{\rm P1} = 2.07$ and $W_1 - W_2 = -0.25$, it does not fulfill the criteria of Section 2.2.1.1 nor our *WISE* prioritization criteria (see Figure 2.4).

SDSS J2310+1855 (z = 6.00): This quasar was first reported by Wang et al. (2013). Interestingly, even though it has the brightest 250 GHz continuum flux and CO(6–5) and [C II] emission lines among all the $z > 6$ quasars, its optical or NIR spectra have not been reported in the literature. Its PS1 colors are $i_{\rm P1} - z_{\rm P1} = 2.08$ and $z_{\rm P1} - y_{\rm P1} = 0.64$, which place it in a color region highly dominated by L dwarfs. Our current criteria do not select this quasar.

SDSS J0927+2001 (z = 5.77): This quasar was discovered by Fan et al. (2003). It has PS1 colors that make it hard to distinguish from the more abundant cool dwarfs ($i_{\rm P1} - z_{\rm P1} = 1.79$).

SDSS J1621+5155 (z = 5.71): This quasar was first reported by Wang et al. (2008) as a 250 GHz continuum flux non-detection. They also mention that this quasar shows a very weak Lyα line with an equivalent width less than 5 Å. However, an optical or NIR spectrum of this quasar has not yet been published. We note that this is among the brightest sources in the *WISE* bands (see Table A.2). Our criteria do not select this quasar because of its $i_{\rm P1} - z_{\rm P1} = 1.95$ color, although it does satisfy all of our *WISE* prioritization criteria (Figure 2.4).

NDWFS J142729.7+352209 (z = 5.53): This is the only quasar currently reported in the literature in the redshift range $5.5 < z < 5.6$. It was discovered by Cool et al. (2006) using a mid-infrared selection. At these redshifts the optical colors of quasars are practically indistinguishable from M dwarfs. Indeed, this quasar has a blue $i_{\rm P1} - z_{\rm P1} = 0.56$ color. We note, however, that this quasar satisfies all of our *WISE* prioritization criteria (Figure 2.4). A selection exploiting the information provided by *WISE* and *PS1* may be a promising way to find quasars at these redshifts.

2.7 Summary

We have presented the discovery of 54 new quasars at $z > 5.6$, placing the Pan-STARRS1 survey as the leading survey for high-redshift quasar searches. Follow-up observations are still ongoing and the discovery of more quasars is imminent, especially at the highest redshifts. The discoveries presented in this chapter almost doubled the number of $z > 5.5$ quasars discovered in the decade prior to this thesis. We have also doubled the number of quasars at $z > 6.5$ from four to eight. It is important to note that most of these newly discovered quasars are in the southern sky (see Figure 2.8), which constitutes the ideal ground for follow-up investigations using facilities such as ALMA, VLT, and the Magellan Telescopes.

We have introduced the PS1 distant quasar sample, currently consisting of 92 quasars that were PS1 discovered or selected by the PS1 criteria presented in this thesis. This sample shows a broad variety of spectral features, including quasars with very bright emission lines and others with almost no detectable emission lines (see for example Figure 2.5). The PS1 distant quasar sample spans a factor of ~20 in luminosity (see Figure 2.6). So far, most of the follow-up studies of high-redshift quasars have focused on individual objects or a few sources (see for instance the targeted studies presented in Chapters 4 and 5). The increase in source number and luminosity range provided by our sample paves the way for a plethora of follow-up studies that will allow us to provide an accurate characterization of the earliest massive black holes and galaxies in the universe (see further discussion in Chapter 6).

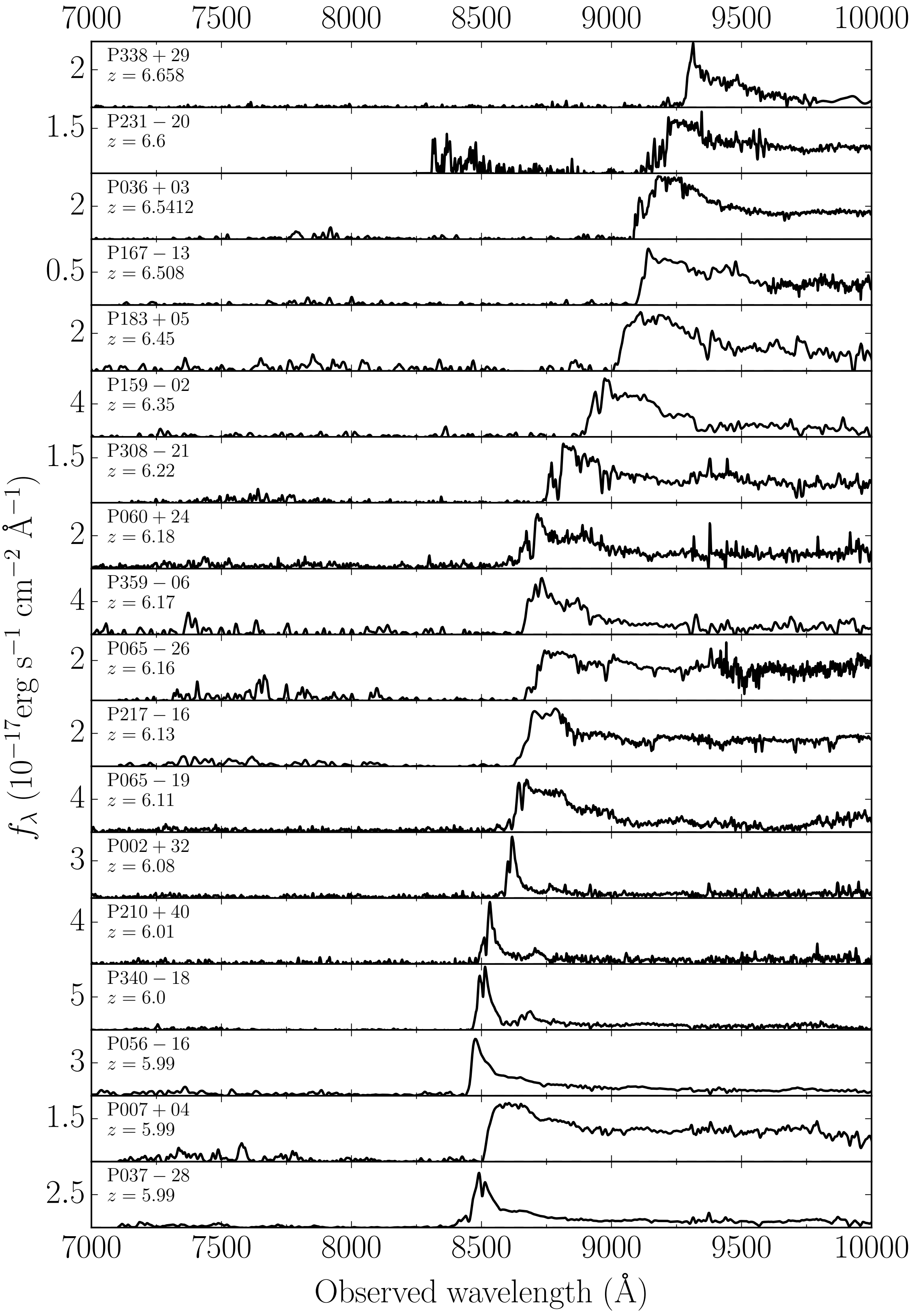

Figure 2.5: Spectra of the 54 Pan-STARRS1 discovered quasars at $z \geq 5.6$. Sorted by decreasing redshift.

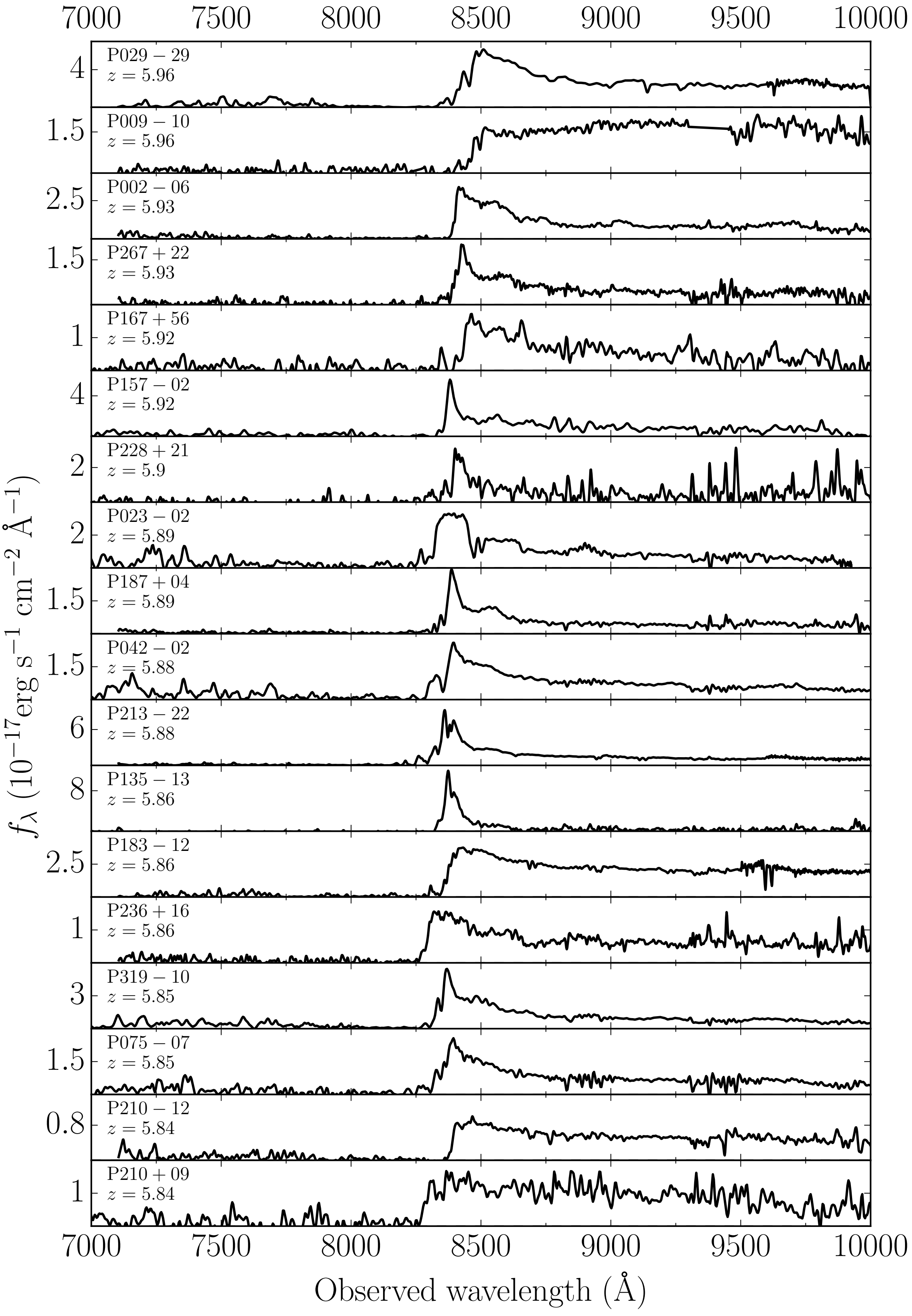

Figure 2.5: Continuation

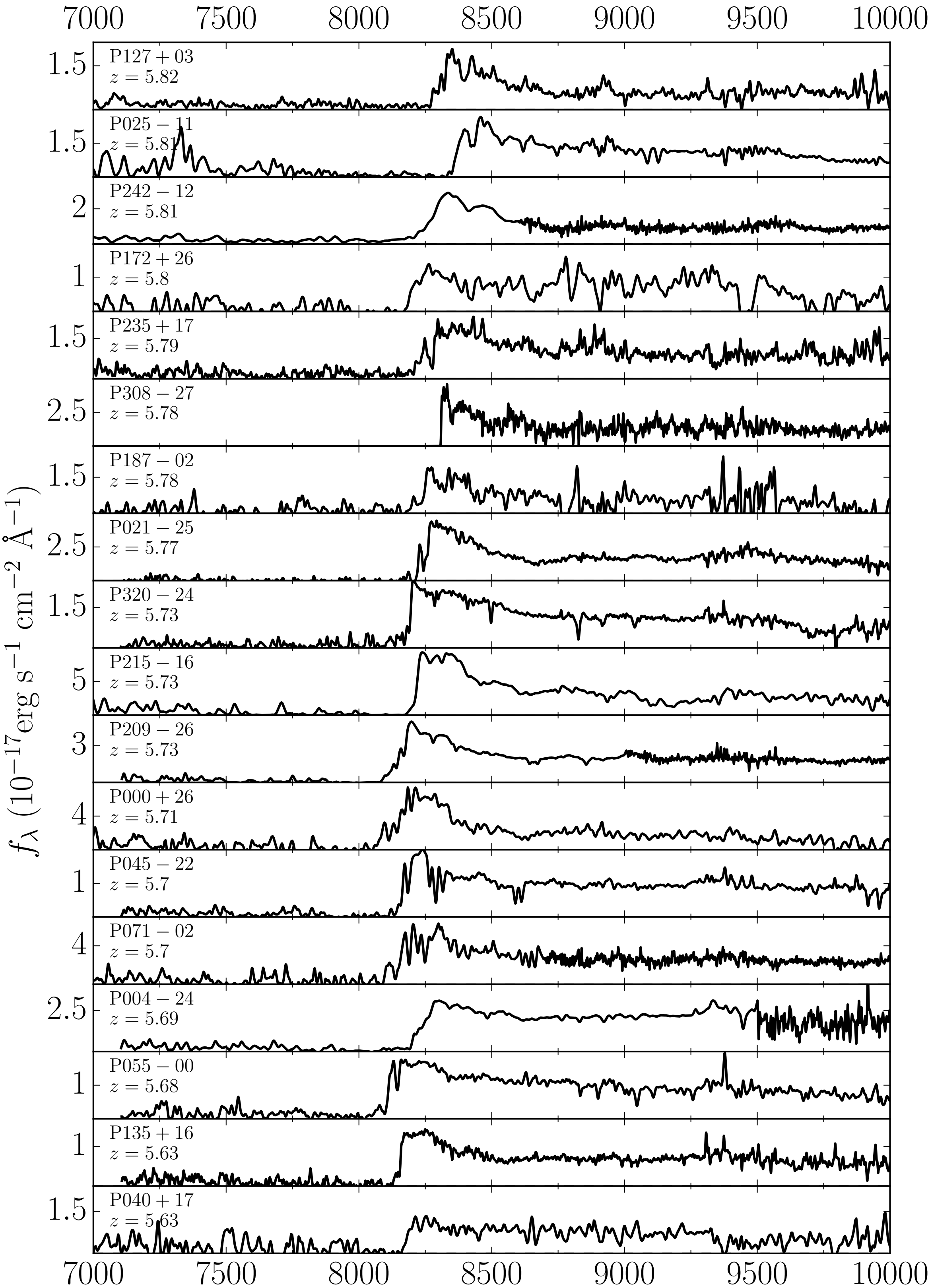

Figure 2.5: Continuation

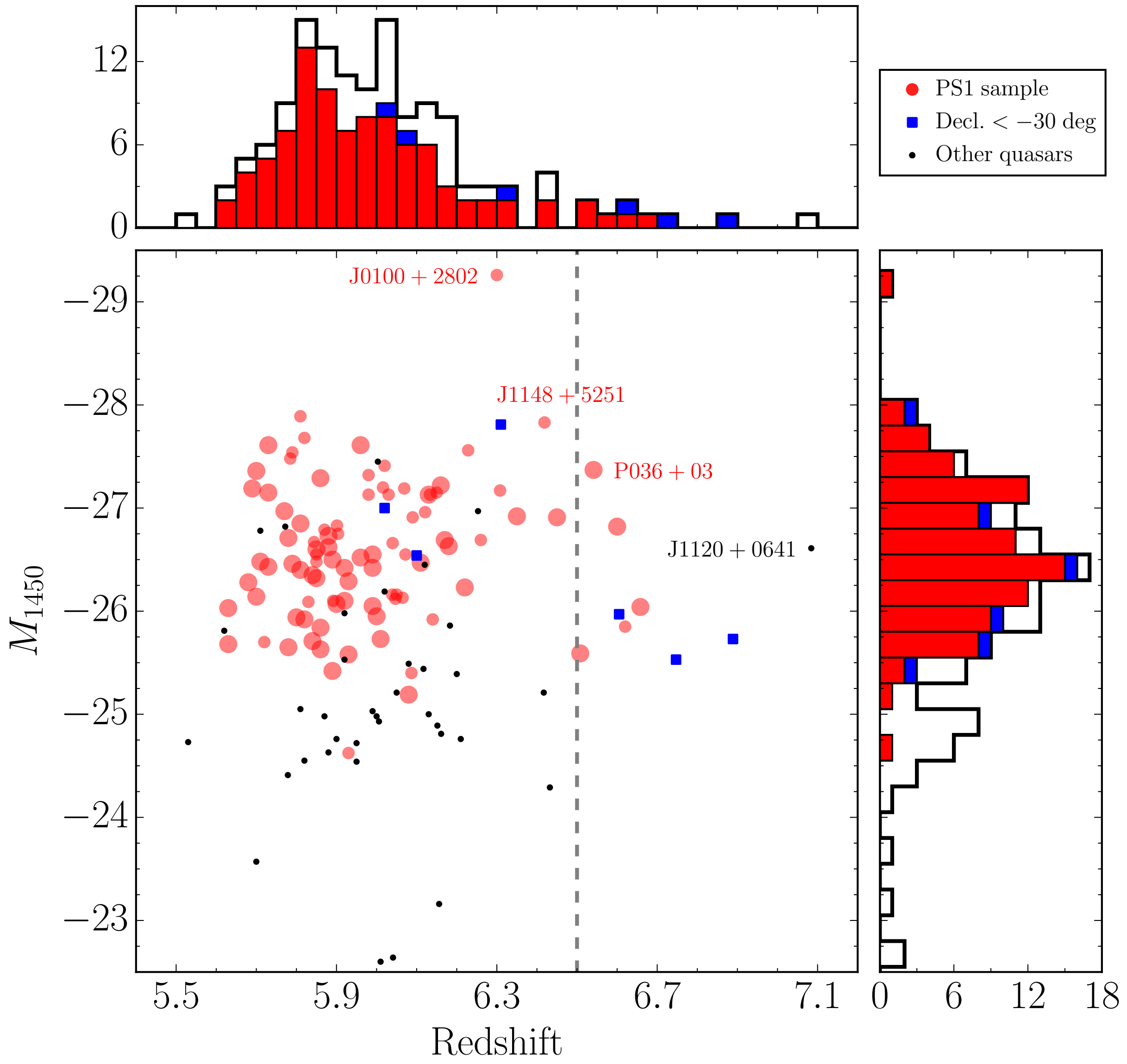

Figure 2.6: Redshift and absolute UV magnitude (M_{1450}) distribution of all the known $z > 5.5$ quasars. The red circles/histograms show the 92 quasars that belong to the PS1 distant quasar sample. Larger symbols represent PS1 discoveries. The blue squares/histograms are quasars at Decl.$< -30°$ and therefore outside the PS1 footprint. The dashed line indicates the minimum redshift probed by typical z-dropout techniques (Venemans et al. 2013). The quasars J1120+0641 (Mortlock et al. 2011), P036+03 (Venemans et al. 2015), J1148+5251 (Fan et al. 2003), and J0100+2802 (Wu et al. 2015) are labeled for references in the text.

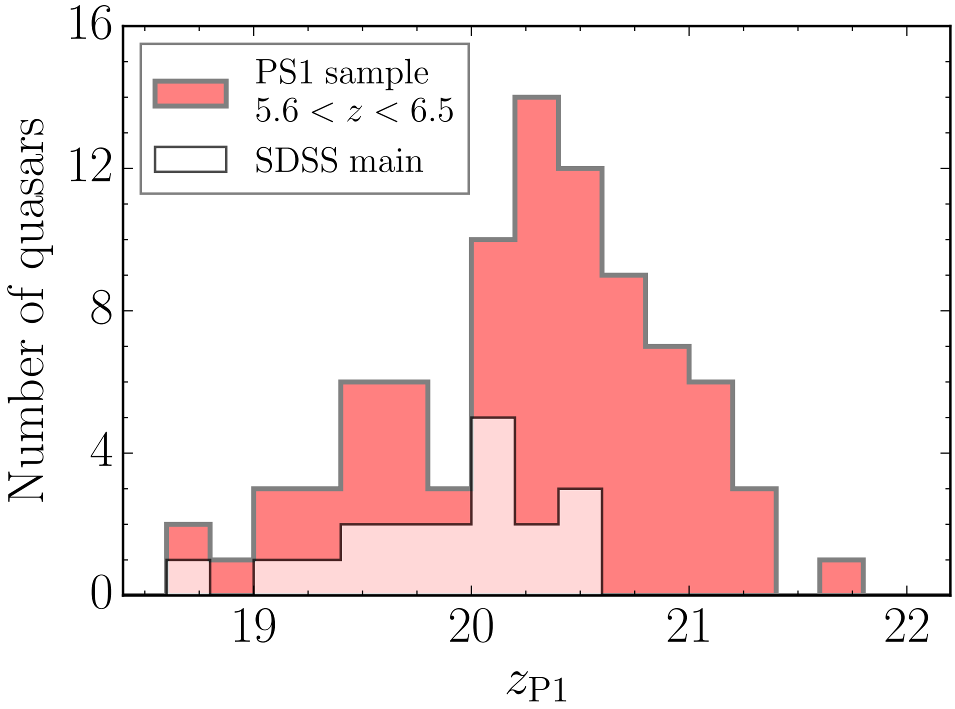

Figure 2.7: $z_{\rm P1}$-band distribution of $5.6 < z < 6.5$ quasars with a S/N > 10 in the $z_{\rm P1}$ band from the PS1 quasar sample and the SDSS main quasar survey (Fan et al. 2006c).

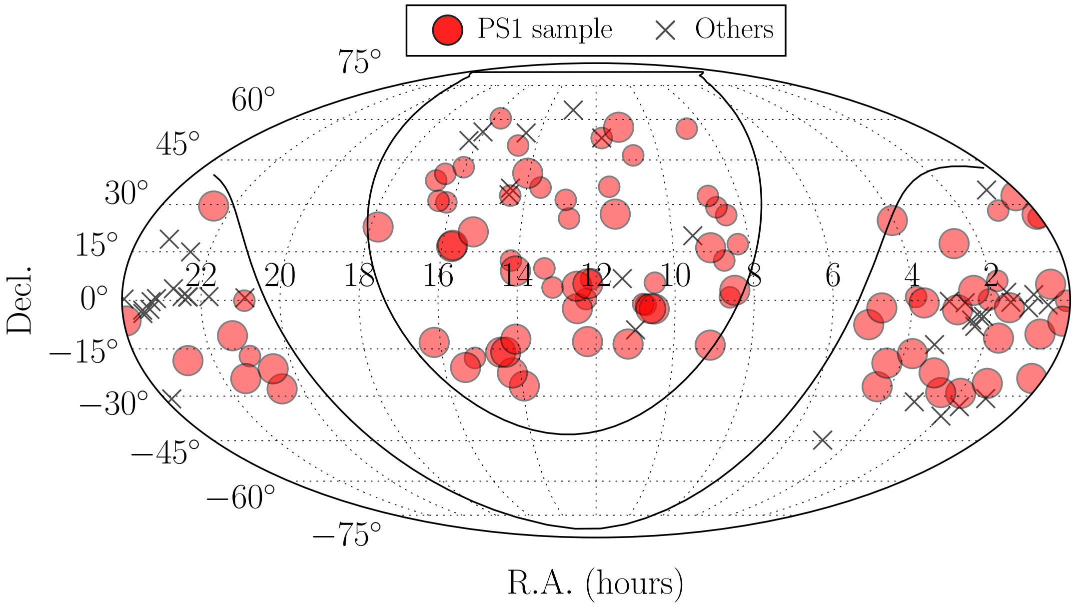

Figure 2.8: Sky distribution of all known $z > 5.5$ quasars. Red circles represent the PS1 distant quasar sample. Larger symbols are PS1 discoveries. Gray crosses are quasars that do not belong to the PS1 distant quasar sample. Note that high-redshift quasar surveys avoid the plane of the Milky Way ($|b| < 20°$).

Chapter 3

Constraining the radio-loud fraction of quasars at $z > 5.5$ [†]

3.1 Context

The study of $z \sim 6$ quasars has shown the presence of almost complete Gunn–Peterson absorption troughs in their spectra, corresponding to Lyα absorption by the neutral Hydrogen in the intergalactic medium (IGM). This indicates a rapid increase in the neutral fraction of the IGM above $z > 6$, providing strong constraints on the end of the epoch of reionization (EoR) (Fan et al. 2006a). The study of the IGM through Gunn-Peterson absorption has its limitations: quasar spectra suffer from saturated absorption at $z \gtrsim 6$, and thus it becomes increasingly difficult to study the IGM during the EoR (e.g., Furlanetto et al. 2006).

On the other hand, the 21 cm line (unlike the Lyα line) does not saturate, allowing the study of the IGM even at large neutral fractions of Hydrogen (e.g., Carilli et al. 2004a). Therefore, the identification of radio-loud sources at the highest redshifts will be critical for current and future radio surveys. These objects will serve as background sources to study the IGM beyond the EoR through 21 cm absorption measurements (for example the Low-frequency Array and the Square Kilometre Array; e.g., see Carilli et al. 2002).

Typical high-redshift quasar searches are based on strict optical and near-infrared color criteria chosen to avoid the more numerous cool dwarfs which have similar colors to high-redshift quasars (see chapter 2). An alternative to find elusive quasars with optical colors indistinguishable from stars is to require a radio detection. Most of the cool stars that could be confused

---

[†] This chapter is a version of the article Bañados et al. (2015b).

with high-redshift quasars are not radio-bright at mJy sensitivities (Kimball et al. 2009); therefore, complementing an optical color-based selection with a bright radio detection reduces the contamination significantly (e.g., McGreer et al. 2009).

Currently, there are only three $z > 5.5$ quasars known with 1.4 GHz peak flux density > 1 mJy (J0836+0054, $z = 5.81$, Fan et al. 2001; J1427+3312, $z = 6.12$, McGreer et al. 2006, Stern et al. 2007; and J1429+5447, $z = 6.18$, Willott et al. 2010a). There are two other $z \sim 6$ quasars in the literature classified as radio-loud, but with fainter radio emission (J2228+0110, $z = 5.95$, Zeimann et al. 2011; and J0203+0012, $z = 5.72$, Wang et al. 2008).

This small sample of currently identified radio-loud quasars at $z \sim 6$ has already provided important insights into Active Galactic Nuclei (AGNs) and galaxy evolution, emphasizing the importance of finding more of such objects. For example, there is evidence that a radio-loud $z \sim 6$ quasar might be located in an overdensity of galaxies (Zheng et al. 2006), similar to what has been found in radio-loud AGN at lower redshifts (e.g., Wylezalek et al. 2013). It has also been shown that another $z \sim 6$ radio-loud quasar resides in one of the most powerful known starbursts at $z \sim 6$ (Omont et al. 2013a).

In this chapter we take advantage of the large area coverage and photometric information provided by the Faint Images of the Radio Sky at Twenty cm survey (FIRST; Becker et al. 1995) and the Panoramic Survey Telescope & Rapid Response System 1 (Pan-STARRS1, PS1; Kaiser et al. 2002, 2010) to search for radio-loud quasars at $5.5 \lesssim z \lesssim 7.2$. We also revisit the issue of a possible evolution of the radio-loud fraction (RLF) of quasars with redshift discussed in Section 1.6. In brief, at lower redshifts, it is well established that roughly 10–20% of all quasars are radio-loud. However, some studies find that the RLF decreases strongly with increasing redshift at a given luminosity (e.g., Jiang et al. 2007a). If such evolution exists, it should be most evident at the highest accessible redshifts (i.e., the redshifts probed in this thesis).

The chapter is organized as follows. We briefly describe the catalogs used for this work in Section 3.2. The color selection procedures for $5.5 \lesssim z \lesssim 6.4$ and $z \gtrsim 6.4$ quasars with radio counterparts are presented in Section 3.3. In Section 3.4, we present our follow-up campaign and the discovery of two new radio-loud $z \gtrsim 5.5$ quasars. The radio-loud definition used in this chapter and details on how it is calculated are introduced in Section 3.5. In Section 3.6, we investigate the radio-loud fraction of $z > 5.5$ quasars by compiling radio information on all such quasars currently in the literature. This work identifies two additional high-redshift, radio-loud quasars that had not previously been noted to be radio-loud. We summarize our results in Section 3.7. Magnitudes throughout the chapter are given in the AB system. We employ a cosmology with $H_0 = 69.3\,\mathrm{km\,s^{-1}\,Mpc^{-1}}$, $\Omega_M = 0.29$, and $\Omega_\Lambda = 0.71$ (Hinshaw et al. 2013).

3.2 Survey data

3.2.1 FIRST

The FIRST survey was designed to observe the sky at 20 cm (1.4 GHz) matching a region of the sky mapped by the Sloan Digital Sky Survey (SDSS; York et al. 2000), covering a total of about 10,600 deg^2. The survey contains more than 900,000 unique sources, with positional accuracy to $\lesssim 1''$. The catalog has a 5σ detection threshold which typically corresponds to 1 mJy although there is a deeper equatorial region where the detection threshold is about 0.75 mJy.

3.2.2 Pan-STARRS1

The PS1 3π survey has mapped all the sky above decl. -30 deg over a period of ~ 3 yr in five optical filters $g_{\rm P1}$, $r_{\rm P1}$, $i_{\rm P1}$, $z_{\rm P1}$, and $y_{\rm P1}$ (Stubbs et al. 2010; Tonry et al. 2012). The PS1 catalog used in this work comes from the first internal release of the 3π stacked catalog (PV1), which is based on the co-added PS1 exposures (see Metcalfe et al. 2013). This catalog includes data obtained primarily during the period 2010 May–2013 March and the stacked images consist on average of the co-addition of ~ 8 single images per filter. The 5σ median limiting magnitudes of this catalog are $g_{\rm P1} = 22.9$, $r_{\rm P1} = 22.8$, $i_{\rm P1} = 22.6$, $z_{\rm P1} = 21.9$, and $y_{\rm P1} = 20.9$. PS1 goes significantly deeper than SDSS in the i and z bands which together with the inclusion of a near-infrared y band allow it to identify new high-redshift quasars even in areas already covered by SDSS.

3.3 Candidate selection

3.3.1 The FIRST/Pan-STARRS1 catalog

In this chapter we use the multiwavelength information and large area coverage of the FIRST and Pan-STARRS1 surveys to find radio-loud high-redshift quasars. We cross match the FIRST catalog (13Jun05 version) and the PV1 PS1 stack catalog using a $2''$ matching radius. This yields a catalog containing 334,290 objects. Given the similar astrometric accuracy of Pan-STARRS1 and SDSS, we use the same matching radius utilized by the SDSS spectroscopic target quasar selection (Richards et al. 2002b). The peak of the SDSS-FIRST positional offsets occurs at $\sim 0.2''$ and the fraction of false matches within $2''$ is about 0.1% (Schneider et al. 2007, 2010see their Figure 6). Although this matching radius introduces a bias against quasars with extended radio morphologies (e.g., double-lobe quasars without radio cores or lobe-dominated quasars), Ivezić et al. (2002) show that less than 10% of SDSS-FIRST quasars have complex radio morphologies.

As redshift increases, the amount of neutral hydrogen in the universe also increases. At $z \gtrsim 6$ the optically thick Lyα forest absorbs most of the light coming from wavelengths $\lambda_{\rm rest} < 1216$ Å. This implies that objects at $z \sim 7$ ($z \sim 6$) are undetected or very faint in the z-band (i-band), showing a 'drop' in their spectra. They are thus called z-dropouts (i-dropouts). This 'drop' can be measured by their red $z - y$ and $i - z$ colors for z-dropouts and i-dropouts, respectively.

Given that the radio detection requirement significantly decreases the amount of contaminants (especially cool dwarfs), we perform a much broader selection criteria in terms of colors and signal-to-noise ratio (S/N) in comparison with our z- and i-dropout criteria presented in chapter **??**. In particular for the z-dropouts in this chapter, we allow for objects undetected in the $z_{\rm P1}$ band to be 0.1 mag bluer than in Section 2.2.1 and relax the S/N criteria in their $g_{\rm P1}$ and $r_{\rm P1}$ bands to be $\mathrm{S/N} < 5$ instead of $\mathrm{S/N} < 3$ (see Section 3.3.2). For the i-dropouts in this chapter, we relax the selection limits in comparison with Section 2.2.1. We allow the candidates to be 0.7 mag and 0.4 mag bluer in the $i_{\rm P1} - z_{\rm P1}$ and $r_{\rm P1} - z_{\rm P1}$ colors, respectively. For this selection we do not put any constrain in $z_{\rm P1} - y_{\rm P1}$ color (see Section 3.3.3). In this way we can detect $z > 5.5$ quasars which have similar colors to cool stars that are missed by typical color-based criteria.

3.3.2 z-dropout catalog search ($z \gtrsim 6.4$)

We require that more than 85% of the expected point-spread function (PSF)-weighted flux in the $z_{\rm P1}$ and the $y_{\rm P1}$ bands is located in valid pixels (i.e., that the PS1 catalog entry has `PSF_QF` > 0.85). We require a $\mathrm{S/N} > 7$ in the $y_{\rm P1}$ band and exclude those measurements in the $y_{\rm P1}$ band flagged as suspicious by the Image Processing Pipeline (IPP; Magnier 2006, 2007) (see Table B.1). The catalog selection can be summarized as:

$$\mathrm{S/N}(y_{\rm P1}) > 7 \tag{3.1a}$$

$$((\mathrm{S/N}(z_{\rm P1}) \geq 3)\ \mathrm{AND}\ (z_{\rm P1} - y_{\rm P1} > 1.4))\ \mathrm{OR}$$
$$((\mathrm{S/N}(z_{\rm P1}) < 3)\ \mathrm{AND}\ (z_{\rm P1,lim} - y_{\rm P1} > 1.3)) \tag{3.1b}$$

$$(\mathrm{S/N}(i_{\rm P1}) < 5)\ \mathrm{OR}\ (i_{\rm P1} - y_{\rm P1} > 2.0) \tag{3.1c}$$

$$(\mathrm{S/N}(r_{\rm P1}) < 5) \tag{3.1d}$$

$$(\mathrm{S/N}(g_{\rm P1}) < 5) \tag{3.1e}$$

where $z_{\rm P1,lim}$ is the 3σ $z_{\rm P1}$ limiting magnitude. This selection yields 66 candidates.

3.3.3 *i*-dropout catalog search ($5.5 \lesssim z \lesssim 6.4$)

Similar to the z-dropout catalog search, we require that more than 85% of the expected PSF-weighted flux in the $i_{\rm P1}$ and the $z_{\rm P1}$ bands is located in valid pixels. We require a S/N > 10 in the $z_{\rm P1}$ band and exclude those measurements flagged as suspicious by the IPP in the $z_{\rm P1}$ band.

We do not put any constraint on the $y_{\rm P1}$ band. This allows us to identify quasar candidates across a broad redshift range ($5.5 \lesssim z \lesssim 6.4$) and make better use of the $z_{\rm P1}$ band depth (which is deeper than the $y_{\rm P1}$ band). The $y_{\rm P1}$ information is used later on for the follow-up campaign.

We can summarize the catalog selection criteria as follows:

$$
\begin{align}
\mathrm{S/N}(z_{\rm P1}) > 10 \tag{3.2a}\\
((\mathrm{S/N}(i_{\rm P1}) \geq 3)\ \mathrm{AND}\, (i_{\rm P1} - z_{\rm P1} > 1.5))\ \mathrm{OR} \nonumber\\
((\mathrm{S/N}(i_{\rm P1}) < 3)\ \mathrm{AND}\, (i_{\rm P1,lim} - z_{\rm P1} > 1.0)) \tag{3.2b}\\
(\mathrm{S/N}(r_{\rm P1}) < 3)\ \mathrm{OR}\ (r_{\rm P1} - z_{\rm P1} > 1.8) \tag{3.2c}\\
(\mathrm{S/N}(g_{\rm P1}) < 3)\ \mathrm{OR}\ (g_{\rm P1} - z_{\rm P1} > 1.8) \tag{3.2d}
\end{align}
$$

where $i_{\rm P1,lim}$ is the 3σ $i_{\rm P1}$ limiting magnitude. This query yields 71 candidates.

3.3.4 Visual inspection

The number of candidates obtained from Sections 3.3.2 and 3.3.3 are small enough to visually inspect all of them. We use the latest PS1 images available for the visual inspection, which are usually deeper than the images used to generate the PS1 PV1 catalog. We also perform forced photometry on them to corroborate the catalog colors (as described in Bañados et al. 2014), especially when PV1 only reports limiting magnitudes. Thus, we visually inspect all the PS1 stacked, FIRST, and $z_{\rm P1}$ and $y_{\rm P1}$ PS1 single epoch images (where the S/N is expected to be the highest) for every candidate. The most common cases eliminated by visually inspection are PS1 artifacts due to some bad single epoch images, objects that lacked information in the PV1 catalog, and objects with evident extended morphology in the optical images. Based on the visual inspection, we assign priorities for the follow-up. Low-priority candidates are the ones whose PS1 detections look questionable, in the limit of our S/N cut, and/or objects with extended radio morphology which produces slightly positional offsets ($\gtrsim 1''$) between the optical and radio sources.

3.3.4.1 *z*-dropouts

Almost all the candidates can be ruled out by their PS1 stack images and/or single epoch images. There are only two objects we cannot completely rule out although there are some lines of evidence pointing us to believe they are unlikely to be quasars. For both PSO J141.7159+59.5142 and PSO J172.3556+18.7734, the $y_{\rm P1}$ detection looks questionable, in the limit of our S/N cut: 7.5 and 7.0, respectively. Their $y_{\rm P1}$ catalog aperture and PSF magnitudes differ by 0.3 and 0.28 mag which could indicate they are extended sources but it is hard to tell at this low S/N. The optical and radio positional offsets are somewhat larger than for most of the candidates: 0.6″ and 1.5″. All of this combined makes them low priority candidates. The PS1 and FIRST information for these sources is listed in Table 3.1.

3.3.4.2 *i*-dropouts

One of the candidates we selected is the known radio-loud quasar J0836+0054 at $z = 5.82$ (Fan et al. 2001). Its images look good and we would have followed it up. There are two low-redshift quasars that could have been selected for follow-up, J0927+0203 a quasar with a bright Hα line at ∼9200 Å ($z = 0.39$; Schneider et al. 2010) and J0943+5417, an Fe II low-ionization broad absorption line quasar ($z = 2.22$; Urrutia et al. 2009). After the visual inspection and literature search, there are 10 remaining candidates, out of which 9 are high priority candidates. Their PS1 and FIRST photometry are listed in Table 3.1.

3.4 Follow-up

3.4.1 Imaging

We use a variety of telescopes and instruments to confirm the optical colors and to obtain near-infrared photometry of our candidates, thereby allowing efficient removal of interlopers.

GROND (Greiner et al. 2008) at the 2.2m telescope in La Silla was used to take simultaneous images in the filters *grizJHK* during 2014 January 24 – February 5. Typical on-source exposure times were 1440 s in the near-infrared and 1380 s in the optical. The ESO Faint Object Spectrograph and Camera 2 (EFOSC2; Buzzoni et al. 1984) and the infrared spectrograph and imaging camera Son of ISAAC (SofI; Moorwood et al. 1998) at the ESO New Technology Telescope (NTT) were used to perform imaging in the $I_{\rm N}$ (*i*#705), $Z_{\rm N}$ (*z*#623), and $J_{\rm N}$ bands during 2014 March 2–6 with on-source exposure times of 600 s in the $I_{\rm N}$ and $Z_{\rm N}$ bands and 300 s in the J_N band. The data reduction consisted of bias subtraction, flat fielding, sky subtraction, image alignment, and stacking. The photometric zeropoints were determined as in Section 2.4.1. All of our high-priority candidates were photometrically followed up except for one which we directly observed spectroscopically (see next Section). Two low-priority *z*-dropouts and one low-priority *i*-dropout are still awaiting follow-up. Table 3.2 shows the follow-up photometry of our candidates.

Table 3.1. PS1-FIRST quasar candidates after visual inspection

Candidate	R.A. (J2000)	Decl. (J2000)	$g_{\rm P1}$ (mag)	$r_{\rm P1}$ (mag)	$i_{\rm P1}$ (mag)	$z_{\rm P1}$ (mag)	$y_{\rm P1}$ (mag)	$S_{\rm 1.4\,GHz,peak}$ (mJy)	Prio. [a]
PSO J141.7159+59.5142	09:26:51.83	+59:30:51.2	> 23.69	> 23.39	> 23.27	> 22.71	20.64 ± 0.14	1.11 ± 0.15	L
PSO J172.3556+18.7734	11:29:25.36	+18:46:24.3	> 23.64	> 23.41	> 23.26	> 22.78	20.68 ± 0.16	1.02 ± 0.14	L
PSO J044.9329–02.9977	02:59:43.91	–02:59:51.9	> 22.81	> 23.33	22.88 ± 0.28	21.16 ± 0.08	20.89 ± 0.17	5.86 ± 0.08	H
PSO J049.0958–06.8564	03:16:23.00	–06:51:23.2	> 22.57	> 23.11	23.07 ± 0.28	21.37 ± 0.10	20.76 ± 0.17	2.77 ± 0.14	H
PSO J055.4244–00.8035	03:41:41.86	–00:48:12.7	> 22.88	> 23.08	> 21.54	20.28 ± 0.05	20.27 ± 0.10	2.14 ± 0.14	H
PSO J106.7475+40.4145	07:06:59.40	+40:24:52.3	> 23.57	> 23.44	> 22.73	21.39 ± 0.10	20.85 ± 0.17	1.37 ± 0.13	L
PSO J114.6345+25.6724	07:38:32.30	+25:40:20.8	> 23.55	22.95 ± 0.14	22.48 ± 0.25	20.89 ± 0.10	20.62 ± 0.15	6.75 ± 0.13	H
PSO J135.3860+16.2518	09:01:32.65	+16:15:06.8	23.61 ± 0.24	> 23.97	22.38 ± 0.17	20.67 ± 0.05	20.82 ± 0.15	3.04 ± 0.14	H
PSO J164.9800+07.4459	10:59:55.22	+07:26:45.5	> 23.08	> 22.68	21.71 ± 0.14	20.17 ± 0.05	> 21.39	3.35 ± 0.14	H
PSO J208.4897+11.8071	13:53:57.54	+11:48:25.6	> 23.46	23.27 ± 0.28	22.73 ± 0.15	20.96 ± 0.09	20.79 ± 0.14	2.28 ± 0.13	H
PSO J238.0370–03.5494	15:52:08.89	–03:32:58.0	> 23.57	> 23.6	22.85 ± 0.33	21.15 ± 0.07	20.84 ± 0.19	6.01 ± 0.15	H
PSO J354.6110+04.9453	23:38:26.65	+04:56:43.3	> 23.46	23.01 ± 0.19	22.77 ± 0.18	20.88 ± 0.09	20.98 ± 0.29	6.44 ± 0.13	H

Note. — The two entries at the top are z-dropouts and the ten at the bottom are i-dropouts. The lower limits correspond to 3σ limiting magnitudes.

[a] Priorities. H: High. L: Low

Table 3.2. High priority PS1-FIRST *i*-dropout candidates follow-up.

Candidate	g_G (mag)	r_G (mag)	i_G (mag)	z_G (mag)	J_G (mag)	H_G (mag)	K_G (mag)	I_N (mag)	Z_N (mag)	J_N (mag)	Note [a]
PSO J044.9329–02.9977	> 23.72	23.37 ± 0.29	22.20 ± 0.18	22.14 ± 0.23	20.35 ± 0.17	19.92 ± 0.17	19.20 ± 0.28	–	–	–	3
PSO J049.0958–06.8564	24.47 ± 0.33	23.90 ± 0.23	23.12 ± 0.26	21.98 ± 0.12	20.52 ± 0.15	20.01 ± 0.18	19.19 ± 0.24	–	–	–	3
PSO J055.4244–00.8035	> 23.73	> 23.77	22.16 ± 0.18	20.58 ± 0.05	20.08 ± 0.16	20.03 ± 0.22	> 19.09	–	–	–	1
PSO J114.6345+25.6724	–	–	–	–	–	–	–	22.04 ± 0.18	20.95 ± 0.28	20.48 ± 0.11	2
PSO J135.3860+16.2518	> 24.57	24.32 ± 0.36	22.70 ± 0.18	20.85 ± 0.04	20.30 ± 0.12	20.91 ± 0.33	> 19.71	–	–	–	1
PSO J164.9800+07.4459	23.66 ± 0.15	22.19 ± 0.06	21.15 ± 0.05	20.49 ± 0.02	19.96 ± 0.10	19.72 ± 0.13	19.45 ± 0.27	20.64 ± 0.04	20.27 ± 0.04	–	3
PSO J208.4897+11.8071	> 24.50	23.21 ± 0.18	22.08 ± 0.25	21.66 ± 0.11	20.53 ± 0.23	19.83 ± 0.19	> 19.46	–	–	–	3
PSO J238.0370–03.5494	> 24.47	23.44 ± 0.18	22.03 ± 0.11	21.32 ± 0.07	19.99 ± 0.11	19.74 ± 0.16	> 19.70	–	–	–	3
PSO J354.6110+04.9453	–	–	–	–	–	–	–	–	–	–	2

Note. — The magnitude lower limits correspond to 3σ limiting magnitudes.

[a] 1: $z > 5.5$ quasar spectroscopically confirmed in this work. 2: Not a $z > 5.5$ quasar based on follow-up spectroscopy. 3: Not a $z > 5.5$ quasar based on follow-up photometry.

3.4.2 Spectroscopy

We have taken spectra of four high-priority objects that were not rejected by the follow-up photometry. We processed the data using standard techniques, including bias subtraction, flat fielding, sky subtraction, combination of individual frames, wavelength calibration, and spectrum extraction. The spectra were flux calibrated using standard stars from Massey & Gronwall (1990) and Hamuy et al. (1992, 1994).

The candidate PSO J114.6345+25.6724 was observed with the FOcal Reducer/low dispersion Spectrograph 2 (FORS2; Appenzeller & Rupprecht 1992) at the Very Large Telescope (VLT) on 2014 April 26 with an exposure time of 1497 s. The spectrum shows no clear break in the continuum and we classify this object as a radio galaxy at $z = 1.17$ by the identification of the narrow [O II] $\lambda3728$ emission line.

We obtained an optical spectrum of the candidate PSO J354.6110+04.9453 using the Double Spectrograph on the 5 m Hale telescope at Palomar Observatory (DBSP) on 2014 July 21 for a total integration time of 1800 s. The object has a red spectrum lacking the clear (Lyα) break which is a typical signature of high-redshift quasars. The spectrum does not clearly identify lines to determine a redshift. We believe this object is most likely a radio galaxy, but it is definitely not a $z > 5.5$ quasar. The other two spectroscopically followed up objects—PSO J055.4244–00.8035 and PSO J135.3860+16.2518—were confirmed to be high-redshift quasars. These two newly discovered quasars would not have been selected as candidates by the optical selection criteria presented in the chapter 2 of this thesis (see the individual notes on Section 2.5.1). The observations for these quasars are outlined in more detail below.

3.4.2.1 PSO J055.4244–00.8035 ($z = 5.68 \pm 0.05$)

The discovery spectrum was taken on 2014 February 22 using the DBSP spectrograph with a total exposure time of 2400 s. These observations were carried out in $\sim 1''$ seeing using the $1\farcs5$ wide longslit. This spectrum shows a sharp Lyα break indicating that the object is unambiguously a quasar at $z > 5.5$ but the S/N does not allow us to determine an accurate redshift. We took a second spectrum with FORS2 at the VLT on 2014 August 4; the seeing was $1\farcs1$ and it was observed for 1467 s. This spectrum is shown in Figure 3.1 and there are no obvious lines to fit and use to derive a redshift. There is, however, a tentative Si IV + O IV] line which falls in a region with considerable sky emission and telluric absorption making it not reliable for redshift estimation. We estimate the redshift instead by comparing the observed quasar spectrum with the composite SDSS $z \sim 6$ quasar spectrum from Fan et al. (2006b). We assume the redshift that minimizes the χ^2 between the observed spectrum and the template (the wavelength range where the minimization is performed is $\lambda_{\rm rest} = 1240 - 1450$ Å). The estimated redshift is $z = 5.68$. However, because of the lack of strong features in the spectrum, the χ^2 distribution is relatively flat around the minimum and thus a range of redshifts is acceptable. We follow Bañados et al. (2014) and assume a redshift uncertainty of 0.05.

3.4.2.2 PSO J135.3860+16.2518 ($z = 5.63 \pm 0.05$)

The discovery spectrum was taken with EFOSC2 at the NTT on 2014 March 3. The observations were carried out with the Gr#16 grism, 1.″5 slit width, 1.″3 seeing, and a total exposure time of 3600 s. The spectrum is very noisy but it resembles the shape of a high-redshift quasar with a tentative Lyα line at $\sim$ 8100 Å. In order to increase the S/N and confirm the quasar redshift, we took two additional spectra and combined them. One spectrum was taken on 2014 April 5 with the Multi-Object Double Spectrograph (MODS; Pogge et al. 2010) at the Large Binocular Telescope (LBT). The observations were carried out under suboptimal weather conditions with the 1.″2 wide longslit for a total exposure time of 2400 s. The second spectrum was taken with FORS2 at the VLT on 2014 April 26 with a total exposure time of 1467 s. The observing conditions were excellent with 0.″55 seeing and we used the 1.″3 width longslit. The combined MODS-FORS2 spectrum is shown in Figure 3.1. The estimated redshift by matching to the $z \sim 6$ quasar composite spectrum from Fan et al. (2006b) is $z = 5.63 \pm 0.05$. The redshift estimate for PSO J135.3860+16.2518 is quite uncertain as represented by its error bar. There might be a tentative Si IV + O IV] line which would place this quasar at a slightly higher redshift. However, this line falls in the same region as the tentative line in the quasar PSO J055.4244–00.8035, which is not a reliable region for redshift determination. A higher S/N optical spectrum and/or a near-infrared spectrum would be beneficial to obtain a more accurate redshift.

3.5 Radio-loudness

A clear consensus on a boundary between radio-loud and radio-quiet quasars has been difficult to achieve and there are several radio-loudness criteria in the literature (for a comparison of the different criteria see Hao et al. 2014). We adopt the most widespread definition in the literature. This is the radio/optical flux density ratio, $R = f_{\nu,5\,{\rm GHz}}/f_{\nu,4400\,\text{Å}}$ (Kellermann et al. 1989), where $f_{\nu,5\,{\rm GHz}}$ is the 5 GHz radio rest-frame flux density, $f_{\nu,4400\,\text{Å}}$ is the 4400 Å optical rest-frame flux density, and a quasar is considered radio loud if $R > 10$.

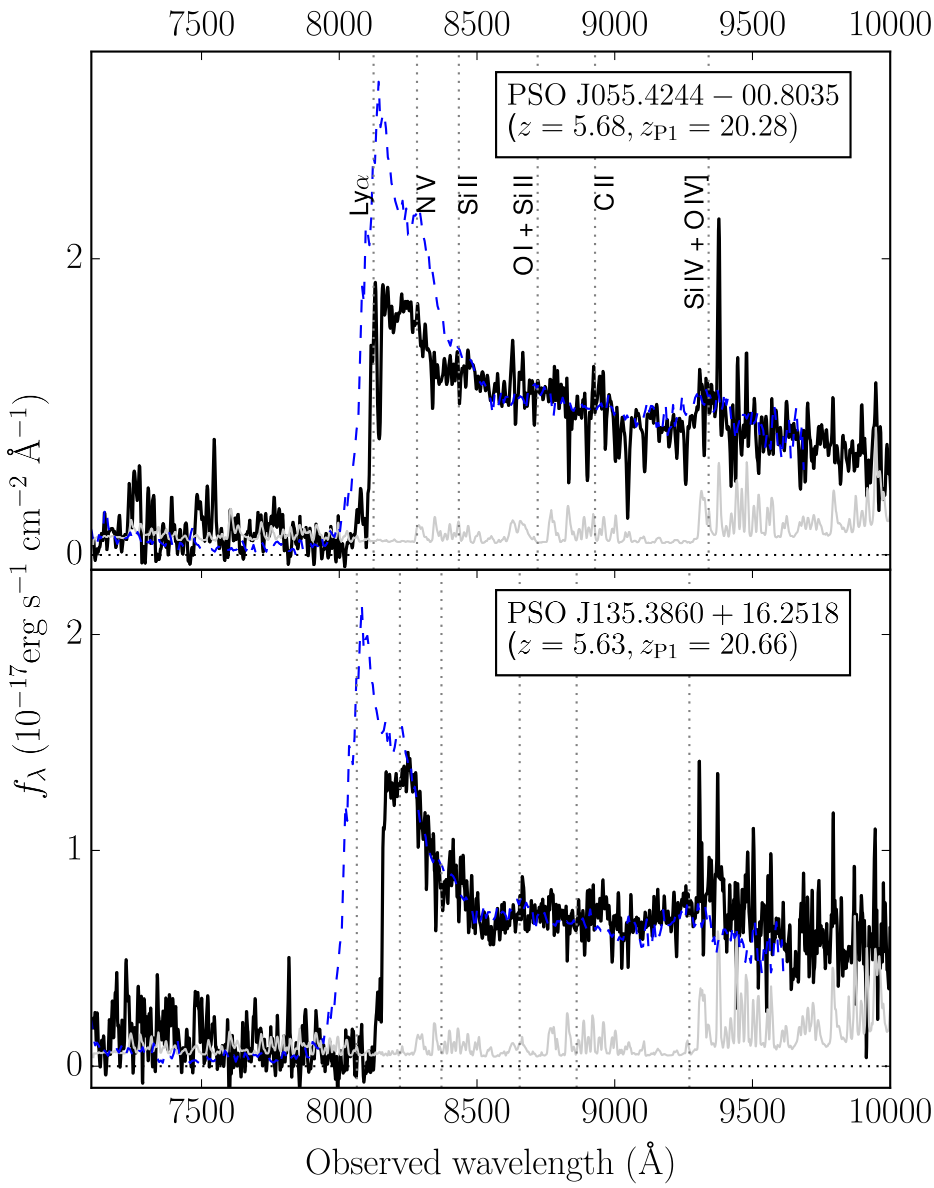

Figure 3.1: Spectra of the two radio-loud quasars discovered in this chapter. The gray solid lines show the 1σ error in the spectra. The blue dashed line is the SDSS $z \sim 6$ composite quasar spectrum from Fan et al. (2006b) at the redshift of the quasars for comparison. Vertical dotted lines indicate the observed wavelengths of key spectral lines, as given in the top panel.

3.5.1 The radio emission

The rest-frame 5 GHz radio flux density is obtained from the observed peak flux density at 1.4 GHz. We use the peak flux density since most of the $z \sim 6$ quasars appear to be unresolved on the radio maps (e.g., Wang et al. 2007, 2011a, but see also Cao et al. 2014, where they claim that there may be extended structures around the radio-loud quasar J2228+0110 on arcsecond scales).

We assume a power-law ($f_\nu \sim \nu^\alpha$) radio spectral energy distribution, adopting a typical radio spectral index $\alpha_R = -0.75$ as used in other high-redshift studies (e.g., Wang et al. 2007; Momjian et al. 2014). This index appears to be appropriate as Frey et al. (2005, 2008, 2011) find that at least three $z \sim 6$ radio-loud quasars show a steep radio spectrum.

3.5.2 The optical emission

The optical spectral indices of quasars span a fairly large range (at least $-1 < \alpha_\nu < 0$). When a direct measurement of the optical rest-frame flux density at 4400 Å is not possible, this is typically extrapolated from the AB magnitude at rest frame 1450 Å (m_{1450}) assuming an average optical spectral index of $\alpha_\nu = -0.5$ (e.g., Wang et al. 2007). These fairly large extrapolations could lead to dramatic errors if the studied quasars are not average quasars. At $z \sim 6-7$ we can take advantage of infrared space missions such as *Spitzer* and the *Wide-field Infrared Survey* (*WISE*; Wright et al. 2010) to reduce the extrapolation error by using $\sim 3\,\mu$m ($\lambda_{\rm rest} = 4286$ Å at $z = 6$) photometry.

Following previous works, we also assume an optical spectral index of $\alpha_\nu = -0.5$ but we estimate $f_{\nu,4400\,\text{Å}}$ from IRAC (Fazio et al. 2004) 3.6μm ($S_{3.6\mu m}$) observations when available ($\lambda_{\rm rest,eff} = 5071$ Å at $z = 6$). Otherwise, $f_{\nu,4400\,\text{Å}}$ is calculated from the *WISE* W_1 magnitude ($\lambda_{\rm rest,eff} = 4811$ Å at $z = 6$) reported in the ALLWISE Source catalog or reject table (with $S/N > 2.5$). Table 3.3 lists $S_{3.6\mu\rm m}$, W_1, and m_{1450} for all $z > 5.5$ quasars with published measurements at 1.4 GHz in the literature. There are five quasars without IRAC or *WISE* measurements. For these objects, $f_{\nu,4400\,\text{Å}}$ is estimated from m_{1450}. To estimate the error we determine $f_{\nu,4400\,\text{Å}}$ from m_{1450} for the quasars having IRAC or *WISE* ($\sim 3\,\mu$m) measurements. Then, for each object we compute the ratio $(f_{\nu,4400\,\text{Å}}(3\,\mu\text{m}) - \text{f}_{\nu,4400\,\text{Å}}(\text{m}_{1450}))/\text{f}_{\nu,4400\,\text{Å}}(3\,\mu\text{m})$. This results in a symmetric distribution, centered on zero, and with a standard deviation of 0.4. Finally, we take the absolute value of the previous distribution and assume its median as a representative error for $f_{\nu,4400\,\text{Å}}$ derived from m_{1450}. This corresponds to a relative error of 0.30 (i.e., analogous to assuming a measurement of $f_{\nu,4400\,\text{Å}}$ with $S/N = 3.3$). These errors must be taken with caution since they are just representative uncertainties and there could be objects with considerably larger errors, as exemplified in Section 3.6.1.

3.6 Results

We determine the radio-loudness parameter R and the optical and radio luminosities $L_{4400\,\text{Å}}$ and $L_{5\text{GHz}}$ ($L = \nu L_\nu$) for all the $z > 5.5$ quasars having 1.4 GHz data published in the literature. These parameters are included in Table 3.3. Figure 3.2 shows the rest-frame 5 GHz radio luminosity versus rest-frame 4400 Å optical luminosity. Eight quasars are classified as radio-loud ($R > 10$), including the two quasars discovered in Section 3.4.2 and two additional possible radio-loud quasars which will be introduced in Section 3.6.2. There are 33 objects robustly classified as radio-quiet quasars ($R < 10$). Two quasars need deeper radio data to classify them unambiguously (with radio loudness upper limit > 10). In this chapter we do not find any radio-loud quasar at $z \sim 7$ in an area of about 10,600 square degrees of sky to the sensitivities of the FIRST and Pan-STARRS1 surveys (~ 1 mJy and 7σ-limiting magnitude $y_{\text{P1}} \sim 20.5$, respectively). Conclusions on the RLF at $z > 6.5$ are not possible at this time, since there are currently only seven quasars known at $z > 6.5$ (Mortlock et al. 2011; Venemans et al. 2013, 2015). From these seven quasars, only one has dedicated radio follow-up (Momjian et al. 2014) while a second one is in the FIRST footprint but it is a non-detection (see Section 3.6.3; Venemans et al. 2015). The RLF at $z \sim 6$ is discussed in Section 3.6.3.

3.6.1 J0203+0012: a radio-loud quasar?

The quasar J0203+0012 at $z = 5.72$ was classified as radio-loud quasar by Wang et al. (2008). They derived the rest-frame 4400 Å flux density from the 1450 Å magnitude. As discussed previously, these large extrapolations can carry large uncertainties and can be critical for the classification and derived parameters for specific objects. This is the case for J0203+0012, a broad-absorption line quasar (Mortlock et al. 2009) whose m_{1450} could have been underestimated, resulting in a low optical luminosity (see also its spectral energy distribution in Figure 14 of Leipski et al. 2014). This quasar has a radio-loudness parameter $R = 4.3 \pm 0.5$ or $R = 12.1 \pm 3.2$ depending if the rest-frame 4400 Å flux density is extrapolated from the IRAC 3.6 μm photometry or from m_{1450}, respectively (see Figure 3.2). It is clear that the difference is dramatic and that by using the m_{1450} proxy this quasar would be classified (barely) as radio-loud. We argue that the value of $L_{4400\,\text{Å}}$ obtained from the observed 3.6 μm photometry is more reliable for $z > 5.5$ quasars since it relies less on extrapolation (for this particular case, the extrapolation is less by approximately a factor of three). Also, while radio-loud AGN are typically located in dense environments (e.g., Venemans et al. 2007b; Hatch et al. 2014), we found that J0203+0012 does not live in a particularly dense region but rather comparable with what is expected in blank fields (see Chapter 4).

3.6.2 Pushing the FIRST detection threshold

The FIRST survey has a typical source detection threshold of 1 mJy beam^{-1} which assures that the catalog has reliable entries with typical S/N greater than five. There are 30 known $z > 5.5$ quasars that are not in the FIRST catalog or in the Stripe 82 VLA Survey catalog (Hodge et al. 2011) but that are located in the FIRST footprint. The discovery papers of these quasars are Mahabal et al. (2005); Cool et al. (2006); Jiang et al. (2009); Willott et al. (2009, 2010a,b); McGreer et al. (2013); Bañados et al. (2014); Venemans et al. (2015); Bañados et al. (in prep.); Venemans et al. (in prep.); and Warren et al. (in prep.).

We checked for a radio detection beyond the FIRST catalog threshold as follows: we obtained the 1.4 GHz FIRST images for all 30 quasars and checked for radio emission within 3″ of the optical quasar position with a S/N≥ 3. We find that the quasars J1609+3041 at $z = 6.14$ (Warren et al. in prep) and J2053+0047 at $z = 5.92$ (Jiang et al. 2009) have tentative 1.4 GHz detections at S/N of 3.5 and 3, respectively. Their radio postage stamps are shown in Figure 3.3. The two quasars have optical-to-radio positional differences less than 1.″8 (1 pixel). In order to quantify the probability of finding a spurious association with a 3σ fluctuation given our sample of 30 quasars we performed the following steps. We placed 100 random positions in each 1 arcmin^2 FIRST image centered on a quasar and measured the maximum peak flux within 1.″8. We removed points falling within 1.″8 from an optical source in the PS1 catalog. There are no radio sources in the FIRST catalog for any of these 1 arcmin^2 fields. We computed the fraction of measurements with S/N ≥ 3. We repeated this procedure 100 times and the fraction of measurements with S/N ≥ 3 was always < 1%. The full distribution is centered on 0.5% with a standard deviation of 0.1%. Therefore, in our sample of 30 quasars, the expected number of spurious $\sim 3\sigma$ associations within 1.″8 is 0.15 and being conservative less than 0.3. This analysis suggests that these identifications are unlikely to be spurious. If these detections are real, these quasars are classified as radio-loud with $R = 28.3 \pm 8.6$ and $R = 44.1 \pm 18.7$ (see Table 3.3). In Figure 3.2, these new tentative radio detections are marked as red downward triangles.

We make a mean stack of the 28 remaining quasars in the FIRST footprint that have $S/N < 3$ in their individual images. We find no detection in the stacked image with an upper limit of $f_\nu = 84\,\mu$Jy (see Figure 3.2).

3.6.3 Constraining the radio-loud fraction of quasars at $z \sim 6$

Considering all the quasars in Table 3.3, there are eight known radio-loud quasars at $z \sim 6$, 32 radio-quiet (excluding J1120+0641 at $z = 7.08$), and two ambiguous. There is one additional quasar that is robustly classified by a non-detection in FIRST as radio-quiet: J0148+0600 at

$z = 5.98$ (Bañados et al. 2014; Becker et al. 2015). This radio-quiet quasar has $\log L_{4400\,\text{Å}}\,(L_\odot) = 13.04 \pm 0.2$, $\log L_{5\,\text{Ghz}}(L_\odot) < 8.7$, and $R < 5.6$ (see Figure 3.2). We can provide a rough estimation of the radio-loud fraction of quasars at $z \sim 6$ of $\text{RLF} = 8/(8+(34+1)) \sim 19\%$. In this statistics we considered the two ambiguous cases as radio-quiet. This is a relatively large fraction; however, these quasars were selected by several methods which could potentially bias the results. As we have included radio-loud quasars that could not have been discovered based on their optical/near-infrared properties alone, the actual fraction of radio-loud quasars is overestimated. Therefore, this value has to be taken only as an upper limit.

In order to set a lower limit in the RLF at $z \sim 6$, we consider quasars that were selected based on their optical properties (i.e., we exclude the two quasars discovered in this chapter, J2228+0110 which was discovered by its radio emission by Zeimann et al. 2011, and J1427+3312 which was discovered by its radio emission by McGreer et al. 2006[1]). We also exclude quasars at $z > 6.5$, i.e., J1120+0641 at $z = 7.08$ and PSO J036.5078+03.0498 at $z = 6.527$. The latter quasar was discovered in Venemans et al. (2015). It is not detected in FIRST and has $\log L_{4400\,\text{Å}}\,(L_\odot) = 12.87 \pm 0.03$, $\log L_{5\,\text{Ghz}}(L_\odot) < 8.8$, and $R < 10.7$ (see Figure 3.2). Considering all the FIRST non-detections from the previous section as radio-quiet, we find a lower limit of $\text{RLF} = 4/(4 + (34 + 27)) \sim 6\%$. This is a lower limit because there is still the possibility that a fraction of the FIRST non-detections are radio-loud (see Figure 3.2). Therefore, in this case we are potentially underestimating the number of radio-loud quasars.

Additionally, in order to fully use the information provided by both the radio detections and upper limits, we estimate the radio-loud fraction using the Kaplan–Meier estimator (Kaplan & Meier 1958). The RLF estimated with this method, after excluding quasars at $z > 6.5$ and quasars selected by their radio emission, is $8.1^{+5.0}_{-3.2}\%$.

3.6.4 What changes with an alternative radio-loudness definition?

Another common definition for radio-loudness in the literature (besides our adopted criteria in Section 3.5), is a simple cut on rest-frame radio luminosity. This criteria is a better indicator of radio-loudness if the optical and radio luminosities are not correlated (Peacock et al. 1986; Miller et al. 1990; Ivezić et al. 2002 Appendix C). We here explore how our results would change if we adopt a fixed radio luminosity as a boundary between radio-quiet and radio-loud objects. We use the alternative criteria adopted by Jiang et al. (2007a), where a radio-loud quasar is defined with a luminosity density at rest-frame 5 GHz, $L_{\nu,5\text{Ghz}} > 10^{32.5}\,\text{ergs s}^{-1}\,\text{Hz}^{-1}$. This is equivalent to requiring $\log L_{5\,\text{Ghz}}(L_\odot) > 8.61$ (see the horizonal line in Figure 3.2).

---

[1] We note however, that J1427+3312 was independently discovered by Stern et al. (2007) without using the radio information, but using a mid-infrared selection instead.

One caveat with this definition is that J2228+0110 is just below the radio-loud cut although is still consistent with being radio-loud within the uncertainties: $\log L_{5\mathrm{Ghz}}(L_\odot) = 8.59 \pm 0.08$. Note that the quasar J0203+0012, discussed in Section 3.6.1, is also classified as radio-quiet by this definition.

We estimate the radio-loud fraction using the Kaplan–Meier estimator, following the approach of the previous section. The estimated RLF with this definition is $6.6^{+4.1}_{-1.6}\%$. This result agrees with the one obtained in Section 3.6.3, and they are both consistent with no strong evolution of the radio-loud fraction of quasars with redshift.

3.7 Summary

We perform a search for high-redshift, radio-loud quasars (i- and z-dropouts) by combining radio and optical observations from the FIRST and Pan-STARRS1 surveys. The multiwavelength information of these surveys allows the identification of quasars with optical colors similar to the more numerous cool dwarfs and therefore missed by typical color selection used by high-redshift quasar surveys (e.g., Fan et al. 2006c; Bañados et al. 2014). We do not find good quasar candidates at $z \gtrsim 6.4$ (z-dropouts). We discover two of the radio loudest quasars at $z \gtrsim 5.6$: PSO J055.4244–00.8035 ($z = 5.68$) with a radio-loudness parameter $R = 178.0 \pm 40.5$ and PSO J135.3860+16.2518 ($z = 5.63$) with $R = 91.4 \pm 8.8$. These two quasars are at the low-redshift end of the i-dropout selection technique ($5.5 \lesssim z \lesssim 5.7$) and they are too blue in $i - z$ to have been selected by color cuts usually applied in optical searches for high-redshift quasars. Currently, there is an apparent lack of quasars at $5.2 < z < 5.7$ (see Figure 2.6 and McGreer et al. 2013). This is due to the similarity between optical colors of quasars and M dwarfs which are the most numerous stars in the Galaxy (Rojas-Ayala et al. 2014). The identification of these two radio-loud quasars in our extended selection criteria implies that there must be a significant number of radio-quiet quasars at these redshifts that are just being missed by standard selection criteria. The use of additional wavelength information, for example using *WISE* photometry, might help to find quasars in this still unexplored redshift range.

We inspect all the 1.4 GHz FIRST images of the known quasars that are in the FIRST survey footprint but not in the catalog. Based on this inspection, we identify two additional $z \sim 6$ radio-loud quasars which are detected at S/N$\gtrsim 3$ and therefore would benefit from deeper radio imaging.

We highlight the importance of infrared photometry (e.g., from *Spitzer* or *WISE*) for $z > 5.5$ quasars in order to have an accurate measurement of the rest-frame 4400 Å luminosity which allows us to robustly classify quasars as radio-loud or radio-quiet. By using *Spitzer* photometry

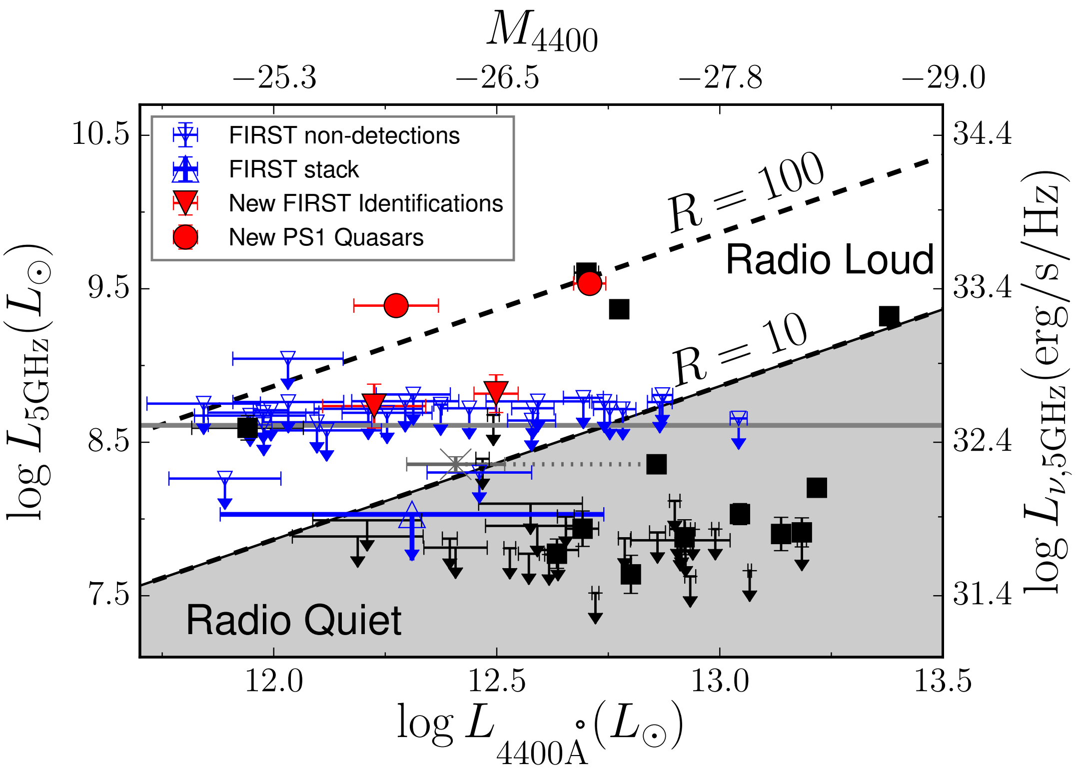

Figure 3.2: Rest-frame 5 GHz radio luminosity vs. rest-frame 4400Å optical luminosity for all $z > 5.5$ quasars in the literature observed at 1.4 GHz (see Table 3.3). Filled symbols are 1.4 GHz detections and arrows represent 3σ upper limits in the rest-frame 5GHz luminosity. The dashed lines represent the radio-to-optical ratios (R) of 100 and 10 (separation of radio-loud and radio-quiet). The red circles are the two new Pan-STARRS1 radio-loud quasars presented here. These quasars are among the most radio loud quasars at these redshifts. The red downward triangles are two quasars that we identify as radio-loud by inspecting their FIRST images (see Section 3.6.2). The blue downward triangles are upper limits for 28 quasars that are located in the FIRST survey footprint. The blue upward triangle represents the location of the stack of the 28 undetected quasars in the FIRST survey assuming their average redshift of 6. The gray cross represents the position of J0203+0012 if its $L_{4400\,\text{Å}}$ is calculated from extrapolating m_{1450} and it is connected by a dotted line with the position determined by estimating $L_{4400\,\text{Å}}$ from the IRAC 3.6 μm photometry (see Section 3.6.1). The horizontal gray line denotes the division of radio-loud and radio-quiet quasars employed by Jiang et al. (2007a) (see Section 3.6.4).

we reclassify the quasar J0203+0012 at $z = 5.72$ as radio-quiet ($R = 4.3 \pm 0.5$). This quasar was previously classified as radio-loud by estimating its rest frame 4400 Å luminosity from the magnitude at 1450 Å (Wang et al. 2008). The estimate based on an infrared proxy is much better than the one based on the m_{1450} proxy because less extrapolation is needed. Thus, the estimated rest-frame 4400 Å luminosity is less affected by spectral energy distribution assumptions.

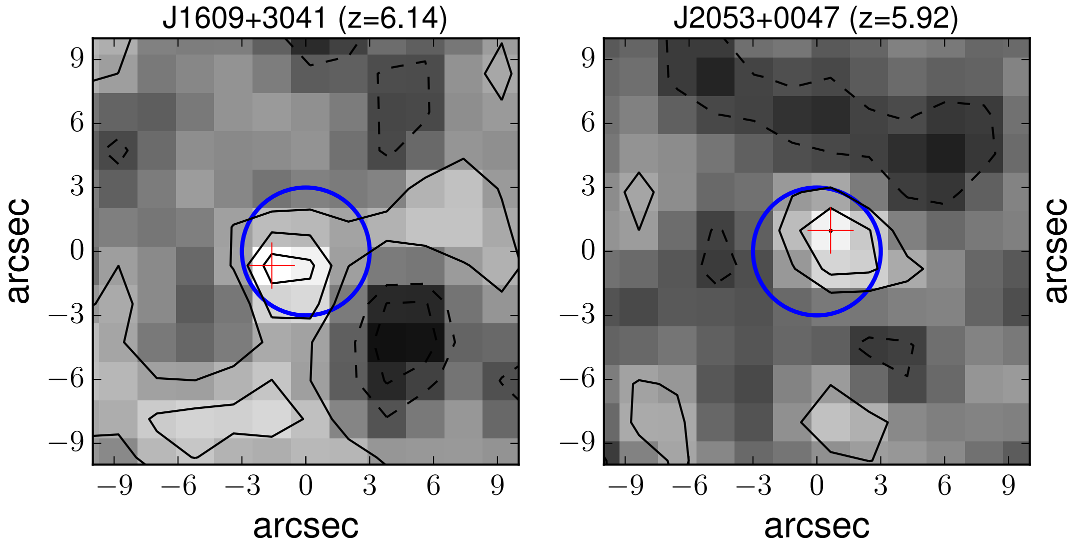

Figure 3.3: 1.4 GHz postage stamp images from the FIRST Survey (typical resolution of 5″) of the quasars J1609+3041 (left) and J2053+0047 (right). The blue circles have a radius of 3″ and are centered on the quasar optical positions. These positions have J2000 coordinates corresponding to (R.A., Decl.) = (16:09:37.28, +30:41:47.7) for J1609+3041, and (R.A., Decl.) = (20:53:21.77, +00:47:06.8) for J2053+0047. The red crosses show the 1.4 GHz peak pixel. The black solid (dashed) lines are the positive (negative) $1, 2, 3\sigma$ -contours. J1609+3041 and J2053+0047 have a S/N of 3.5 and 3.0, respectively. Using these radio flux densities, both quasars are classified as radio-loud with $R = 28.3 \pm 8.6$ and $R = 44.1 \pm 18.7$, respectively (see Table 3.3).

We compile all the $z > 5.5$ quasars having 1.4 GHz data in the literature and, by making simple assumptions (see Section 3.6.3), we find that the radio-loud fraction of quasars at $z \sim 6$ is between 6% and 19%. We also estimate the radio-loud fraction using the Kaplan–Meier estimator which takes into account both radio detections and upper limits, obtaining RLF = $8.1^{+5.0}_{-3.2}$%. This fraction suggests no strong evolution of the radio-loud fraction with redshift. This result contrasts with some lower redshift studies that show a decrease of the radio-loud fraction of quasars with redshift (e.g., Jiang et al. 2007a).

The study of the RLF of quasars at $z \gtrsim 6$ has the potential to give a definitive answer to the issue of a possible evolution of the RLF of quasars with redshift. For this, a homogeneous radio (and infrared) follow-up of a well-defined sample of $z \sim 6$ quasars (or $z \sim 7$ when more of these objects are discovered) selected in a consistent manner is crucial to test whether there is evolution in the RLF of quasars.

Table 3.3. Data and derived parameters of the $z > 5.5$ quasars with 1.4 GHz data in the literature.

Quasar	z	$S_{1.4\,\mathrm{GHz,peak}}$ (μJy)	Ref.(z,1.4 GHz)	m_{1450} [a] (mag)	W_1 [b] (mag)	$S_{3.6\mu\mathrm{m}}$ [c] (mag)	$\log L_{5\,\mathrm{GHz}}$ ($L_\odot$)	$\log L_{4400\,\text{Å}}$ [d] ($L_\odot$)	R [d]
J0002+2550	5.82	89 ± 14	1,2	19.0	18.86 ± 0.06	18.71 ± 0.02	8.03 ± 0.07	13.05 ± 0.01	1.3 ± 0.2
J0005–0006	5.85	< 390	3,4	20.2	20.00 ± 0.16	20.10 ± 0.03	< 8.7	12.49 ± 0.01	< 20.9
J0033–0125	6.13	< 57	5,4	21.8	20.99 ± 0.40	–	< 7.9	12.19 ± 0.15	< 6.8
J0203+0012	5.72	195 ± 22	6,4	21.0	19.39 ± 0.09	19.14 ± 0.03	8.36 ± 0.05	12.86 ± 0.01	4.3 ± 0.5
J0303–0019	6.08	< 186	7,4	21.3	–	20.24 ± 0.04	< 8.4	12.47 ± 0.01	< 11.4
P055–00	5.68	2140 ± 137	8,9	20.4	20.62 ± 0.26	–	9.39 ± 0.03	12.27 ± 0.09	178.0 ± 40.5
J0353+0104	6.049	< 57	10,4	20.2	19.34 ± 0.09	19.44 ± 0.04	< 7.9	12.79 ± 0.01	< 1.7
J0818+1722	6.02	123 ± 12	1,2	19.3	–	18.35 ± 0.01	8.20 ± 0.04	13.22 ± 0.01	1.3 ± 0.1
J0836+0054	5.81	1740 ± 40	3,2	18.8	18.00 ± 0.04	17.87 ± 0.01	9.32 ± 0.01	13.38 ± 0.01	11.9 ± 0.3
J0840+5624	5.8441	< 27	11,2	20.0	19.46 ± 0.14	19.53 ± 0.02	< 7.5	12.72 ± 0.01	< 0.9
J0841+2905	5.98	< 81	1,4	19.6	19.91 ± 0.16	19.74 ± 0.05	< 8.0	12.65 ± 0.02	< 3.1
J0842+1218	6.08	< 57	12,4	19.6	–	19.13 ± 0.01	< 7.9	12.91 ± 0.01	< 1.3
P135+16	5.63	3040 ± 145	8,9	20.6	19.51 ± 0.11	–	9.53 ± 0.02	12.71 ± 0.04	91.4 ± 8.8
J0927+2001	5.7722	50 ± 11	13,4	19.9	19.40 ± 0.11	19.72 ± 0.05	7.77 ± 0.10	12.63 ± 0.02	1.9 ± 0.4
J1030+0524	6.308	< 60	3,2	19.7	19.28 ± 0.09	19.23 ± 0.04	< 7.9	12.91 ± 0.02	< 1.5
J1044–0125	5.7847	< 72	14,2	19.2	19.05 ± 0.07	18.84 ± 0.02	< 7.9	12.99 ± 0.01	< 1.2
J1048+4637	6.2284	< 33	1,2	19.2	19.05 ± 0.06	18.80 ± 0.01	< 7.7	13.07 ± 0.01	< 0.5
J1120+0641	7.0842	< 23	15,16	20.4	19.61 ± 0.11	19.39 ± 0.03	< 7.6	12.93 ± 0.01	< 0.7
J1137+3549	6.03	< 51	1,2	19.6	19.16 ± 0.07	19.09 ± 0.03	< 7.8	12.92 ± 0.01	< 1.1
J1148+5251	6.4189	55 ± 12	1,17	19.0	18.67 ± 0.05	18.57 ± 0.02	7.91 ± 0.09	13.18 ± 0.01	0.7 ± 0.2
J1250+3130	6.15	< 63	1,2	19.6	19.11 ± 0.07	19.09 ± 0.01	< 7.9	12.94 ± 0.01	< 1.3
J1306+0356	6.016	< 63	3,2	19.6	19.57 ± 0.10	19.24 ± 0.04	< 7.9	12.86 ± 0.02	< 1.5
J1319+0950	6.133	64 ± 17	14,18	19.6	19.73 ± 0.11	–	7.94 ± 0.12	12.69 ± 0.04	2.4 ± 0.7
J1335+3533	5.9012	35 ± 10	1,2	19.9	19.41 ± 0.07	19.35 ± 0.02	7.64 ± 0.12	12.80 ± 0.01	0.9 ± 0.3
J1411+1217	5.904	61 ± 16	3,2	20.0	19.29 ± 0.07	19.05 ± 0.02	7.88 ± 0.11	12.92 ± 0.01	1.2 ± 0.3
J1425+3254[e]	5.8918	< 60	1,4	20.6	19.67 ± 0.08[e]	20.36 ± 0.06[e]	< 7.9	12.39 ± 0.02	< 4.1[e]
J1427+3312	6.12	1730 ± 131	19,9	20.3	19.52 ± 0.08	19.49 ± 0.02	9.37 ± 0.03	12.77 ± 0.01	53.3 ± 4.1
J1429+5447	6.1831	2930 ± 152	18,9	20.9	19.73 ± 0.08	–	9.60 ± 0.02	12.70 ± 0.03	109.2 ± 8.9
J1436+5007	5.85	< 48	1,2	20.2	19.87 ± 0.09	19.79 ± 0.02	< 7.8	12.62 ± 0.01	< 1.9
J1509–1749	6.121	< 54	20,18	19.8	–	–	< 7.9	12.91 ± 0.11	< 1.2
J1602+4228	6.09	60 ± 15	1,2	19.9	18.75 ± 0.04	18.57 ± 0.02	7.90 ± 0.11	13.14 ± 0.01	0.8 ± 0.2
J1609+3041	6.14	484 ± 137	21,22	20.9	20.22 ± 0.14	–	8.82 ± 0.12	12.50 ± 0.05	28.3 ± 8.6
J1621+5155	5.71	< 63	4,4	19.9	18.35 ± 0.03	–	< 7.9	13.18 ± 0.01	< 0.7
J1623+3112	6.26	< 93	18,2	20.1	19.22 ± 0.06	19.23 ± 0.03	< 8.1	12.90 ± 0.01	< 2.3
J1630+4012	6.065	< 45	1,4	20.6	20.19 ± 0.12	19.98 ± 0.06	< 7.8	12.57 ± 0.02	< 2.2
J1641+3755	6.047	< 96	20,4	20.6	–	–	< 8.1	12.58 ± 0.12	< 4.6
J2053+0047	5.92	434 ± 143	23,22	21.2	20.82 ± 0.32	–	8.74 ± 0.14	12.23 ± 0.12	44.1 ± 18.7
J2054–0005	6.0391	< 69	14,4	20.6	–	–	< 8.0	12.59 ± 0.12	< 3.2
J2147+0107	5.81	< 54	23,18	21.6	20.33 ± 0.20	–	< 7.8	12.41 ± 0.07	< 3.5
J2228+0110	5.95	310 ± 57	24,24	22.2	–	–	8.59 ± 0.08	11.94 ± 0.13	61.3 ± 20.9
J2307+0031	5.87	< 51	23,18	21.7	19.78 ± 0.13	–	< 7.8	12.64 ± 0.05	< 2.0
J2315–0023	6.117	< 48	10,4	21.3	20.26 ± 0.20	20.10 ± 0.03	< 7.8	12.53 ± 0.01	< 2.6
J2329–0301	6.417	< 66	20,4	21.6	–	–	< 8.0	12.21 ± 0.12	< 8.3

References. — (1) Carilli et al. (2010), (2) Wang et al. (2007), (3) Kurk et al. (2007), (4) Wang et al. (2008), (5) Willott et al. (2007), (6) Mortlock et al. (2009), (7) Kurk et al. (2009), (8) This Work, (9) FIRST Becker et al. (1995), (10) Jiang et al. (2008), (11) Wang et al. (2010), (12) De Rosa et al. (2011), (13) Carilli et al. (2007), (14) Wang et al. (2013), (15) Venemans et al. (2012), (16) Momjian et al. (2014), (17) Carilli et al. (2004b), (18) Wang et al. (2011a), (19) McGreer et al. (2006), (20) Willott et al. (2010a), (21) Warren et al. (in prep.), (22) This Work: new radio identification (see Section 3.6.2), (23) Jiang et al. (2009), (24) Zeimann et al. (2011)

Note. — Reported upper limits correspond to 3σ.

[a] All m_{1450} are taken from Calura et al. (2014) except for J2228+0110 for which is taken from Zeimann et al. (2011), for J1609+3041 for which is calculated from its y_{P1} band (Bañados et al. in prep.), and for P055–00 and P135+16 for which are calculated in this work as in Bañados et al. (2014).

[b] All W_1 measurements have $S/N > 2.5$. Magnitudes are taken from the main ALLWISE source catalog with exception of J0033-0125, P055–00, and J2053+0047, for which are taken from the ALLWISE reject table.

[c] $S_{3.6\mu m}$ measurements are from Leipski et al. (2014) with exception of J1120+0641 and J1425+3254 for which are taken from Barnett et al. (2015) and Cool et al. (2006), respectively.

[d] $\log L_{4400\,\text{Å}}$ and $f_{\nu,4400\,\text{Å}}$ in $R = f_{\nu,5\,\mathrm{GHz}}/f_{\nu,4400\,\text{Å}}$ are based on $S_{3.6\mu m}$ measurements when available, otherwise from W_1. If the quasar does not have $S_{3.6\mu m}$ nor W_1 data, the quantities are extrapolated from m_{1450} (see text in Section 3.5.2).

[e] We note a large discrepancy between the reported *WISE* and *Spitzer* magnitudes for J1425+3254. If W_1 is used instead of $S_{3.6\mu m}$ to estimate $f_{\nu,4400\,\text{Å}}$, R would be < 2.1.

Chapter 4

No galaxy overdensity around a quasar at $z = 5.7$[†]

4.1 Context

Based on the premise that high-redshift quasars trace massive dark matter halos (e.g., Sijacki et al. 2009) and could therefore pinpoint protoclusters (the progenitors of galaxy clusters in the local Universe), several studies have searched for overdensities around $z \sim 6$ quasars (e.g., Stiavelli et al. 2005). However, despite many efforts, the relationship between galaxy overdensities and $z \sim 6$ quasars is ambiguous (e.g., Kim et al. 2009). This can possibly be attributed to the difficulty of finding galaxies with accurate redshifts in the vicinity of $z \sim 6$ quasars. So far, overdensity searches around $z \sim 6$ quasars have been based on studies of Lyman break galaxies (LBGs), which probe a redshift range of $\Delta z \approx 1$. This range is large enough to select galaxies that may not be physically related to the quasar. Alternatively, Lyman Alpha Emitters (LAEs) might currently be the best tracers of large scale structure at high redshift because they can be efficiently found in a small redshift range using narrow-band imaging (Overzier et al. 2009).

In this chapter, we use deep narrow- and broad-band imaging to study the environment of the broad-absorption line quasar ULAS J0203+0012 (hereafter J0203+0012; Venemans et al. 2007a; Jiang et al. 2008; Mortlock et al. 2009), one of the first $z \sim 6$ quasars known with a redshift that shifts the Lyα line into an atmospheric window that allows for deep narrow-band imaging. We assume the quasar redshift of $z = 5.72$ determined by Mortlock et al. (2009), which is based on the N v, Si iv, C iv, and C iii lines from a combined optical and near-infrared spectrum. However,

---

[†] This chapter is a version of the paper Bañados et al. (2013).

we have to keep in mind that any redshift in the range of $5.70 < z < 5.74$ is consistent with their data. Ryan-Weber et al. (2009), using a Keck/NIRSPEC spectrum, independently confirmed this quasar, reporting a redshift of $z = 5.706$ based on a broad emission feature that they presume to be C IV $\lambda\,1549.062$. In any case, the uncertainty in redshift does not shift the Lyα line outside the narrow-band filter used in our work.

In Section 4.2 we describe the data used in this study, photometry, and object detection. Section 4.3 describes how LAE and dropout or Lyman break galaxy (LBG) candidates were selected. In Section 4.4 we present our results, including a number count comparison with blank fields, photometric properties of the LAE sample, and our estimation of the black hole mass of the quasar. Finally, in Section 4.5 we discuss the results and present our conclusions.

In this chapter, all magnitudes are given in the AB system and are corrected for Galactic extinction (Schlafly & Finkbeiner 2011). We employ a ΛCDM cosmology with $H_0 = 70\,\mathrm{km\,s^{-1}}$ $\mathrm{Mpc^{-1}}$, $\Omega_M = 0.3$, and $\Omega_\Lambda = 0.7$, which yields an age of the universe of 0.976 Gyr and a spatial scale of 39.9 kpc arcsec^{-1} in comoving units at $z = 5.7$.

4.2 Data, reduction and photometry

The field centered on the quasar J0203+0012 at $z = 5.72$ was observed during 2010 November–December. Narrow- and broad-band imaging was carried out with the FOcal Reducer/low dispersion Spectrograph 2 (FORS2; Appenzeller & Rupprecht 1992) using the red sensitive detector consisting of two 2k × 4k MIT CCDs at the Very Large Telescope (VLT). The pixels were 2 × 2 binned to decrease the readout time and noise, giving a spatial scale of 0.25 arcsec pixel^{-1}. The field-of-view was $6'.8 \times 6'.8$. The field was observed in the narrow-band filter (FILT_815_13, λ_c = 8150 Å, $\Delta\lambda$ = 130 Å, hereafter NB) and the broad-band filters Z (Z_GUNN, λ_c = 9100 Å, $\Delta\lambda$ = 1305 Å) and R (R_SPECIAL, λ_c = 6550 Å, $\Delta\lambda$ = 1650 Å). The filter transmission curves are shown in Figure 4.1. This filter set allowed us to sample both LAEs in a redshift range of $5.66 \lesssim z \lesssim 5.75$ with the narrow-band filter and LBGs in a broader redshift range $5.2 \lesssim z \lesssim 6.8$ with the broad-bands ($5.2 \lesssim z \lesssim 5.8$, if we add the narrow-band filter to the selection).

The individual exposure times in NB, Z, and R were 800s, 110s, and 240s per pointing, respectively. The individual exposures were shifted by $\sim 10''$ with respect to each other to facilitate the removal of bad pixels and flat field errors associated with a fixed position of the CCD pixel. The total integration times were 6 hr in NB, 1.5 hr in Z, and 48 minutes in R.

Standard data reduction was performed, which consisted of bias subtraction, flat fielding, sky subtraction, image alignments, and stacking. We calculated the photometric zero points by using the magnitudes and colors of stellar objects in the Sloan Digital Sky Survey (SDSS) catalog

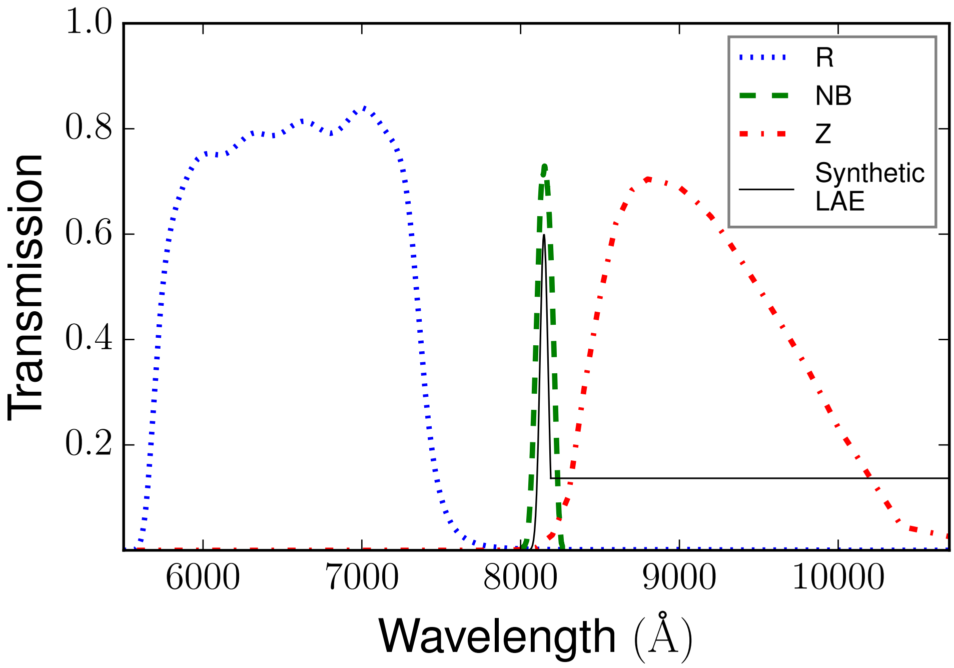

Figure 4.1: Transmission curves of the filters used in this chapter and the synthetic spectrum of a LAE at $z = 5.7$.

(Abazajian et al. 2009). With this procedure, the flux losses for point sources are corrected, which is appropriate for this study since we are interested in high-redshift LAEs that are expected to be unresolved. The accuracy of the photometric zero points was 0.04, 0.04, and 0.05 for the NB, Z, and R frames, respectively.

The area covered by the reduced images was ~ 44.4 arcmin^2. The seeing for the final NB, Z, and R images was $0''.84$, $0''.86$, and $0''.76$ respectively. The 5σ limiting magnitudes of the reduced images with a $1''.5$ diameter aperture were NB = 25.34, $Z = 25.14$, and $R = 26.29$.

In order to determine appropriate colors, the NB and R images were convolved to match the PSF of the Z image, the image with the worst seeing, using the IRAF task *psfmatch*. The NB total magnitudes were calculated from the unconvolved image.

The source catalog was created running SExtractor (Bertin & Arnouts 1996) in dual image mode with the narrow-band frame as the detection image. Aperture magnitudes were calculated using a $1''.5$ diameter aperture ($\sim 1.75\times$FWHM of the seeing). The chosen aperture was a good balance between optimizing the signal-to-noise (S/N) photometry of point sources and minimizing the amount of flux outside the aperture (Labbé et al. 2003). This size assured that at least 70% of the flux of a point source was inside the aperture. We also tested larger apertures (e.g., $1''.8$ diameter) and the results did not change, but the S/N of the objects slightly decreased. Magnitudes of objects not detected or fainter than 2σ limiting magnitudes either in Z or R were replaced by the corresponding 2σ limiting magnitude. Finally, we only considered objects with S/N greater than 4, objects with $\mathrm{NB} > 18$, and with SExtractor flag ≤ 4 in order to eliminate objects flagged as truncated (too close to an image boundary), incomplete or corrupted. The final catalog contained 2424 objects.

In order to conclude whether or not an overdensity around the quasar was present, we needed a comparison field obtained at similar depth in a region that did not target a $z \gtrsim 5.7$ quasar. For LAEs we were able to use results from the literature (see Section 4.4.1.1), whereas for LBGs there were no $R - Z$ dropout searches with large spectroscopic follow-up in the literature. We performed our own selection of $R-Z$ dropouts using the public catalogs of the Subaru Deep Field (SDF) imaging survey (Kashikawa et al. 2004), which (after removing low-quality regions) had an effective area of ~ 876 arcmin^2. The SDF had several characteristics that made it a suitable comparison field for our study. (1) It is a large field, which helps to reduce cosmic variance. (2) It has R and Z bands covering similar wavelength ranges compared to the ones in FORS2. (3) There are 42 spectroscopically confirmed i-dropout galaxies discovered in different studies (Nagao et al. 2004, 2005, 2007; Ota et al. 2008; Jiang et al. 2011; Toshikawa et al. 2012; Jiang et al. 2013), which can be directly used to quantify the accuracy of our LBG selection.

The confirmed i-dropout galaxies in the SDF were originally selected in the Z-band and all of them have a redshift $z > 5.9$ (with one exception at $z = 5.762$). For that reason, these galaxies would either not be detected or have negligible flux in our NB filter. Thus, in order to perform a consistent comparison, we created a second catalog for the J0203+0012 field this time using the Z-band frame as the detection image (see Section 4.4.1.2).

4.3 Candidates selection

Figure 4.2 shows the two-color diagram of $Z - \mathrm{NB}$ and $R - Z$ for the objects detected in the narrow-band filter and summarizes the selection criteria for LAE and dropout candidates.

4.3.1 Lyman Alpha Emitters

Lyman Alpha Emitters (LAEs) are a population of high-redshift galaxies whose spectra are dominated by a strong Lyα emission line and have a very flat and faint continuum. The LAE candidates were selected according to the following criteria:

- *Narrow-band excess.* A positive $Z - \mathrm{NB}$ indicates an excess in the narrow-band flux intensity. We determine a color cut such that the flux in the narrow-band is twice that in the Z band: $Z - \mathrm{NB} > 0.75$. This cut corresponds to selecting objects with a rest-frame equivalent width greater than 17.7 Å (see Section 4.4.2).
- *Continuum break.* To differentiate between high-redshift LAEs and low-redshift emission line interlopers, we require a break in the continuum: $R - Z > 1.0$.
- *Significance of the narrow-band excess.* To avoid contamination by objects that satisfy the color criteria only due to photometric errors, we require: $|(Z - \mathrm{NB})| > 2.5\sqrt{\sigma_Z^2 + \sigma_{\mathrm{NB}}^2}$.

As seen in Figure 4.2, there is one object that satisfies our criteria (LAE 1). There is another one that is not detected in either of the broad-band images (LAE 2). LAE 2 has a lower limit in the narrow-band excess of $Z - \mathrm{NB} > 0.62$. Additionally, when visually inspecting the Z-band image of LAE 2 a faint source is apparent. Forced photometry in the Z-band image at the position of LAE 2 gives a 1.9σ signal, thus, increasing the chances of LAE 2 being a real object. We consider LAE 2 to be a tentative LAE candidate, although deeper observations and/or spectroscopy are needed to confirm its nature.

4.3.2 Lyman Break Galaxies

Dropout galaxies are also known as Lyman Break Galaxies (LBGs) given that they are selected using the Lyman break technique (Steidel et al. 1996). The basis of this method is the fact that hydrogen is very effective at absorbing radiation at wavelengths shorter than 912 Å (the Lyman limit). Therefore, radiation with $\lambda \lesssim 912$ Å is strongly suppressed by intergalactic and interstellar absorption, so a very small fraction of these photons will reach us, forming the so-called Lyman Break. At high-redshifts, the Lyα forest becomes so optically thick that a large fraction of the light coming from $\lambda_{\mathrm{rest}} = 912$ Å to $\lambda_{\mathrm{rest}} = 1216$ Å is also absorbed. At this point the Lyman break selection becomes, in effect, a selection of objects with a sharp break at $\lambda_{\mathrm{rest}} = 1216$ Å.

Dropout candidates were selected with the following criteria:

- *Continuum break.* A prominent break in the continuum is expected for high-redshift galaxies due to the hydrogen absorption. We require a continuum break of $R - Z > 2.0$. Additionally, in an attempt to bias our high-redshift candidates toward a redshift closer to the redshift of the quasar, we require a break between the flux in the NB and R filters: $R - \mathrm{NB} > 1.5$. However, this last criterion has a small effect and excludes only one candidate.

Table 4.1. Coordinates of the candidates

Object	R.A. (J2000)	Decl. (J2000)	Distance (arcmin)	Distance (cMpc[a])	Distance (pMpc[b])
LAE 1	02:03:38.23	+00:11:09.9	1.97	4.65	0.69
LAE 2	02:03:21.02	+00:10:40.2	3.37	7.96	1.19
Drop 1	02:03:27.15	+00:10:32.7	2.34	5.52	0.82
Drop 2	02:03:19.76	+00:11:25.8	3.33	7.85	1.17
Drop 3	02:03:37.12	+00:15:29.9	3.24	7.64	1.14
Drop 4	02:03:34.04	+00:14:34.2	2.13	5.02	0.75
Drop 5	02:03:39.69	+00:15:35.0	3.60	8.49	1.27
Drop 6	02:03:39.92	+00:13:38.5	2.21	5.22	0.78
Drop 7	02:03:42.04	+00:12:56.3	2.46	5.78	0.86
Drop 8	02:03:32.71	+00:09:58.6	2.51	5.92	0.88

Note. — Coordinates of the candidates of Figure 4.3 and their projected distances with respect to the quasar

[a] Comoving Mpc at $z = 5.7$

[b] Physical Mpc at $z = 5.7$

- *Significance of the break.* To avoid contamination by objects that only satisfy the color criteria due to photometric errors, we require: $|(R - Z)| > 2.5\sqrt{\sigma_R^2 + \sigma_Z^2}$.

- *Faintness.* Since high-redshift galaxies are expected to be faint, we impose a minimum magnitude of $Z > 21$.

As shown in Figure 4.2, there are eight LBG candidates satisfying the criteria.

The coordinates of the LAE and LBG candidates and their projected distances to the quasar are presented in Table 4.1. Figure 4.3 shows the color image of the field overlaid with the positions of the LAE and LBG candidates, and the quasar. Postage-stamp images of these objects are shown in Figure 4.4.

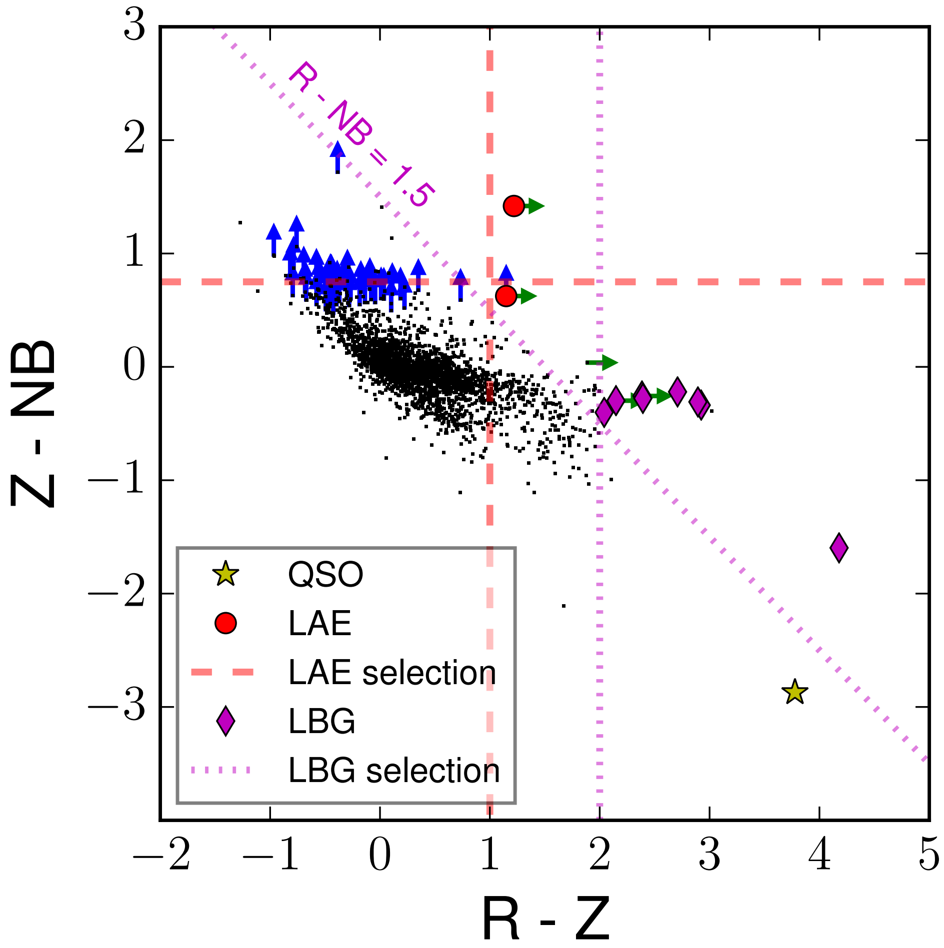

Figure 4.2: Z-NB vs. R-Z color-color diagram with objects detected in the narrow-band filter. Vertical blue and horizontal green arrows show 2σ limiting magnitudes in Z and R for objects not detected in the respective filters. The selection criteria for LAE and dropouts are explained in Section 4.3.

4.4 Results

4.4.1 Blank field comparison

4.4.1.1 LAEs

The selection criteria used in the present work (see Section 4.3.1) is close to that used by Ouchi et al. (2005, 2008). Thus, it is natural to use their LAE sample for comparison. Their observations cover a larger area and reach fainter luminosities than this work: the area they imaged is 1.04 deg^2 on the sky and a 5σ limiting magnitude of NB = 26.0 (λ_c = 8150 Å, $\Delta\lambda$ = 120 Å). Unlike

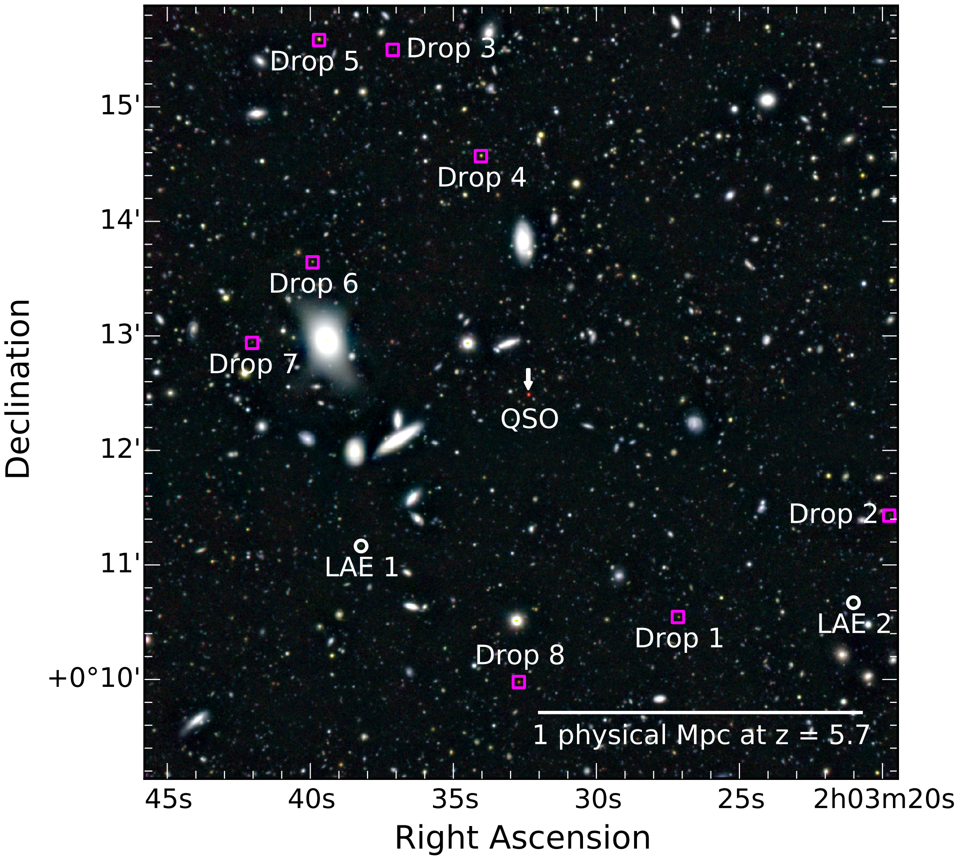

Figure 4.3: Color image of the 44.4 arcmin^2 field centered on ULAS J0203+0012. The objects of interest are highlighted.

our field, the Ouchi et al. (2008) sample is not centered on a quasar, which is why we consider it a blank field. However, even in blank fields, protoclusters can exist. In fact, Ouchi et al. (2005) detected two overdensities that could be clusters in a formation phase.

In Figure 4.5, we show our cumulative number of LAEs and also the numbers from Ouchi et al. (2008) scaled to our area. Our results are in good agreement with the expected number from Ouchi et al. (2008). Figure 4.6 shows the distribution on the sky of the 401 LAEs at $z = 5.7 \pm 0.05$ detected by Ouchi et al. (2008). Masked regions due to bright stars or image artifacts are shown in gray. The dashed square in the bottom-left corner represents the effective size of the FORS2 field-of-view used in this work. With the goal of estimating the probability of detecting, in a blank field, the number of LAEs that we find in this work, we placed 100,000 FORS2 fields-of-view at random positions in the Ouchi et al. (2008) field. Only fields where less than 10% of the region is masked out were considered. We counted how many LAEs fell in each FORS2 field and the result is summarized in the histogram of Figure 4.7. Even considering that Ouchi et al. (2008) would have detected more galaxies since they were sensitive to fainter magnitudes, we find from Figure 4.7 that the number of LAEs in our field-of-view is consistent with the most typical number expected in their blank field, i.e., one or two galaxies.

Our results also compare with the study by Hu et al. (2010), which is based on a sample of 88 spectroscopically confirmed LAEs at $z \sim 5.7$ in an area of 1.16 deg^2. Figure 4.5 shows their cumulative number of LAEs scaled to our area. The fact that their numbers are lower than the numbers of the Ouchi et al. (2008) sample, could be explained by the fact that Hu et al. (2010) could not spectroscopically confirm approximately half of their photometric candidates. Nevertheless, our results are still consistent, within the errors, with the number expected from Hu et al. (2010). We conclude that there is no overdensity of LAEs in the quasar field.

4.4.1.2 LBGs

As stated in Section 4.3.2 and shown in Figures 4.3 and 4.4, we found eight objects satisfying our LBG criteria. These objects were detected in the NB filter and our criteria place them in the redshift range: $5.2 \lesssim z \lesssim 5.8$. However, we cannot follow the same approach if we want to exploit the information of the 42 confirmed *i*-dropout galaxies in our comparison field (SDF), due to the fact that essentially all of these confirmed galaxies have a redshift $z > 5.9$ (except one that has a redshift of $z = 5.762$, ID = 1 in Toshikawa et al. 2012) and would not be detected in our NB filter.

We consider the SDF to be a blank field because it does not contain known $z \gtrsim 5.7$ quasars. The only caveat, is that it has been claimed that the SDF contains two overdensities. One is at $z \sim 4.9$ (Shimasaku et al. 2003), from which we expect minimal contamination due to our selection criteria. The other one is a protocluster at $z \sim 6$ (Ota et al. 2008; Toshikawa et al. 2012), which in principle could complicate our analysis.

The creation of the source catalogs for both the quasar and comparison fields was carried out in the same manner as for the J0203+0012 field in Section 4.2, but this time using the Z-frame as the detection image. We applied the same selection criteria as in Section 4.3.2, except for the narrow-band constraints. Additionally, since the depth of the fields are different, in order to make a consistent comparison, we have constrained our LBG candidates to have a magnitude brighter than the 5σ limiting magnitude in the quasar field, i.e., $Z < 25.14$. Since all the confirmed members of the protocluster at $z \sim 6$ have magnitudes $Z > 25.5$ (Toshikawa et al. 2012), our $Z < 25.14$ selection cut should at least prevent us from dealing with a large fraction of the protocluster galaxies.

Figures 4.8 and 4.9 present the color–magnitude diagram and the selection criteria of the Z-band selected objects in the J0203+0012 and SDF fields respectively. In red circles we show the LBG candidates detected in these fields. There were 20 LBG candidates in the quasar field, and this sample contained the 8 NB-selected LBGs from Section 4.3.2. We found 370 LBG candidates in the SDF. Scaling the LBG candidates in the SDF to our effective area, the expected number of candidates is ~ 19. Additionally, we placed 100,000 FORS2 fields-of-view at random positions in the SDF. Counting how many LBG candidates fell in each FORS2 field, resulted in a Gaussian distribution with mean $\mu = 16$ and standard deviation $\sigma = 5$. We concluded that the density of LBG candidates in the quasar field is consistent with that of a blank field.

Figure 4.9 also presents the compilation of known i-dropout galaxies in the SDF. With our depth we could not detect any of the 42 spectroscopically confirmed galaxies. We were only able to recover the brightest candidate of Nagao et al. (2007), a source that could not be confirmed or ruled out as a galaxy at $6.0 < z < 6.5$ by its spectrum. Additionally, if we used the extra information of the SDF provided by the i band, we noticed that the majority of the objects that we selected as possible LBGs seemed to be contaminants with a rather shallow slope in the $R - i$, $i - Z$ colors instead of having a sharp break.

From this analysis, we concluded that our LBG sample is very likely to be highly contaminated. We therefore cannot reliably estimate the (over)density of LBGs around our quasar. In the following sections we thus focus primarily on the LAE results.

4.4.2 Photometric properties of the LAEs

We assume a simple model where the LAE spectrum consists of the Lyα line with flux $F_{\mathrm{Ly}\alpha}$, a continuum flux density redward of Lyα with strength C and a power law slope β ($f_\lambda \propto \lambda^\beta$). Then, the flux density in the NB ($f_{\lambda,\mathrm{NB}}$) and Z ($f_{\lambda,Z}$) can be written as:

$$f_{\lambda,\mathrm{NB}} = C\lambda^{\beta}_{\mathrm{eff,NB}} + F_{\mathrm{Ly}\alpha}/\Delta\lambda_{\mathrm{NB}} \qquad (4.1)$$

$$f_{\lambda,Z} = C\lambda^{\beta}_{\mathrm{eff},Z}, \qquad (4.2)$$

with $\lambda_{\mathrm{eff},i}$ the effective wavelength of the i filter and $\Delta\lambda$ the width of the filter. Dunlop et al. (2012) found that high redshift galaxies ($5 < z < 7$) have an average slope of $\beta \simeq 2$ and this does not show a significant trend with either redshift or M_{UV}. Assuming a flat continuum, i.e., $\beta = -2$, we solve the previous 2×2 linear system and estimate the line flux and continuum flux density.

To calculate $L_{\mathrm{Ly}\alpha}$ and equivalent width, we use the relations:

$$L_{\mathrm{Ly}\alpha} = 4\pi d_L^2(z = 5.7)F_{\mathrm{Ly}\alpha} \qquad (4.3)$$

$$\mathrm{EW}_{\mathrm{obs}} = \frac{F_{\mathrm{Ly}\alpha}}{C(\lambda_{\mathrm{Ly}\alpha}(1+z)^{\beta})} \qquad (4.4)$$

with d_L the luminosity distance and $\lambda_{\mathrm{Ly}\alpha}$ the wavelength of the Lyα line. The rest-frame equivalent width is given by $\mathrm{EW}_0 = \mathrm{EW}_{\mathrm{obs}}/(1+\mathrm{z})$.

To calculate star formation rates (SFRs), we follow the approach of Ouchi et al. (2008):

$$\mathrm{SFR}(M_\odot\ \mathrm{yr}^{-1}) = \frac{L_{\mathrm{Ly}\alpha}}{1.1\times10^{42}\ \mathrm{erg\ s}^{-1}} \tag{4.5}$$

where they used the relation of Hα luminosity and star formation rate (Kennicutt 1998) and assumed the standard case B recombination factor of 8.7 for the Lyα/Hα luminosity ratio (Brocklehurst 1971).

We calculate the input parameters for the filters used in this project, taking into account both the filter curves and the quantum efficiency of the CCD: $\lambda_{\mathrm{eff,NB}} = 8150.2$ Å, $\lambda_{\mathrm{eff},Z} = 9180.2$ Å, and $\Delta\lambda_{\mathrm{NB}} = 119$ Å. The star formation rates and rest-frame equivalent widths for our two LAE candidates from Section 4.3.1 are (SFR, EW$_0$) = ($6.0 \pm 1.3\ M_\odot\,\mathrm{yr}^{-1}$, 47^{+222}_{-16} Å) and (SFR, EW$_0$) = ($1.7 \pm 0.9\ M_\odot\,\mathrm{yr}^{-1}$, ≥ 14 Å) for LAE 1 and LAE 2, respectively (see Figures 4.3 and 4.4).

The properties derived for LAE 1 are within the expected range for typical LAEs (see Ouchi et al. 2008 SFR = $6.2^{+2.7}_{-1.9}\ M_\odot\,\mathrm{yr}^{-1}$ for L^* LAEs at $z = 5.7$), whereas for LAE 2, the SFR is lower than for typical LAEs and the equivalent width is only a lower limit.

4.4.3 Black hole mass of the quasar

High-redshift quasars hosting black holes with masses $> 10^9 M_\odot$ are thought to be hosted by supermassive dark matter halos as suggested by their extremely low comoving density and large black hole masses (e.g., Volonteri & Rees 2006). No black hole measurement exists for J0203+0012. Typically, black hole masses of high-redshift quasars are estimated using the single-epoch black hole mass estimators based on continuum luminosities and broad emission lines such as Mg II and C IV (e.g., Jiang et al. 2007b; Kurk et al. 2007; De Rosa et al. 2011). For a source at $z = 5.72$, the Mg II line appears at 1.88 μm, in the middle of the strong telluric absorption band at $\sim 1.9\,\mu$m. Moreover, since J0203+0012 is a broad absorption line quasar, the C IV line is strongly absorbed (see Figure 7 in Mortlock et al. 2009). That is why we cannot use these lines to measure the black hole mass of J0203+0012. Instead, we estimate the quasar Eddington luminosity in order to determine the black hole mass, assuming that the central black hole accretes at the Eddington limit. We measure the flux at $\lambda = 1350$ Å, yielding a monochromatic luminosity of 3.7×10^{46} erg s^{-1}. Using the bolometric correction of 3.81 from Richards et al. (2006), we obtain a bolometric luminosity of 1.4×10^{47} erg s^{-1} with 0.2 dex of uncertainty. De Rosa et al. (2011) found that $L_{\mathrm{bol}}/L_{\mathrm{Edd}} \sim 0.43$ with a scatter of 0.2 dex for luminous ($L_{\mathrm{bol}} \gtrsim 10^{47}$ erg s^{-1}) $z > 4$ quasars. Assuming this ratio applies to J0203+0012, our estimate of the black hole mass is $2.5 \times 10^9\ M_\odot$ with 0.3 dex uncertainty. This mass is comparable to the typical black hole masses of the brightest SDSS quasars, thus it is plausible that J0203+0012 resides in a massive dark matter halo.

4.5 Discussion and conclusions

We present a deep study of the LAE and $R - Z$ dropout population centered on the $z = 5.72$ quasar J0203+0012 with an estimated black hole mass of $\sim 2.5 \times 10^9\ M_\odot$. The redshift of the quasar enables a LAE narrow-band search in its vicinity. We detect 2 LAE and 20 $R - Z$ dropout candidates (the number of dropout candidates decreases to 8 if we use the narrow band for detection and selection). The LAE sample spans a very narrow redshift range around the quasar: $5.66 < z < 5.75$. On the other hand, the $R - Z$ dropout sample spans a larger redshift range as is typical for dropout selections: $5.2 \lesssim z \lesssim 6.8$ ($5.2 \lesssim z \lesssim 5.8$, if the narrow-band filter is added to the selection).

Comparing our LAE counts with the luminosity functions of two LAE surveys that do not target a quasar (Ouchi et al. 2008; Hu et al. 2010), we find that our number counts are consistent with what is observed in blank fields.

The number of $R-Z$ dropout candidates in the field of J0203+0012 is consistent with the expected number from the SDF blank field. However, we find that with our depth and using only two broad bands for the selection, it is very likely that our candidates are highly contaminated. This implies that we cannot establish a reliable estimate of the (over)density of LBGs around J0203.

There are various ways to explain the non-detection of an overdensity of LAEs around the quasar.

1. Low number statistics may prevent us from detecting a possible overdensity of emission line galaxies. If there were an overdensity it would be at least a factor of $\sim$ 3–5, based on environmental studies of radio galaxies. Since we are studying only one quasar, it could be that we are targeting a rare source and that other quasars still harbor overdensities in their surroundings. This is certainly a possibility, but we believe that it is unlikely given the relatively low counts of LAEs and LBGs toward other $z \sim 6$ quasars studied to date.
2. The lack of neighbors in the immediate vicinity could be due to mergers of galaxies in the halo that hosts the quasar. However, we believe that such mergers should not prevent us from detecting an overdensity based on the protoclusters found around radio galaxies (e.g., Venemans et al. 2007b) and the recently spectroscopically confirmed LBGs in the vicinities of quasars at $z \sim 5$ found by Husband et al. (2013), which in principle should have been affected in the same manner.

3. The strong ionizing radiation from the quasar may prevent galaxy formation in its surroundings. There are several studies that support this claim (e.g., Bruns et al. 2012; Francis & Bland-Hawthorn 2004) and therefore it would be important to understand and quantify this effect in order to consider it in simulations. Indeed, our results present evidence to support this idea because none of our candidates are at a distance closer than ~ 4.5 comoving Mpc (~ 0.7 physical Mpc), as can be seen in Figure 4.3 and Table 4.1. This is similar to the results presented by Kashikawa et al. (2007) and Utsumi et al. (2010), i.e., that galaxies avoid the vicinity of a quasar within distances of ~ 4.5 comoving Mpc and ~ 15 comoving Mpc, respectively.

   Yet, the quasar ionization hypothesis fails to explain why apparent overdensities are found in the vicinities of other high-redshift quasars (e.g., Stiavelli et al. 2005). Further, we believe that is hard to reconcile a hypothesis in which the radiation affects the environment isotropically, with the unified AGN model where quasars have two collimated beams. However, contrary to the ionization hypothesis, Cantalupo et al. (2012) suggest that the radiation of the quasar may enhance the number of LAEs in its surroundings. They show that gas-rich objects with little or no associated star formation, known as proto-galactic clouds or dark galaxies, can be detected thanks to the Lyα fluorescence induced by a nearby quasar. One of the main characteristics of these sources is a high Lyα equivalent width ($\mathrm{EW}_0 > 240$ Å). A detailed comparison with Cantalupo et al. (2012) is challenging because of the different redshifts and because the Lyman limit luminosity of our quasar, calculated following Hennawi et al. (2006), is about one order of magnitude smaller than the luminosity of the hyperluminous quasar (HLQSO) observed by Cantalupo et al. (2012). Additionally, since J0203+0012 is a broad absorption line quasar (Mortlock et al. 2009), it is possible that the amount of escaping ionizing radiation is lower than expected in typical quasars.

   Nevertheless, in our study, we do not find such fluorescent clouds. It should be noted that in our work, LAE 1 has an $\mathrm{EW}_0 = 47^{+222}_{-16}$ Å which has a 4% probability of having $\mathrm{EW}_0 > 240$ Å based on the uncertainties of the measured fluxes and LAE 2 only has a lower limit of $\mathrm{EW}_0 \geq 14$ Å.

4. High-redshift quasars may not reside in the most massive halos. It is expected that the relation between black hole mass and halo mass that arises from combining the local relations between black hole and bulge mass on the one hand, and the relation between galaxy and halo mass on the other, is significantly different (both in slope and in scatter) at high redshift. Evidence for this has been found recently at $z \sim 2.7$ by Trainor & Steidel (2012) who studied fifteen HLQSOs ($\gtrsim 10^{14} L_\odot$; $M_{1450} \simeq -30$) that are associated with galaxy overdensities. The authors conclude that HLQSOs do not require environments very different from their much less luminous quasar counterparts and are not being hosted by rarer dark matter halos. However, if this applies to the $z \sim 6$ quasars as well, one would have to

explain their extremely low space density. One possibility is that, due to selection effects, the bright quasars thus far discovered are biased toward more average-sized halos that are inhabited by very massive black holes.

5. High-redshift quasars may not always reside in highly overdense, large-scale environments. All observational evidence considered, there appears to be a trend for $z \sim 6$ quasars to sit in low-to-average galaxy environments on megaparsec scales. ΛCDM predictions have shown that the most massive halos at high redshift do not invariably grow into the most massive ones at low redshift. Moreover, the most massive present-day structures (clusters) originated primarily from regions that were overdense on very large scales (tens of megaparsec) at $z \sim 6$ (De Lucia & Blaizot 2007; Overzier et al. 2009; Angulo et al. 2012). Although few studies have probed out to such large radii and with significant sensitivity, the lack of companion galaxies on megaparsec scales may indicate that the quasars do not pinpoint progenitors of the most massive clusters even if the quasars themselves are hosted by very massive halos. It is also possible that quasars reside in large-scale overdense environments, but just not in the center of them. Studies with larger fields-of-view are required to test this hypothesis.

One question that emerges naturally is why radio-galaxy-based protocluster surveys have been much more successful than any quasar-based protocluster survey. From a theoretical perspective, Fanidakis et al. (2013b,a) suggest that radio galaxies and quasars are observational manifestations of different accretion states, which are determined by the accretion and black hole properties and the large scale environment. Quasars accrete vast amounts of gas and form in the gas-rich environments of intermediate mass ($\sim 10^{12}\,M_\odot$) dark-matter halos (Fanidakis et al. 2013a). Radio galaxies, in comparison, are powered by rapidly spinning black holes that typically inhabit the centers of the most massive ($\gtrsim 10^{13}\,M_\odot$) dark matter halos in the universe and accrete low-density gas (for the properties of their AGN model; see Fanidakis et al. 2011, 2012). The largest concentrations of baryons are expected to be found within these halos and thus, radio galaxies can be used to pinpoint the location of large galaxy overdensities. The suggestion of a discrete halo environment of quasars and radio galaxies is also supported by clustering analysis of AGNs in the low-redshift universe ($0 < z < 2$; e.g., Ross et al. 2009; Donoso et al. 2010; Wake et al. 2011).

More detailed studies of the environment and of the host galaxy of high-redshift quasars are needed to clarify the picture of overdensities around quasars. Future observational campaigns targeting high-redshift quasars either at $z = 5.7$, $z = 6.6$, or $z = 7.0$ (corresponding to the few gaps of OH night-sky emission bands where narrow-band filters can be most effectively targeted to detect Lyα emission) will be crucial to increase the sample and to quantify possible object-to-object variations.

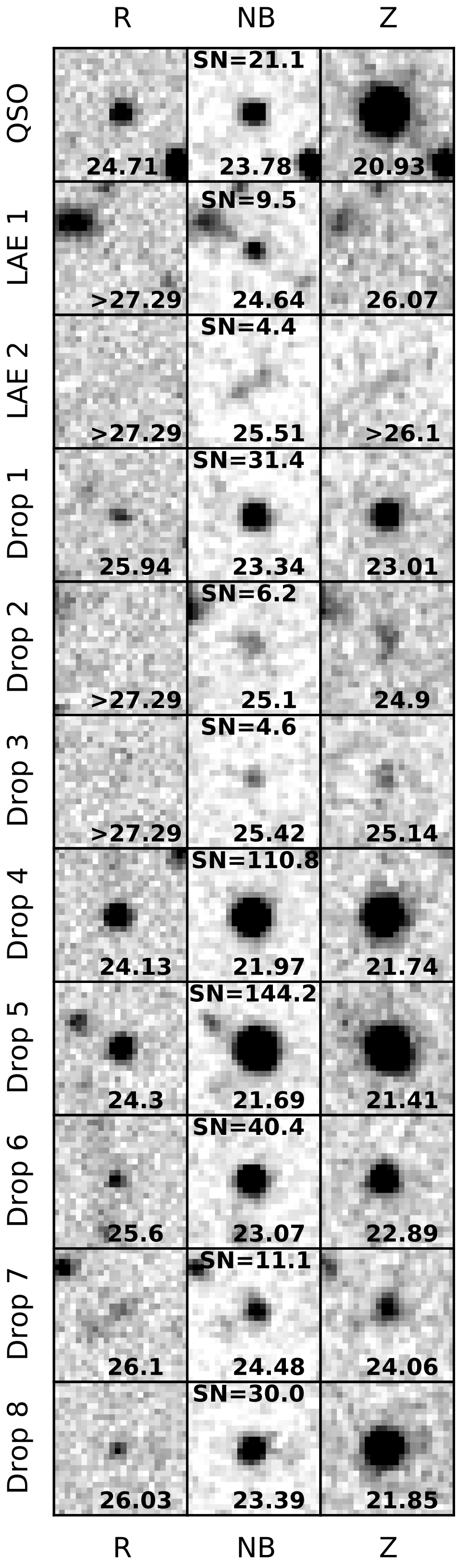

Figure 4.4: Postage stamp images for the QSO and our candidates, each presented in a $6'' \times 6''$ box. For every stamp, the respective magnitude (or 2σ limiting magnitude) is given. The signal-to-noise ratio (S/N) in the narrow-band is also shown.

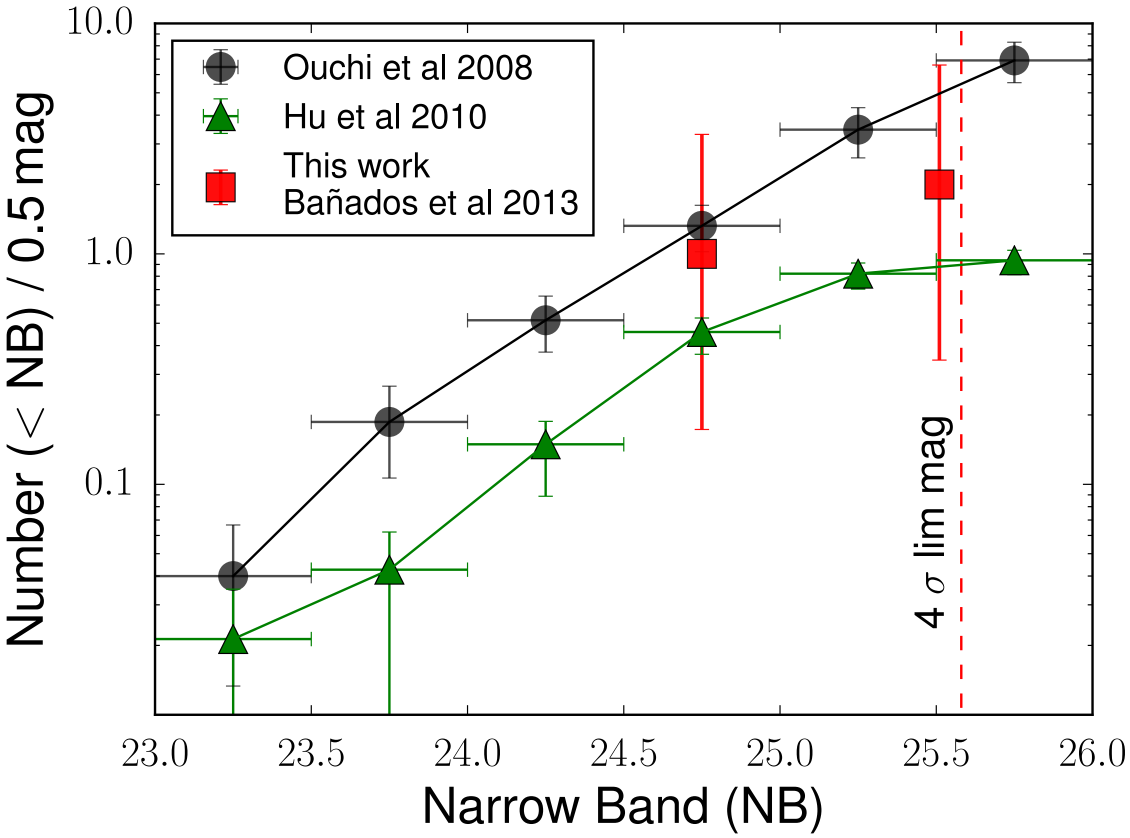

Figure 4.5: Cumulative number of LAEs scaled to our area. Black circles, green triangles, and red squares correspond respectively to the samples from Ouchi et al. (2008), Hu et al. (2010), and Bañados et al. (2013) (this work). The vertical dashed line shows the 4σ limiting magnitude in the current work. Our measurements are consistent with no overdensity in our quasar field.

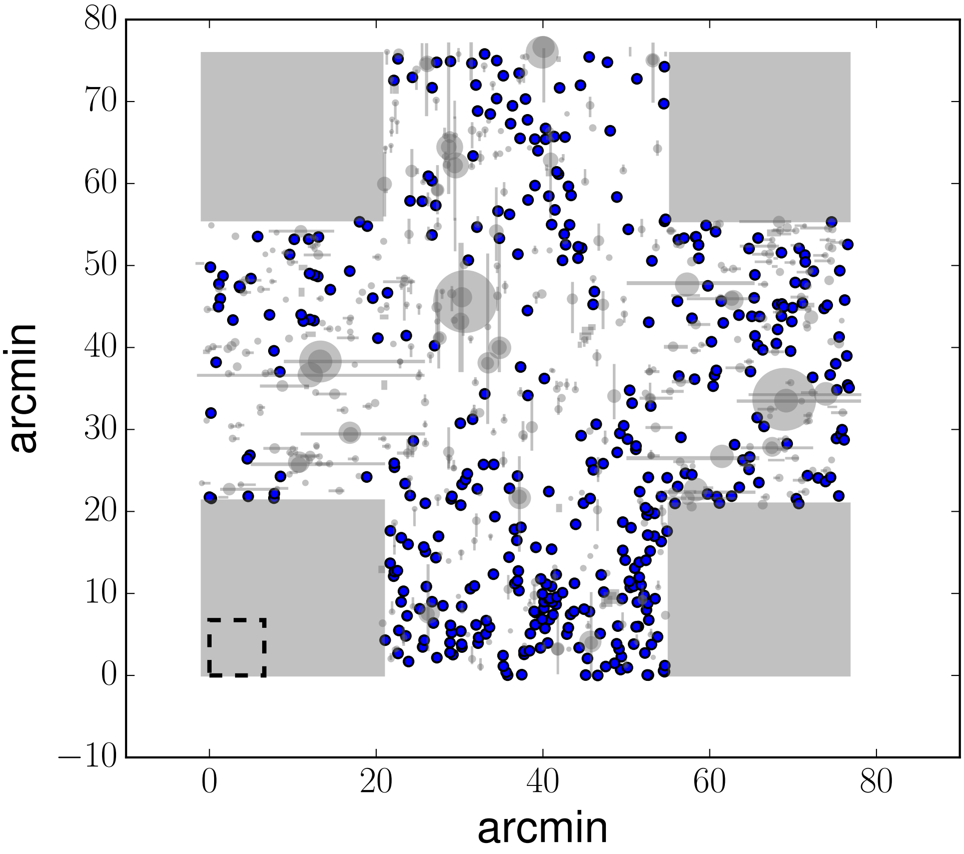

Figure 4.6: The distribution on the sky of the $z = 5.7$ LAE candidates found by Ouchi et al. (2008). Masked regions are shown in gray. The size of the field-of-view (FORS2) used in this work is represented by the dashed box in the bottom left corner.

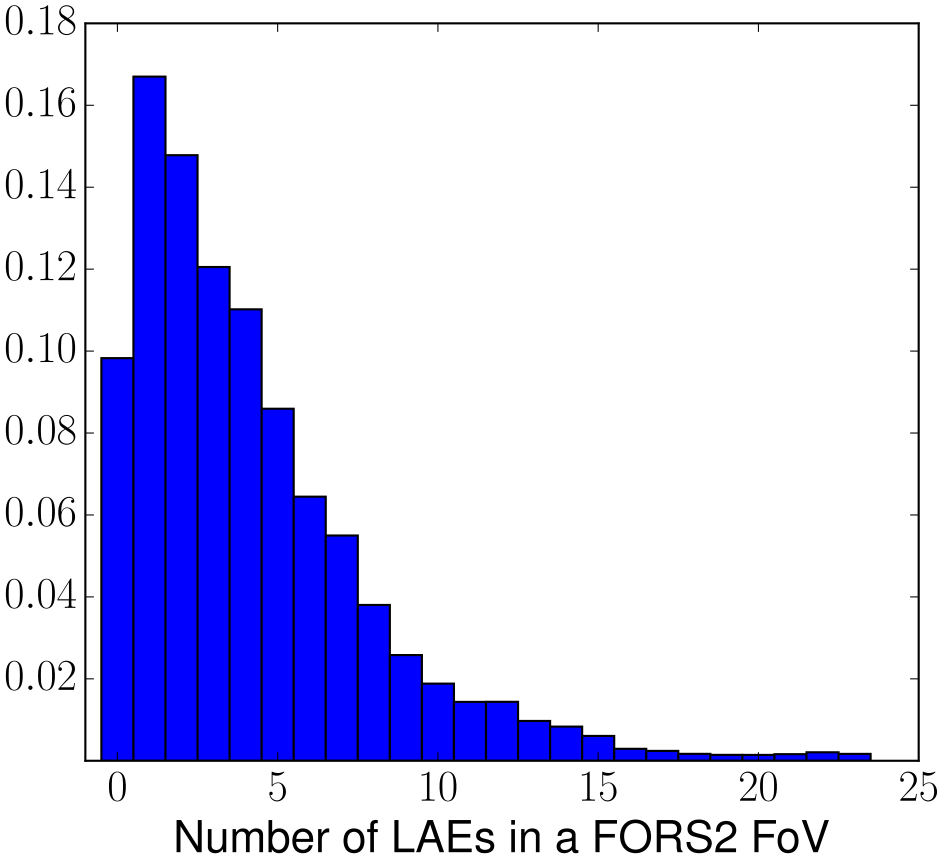

Figure 4.7: Normalized histogram of the number of LAEs found within a FORS2 field-of-view. We count the number of LAEs in $100,000$ fields-of-view randomly placed in the Ouchi et al. (2008) LAE sample (see Figure 4.6).

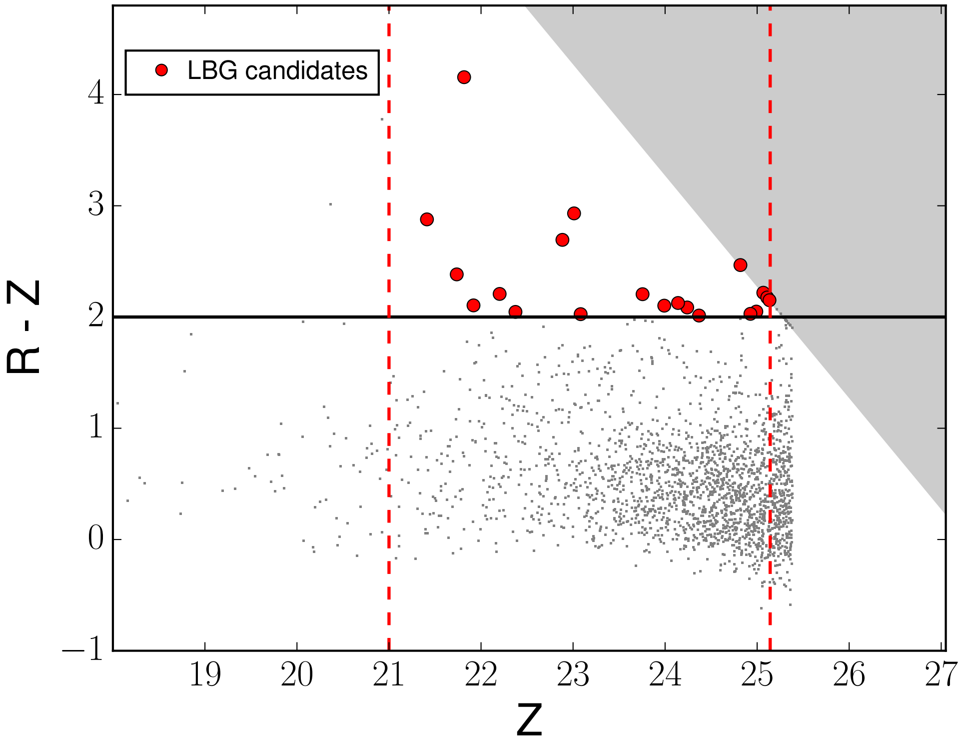

Figure 4.8: Color–magnitude diagram for J0203+0012 field using the *Z*-frame as the detection image. Gray points represent all the objects in the field. The horizontal solid line is our criteria for selecting LBGs with a break larger than $R - Z = 2$. The vertical dashed lines are the brighter and fainter magnitudes considered for our candidates, $Z = 21$ and $Z = 25.14$, respectively (see the text). The gray region shows *R*-band magnitudes fainter than 2σ limiting magnitude ($R = 27.29$). The 20 LBG candidates are indicated with red circles.

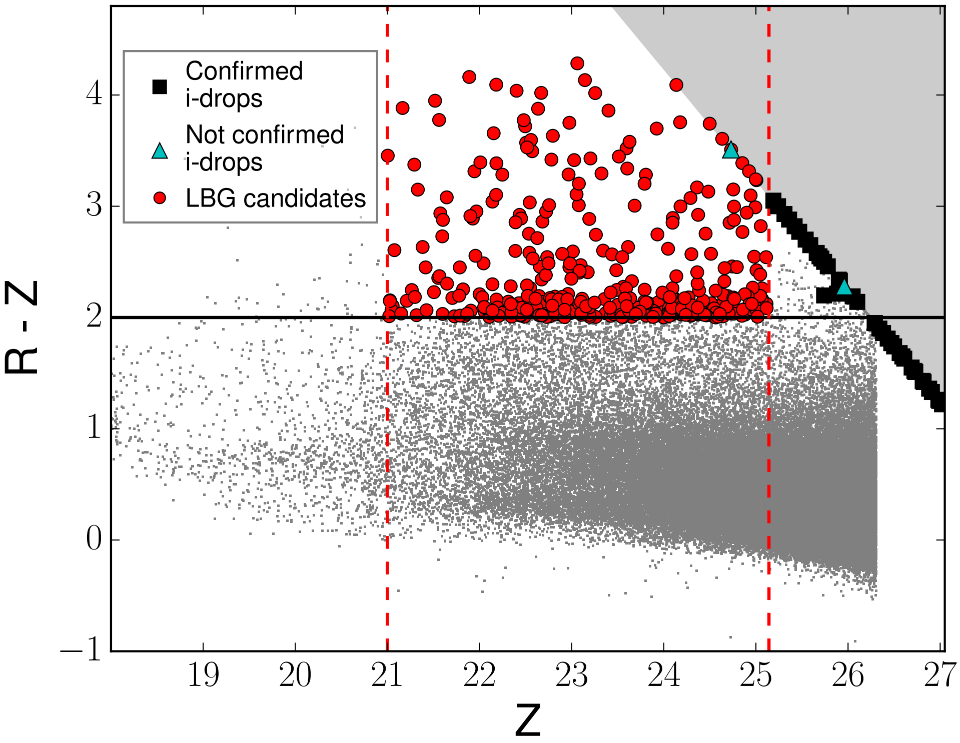

Figure 4.9: Color–magnitude diagram for the Subaru Deep field (SDF). Gray points represent all the objects in the field. The black squares correspond to the 42 spectroscopically confirmed *i*-dropout galaxies in Nagao et al. (2004, 2005, 2007), Ota et al. (2008), Jiang et al. (2011), Toshikawa et al. (2012), and Jiang et al. (2013). The cyan triangles are *i*-dropout candidates reported by Nagao et al. (2007) that could not be confirmed or rejected as galaxies at $6.0 < z < 6.5$ by their spectra. When the *i*-dropout galaxies are not in our SDF catalog, the *Z*-band magnitude of the discovery papers are used. The horizontal solid line is our criteria for selecting LBGs with a break larger than $R - Z = 2$. The vertical dashed lines are the brighter and fainter magnitudes considered for our candidates, $Z = 21$ and $Z = 25.14$, respectively (see the text). The gray region shows *R*-band magnitudes fainter than 2σ limiting magnitude ($R = 28.24$). The 370 LBG candidates in this field are indicated with red circles.

Chapter 5

Bright [C II] 158 μm emission in a quasar host galaxy at z=6.54 †

5.1 Context

The [C II] 158 μm fine-structure line (hereafter [C II]) is known to trace regions of active star formation and is the main coolant of the cold, neutral atomic medium. Several groups have tried to identify the [C II] line in the first spectroscopically identified galaxies far back into the epoch of reionization ($z > 6.5$). However, thus far, there are no convincing detections of [C II] emission from star-forming galaxies at these redshifts (Walter et al. 2012a; Kanekar et al. 2013; Ouchi et al. 2013; González-López et al. 2014; Ota et al. 2014; Schaerer et al. 2015; Watson et al. 2015; but see also the recent work of Maiolino et al. 2015).

On the other hand, the [C II] line has been identified in a number of more extreme objects such as submillimeter galaxies and quasar host galaxies at $z \sim 6$ (Maiolino et al. 2005; Walter et al. 2009a; Riechers 2013; Wang et al. 2013; Willott et al. 2013, 2015). These objects are most likely the progenitors of massive early-type galaxies seen in the present universe (Volonteri 2010). Thus, luminous quasars are thought to be signposts of the location of these extreme galaxies in the early universe. Indeed, the [C II] line has been detected even in the host galaxy of the currently most distant quasar known at $z = 7.1$ (Venemans et al. 2012).

For more than a decade, the quasar SDSS J1148+5251 at $z = 6.42$ (hereafter J1148+5251), discovered by Fan et al. (2003), has been the brightest quasar known at $z > 6$ ($M_{1450} = -27.8$).

---

†This Chapter is a version of the article Bañados et al. (2015a), accepted for publication in the Astrophysical Journal Letters.

As such, it is by far the best studied quasar at these redshifts, being fundamental in shaping our current understanding of the universe when it was less than 1 Gyr old. It was the first source detected in [C II] at $z > 0.1$ (Maiolino et al. 2005), and for several years it remained the only $z > 6$ quasar detected also in CO emission (Bertoldi et al. 2003b; Walter et al. 2003, 2004; Riechers et al. 2009). The [C II] line in this quasar has been studied in detail (e.g., Walter et al. 2009a; Maiolino et al. 2012). Neutral carbon [C I] has also been detected (Riechers et al. 2009), while deep limits on the [N II] line could also be placed (Walter et al. 2009b).

Recently, and after more than 10 years, three quasars that rival (and in one case even surpass) J1148+5251 in UV luminosity have been discovered. These quasars are SDSS J0100+2802 ($z = 6.30; M_{1450} = -29.3$; Wu et al. 2015), ATLAS J025.6821–33.4627 ($z = 6.31; M_{1450} = -27.8$; Carnall et al. 2015), and PSO J036.5078+03.0498 (hereafter P036+03; $z = 6.527; M_{1450} = -27.4$; Venemans et al. 2015).

In this chapter, we focus on P036+03, which is the brightest quasar known at $z > 6.5$ (see Figure 2.6). We report a bright detection of the [C II] line with the IRAM NOEMA interferometer. We also detect the underlying dust FIR continuum emission and present a tentative detection of a water transition in this quasar. As a result, P036+03 (that is also accessible from telescopes in the southern hemisphere) competes with the current archetypal high-redshift quasar J1148+5251 in both rest-frame UV and [C II] luminosities.

We employ a cosmology with $H_0 = 67.8\,\mathrm{km\,s^{-1}\,Mpc^{-1}}$, $\Omega_M = 0.307$, and $\Omega_\Lambda = 0.691$ (Planck Collaboration et al. 2014). This implies that for $z = 6.5412$, the proper spatial scale is 5.6 kpc arcsec^{-1} and the age of the universe is 833 Myr, i.e., 6% of its present age.

5.2 Observations and results

We use the IRAM NOEMA interferometer to observe the [C II] line in the quasar P036+03, as a director's discretionary time proposal (ID: E14AG). The tuning frequency is 252.496 GHz which corresponds to the expected [C II] frequency ($\nu_{rest} = 1900.539$ GHz) based on the quasar redshift estimated from the Mg II line: $z_{\mathrm{Mg\,II}} = 6.527$ (Venemans et al. 2015). The observations were carried out in 2015 February 09 and 10 in the D configuration with a total time on source of only 3.55 hr (5 antenna equivalent). The synthesized beam size is $2''.2 \times 1''.6$. The data were calibrated and analyzed with the IRAM GILDAS[1] software package (Guilloteau & Lucas 2000).

The final NOEMA spectrum of P036+03 is shown in Figure 5.1. Two lines are visible, a bright one, and a second fainter line on top of the underlying dust continuum. We fit two Gaussians

---

[1] http://www.iram.fr/IRAMFR/GILDAS

plus continuum to the data and identify [C II] as the brightest of these lines. The [C II] line peaks at 252.02 ± 0.06 GHz, yielding a redshift of $z_{\rm [C\,II]} = 6.54122 \pm 0.0018$ (i.e., redshifted by $566 \pm 72\,{\rm km\,s^{-1}}$ with respect to the Mg II redshift). The line has a FWHM= $360 \pm 50\,{\rm km\,s^{-1}}$ and a velocity integrated flux of $5.2 \pm 0.6\,{\rm Jy\,km\,s^{-1}}$. This corresponds to a [C II] luminosity of $L_{\rm [C\,II]} = (5.8 \pm 0.7) \times 10^9\,L_\odot$ which is a factor of ~1.4 brighter than the [C II] line in J1148+5251 ($4.2 \pm 0.4 \times 10^9\,L_\odot$; Maiolino et al. 2005; Walter et al. 2009a). The second line peaks at 254.45 ± 0.14 GHz, i.e., blueshifted by $-2863 \pm 178\,{\rm km\,s^{-1}}$ with respect to the [C II] line. This fainter line has a FWHM= $160 \pm 100\,{\rm km\,s^{-1}}$ and an integrated flux of $1.2 \pm 0.7\,{\rm Jy\,km\,s^{-1}}$. At our resolution, the most likely identification for this line is a blended water vapor emission from the adjacent $3_{22} - 3_{13}$ and $5_{23} - 4_{32}$ H_2O transitions ($\nu_{rest} = 1919.359$ GHz and $\nu_{rest} = 1918.485$ GHz, respectively). Figure 5.2 shows the maps of the FIR continuum emission and the continuum subtracted [C II] emission.

Fitting the continuum flux density yields a value of 2.5 ± 0.5 mJy. We convert the measured dust continuum flux density to FIR luminosity, $L_{\rm FIR}$, by modeling the FIR emission with an optically thin gray body spectrum and scale the model to match the observed dust continuum flux density. We use typical parameters in the model to reproduce the spectral energy distribution for high-redshift quasar host galaxies, i.e., a dust temperature of $T_d = 47$ K and a emissivity index of $\beta = 1.6$ (following for example, Wang et al. 2011b; Venemans et al. 2012; Willott et al. 2015). Integrating the model from rest-frame 42.5 μm to 122.5 μm we obtain the following $L_{\rm FIR}$ for P036+03: $L_{\rm FIR} = (5.4 \pm 1.1) \times 10^{12}\,L_\odot$. Integrating the model from rest-frame 8 μm to 1000 μm we get a total infrared luminosity, $L_{\rm TIR}$, of $L_{\rm TIR} = (7.6 \pm 1.5) \times 10^{12}\,L_\odot$. We can use the total infrared luminosity to estimate the star formation rate using the relation ${\rm SFR_{TIR}}(M_\odot\,{\rm yr^{-1}}) = \delta_{\rm MF} \times 1.0 \times 10^{-10}\,L_{\rm TIR}\,(L_\odot)$ (Carilli & Walter 2013and references therein), where δ_{MF} depends on the stellar population. We use $\delta_{MF} = 1.0$ which is appropriate for a Chabrier IMF. For P036+03, this relation results in ${\rm SFR_{TIR}} = 720 \pm 150\,M_\odot\,{\rm yr^{-1}}$. Alternatively, Sargsyan et al. (2014) show that even in sources dominated by active galactic nucleus (AGNs), the star formation rate can be estimated from $L_{\rm [C\,II]}$ to a precision of ~ 50% with the relation ${\rm SFR_{[C\,II]}}(M_\odot\,{\rm yr^{-1}}) = 10^{-7}\,L_{\rm [C\,II]}$ ($L_\odot$). This relation yields ${\rm SFR_{[C\,II]}} = 580 \pm 70\,M_\odot\,{\rm yr^{-1}}$, broadly consistent with the estimate above.

5.3 Discussion

5.3.1 [C II]–IR luminosity relation

It has been shown that in local star-forming galaxies the ratio between the [C II] and IR luminosities is about 0.1%–1% but it decreases in galaxies with larger IR luminosities ($L_{\rm TIR} > 10^{11}\,L_\odot$)

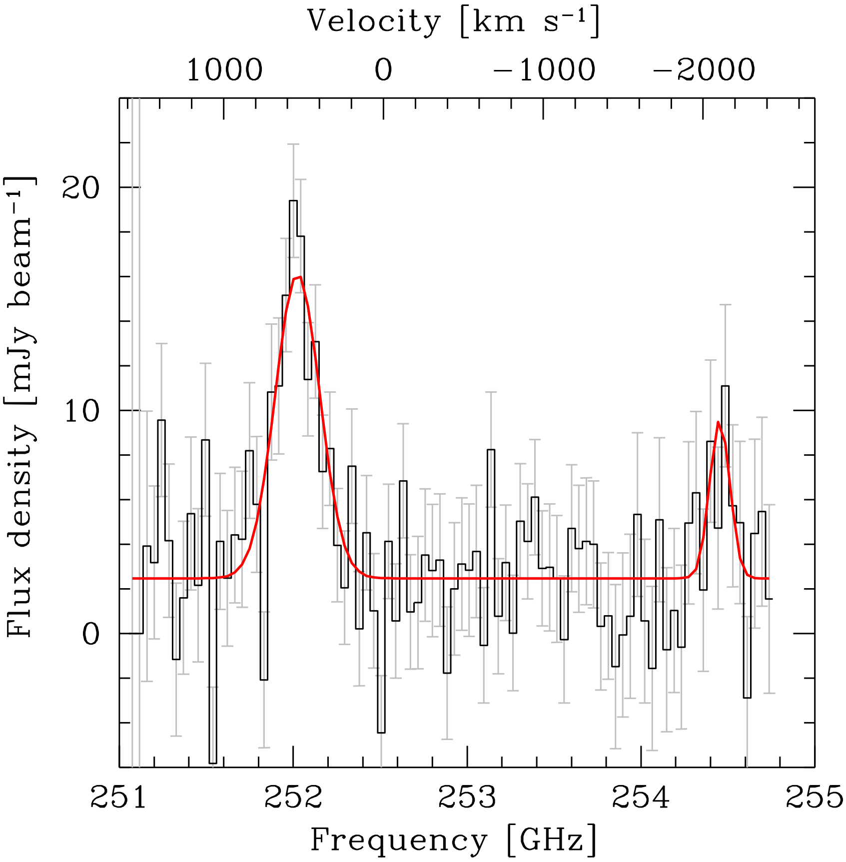

Figure 5.1: NOEMA spectrum at 1 mm (observed) wavelengths of P036+03. The tuning frequency was centered on the expected position of [C II] based on the redshift determined from the Mg II line (ν_{obs} = 252.496 GHz). This tuning frequency is shown here as zero point of the velocity scale. The red solid curve is a fit to the data consisting of two Gaussians plus continuum. The [C II] line is detected at high significance and is redshifted by 566 ± 72 km s^{-1} with respect to the Mg II redshift ($z_{[\mathrm{C\,II}]}$ = 6.54122, $z_{\mathrm{Mg\,II}}$ = 6.527). A second, fainter line is observed at 254.45 ± 0.14 GHz. We find that the most likely identification for this line is a blended emission from the adjacent $3_{22} - 3_{13}$ and $5_{23} - 4_{32}$ H_2O emission lines (see text).

such as LIRGs and ULIRGs. This has been known as the “[C II] deficit”. Similar deficits have been observed in other FIR lines such as [O I] 63.2 μm, [O I] 145 μm, and [N II] 122 μm. As a consequence, these trends are now being referred to as the “FIR lines deficit” (Graciá-Carpio et al. 2011). In Figure 5.3 we show the ratio of [C II] to TIR luminosity for different type of sources. The “[C II] deficit” can be clearly appreciated in the local samples: star-forming galax-

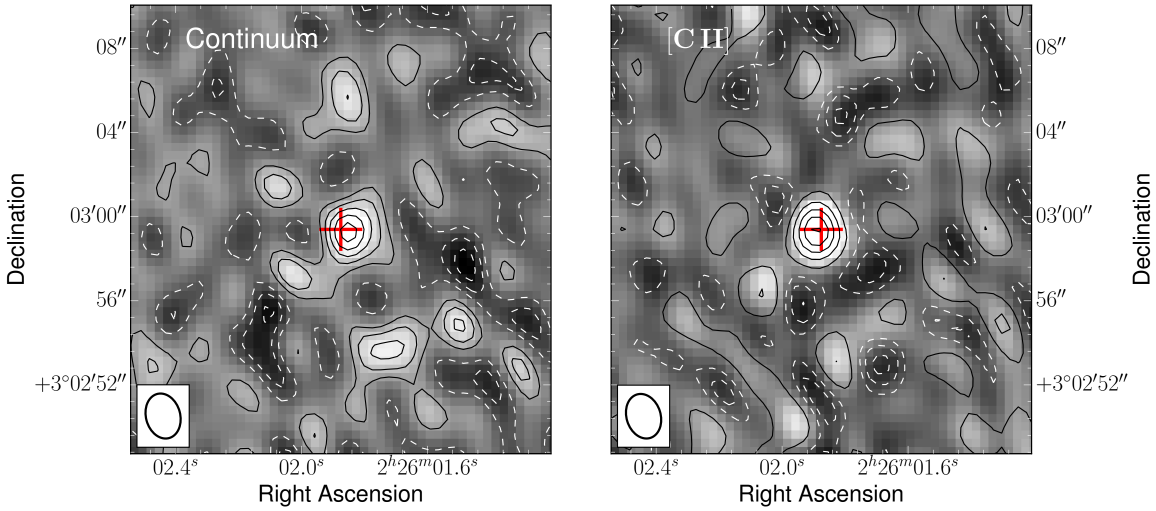

Figure 5.2: NOEMA maps of the $z = 6.5412$ quasar P036+03. The red cross in each panel shows the near-infrared location of the quasar. The beam size of 2.″2 × 1.″6 is shown at the bottom left of each panel. *Left:* far-infrared continuum emission obtained from line-free channels in the frequency range: 254.274–252.524 GHz (i.e., 2100 km s^{-1}, see Figure 5.1). The contours correspond to -3σ, -2σ, -1σ (white dashed lines), 1σ, 2σ, 3σ, 4σ, and 5σ (black solid lines), with σ being the rms noise of 0.418 mJy beam^{-1}. *Right:* continuum subtracted [C II] emission integrated from the channels 251.372 to 251.782 GHz (i.e., 750 km s^{-1}). The contours are -3σ, -2σ, -1σ (white dashed lines), 1σ, 3σ, 5σ, 7σ, and 9σ (black solid lines), with $\sigma = 0.85$ mJy beam^{-1}. The apparent excess of 3σ sources in the maps is due to the modest u, v coverage in our data.

ies (Malhotra et al. 2001), LIRGs (Díaz-Santos et al. 2013), and ULIRGs (Luhman et al. 2003). The sample of IR-luminous star-forming galaxies, submillimeter galaxies, and quasars at $z > 1$ compiled by De Looze et al. (2014) and Brisbin et al. (2015) shows a larger scatter in the [C II] to TIR luminosity ratio ($\sim 10^{-4} - 10^{-1.5}$). The sample of $z \sim 6$ quasars with high IR luminosities studied by Maiolino et al. (2005); Walter et al. (2009b); Wang et al. (2013) shows small [C II] to FIR luminosity ratios, similar to what is observed in local ULIRGs ($\sim 10^{-3.5}$). One interpretation of such low ratios could be in part due to the central AGN contributing to the IR luminosity (Wang et al. 2013), but note that there is a big literature dealing with possible explanations for the deficit (e.g., Malhotra et al. 2001; Stacey et al. 2010; Graciá-Carpio et al. 2011; Díaz-Santos et al. 2013; Ibar et al. 2015). Willott et al. (2015) studied a sample of $z \sim 6$ quasars two order of magnitudes fainter in the infrared ($L_{\rm TIR} = 10^{11-12}\,L_\odot$). These quasars show ratios consistent with the local star-forming galaxies ($\sim 10^{-3} - 10^{-2.5}$). Venemans et al. (2012) report that the quasar J1120+0641 at $z = 7.1$ has a TIR luminosity that is between the Willott et al. (2015) sample and the IR-bright $z \sim 6$ quasars. The $L_{\rm [C\,II]}/L_{\rm TIR}$ ratio for J1120+0641 is more consistent with local star-forming galaxies than to ULIRGs. The quasar of the present study, P036+03, has a $L_{\rm TIR}$ comparable to other $z \sim 6$ quasars ($L_{\rm TIR} \sim 10^{13}\,L_\odot$). However, it has a significant larger

$L_{[\text{C II}]}/L_{\text{TIR}}$ ratio ($\sim 0.8 \times 10^{-3}$), similar to J1120+0641, and consistent with the lower-end of local star-forming galaxies. This ratio is 2.7 times larger than the ratio reported for J1148+5251.

Together, this emphasizes the differences between the host galaxies of the most distant quasars. However, the number of quasars with [C II] and dust FIR continuum information is still to small to derive statistically meaningful trends or correlations.

5.3.2 Water vapor detection

The water vapor lines arise in the warm, dense phase of the ISM. They are one of the main coolants of this phase, thus playing a key role in the fragmentation and collapse of gas clouds (Carilli & Walter 2013). To date, there are only a handful of water vapor lines reported at high redshift, mostly in strongly magnified sources (e.g., van der Werf et al. 2011; Combes et al. 2012; Omont et al. 2013b) and in one extreme submillimeter galaxy at $z = 6.3$ (Riechers 2013), being the most distant detection of interstellar water to date. Recently, Bialy et al. (2015) show that high abundances of water vapor could exist in galaxies with extremely low metallicity ($\sim 10^{-3}$ solar), as expected for the first generations of galaxies at high redshifts.

As discussed in Section 5.2, we identify a tentative detection of blended water vapor emission from the $3_{22} - 3_{13}$ and $5_{23} - 4_{32}$ H_2O transitions (see Figure 5.1). Owing to the low significance of the detection is difficult to make any strong conclusions, especially because the water emission is complex and hard to interpret if only one transition is measured (González-Alfonso et al. 2014). However, additional water transitions could be detectable in this source. For example, the $3_{21} - 3_{12}$ H_2O transition ($\nu_{rest} = 1162.912$ GHz) at $z = 6.5412$ is shifted into the 2 mm band and could simultaneously be observed with the CO(J= $10 \rightarrow 9$) line ($\nu_{rest} = 1151.985$ GHz). The detection of these transitions would lead to an improved excitation model for one of the earliest galaxies known in the universe and to the confirmation of the most distant water detection to date.

5.4 Summary

We detect a bright [C II] emission and the underlying continuum emission in P036+03, the most luminous quasar known so far at $z > 6.5$. A second line is tentatively detected which we identify with blended water emission from the adjacent $3_{22} - 3_{13}$ and $5_{23} - 4_{32}$ H_2O transitions. If confirmed, this would be the highest-redshift detection of water vapor available to date.

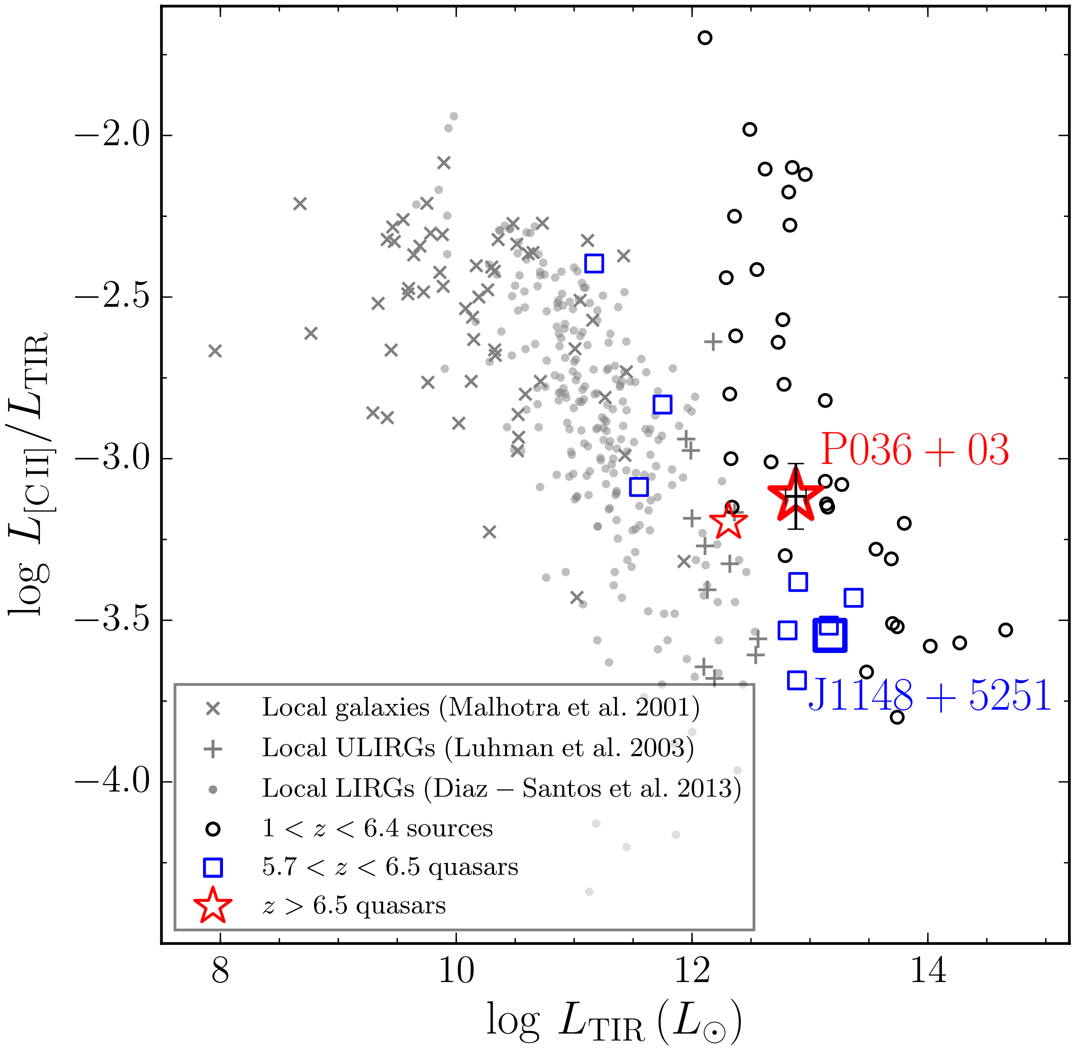

Figure 5.3: The ratio of [C II] to total IR luminosity (TIR; 8–1000 μm) vs. TIR luminosity. The sources at $1.0 < z < 6.4$ include the compilation of star-forming galaxies, submillimiter galaxies, and quasars by De Looze et al. (2014) and 8 star-forming galaxies recently reported by Brisbin et al. (2015). The $5.7 < z < 6.5$ quasars are from Bertoldi et al. (2003a); Maiolino et al. (2005); Walter et al. (2009a); Wang et al. (2013); Willott et al. (2013, 2015). The $z > 6.5$ quasars are P036+03 (this work) and J1120+0641 at $z = 7.1$ (Venemans et al. 2012). Luminosities have been calculated with the cosmology used in this chapter. The TIR luminosities for the $z > 5.7$ quasars have been consistently calculated as for P036+03 (see text Section 5.2). The FIR (42.5–122.5 μm) luminosities from Díaz-Santos et al. (2013) have been converted to TIR luminosities using a common conversion factor of 1.75 (Calzetti et al. 2000). Error bars are only plotted for P036+03 to enhance the clarity of the figure.

The [C II] to TIR luminosity ratio in P036+03 is $\sim 0.8 \times 10^{-3}$, i.e., consistent with low-L_{TIR} star-forming galaxies and high compared to other IR-luminous quasars at $z > 6$. This ratio is a factor

~ 3 higher than in J1148+5251, and consistent with the ratio in the most distant quasar known to date (Figure 5.3), emphasizing the diversity of quasar host galaxies in the early universe.

P036+03 rivals the current archetypal high-redshift quasar, J1148+5251 ($z = 6.42$), in both UV and [C II] luminosities. Thanks to its brightness and given its convenient equatorial location, P036+03 can be studied from facilities in both hemispheres (in contrast to the northern source J1148+5251). For example, P036+03 would be an ideal target for high-resolution ALMA imaging to study the ISM physics and to search for signs of mergers, outflows, and feedback in one of the earliest galaxies in the universe. This quasar will thus likely become one of the key targets to study star formation and the ISM in the early universe.

Chapter 6

Summary and outlook

6.1 Review of this thesis

We have studied high-redshift ($z > 5.5$) quasars—the only direct probes of the growth of supermassive black hole (SMBH) and structure formation in the early universe—from different perspectives. We have almost doubled the number of known quasars in the first Gyr of the universe using the Pan-STARRS1 survey, constrained the radio-loud fraction of quasars at $z \sim 6$, investigated the galaxy environment of a quasar at $z = 5.7$, and studied a quasar host galaxy at $z = 6.54$ using millimeter observations.

In Chapter 2, we presented the criteria to identify $z > 5.5$ quasars using the Pan-STARRS1 survey. These selection criteria resulted in 54 newly discovered quasars, leading to a total of 92 known quasars at $z > 5.5$ that satisfy the selection criteria introduced in this thesis (out of 135 quasars, see Figure 2.6). The quasar sample shows a diverse range of properties and spans a factor of ~20 in luminosity. It is important to emphasize that the number of quasars at $z > 5.5$ presented in this thesis marks the transition phase from studies of individual sources to statistical studies of the high-redshift quasar population, which was impossible with earlier, smaller samples.

In Chapter 3, we searched for $5.5 \lesssim z \lesssim 7.2$ quasars by cross–matching the optical Pan-STARRS1 and radio FIRST surveys. The radio information allows identification of quasars missed by typical color-based selections. While we found no good $6.4 \lesssim z \lesssim 7.2$ quasar candidates at the sensitivities of these surveys, we discovered two new radio-loud quasars at $z \sim 6$. Furthermore, we identified two additional $z \sim 6$ radio-loud quasars which were not previously known to be radio-loud, nearly doubling the current $z \sim 6$ sample. We showed the importance of having infrared photometry for $z > 5.5$ quasars to robustly classify them as radio-quiet or radio-loud. Based on this, we reclassified the quasar J0203+0012 ($z = 5.72$), previously considered radio-loud, as radio-quiet. Using the available data in the literature (see Figure 3.2), we constrained the radio-loud fraction (RLF) of quasars at $z \sim 6$ to RLF = $8.1^{+5.0}_{-3.2}\%$. This result is consistent with a non-evolving RLF of quasars up to $z = 6$, in contrast to some studies suggesting a decline of the RLF with redshift (e.g., Jiang et al. 2007a).

In Chapter 4, we performed the first narrow-band imaging search for an overdensity of galaxies around a $z \sim 6$ quasar. Such overdensities are expected by models that propose that high-redshift quasars reside in some of the most massive dark matter halos. We found no enhancement of galaxies in the area surrounding the quasar in comparison with blank fields (see Figure 4.5). We explored different explanations and interpretations for this non-detection of a galaxy overdensity, including (1) the strong ionizing radiation from the quasar may prevent galaxy formation in its immediate vicinity and (2) high-redshift quasars may not reside in the center of the most massive dark matter halos.

In Chapter 5, we reported a strong detection of the [C II] line in the host galaxy of the brightest quasar known at $z > 6.5$ (see Figure 5.1), the PS1-discovered quasar P036+03. Its [C II] and total far-infrared luminosities are $(5.8 \pm 0.7) \times 10^9\,L_\odot$ and $(7.6 \pm 1.5) \times 10^{12}\,L_\odot$, respectively. This results in a $L_{[\mathrm{C\,II}]}/L_{\mathrm{TIR}}$ ratio of $\sim 0.8 \times 10^{-3}$, which is at the high end for those found for active galaxies, though it is lower than the average found in typical main sequence galaxies at $z \sim 0$. We also reported a tentative additional line, which we identified as a blended emission from the $3_{22} - 3_{13}$ and $5_{23} - 4_{32}$ H_2O transitions. If confirmed, this would be the most distant detection of water emission to date. P036+03 rivals the current prototypical luminous J1148+5251 quasar at $z = 6.42$, in both rest-frame UV and [C II] luminosities. Given its high luminosity and because it is visible from both hemispheres (unlike J1148+5251), P036+03 has the potential of becoming an important laboratory for the study of star formation and of the interstellar medium only $\sim$ 800 Myr after the Big Bang.

In the following sections, we will discuss the future directions arising from the open questions, puzzles, and challenges unveiled by the quasar sample presented in thesis. Afterwards, we will look further into the future and briefly describe the planned surveys that will continue the ambitious enterprise of finding the earliest cosmic objects.

6.2 The PS1 distant quasar sample: future directions

The quasar luminosity function at $z \sim 6$

One of the most fundamental observational probes of the growth of black holes over cosmic time is the evolution of the quasar luminosity function. This is also the main tool to determine the contribution of quasars to the reionization of the universe. However, at the highest accessible redshifts, the luminosity function is still not well constrained, primarily due to the low-number statistics. The most widely used quasar luminosity function at $z \sim 6$ was presented by Willott et al. (2010b) from a sample of 40 SDSS and CFHQS quasars at redshifts $5.74 < z < 6.42$, while the first constraints on the quasar luminosity function were placed at $z = 7$ in Venemans et al. (2013) from a sample of three VIKING quasars at redshifts $6.6 < z < 6.9$. Recently, McGreer et al. (2013) determined the $z = 5$ quasar luminosity function and found that the number density of quasars from $z = 5$ to $z = 6$ decreased faster than previously thought. As a consequence, they suggested that previous predictions for high-redshift quasar surveys should be revised downward by a factor of ~ 2. The PS1 distant quasar sample provides a unique opportunity to constrain and reduce uncertainties in the luminosity function at different redshift bins (e.g., $z \sim 5.9$, 6.3, and 6.8). However, conclusions on the number density and the luminosity function of quasars from the PS1 sample are not possible at the time of writing, since our observations are still ongoing and is expected that more quasars will be found. In the short term, we will update the quasar luminosity function in the redshift range $5.7 < z < 6.2$ in which we are closer to having a complete sample. This will further constrain the strong evolutions reported by McGreer et al. (2013) and will be an important milestone for the forecast of the expected number of quasars in the next generation of surveys.

Recently, Kashikawa et al. (2015) updated the Willott et al. (2010b) $z \sim 6$ luminosity function by adding one or two additional faint quasars at $z \sim 6$. Even though the number of quasars added is low, it did have a significant effect on the shape of the luminosity function. The addition of these quasars made the faint end of the luminosity function steeper and produced a brighter luminosity break. These new parameters imply that the emission rate of ionizing photons from quasars is a factor $\sim 2 - 6$ higher than previously believed. However, Kashikawa et al. (2015) found that even with this increased photon budget from quasars, star-forming galaxies are still probably the dominant sources that caused the reionization of the universe.

As an exercise, we will use the Kashikawa et al. (2015) $z \sim 6$ luminosity function to predict the number of quasars expected in PS1 (and in future surveys below). However, we should keep in mind that when extrapolating to higher redshifts, these numbers might need to be revised downwards by a factor of ~ 2. Ignoring any incompleteness, the expected numbers of quasars in the PS1 survey up to a magnitude of $M_{1450} < -26$ are ~135, 50, and 60 for the redshift ranges

$5.7 < z < 6.2$, $6.2 < z < 6.5$, and $6.5 < z < 7.2$, respectively. The current number of quasars in the PS1 sample to the same absolute magnitude and redshift ranges are 63, eight, and three, respectively (see Figure 2.6). In the last two redshift bins our follow-up is far from complete, while for $5.7 < z < 6.2$ we are approaching that point and we expect to find $\sim 10 - 15$ additional quasars based on our current candidates. Therefore, the prediction does not seem to be too far off taking into account that is likely that we will miss $\sim 20\%$ of quasars due to color selection (especially affecting the fraction of recovered quasars at $z \sim 5.7$ and $z \sim 6.2$) and incompleteness of the survey (i.e., chip gaps, no coverage in some regions due to weather restrictions, varying depths in different bands across the sky).

Push the redshift barrier to $z > 8$ (i.e., to the first 0.6 Gyr of the universe)

So far, despite exhaustive use of resources and big efforts, only one quasar has been discovered at $z > 7$ (Mortlock et al. 2011). It should be noted that black hole growth is relatively rapid, with an e-folding time of the order of a few Myr (e.g., Shapiro 2005; Volonteri & Rees 2005; Alexander & Natarajan 2014). Therefore, building a statistical sample of quasars at $z \gtrsim 7$ is mandatory not only to address cosmic variance, but also to put constraints on massive galaxies and black hole formation models. For example, a supermassive black hole of $2 \times 10^9\, M_\odot$ at $z = 7.1$ (age of the universe ~750 Myr; e.g., Mortlock et al. 2011) set stronger constraints on early black hole growth than a $10^{10}\, M_\odot$ black hole at $z = 6.3$ (~130 Myr later; e.g., Wu et al. 2015).

As presented in Chapter 2, we have recently started to search for z-dropout quasars ($6.5 < z < 7.2$). The results look extremely promising: we have already discovered four quasars at $z > 6.5$, increasing the number of quasars at these redshifts from four to eight. The next step is to push the frontier to even higher redshifts. We are developing a method to use the multiwavelength information provided by PS1 and other infrared surveys (e.g., UKIDSS, UHS, *WISE*) to search for "PS1-drops", i.e., $z \sim 8$ quasars. If this luminous quasars indeed exist at these redshifts, the large area provided by PS1 and *WISE* would even allow us to identify ~ 4 quasars brighter than $M_{1450} < -27$ at $z > 8.1$. This is challenging, but potentially very rewarding, as it will put stringent constraints on black hole formation models.

The host galaxies of the most distant quasars

Studies of the stellar population of $z > 5.5$ quasar hosts have been thus far unsuccessful at (observed) optical and NIR wavelengths, as the bright central AGN outshines its surrounding host galaxy (e.g., Decarli et al. 2012; Mechtley et al. 2012). These studies will probably have to wait for 30 m class telescopes or *JWST*. Fortunately, millimeter and radio observations provide an alternative, since at these wavelengths the radiation is dominated by dust and molecular/fine-structure line emission from the host galaxy (e.g., Leipski et al. 2014). In fact, all the information we know about the hosts of the most distant quasars has come from these wavelengths—primarily from observations of gas tracers such as CO and [C II].

By the end of this thesis, only 11 quasars at $z > 5.5$ have been studied in [C II] (one of the brightest lines in the spectrum of star-forming galaxies), including the work presented in Chapter 5 (see Figure 5.3). Most of these objects were from biased samples, targeting the optically or (sub)mm brightest quasars. As a consequence, the fundamental characteristics of quasar host galaxies (gas mass, dynamics, star formation) could only be studied in any detail for a few extreme objects.

With ALMA now fully operational and with the large sample of quasars in the southern sky presented in this thesis, the current panorama could change dramatically. It will be possible to carry out statistical studies of SMBH-galaxy co-evolution at the highest accessible redshifts. This was simply inconceivable just a few years ago. For example, in the near future we will be able to a) obtain black hole masses (via NIR spectroscopy) and dynamical masses for a large sample of quasar host galaxies. This will give us a more complete picture of the co-evolution of black holes and their host galaxies in the early universe. b) By measuring multiple CO rotational level transition, constrain physical conditions of the interstellar medium, such as density and temperature, in the first massive star-forming galaxies in the universe. c) Using the full configuration of ALMA, we will be able to resolve the [C II] line and FIR dust continuum emission on sub-kpc scales. This will allow us to produce maps of the star formation and search for signs of mergers, outflows, and feedback in the earliest massive galaxies in the universe. Such observations would provide important observational constraints on models of massive galaxy and dust formation and for predictions by cosmological simulations (e.g., Di Matteo et al. 2012; Volonteri & Bellovary 2012; Valiante et al. 2014; Michałowski 2015).

Understanding weak-line emission quasars

Perhaps one of the most surprising findings in high-redshift quasar studies is that many, if not most, quasar properties appear to be indistinguishable across cosmic time. It has been claimed, however, that the fraction of quasars with weak emission lines evolves from 1% at $z \sim 3$ to 6% at $z \sim 5$ (Diamond-Stanic et al. 2009). Several scenarios have been proposed to explain the existence of these intriguing weak-line quasars (e.g., Shemmer et al. 2010; Lane et al. 2011; Laor & Davis 2011; Wang et al. 2014; Shemmer & Lieber 2015). Nevertheless, no consensus has yet been reached. To our surprise, we found that 25% of our initial sample of eight $z \sim 6$ PS1 quasars lacked strong emission lines (Bañados et al. 2014). This was a much larger fraction than that found at lower redshifts, although the discrepancy could be explained by our small sample of quasars. However, our preliminary analysis of the quasars discovered in this thesis seems to support our previous claims. One third of the PS1-discovered quasars at $z > 5.5$ are classified as weak-line quasars (see Figure 6.1). To determine whether this is due to selection effects or whether weak-line quasars are more common at the highest redshifts than previously thought, further investigation is required. A multiwavelength follow-up of these objects is necessary to study possible differences within the quasar population and test whether this trend also holds with the strength of other strong broad emission lines such as the C IV and Mg II lines. An interesting scenario, that seems to be supported by the observed large fraction of weak-line quasars at the highest accessible redshifts, is that we may be witnessing these objects in such an early formation phase that they are not yet chemically enriched enough to show strong metal lines.

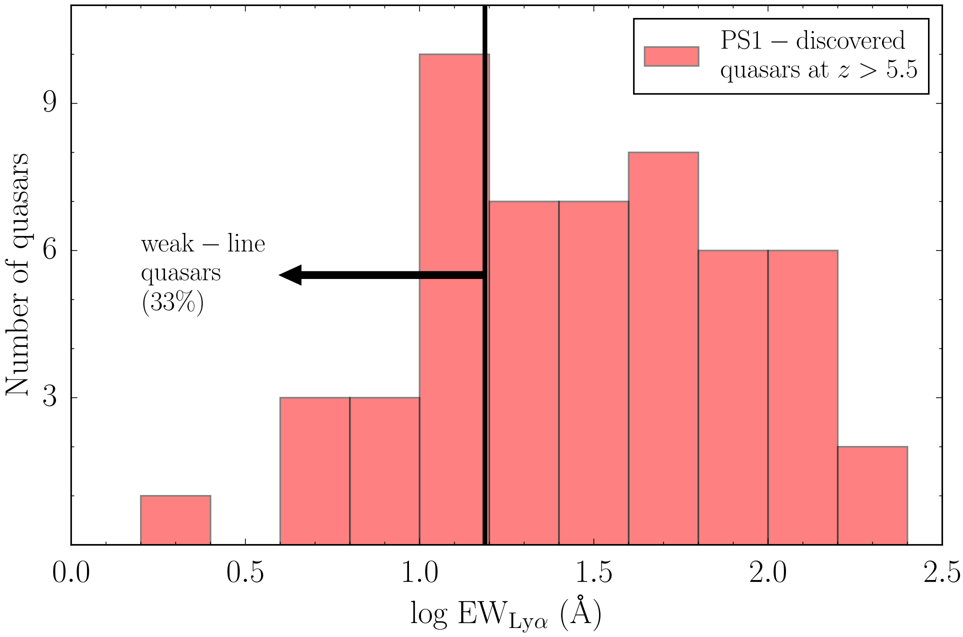

Figure 6.1: Distribution of rest-frame equivalent widths of Lyα ($\mathrm{EW_{Ly\alpha}}$) for the $z > 5.5$ quasars discovered in this thesis. The definition of weak-line quasars at $\mathrm{EW_{Ly\alpha}} = 15.4$ Å is indicated (Diamond-Stanic et al. 2009).

Do quasars live in the most massive dark matter halos?

In Chapter 4, we found that a quasar at $z = 5.7$ was not located in a region with an overdensity of Lyα emitters (LAEs). One of the possible and somewhat controversial interpretations of this result is that high-redshift quasars may not reside in the center of the most massive dark matter halos. However, these interpretations were based on a 'sample of one'. Therefore, increasing the number of these studies is crucial to make significant progress in understanding the environment in which high-redshift quasars live. Following these lines, we are carrying out a similar study in a PS1-discovered quasar at $z = 5.7$. Our preliminary results are in agreement with our previous findings, i.e., there is no overdensity of galaxies around this quasar either (C. Mazzucchelli et al. in prep.). Recently, Simpson et al. (2014) reported that there is no excess of bright galaxies within 1 Mpc of the most distant quasar currently known at $z = 7.1$. All this mounting evidence is bringing our initial surprising results into a more coherent picture. It is important to emphasize that stronger interpretations and conclusions are still restricted by the limited number of studies. To overcome current limitations, a systematic study (preferentially with larger fields-of-view than previous investigations) of the environment of a significant sample of quasars is needed. The sample of $z > 5.5$ quasars presented in this thesis will allow the study of the environment of quasars with a range of different luminosities and spectral features in order to clarify whether they (or some of them) reside in massive dark matter halos.

6.3 Future surveys

Subaru Hyper-Suprime Cam

The Hyper-Suprime Cam survey[1][2] (HSC) using the 8.2 m Subaru telescope has already initiated its observations that will continue until 2019. The *wide* layer of this survey will map 1400 deg^2 in various narrow-band filters and in the *grizY* bands. Therefore, similarly to PS1, HSC will be able to identify quasars up to $z \sim 7.2$. The estimated 5σ limiting magnitudes for the wide layer are $g = 26.5$, $r = 26.0$, $i = 25.6$, $z = 25.0$, and $Y = 24.5$, i.e., about 2–3 mag fainter than PS1. This will allow us to identify a sizable number of $z \sim 6$ and ~ 7 quasars to absolute magnitudes as faint as $M_{1450} \sim -23$ and $M_{1450} \sim -24$, respectively. This will be extremely important in setting strong constraints on the faint end of the $z = 6$ and $z = 7$ quasar luminosity functions, complementing the constraints that PS1 will provide on the bright ends (see above). The predicted number of quasars identified by HSC are ~ 350 at $5.7 < z < 6.5$ and ~ 58 at $6.5 < z < 7.2$, down to $M_{1450} = -23$ and $M_{1450} = -24$, respectively.

The Large Synoptic Survey Telescope

The Large Synoptic Survey Telescope (LSST; Ivezic et al. 2008; LSST Science Collaboration et al. 2009) will take multiple images of all the sky below decl. < +34.5° in six bands, *ugrizy*.

---

[1] http://www.astro.princeton.edu/~rhl/HSC/

[2] http://www.naoj.org/Projects/HSC/HSCProject.html

The regular survey operations are expected to start by 2022 and last for 10 years. About 90% of the observing time will be dedicated to image a region of $18,000\,\mathrm{deg}^2$ 800 times, providing a unique "high-definition color movie of the universe" (Ivezic et al. 2008). The single epoch images will reach a magnitude of $r \sim 24.5$, while the expected 5σ stacked limiting magnitudes by the end of the survey are 25.8, 27.0, 27.2, 27.0, 25.7, and 24.4, in u, g, r, i, z, and y, respectively. The predicted number of quasars identified by LSST are ~ 3500 at $5.7 < z < 6.5$ and ~ 600 at $6.5 < z < 7.2$, down to $M_{1450} = -23$ and $M_{1450} = -24$, respectively.

Euclid

Euclid (Laureijs et al. 2011, 2014) is a survey space mission under development by the European Space Agency (ESA). The launch of the mission is foreseen in 2020 and it has a nominal duration of six years. The survey is designed to understand the nature of dark energy, dark matter, and gravity, but its legacy data products will allow the identification of thousands of galaxies and quasars at $z > 6$. Euclid will survey $15,000\ \mathrm{deg}^2$ of extra-galactic sky using a 1.2 m telescope. The survey will provide images in the Y, J, and H bands, reaching 5σ limiting magnitudes of ~ 24. Euclid is expected to find about 30 quasars brighter than $M_{1450} < -25$ at $z > 8.1$.

The Wide-Field Infrared Survey Telescope

The Wide-Field Infrared Survey Telescope (WFIRST; Spergel et al. 2013, 2015) is a NASA mission whose launch is expected in the mid-2020s. The current version of the project consists of a 2.4 m telescope with a wide field multi-filter NIR imager and spectrometer, plus a coronograph instrument for the direct imaging of exoplanets. WFIRST will address a broad variety of science cases ranging from planet exploration to revealing the most distant cosmic objects. WFIRST will include a high-latitude survey, which will map $\sim 2,200\ \mathrm{deg}^2$ of sky in the Z, Y, J, and H bands to a 5σ limiting magnitude of 26.5. These deep images of the sky at infrared wavelengths will allow the identification of several hundreds faint quasar and galaxy candidates at $z > 8$. These faint candidates will eventually need spectroscopic confirmation from the *JWST* or the next generation of ground based telescopes such as the Giant Magellan Telescope[3] (GMT), the Thirty Meter Telescope[4] (TMT), and the European Extremely Large Telescope[5] (E-ELT). WFIRST is expected to identify ~ 35 quasars at $z > 8.1$ with absolute magnitudes $M_{1450} < -23$.

---

[3] `http://www.gmto.org/`

[4] `http://www.tmt.org/`

[5] `http://www.eso.org/e-elt`

In summary, the coming years will be crucial to the understanding of the early universe by studying key aspects of the distant quasar population presented in this thesis via combined and dedicated, optical, near-infrared, millimeter, and radio observations. Moreover, the upcoming surveys and facilities will enable us to find fainter quasars and galaxies and push the redshift frontier even further. In conclusion, the future for the field of high-redshift quasars and galaxies looks promising and the work presented in this thesis is merely the start of an exciting transition era towards a statistical characterization of the most distant cosmic objects.

Appendix A

List of quasars at $z > 5.5$

Tables A.1 and A.2 list general information for the 135 $z > 5.5$ quasars known by the end of this thesis (i.e., 2015 April). Table A.1 includes the full names, coordinates, redshifts, and rest-frame 1450 Å magnitudes of the quasars. The quasars were cross-matched to the WISE All-Sky data release products catalog (Cutri 2012) and to the ALLWISE Source catalog and Reject Table[1] (Cutri 2014) within a radius of 3″. Table A.2 presents their magnitudes from *WISE* and from the second data release of the Pan-STARRS1 stacked catalog (PV2). In both tables we include the column "PS1", which is > 0 for quasars that satisfy the selection criteria presented in Chapter 2. There are 92 PS1 selected quasars out of which 54 are new PS1 discoveries.

More than 70% (99/135) of the known $z > 5.5$ quasars are detected in at least one of the *WISE* bands with a S/N> 2.5. More than 80% (112/135) of the known $z > 5.5$ quasars are detected in at least one of the PS1 bands with a S/N> 5, while 74% (100/135) have information in all the most relevant PS1 bands for high-redshift quasar searches: $i_{\rm P1}$, $z_{\rm P1}$, $y_{\rm P1}$. The are six known quasars with decl.< −30, which are therefore outside the PS1 footprint.

---

[1] `http://wise2.ipac.caltech.edu/docs/release/allwise/expsup/sec2_1.html`

Table A.1. Information of the 135 $z > 5.5$ quasars known by the end of this thesis.

Quasar	R.A. °	Decl. °	z	m_{1450} mag	PS1 [a]	References disc./ z/ m_{1450}
PSO J000.3401+26.8358	0.34012	26.83588	5.71	20.2	4	1/1/1
SDSS J0002+2550	0.66412	25.84304	5.82	19.0	1	2/3/4
SDSS J0005–0006	1.46808	−0.11550	5.85	20.2	1	2/5/4
PSO J002.1073–06.4345	2.10739	−6.43456	5.93	20.4	1	1,18/1/1
PSO J002.3786+32.8702	2.37870	32.87026	6.08	21.6	1	1/1/1
PSO J004.8140–24.2991	4.81408	−24.29916	5.69	19.5	1	1/1/1
PSO J007.0273+04.9571	7.02734	4.95713	5.99	20.2	1	6,18/6/6
CFHQS J0033–0125	8.29750	−1.42358	6.13	21.8	0	7/7/4
PSO J009.7355–10.4316	9.73551	−10.43164	5.96	20.2	2	1/1/1
CFHQS J0050+3445	12.52777	34.75600	6.253	19.8	0	8/9/4
CFHQS J0055+0146	13.76212	1.77175	6.006	21.8	0	10/11/4
SDSS J0100+2802	15.05427	28.04053	6.3	17.6	2	12/12/12
CFHQS J0102–0218	15.71100	−2.30275	5.95	22.0	0	10/10/4
VIK J0109–3040	17.47138	−30.79064	6.747	21.4	0	13/14/13
PSO J021.4213–25.8822	21.42134	−25.88229	5.77	19.7	1	1/1/1
SDSS J0129–0035	22.49379	−0.59436	5.7787	22.3	0	15/16/4
PSO J023.0071–02.2675	23.00710	−2.26753	5.89	20.2	1	1/1/1
CFHQS J0136+0226	24.01342	2.43465	6.21	22.0	0	8/8/4
PSO J025.2376–11.6831	25.23764	−11.68319	5.81	19.9	1	1/1/1
ATLAS J025.6821–33.4627	25.68220	−33.46263	6.31	19.0	0	17/17/17
ULAS J0148+0600	27.15681	6.00557	5.98	19.4	1	18,31/19/1
PSO J029.5172–29.0886	29.51726	−29.08868	5.96	19.1	1	1/1/1
ATLAS J029.9915–36.5658	29.99155	−36.56572	6.02	19.8	0	17/17/17
ULAS J0203+0012	30.88491	0.20813	5.72	21.0	1	20/21/4
CFHQS J0210–0456	32.55496	−4.93914	6.4323	22.6	0	9/22/4
CFHQS J0216–0455	34.11588	−4.92614	6.01	24.1	0	10/10/4
CFHQS J0221–0802	35.34463	−8.04764	6.161	22.0	0	8/9/4
PSO J036.5078+03.0498	36.50780	3.04984	6.5412	19.5	3	23/24/23
CFHQS J0227–0605	36.93037	−6.09172	6.2	21.4	0	10/10/4
PSO J037.9706–28.8389	37.97066	−28.83891	5.99	20.7	1	6/6/1
SDSS J0239–0045	39.87600	−0.75150	5.82	22.1	0	15/15/4
PSO J040.0159+17.5458	40.01592	17.54581	5.63	21.0	1	1/1/1
PSO J042.6690–02.9174	42.66909	−2.91745	5.88	20.1	1	1/1/1
PSO J045.1840–22.5408	45.18408	−22.54088	5.7	20.5	1	6/6/1
SDSS J0303–0019	45.88083	−0.32025	6.08	21.3	0	25/26/4
VIK J0305–3150	46.32048	−31.84886	6.605	20.9	0	13/14/13
CFHQS J0316–1340	49.20779	−13.67564	5.99	21.7	0	8/8/4
PSO J055.4244–00.8035	55.42440	−0.80354	5.68	20.4	4	27/27/27

Table A.1 (cont'd)

Quasar	R.A. °	Decl. °	z	m_{1450} mag	PS1 [a]	References disc./ z/ m_{1450}
PSO J056.7168–16.4769	56.71685	−16.47691	5.99	20.3	1	1/1/1
SDSS J0353+0104	58.45722	1.06795	6.072	20.2	1	25/28/4
PSO J060.5529+24.8567	60.55290	24.85678	6.18	20.2	1	1/1/1
PSO J065.4085–26.9543	65.40854	−26.95434	6.16	19.6	2	1/1/1
PSO J065.5041–19.4579	65.50415	−19.45797	6.11	20.3	1	1/1/1
PSO J071.4507–02.3332	71.45075	−2.33329	5.7	19.3	1	1/1/1
DES J0454–4448	73.50745	−44.80864	6.1	20.2	0	29/29/29
PSO J075.9356–07.5061	75.93566	−7.50613	5.85	20.4	1	1/1/1
SDSS J0818+1722	124.61418	17.38111	6.02	19.3	1	30/3/4
ULAS J0828+2633	127.05587	26.56542	6.05	20.6	1	31/31/1
PSO J127.2817+03.0657	127.28174	3.06571	5.82	20.8	1	1/1/1
SDSS J0836+0054	129.18277	0.91479	5.81	18.8	1	32/5/4
SDSS J0840+5624	130.14626	56.40561	5.8441	20.0	1	30/33/4
SDSS J0841+2905	130.33132	29.08460	5.98	19.6	1	34/3/4
SDSS J0842+1218	130.62263	12.31405	6.069	19.6	1	18,28/28/4
SDSS J0850+3246	132.70102	32.77998	5.87	19.9	1	18/18/18
PSO J135.3860+16.2518	135.38604	16.25190	5.63	20.6	4	27/27/27
PSO J135.8704–13.8336	135.87046	−13.83369	5.86	21.1	1	1/1/1
SDSS J0927+2001	141.84091	20.02324	5.7722	19.9	0	30/35/4
SDSS J1030+0524	157.61297	5.41528	6.308	19.7	1	32/5/4
PSO J157.9070–02.6599	157.90704	−2.65991	5.92	20.3	1	1/1/1
PSO J159.2257–02.5438	159.22579	−2.54387	6.35	19.9	2	1/1/1
SDSS J1044–0125	161.13767	−1.41728	5.7847	19.2	1	36/16/4
VIK J1048–0109	162.07951	−1.16119	6.62	21.1	3	37/37/1
SDSS J1048+4637	162.18777	46.62182	6.2284	19.2	1	38/3/4
CFHQS J1059–0906	164.86920	−9.10567	5.92	20.8	0	8/8/4
PSO J167.4726+56.9521	167.47266	56.95211	5.92	20.6	1	1/1/1
PSO J167.6415–13.4960	167.64157	−13.49600	6.508	21.3	3	23/23/23
ULAS J1120+0641	170.00614	6.69014	7.0842	20.4	0	39/40/4
PSO J172.1770+26.8866	172.17701	26.88666	5.8	20.8	1	1/1/1
SDSS J1137+3549	174.32387	35.83245	6.03	19.6	1	30/3/4
RD J1148+5253	177.06754	52.89425	5.7	23.1	0	41/41/42
SDSS J1148+5251	177.06938	52.86400	6.4189	19.0	2	38/3/4
ULAS J1207+0630	181.90597	6.50284	6.04	20.1	1	18/18/18
PSO J183.1124+05.0926	183.11243	5.09264	6.45	19.9	3	1/1/1
PSO J183.2991–12.7676	183.29919	−12.76762	5.86	19.4	1	6/6/1
VIK J1215p0023	183.82030	0.39018	5.93	22.1	1	37/37/37
PSO J187.1047–02.5609	187.10479	−2.56090	5.78	21.0	1	1/1/1

Table A.1 (cont'd)

Quasar	R.A. °	Decl. °	z	m_{1450} mag	PS1 [a]	References disc./ z/ m_{1450}
PSO J187.3050+04.3243	187.30503	4.32437	5.89	21.3	1	6/6/6
ULAS J1243+2529	190.92006	25.48995	5.83	20.6	1	31/31/1
SDSS J1250+3130	192.71636	31.50608	6.15	19.6	1	30/3/4
SDSS J1257+6349	194.48950	63.82699	6.02	20.6	0	18/18/18
SDSS J1306+0356	196.53445	3.94065	6.016	19.6	1	32/5/4
ULAS J1319+0950	199.79709	9.84764	6.133	19.6	1	21/16/4
SDSS J1335+3533	203.96171	35.55439	5.9012	19.9	1	30/3/4
PSO J209.2058–26.7083	209.20586	−26.70840	5.73	19.5	1	1/1/1
PSO J210.7277+40.4008	210.72777	40.40088	6.01	21.0	1	1/1/1
PSO J210.8296+09.0475	210.82970	9.04750	5.84	20.4	1	1,18/1/1
PSO J210.8722–12.0094	210.87222	−12.00948	5.84	21.0	1	6/6/6
SDSS J1411+1217	212.79703	12.29368	5.904	20.0	1	2/5/4
PSO J213.3629–22.5617	213.36299	−22.56174	5.88	20.0	1	6/6/1
PSO J215.1514–16.0417	215.15143	−16.04173	5.73	19.1	1	43/43/6
NDWFS J142516.3+32540	216.31805	32.90265	5.8918	20.6	1	44/3/4
NDWFS J142729.7+352209	216.87372	35.36922	5.53	21.9	0	44/44/44
FIRST J1427+3312	216.91079	33.21167	6.12	20.3	0	45,46/45/4
PSO J217.0891–16.0453	217.08913	−16.04536	6.13	19.6	2	1/1/1
CFHQS J1429+5447	217.46737	54.78825	6.1831	20.9	0	8/47/4
SDSS J1436+5007	219.04890	50.11866	5.85	20.2	1	30/3/4
CFHQS J1509–1749	227.42408	−17.82411	6.121	19.8	1	7/9/4
PSO J228.6871+21.2388	228.68712	21.23882	5.9	20.6	1	1/1/1
PSO J231.6576–20.8335	231.65766	−20.83352	6.6	20.1	3	1/1/1
PSO J235.9450+17.0079	235.94506	17.00790	5.79	20.2	1	1/1/1
PSO J236.2912+16.6088	236.29125	16.60886	5.86	20.9	1	1/1/1
J154552.08+602824.00	236.46705	60.47333	5.79	19.1	1	48/48/1
SDSS J1602+4228	240.72490	42.47360	6.09	19.9	1	2/3/4
ELAIS1091000446 [c]	240.95446	55.17564	6.041	24.1	0	49/49/49
ULAS J1609+3041	242.40530	30.69661	6.14	20.9	1	31/31/1
PSO J242.4397–12.9816	242.43971	−12.98170	5.81	20.3	1	1/1/1
SDSS J1621+5155	245.25389	51.93023	5.71	19.9	0	50/50/4
SDSS J1623+3112	245.88256	31.20014	6.26	20.1	1	2/47/4
SDSS J1630+4012	247.64126	40.20269	6.065	20.6	1	38/3/4
CFHQS J1641+3755	250.34052	37.92226	6.047	20.6	1	7/9/4
PSO J267.0021+22.7812	267.00211	22.78120	5.93	21.1	1	1/1/1
PSO J308.0416–21.2339	308.04164	−21.23397	6.22	20.6	2	1/1/1
PSO J308.4829–27.6485	308.48297	−27.64850	5.78	20.0	1	1/1/1
SDSS J2053+0047	313.34068	0.78518	5.92	21.2	0	15/15/4

Table A.1 (cont'd)

Quasar	R.A. °	Decl. °	z	m_{1450} mag	PS1 [a]	References disc./ z/ m_{1450}
SDSS J2054–0005	313.52704	−0.08744	6.0391	20.6	1	25/16/4
CFHQS J2100–1715	315.22758	−17.25625	6.087	21.4	1	8/9/4
PSO J319.6040–10.9326	319.60403	−10.93262	5.85	20.1	1	1/1/1
PSO J320.8703–24.3604	320.87033	−24.36040	5.73	20.2	1	1/1/1
SDSS J2147+0107	326.98086	1.13203	5.81	21.6	0	15/15/4
VIMOS2911001793	334.82175	1.04692	6.156	23.6	0	49/49/49
SDSS J2220-0101	335.07704	1.02969	5.62	20.8	0	51/51/51
SDSS J2228+0110	337.18141	1.17561	5.95	22.2	0	52/52/52
CFHQS J2229+1457	337.25688	14.95237	6.1517	21.9	0	8/11/4
PSO J338.2298+29.5089	338.22977	29.50898	6.658	20.9	3	23/23/23
PSO J340.2041–18.6621	340.20417	−18.66217	6.0	20.8	1	6/6/6
CFHQS J2242+0334	340.65645	3.57267	5.88	22.1	0	8/8/4
SDSS J2307+0031	346.89733	0.53035	5.87	21.7	0	15/15/4
SDSS J2310+1855	347.66205	18.92220	6.0031	19.3	0	16/16/4
SDSS J2315–0023	348.94404	−0.39947	6.117	21.3	0	25/25/4
CFHQS J2318–0246	349.51166	−2.77611	6.05	21.6	0	10/10/4
CFHQS J2329–0301	352.28450	−3.03300	6.417	21.6	0	7/9/4
CFHQS J2329–0403	352.31025	−4.05669	5.9	22.0	0	10/10/4
VIK J2348–3054	357.13890	−30.90284	6.889	21.2	0	13/14/13
PSO J359.1352–06.3831	359.13521	−6.38313	6.17	20.1	1	1/1/1
SDSS J2356+0023	359.21491	0.39250	6.0	21.8	0	15/15/4

References. — (1) This thesis, (2) Fan et al. (2004), (3) Carilli et al. (2010), (4) Calura et al. (2014), (5) Kurk et al. (2007), (6) Bañados et al. (2014), (7) Willott et al. (2007), (8) Willott et al. (2010b), (9) Willott et al. (2010a), (10) Willott et al. (2009), (11) Willott et al. (2015), (12) Wu et al. (2015), (13) Venemans et al. (2013), (14) De Rosa et al. (2014), (15) Jiang et al. (2009), (16) Wang et al. (2013), (17) Carnall et al. (2015), (18) Jiang et al. (2015), (19) Becker et al. (2015), (20) Venemans et al. (2007a), (21) Mortlock et al. (2009), (22) Willott et al. (2013), (23) Venemans et al. (2015), (24) Bañados et al. (2015a), (25) Jiang et al. (2008), (26) Kurk et al. (2009), (27) Bañados et al. (2015b), (28) De Rosa et al. (2011), (29) Reed et al. (2015), (30) Fan et al. (2006b), (31) S. J. Warren et al. (in prep.), (32) Fan et al. (2001), (33) Wang et al. (2010), (34) Goto (2006), (35) Carilli et al. (2007), (36) Fan et al. (2000b), (37) B. P. Venemans et al. (in prep.), (38) Fan et al. (2003), (39) Mortlock et al. (2011), (40) Venemans et al. (2012), (41) Mahabal et al. (2005), (42) Leipski et al. (2014), (43) Morganson et al. (2012), (44) Cool et al. (2006), (45) McGreer et al. (2006), (46) Stern et al. (2007), (47) Wang et al. (2011a), (48) F. Wang et al. (in prep.), (49) Kashikawa et al. (2015), (50) Wang et al. (2008), (51) McGreer et al. (2013), (52) Zeimann et al. (2011)

Note. — Quasars sorted by right ascension. The reported coordinates are from PS1 when available, otherwise from their discovery papers.

[a] PS1 criteria: 0=None; 1=Criteria of Section 2.2.1.1; 2=Criteria of Section 2.2.1.2; 3=Criteria of Section 2.2.1.3; 4=Extended PS1 criteria.

[b] CFHQS J0216–0455 (J0216–0455) could be a Seyfert galaxy (see Willott et al. 2009 and the Appendix of Willott et al. 2010a).

[c] ELAIS1091000446 (J1603+5510) could be a Lyα emitter (see Kashikawa et al. 2015).

Table A.2. PS1 and WISE photometry of the 135 $z > 5.5$ quasars known by the end of this thesis.

Quasar	$i_{\rm P1}$ mag	$z_{\rm P1}$ mag	$y_{\rm P1}$ mag	W_1 mag	W_2 mag	W_3 mag	PS1 [a]
P000+26	21.31 ± 0.04	19.33 ± 0.02	19.53 ± 0.04	19.07 ± 0.07	18.61 ± 0.11	–	4
J0002+2550	21.91 ± 0.08	19.14 ± 0.02	19.46 ± 0.05	18.86 ± 0.06	18.88 ± 0.13	17.59 ± 0.42	1
J0005–0006	23.11 ± 0.21	20.47 ± 0.05	20.95 ± 0.16	20.00 ± 0.16	–	–	1
P002–06	22.64 ± 0.19	20.26 ± 0.03	20.33 ± 0.12	19.51 ± 0.11	19.02 ± 0.14	–	1
P002+32	> 23.75	21.27 ± 0.08	21.15 ± 0.17	–	–	–	1
P004–24	22.24 ± 0.24	19.57 ± 0.02	19.42 ± 0.05	18.98 ± 0.07	18.91 ± 0.12	17.30 ± 0.34	1
P007+04	23.20 ± 0.27	20.61 ± 0.06	20.17 ± 0.08	19.97 ± 0.16	19.75 ± 0.29	–	1
J0033–0125	–	–	–	20.99 ± 0.40	19.83 ± 0.29	–	0
P009–10	> 23.41	20.82 ± 0.05	20.22 ± 0.10	19.22 ± 0.08	19.20 ± 0.16	–	2
J0050+3445	> 22.83	21.02 ± 0.10	20.21 ± 0.14	19.35 ± 0.07	19.13 ± 0.12	–	0
J0055+0146	–	–	–	–	–	–	0
J0100+2802	20.91 ± 0.03	18.64 ± 0.01	17.65 ± 0.01	17.16 ± 0.03	16.98 ± 0.03	16.89 ± 0.21	2
J0102–0218	–	–	–	–	–	–	0
J0109–3040	–	–	–	20.96 ± 0.32	–	–	0
P021–25	22.19 ± 0.19	19.66 ± 0.03	19.72 ± 0.14	18.91 ± 0.06	18.83 ± 0.11	17.70 ± 0.42	1
J0129–0035	–	22.12 ± 0.19	–	–	–	–	0
P023–02	23.03 ± 0.26	20.20 ± 0.03	20.23 ± 0.09	19.20 ± 0.07	18.82 ± 0.10	–	1
J0136+0226	–	21.87 ± 0.17	–	–	–	–	0
P025–11	22.56 ± 0.24	20.20 ± 0.04	19.89 ± 0.08	19.37 ± 0.08	19.26 ± 0.15	–	1
J0142–3327	–	–	–	18.82 ± 0.05	18.82 ± 0.08	–	0
J0148+0600	22.91 ± 0.25	19.50 ± 0.02	19.42 ± 0.04	18.80 ± 0.06	18.61 ± 0.10	17.35 ± 0.29	1
P029–29	22.24 ± 0.18	19.38 ± 0.03	19.38 ± 0.04	18.81 ± 0.05	18.58 ± 0.08	17.18 ± 0.29	1
J0159–3633	–	–	–	19.39 ± 0.08	19.21 ± 0.12	–	0
J0203+0012	> 23.78	20.73 ± 0.08	20.44 ± 0.11	19.39 ± 0.09	19.36 ± 0.19	17.49 ± 0.40	1
J0210–0456	–	–	–	–	–	–	0
J0216–0455	–	–	–	–	–	–	0
J0221–0802	–	–	–	20.69 ± 0.23	–	–	0
P036+03	22.78 ± 0.21	> 22.13	19.34 ± 0.04	19.43 ± 0.08	19.47 ± 0.18	–	3
J0227–0605	–	–	–	20.85 ± 0.28	–	–	0
P037–28	> 23.06	20.74 ± 0.08	20.59 ± 0.14	20.19 ± 0.15	19.95 ± 0.26	–	1
J0239–0045	–	–	–	–	–	–	0
P040+17	23.46 ± 0.31	20.65 ± 0.06	20.98 ± 0.18	–	–	–	1
P042–02	22.86 ± 0.22	20.49 ± 0.06	20.07 ± 0.08	20.28 ± 0.17	–	–	1
P045–22	> 22.79	20.40 ± 0.06	20.53 ± 0.15	–	–	–	1
J0303–0019	> 23.12	21.04 ± 0.06	21.07 ± 0.22	–	–	–	0
J0305–3150	–	–	–	20.38 ± 0.14	20.09 ± 0.24	–	0
J0316–1340	–	21.74 ± 0.16	–	–	–	–	0
P055–00	22.43 ± 0.24	20.23 ± 0.05	20.28 ± 0.09	20.62 ± 0.26	20.13 ± 0.35	–	4
P056–16	22.66 ± 0.23	20.24 ± 0.07	20.13 ± 0.12	19.50 ± 0.09	19.20 ± 0.14	–	1
J0353+0104	> 23.17	21.10 ± 0.09	20.64 ± 0.17	19.34 ± 0.09	19.62 ± 0.24	–	1
P060+24	> 23.47	20.53 ± 0.04	20.17 ± 0.07	19.17 ± 0.09	19.41 ± 0.21	–	1
P065–26	23.08 ± 0.33	20.54 ± 0.05	19.63 ± 0.07	19.01 ± 0.06	19.00 ± 0.10	–	2
P065–19	> 23.17	19.78 ± 0.03	20.31 ± 0.11	18.67 ± 0.05	18.42 ± 0.07	17.24 ± 0.31	1
P071–02	21.49 ± 0.08	19.18 ± 0.01	19.17 ± 0.03	18.95 ± 0.06	18.90 ± 0.11	–	1
J0454–4448	–	–	–	19.68 ± 0.08	19.62 ± 0.14	–	0
P075–07	> 22.89	20.55 ± 0.05	20.34 ± 0.10	19.70 ± 0.11	19.58 ± 0.20	17.02 ± 0.32	1
J0818+1722	22.15 ± 0.08	19.59 ± 0.02	19.29 ± 0.04	–	–	–	1
J0828+2633	> 23.52	20.86 ± 0.07	20.51 ± 0.11	–	–	–	1
P127+03	> 22.90	20.73 ± 0.05	20.78 ± 0.13	20.07 ± 0.17	19.87 ± 0.28	–	1

Table A.2 (cont'd)

Quasar	i_{P1} mag	z_{P1} mag	y_{P1} mag	W_1 mag	W_2 mag	W_3 mag	PS1 [a]
J0836+0054	21.25 ± 0.08	18.74 ± 0.01	19.08 ± 0.03	18.00 ± 0.04	17.75 ± 0.05	–	1
J0840+5624	21.99 ± 0.12	19.74 ± 0.03	19.61 ± 0.08	19.46 ± 0.14	19.30 ± 0.22	–	1
J0841+2905	> 23.05	20.41 ± 0.05	20.25 ± 0.09	19.91 ± 0.16	19.60 ± 0.25	–	1
J0842+1218	> 23.36	19.91 ± 0.03	19.94 ± 0.06	18.92 ± 0.07	19.31 ± 0.18	–	1
J0850+3246	22.46 ± 0.14	20.17 ± 0.03	20.05 ± 0.06	19.43 ± 0.09	18.98 ± 0.15	–	1
P135+16	22.47 ± 0.16	20.72 ± 0.05	20.83 ± 0.15	19.51 ± 0.11	19.53 ± 0.22	–	4
P135–13	22.73 ± 0.20	20.39 ± 0.04	21.08 ± 0.19	–	–	–	1
J0927+2001	21.69 ± 0.11	19.90 ± 0.03	19.89 ± 0.11	19.40 ± 0.11	20.21 ± 0.42	–	0
J1030+0524	> 23.02	20.28 ± 0.04	19.89 ± 0.07	19.28 ± 0.09	18.91 ± 0.15	–	1
P157–02	> 22.78	20.27 ± 0.03	20.31 ± 0.08	19.54 ± 0.11	19.54 ± 0.22	–	1
P159–02	> 23.00	20.56 ± 0.05	19.92 ± 0.06	19.44 ± 0.09	19.04 ± 0.13	–	2
J1044–0125	21.91 ± 0.13	19.37 ± 0.02	19.38 ± 0.04	19.05 ± 0.07	18.97 ± 0.14	–	1
J1048–0109	> 23.15	> 23.02	20.85 ± 0.15	20.04 ± 0.17	–	–	3
J1048+4637	22.88 ± 0.29	20.12 ± 0.04	19.69 ± 0.09	19.05 ± 0.06	19.20 ± 0.12	–	1
J1059–0906	–	20.99 ± 0.09	–	20.08 ± 0.17	19.75 ± 0.25	–	0
P167+56	> 23.16	20.89 ± 0.08	20.63 ± 0.16	–	–	–	1
P167–13	> 22.70	> 22.91	20.56 ± 0.12	21.13 ± 0.39	–	–	3
J1120+0641	> 22.98	> 23.04	20.76 ± 0.19	19.61 ± 0.11	19.42 ± 0.20	–	0
P172+26	> 23.22	20.63 ± 0.07	20.75 ± 0.16	19.88 ± 0.14	20.04 ± 0.31	–	1
J1137+3549	22.16 ± 0.09	19.46 ± 0.02	19.43 ± 0.04	19.16 ± 0.07	19.23 ± 0.14	–	1
J1148+5253	–	–	–	–	–	–	0
J1148+5251	22.89 ± 0.29	20.59 ± 0.04	19.10 ± 0.06	18.67 ± 0.05	18.79 ± 0.08	–	2
J1207+0630	23.28 ± 0.26	20.52 ± 0.04	20.16 ± 0.07	19.69 ± 0.13	19.43 ± 0.21	–	1
P183+05	> 23.38	21.80 ± 0.13	19.95 ± 0.06	19.66 ± 0.13	19.79 ± 0.33	–	3
P183–12	22.24 ± 0.13	19.58 ± 0.02	19.28 ± 0.03	18.98 ± 0.07	19.18 ± 0.16	–	1
J1215+0023	> 23.74	21.30 ± 0.10	21.40 ± 0.16	–	–	–	1
P187–02	> 23.79	20.91 ± 0.06	20.87 ± 0.12	19.89 ± 0.14	19.97 ± 0.32	–	1
P187+04	23.30 ± 0.27	20.88 ± 0.05	21.11 ± 0.13	–	–	–	1
J1243+2529	> 23.44	20.23 ± 0.03	20.62 ± 0.09	19.40 ± 0.09	18.86 ± 0.11	–	1
J1250+3130	23.37 ± 0.29	19.95 ± 0.03	20.35 ± 0.09	19.11 ± 0.07	18.71 ± 0.09	–	1
J1257+6349	22.90 ± 0.31	20.83 ± 0.08	20.43 ± 0.17	19.61 ± 0.08	19.86 ± 0.19	–	0
J1306+0356	22.65 ± 0.20	20.01 ± 0.04	20.10 ± 0.07	19.57 ± 0.10	–	17.45 ± 0.37	1
J1319+0950	22.91 ± 0.17	20.14 ± 0.03	19.85 ± 0.05	19.73 ± 0.11	19.65 ± 0.21	–	1
J1335+3533	> 23.36	20.25 ± 0.02	20.06 ± 0.07	19.41 ± 0.07	19.33 ± 0.13	–	1
P209–26	21.90 ± 0.14	19.41 ± 0.02	19.52 ± 0.04	–	–	–	1
P210+40	> 23.66	21.02 ± 0.06	21.02 ± 0.13	–	–	–	1
P210+09	22.95 ± 0.20	20.39 ± 0.03	20.36 ± 0.09	19.98 ± 0.12	20.09 ± 0.29	–	1
P210–12	> 23.24	21.18 ± 0.07	21.19 ± 0.17	–	19.93 ± 0.29	–	1
J1411+1217	23.50 ± 0.29	19.64 ± 0.02	20.12 ± 0.07	19.29 ± 0.07	18.87 ± 0.09	–	1
P213–22	22.84 ± 0.23	19.63 ± 0.02	19.98 ± 0.08	19.46 ± 0.17	18.97 ± 0.19	17.40 ± 0.42	1
P215–16	21.74 ± 0.07	19.17 ± 0.02	19.34 ± 0.06	18.27 ± 0.05	18.12 ± 0.07	–	1
J1425+3254	22.88 ± 0.17	20.43 ± 0.04	20.38 ± 0.10	19.67 ± 0.08	19.66 ± 0.16	–	1
J1427+3522	21.96 ± 0.07	21.40 ± 0.08	21.89 ± 0.29	20.09 ± 0.12	19.92 ± 0.22	–	0
J1427+3312	–	–	–	19.52 ± 0.08	19.26 ± 0.12	–	0
P217–16	23.07 ± 0.27	20.61 ± 0.04	19.92 ± 0.07	–	–	–	2
J1429+5447	–	–	–	19.73 ± 0.08	20.49 ± 0.32	–	0
J1436+5007	22.77 ± 0.18	20.17 ± 0.04	20.22 ± 0.06	19.87 ± 0.09	20.30 ± 0.25	–	1
J1509–1749	> 22.37	20.11 ± 0.03	19.70 ± 0.06	–	–	–	1
P228+21	> 23.23	20.97 ± 0.06	20.65 ± 0.11	–	–	–	1

Table A.2 (cont'd)

Quasar	$i_{\rm P1}$ mag	$z_{\rm P1}$ mag	$y_{\rm P1}$ mag	$W1$ mag	$W2$ mag	$W3$ mag	PS1 [a]
P231–20	> 23.11	> 22.58	20.06 ± 0.07	19.91 ± 0.15	19.96 ± 0.35	–	3
P235+17	22.77 ± 0.15	20.28 ± 0.03	20.24 ± 0.08	19.49 ± 0.08	19.85 ± 0.24	17.52 ± 0.31	1
P236+16	> 23.47	20.71 ± 0.05	20.87 ± 0.11	–	–	–	1
J1545+6028	21.38 ± 0.06	18.91 ± 0.02	19.15 ± 0.05	18.71 ± 0.04	18.50 ± 0.05	17.49 ± 0.23	1
J1602+4228	22.54 ± 0.12	20.10 ± 0.03	19.84 ± 0.05	18.75 ± 0.04	18.46 ± 0.06	17.54 ± 0.26	1
J1603+5510	–	–	–	–	–	–	0
J1609+3041	> 23.79	20.98 ± 0.07	20.49 ± 0.09	20.22 ± 0.14	20.42 ± 0.35	–	1
P242–12	23.14 ± 0.29	20.20 ± 0.04	20.19 ± 0.12	19.00 ± 0.07	19.44 ± 0.23	17.04 ± 0.32	1
J1621+5155	21.97 ± 0.09	20.02 ± 0.03	19.84 ± 0.05	18.35 ± 0.03	18.11 ± 0.04	18.06 ± 0.32	0
J1623+3112	23.40 ± 0.35	20.07 ± 0.04	20.27 ± 0.10	19.22 ± 0.06	19.00 ± 0.10	–	1
J1630+4012	22.86 ± 0.18	20.50 ± 0.04	20.63 ± 0.11	20.19 ± 0.12	–	–	1
J1641+3755	> 23.71	21.38 ± 0.08	21.11 ± 0.17	–	20.85 ± 0.36	–	1
P267+22	> 23.77	21.06 ± 0.07	21.15 ± 0.14	–	–	–	1
P308–21	> 23.51	21.16 ± 0.08	20.58 ± 0.12	19.20 ± 0.09	18.78 ± 0.13	–	2
P308–27	22.30 ± 0.13	19.78 ± 0.02	19.95 ± 0.08	19.63 ± 0.12	19.37 ± 0.22	–	1
J2053+0047	–	–	–	20.82 ± 0.32	–	–	0
J2054–0005	> 23.79	21.09 ± 0.08	20.67 ± 0.13	–	–	–	1
J2100–1715	> 23.75	21.62 ± 0.10	21.30 ± 0.21	–	–	–	1
P319–10	23.10 ± 0.24	20.01 ± 0.02	20.10 ± 0.06	18.84 ± 0.07	18.58 ± 0.11	–	1
P320–24	23.21 ± 0.25	20.17 ± 0.04	20.41 ± 0.14	19.85 ± 0.15	19.82 ± 0.34	–	1
J2147+0107	–	21.53 ± 0.10	–	20.33 ± 0.20	–	–	0
J2219+0102	–	–	–	–	–	–	0
J2220–0101	–	–	–	–	–	–	0
J2228+0110	–	–	–	–	–	–	0
J2229+1457	–	21.89 ± 0.13	–	–	–	–	0
P338+29	> 23.45	> 22.67	20.31 ± 0.09	20.51 ± 0.21	–	–	3
P340–18	> 23.43	20.20 ± 0.03	20.42 ± 0.10	19.26 ± 0.09	18.87 ± 0.13	–	1
J2242+0334	–	–	–	–	–	–	0
J2307+0031	–	21.77 ± 0.13	–	19.78 ± 0.13	19.61 ± 0.25	–	0
J2310+1855	21.80 ± 0.08	19.72 ± 0.03	19.08 ± 0.03	18.50 ± 0.05	18.75 ± 0.12	–	0
J2315–0023	–	21.01 ± 0.06	–	20.26 ± 0.20	–	–	0
J2318–0246	–	22.16 ± 0.18	–	–	–	–	0
J2329–0301	–	22.13 ± 0.21	–	–	–	–	0
J2329–0403	–	21.33 ± 0.11	–	–	–	–	0
J2348–3054	–	–	–	20.37 ± 0.17	–	–	0
P359–06	23.26 ± 0.30	19.97 ± 0.03	20.10 ± 0.11	19.26 ± 0.10	19.04 ± 0.19	–	1
J2356+0023	–	22.16 ± 0.23	–	–	–	–	0

Note. — Quasars sorted by right ascension, their full names, coordinates, and redshifts are given in Table A.1. *WISE* magnitudes are reported when their measurements have S/N> 2.5. They are taken from the main ALLWISE source catalog with some exceptions. The magnitudes of J0033–0125, J0109–3040, J0221–0802, J0227–0605, J0239–0045, P055–00, P167–13, J1148+5253, P210–12, J1641+3755, and J2053+0047 are taken from the ALLWISE reject table. The magnitdues of P215–16 are taken from the *WISE* All-Sky data release catalog.

[a] PS1 criteria: 0=None; 1=Criteria of Section 2.2.1.1; 2=Criteria of Section 2.2.1.2; 3=Criteria of Section 2.2.1.3; 4=Extended PS1 criteria.

Appendix B

Pan-STARRS1 low-quality flags

Here we present Table B.1, containing the PS1 flags used to exclude candidates in our quasar selection.

Table B.1: Pan-STARRS1 bit-flags used to exclude bad or low-quality detections.

FLAG1 NAME	Hex Value	Description
FITFAIL	0x00000008	Fit (nonlinear) failed (non-converge, off-edge, run to zero)
POORFIT	0x00000010	Fit succeeds, but low-SN or high-Chisq
PAIR	0x00000020	Source fitted with a double psf
SATSTAR	0x00000080	Source model peak is above saturation
BLEND	0x00000100	Source is a blend with other sources
BADPSF	0x00000400	Failed to get good estimate of object's PSF
DEFECT	0x00000800	Source is thought to be a defect
SATURATED	0x00001000	Source is thought to be saturated pixels (bleed trail)
CR_LIMIT	0x00002000	Source has crNsigma above limit
EXT_LIMIT	0x00004000	Source has extNsigma above limit
MOMENTS_FAILURE	0x00008000	Could not measure the moments
SKY_FAILURE	0x00010000	Could not measure the local sky
SKYVAR_FAILURE	0x00020000	Could not measure the local sky variance
MOMENTS_SN	0x00040000	Moments not measured due to low S/N
BLEND_FIT	0x00400000	Source was fitted as a blend
SIZE_SKIPPED	0x10000000	Size could not be determined
ON_SPIKE	0x20000000	Peak lands on diffraction spike
ON_GHOST	0x40000000	Peak lands on ghost or glint
OFF_CHIP	0x80000000	Peak lands off edge of chip
FLAG2 NAME	**Hex Value**	**Description**
ON_SPIKE	0x00000008	> 25% of pixels land on diffraction spike
ON_STARCORE	0x00000010	> 25% of pixels land on star core
ON_BURNTOOL	0x00000020	> 25%of pixels land on burntool subtraction region

Appendix C

Submillimeter observations of PSO J340.2041–18.6621

The far-infrared (FIR) emission traces the warm dust emission from quasar host galaxies and allows us to estimate their star formation rates. Studies from $z \sim 6$ quasars have shown that $\sim$ 30% of these quasars are bright at millimeter and submillimeter wavelengths (e.g., Wang et al. 2008). With this in mind, we took 870 μm (345 GHz) observations of the $z = 6.0$ quasar PSO J340.2041–18.6621 using the Large APEX Bolometer Camera (LABOCA; Siringo et al. 2009) on the 12 m APEX telescope (Güsten et al. 2006). The observations were carried out during 2012 November for a total of 14.5 hr. The quasar was observed mainly in the afternoon or early evening in mediocre to poor weather conditions. The data were reduced using the standard procedures implemented in the BoA software (Schuller 2012). The quasar remained undetected in the map with an rms noise of 1.6 mJy at the quasar position. In the same map, however, we detected a tentative 4.7σ submillimeter source. Its coordinates are R.A.= 22:40:59.407 and Decl.=-18:39:34.94. It is located at a distance of $\sim 2.'5$ from PSO J340.2041–18.6621 and we did not find an evident optical counterpart. The 870 μm flux of this serendipitous source is 9.50 ± 2.02 mJy. Figure C.1 shows the 870 μm 1 σ-contours overlaid over the GROND $J_{\rm G}$ image.

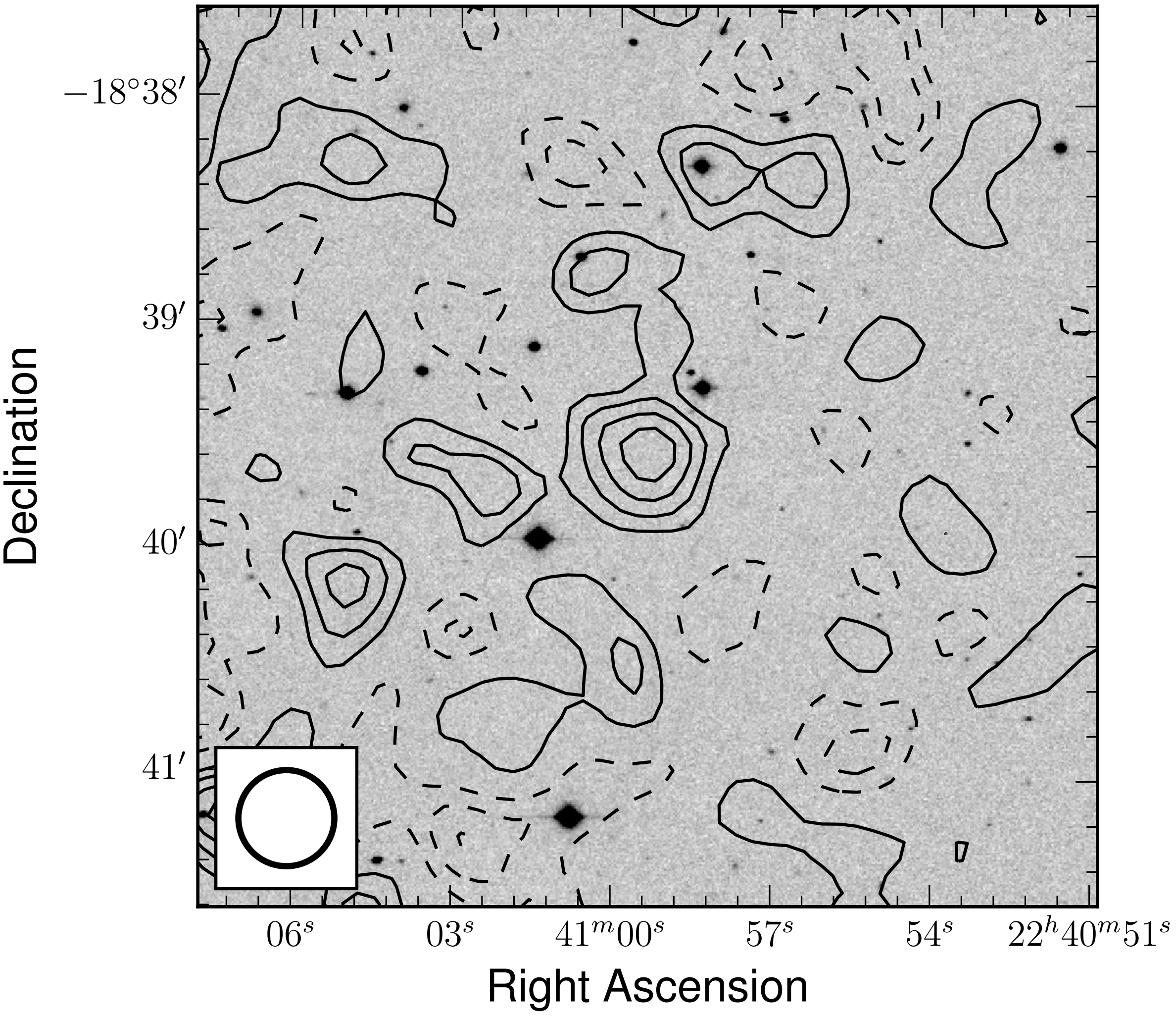

Figure C.1: Image centered on the serendipitous $870\,\mu$m source at a distance of 2.′5 from the $z = 6.0$ quasar PSO J340.2041–18.6621 (outside the image). The solid (dashed) lines are the positive (negative) 1σ-contours overlaid over the $J_{\rm G}$ image. The detection is 9.50 ± 2.02 mJy. There is no evident optical counterpart. The LABOCA beam size of 18.″2 × 18.″2 is shown in the bottom left panel.

Acknowledgements

I wish I could acknowledge everyone who has accompanied me during this long journey, that goes beyond this almost four years of PhD, but I would probably have needed hundred pages more. My sincere apologies if your name is not in the (very incomplete) list below ...

I would like to start thanking Fabian Walter and Bram Venemans, without their supervision, experience, and support this thesis would just had been impossible. I am very much thankful to the *team quasars*: Fabian Walter, Bram Venemans, Roberto Decarli, Emanuele Farina, Chiara Mazzucchelli, Eric Morganson. The day-to-day discussions and our meetings have been extremely important for the success of this thesis—I have learned a lot from all you guys!

I want to thank my referees, Hans-Walter Rix and Jochen Heidt, who were also part of my thesis committee. Their advice and thoughtful suggestions have been important for this work.

Over the course of my PhD I have been lucky enough to travel and meet great people. In particular, I am fortunate to have met Xiaohui Fan and Daniel Stern. They have provided me with insightful comments and ideas, some of which motivated part of this and future work.

I really do not have words for all the people that had made my stay in Heidelberg unforgettable and one of the best experiences of my life. You all know who you are, just to name a few: Alberto, Anahí, Agnese, Elena, Fabrizio, Ilya, Lucy, la tripleta de Mauricios, Mike, Mirko, Salvo ...

I am grateful to Mauricio Carrasco, Nina Hernitschek, Lucy Maxton, Mauricio Ortiz, and Gabor Worseck for taking the time to read parts of my thesis. All of their suggestions have incredibly improved the presentation and quality of this work.

Obviamente no puedo olvidar a mi familia, quienes siempre me han dado su amor y apoyo incondicional. Sin duda alguna, sin ellos no podría haber llegado a donde estoy.

Abbreviations and Acronyms

2MASS	Two Micron All Sky Survey
ACS	Advanced Camera for Surveys
AGN	Active galactic nucleus
ALMA	Atacama Large Millimeter Array
APEX	The Atacama Pathfinder EXperiment
CFHQS	Canada-France High-z Quasar Survey
CMB	Cosmic Microwave Background
DBSP	The Double Spectrograph for the Palomar 200-inch Telescope
E-ELT	European Extremely Large Telescope
EFOSC2	ESO Faint Object Spectrograph and Camera 2
ESO	European Southern Observatories
EoR	Epoch of Reionization
EW	Equivalent width
ESA	European Space Agency
FIR	Far-infrared
FIRE	Folded-port InfraRed Echellette
FIRST	Faint Images of the Radio Sky at Twenty cm survey
FORS2	FOcal Reducer/low dispersion Spectrograph 2
FoV	Field-of-view

HSC	Hyper-Suprime Cam
IAU	International Astronomical Union
IGM	Intergalactic medium
GMT	Giant Magellan Telescope
GOODS	Great Observatories Origins Deep Survey
GRB	Gamma-ray burst
GROND	Gamma-Ray Burst Optical Near-Infrared Detector
HST	Hubble Space Telescope
IPP	Image Processing Pipeline
IR	Infrared
IRAC	The Infrared Array Camera for the Spitzer Space Telescope
IRAM	Institute de Radioastronomie Millimétrique
JWST	James Webb Space Telescope
LABOCA	The Large APEX BOlometer CAmera
LAE	Lyman-α Emitter
LAS	Large Area Survey
LBG	Lyman Break Galaxy
LBT	Large Binocular Telescope
LIRG	Luminous Infrared Galaxy
LRIS	Low Resolution Imaging Spectrometer
LSST	Large Synoptic Survey Telescope
MODS	Multi-Object Double Spectrograph
MPG	Max Planck Gesellschaft
NASA	National Aeronautics and Space Administration
NOEMA	NOrthern Extended Millimeter Array
NTT	The ESO New Technology Telescope
Pan-STARRS1	Panoramic Survey Telescope & Rapid Response System 1
PS1	

PdBI	Plateu de Bure interferometer
PSF	Point-spread function
RLF	Radio-loud fraction
SDF	Subaru Deep Field
SDSS	Sloan Digital Sky Survey
SFR	Star formation rate
SMBH	Supermassive black hole
SoFI	The infrared spectrograph and imaging camera Son of ISAAC
TIR	Total infrared
TMT	Thirty Meter Telescope
UKIDSS	UK infrared Telescope Infrared Deep Sky Survey
UHS	UKIRT Hemisphere Survey
ULIRG	Ultra Luminous Infrared Galaxy
UV	Ultraviolet
VHS	VISTA Hemisphere Survey
VIKING	Visible and Infrared Survey Telescope Kilo-Degree Infrared Galaxy
VISTA	Visible and Infrared Survey Telescope for Astronomy
VLA	Very Large Array
VLT	Very Large Telescope
WFIRST	Wide-Field Infrared Survey Telescope
WISE	Wide-field Infrared Survey

Bibliography

Abazajian, K. N., Adelman-McCarthy, J. K., Agüeros, M. A., et al. 2009, ApJS, 182, 543

Aberasturi, M., Solano, E., & Martín, E. L. 2011, A&A, 534, L7

Ajiki, M., Taniguchi, Y., Murayama, T., et al. 2006, PASJ, 58, 499

Albert, L., Artigau, É., Delorme, P., et al. 2011, AJ, 141, 203

Alexander, T., & Natarajan, P. 2014, Science, 345, 1330

Angulo, R. E., Springel, V., White, S. D. M., et al. 2012, MNRAS, 425, 2722

Antonucci, R. 1993, ARA&A, 31, 473

Appenzeller, I., & Rupprecht, G. 1992, The Messenger, 67, 18

Arp, H. C., Bolton, J. G., & Kinman, T. D. 1967, ApJ, 147, 840

Artigau, É., Doyon, R., Lafrenière, D., et al. 2006, ApJ, 651, L57

Artigau, É., Lafrenière, D., Doyon, R., et al. 2011, ApJ, 739, 48

Bañados, E., Decarli, R., Walter, F., et al. 2015a, ArXiv e-prints, arXiv:1504.05216

Bañados, E., Venemans, B., Walter, F., et al. 2013, ApJ, 773, 178

Bañados, E., Venemans, B. P., Morganson, E., et al. 2014, AJ, 148, 14

—. 2015b, The Astrophysical Journal, 804, 118

Bailer-Jones, C. A., Bizenberger, P., & Storz, C. 2000, in Society of Photo-Optical Instrumentation Engineers (SPIE) Conference Series, Vol. 4008, Optical and IR Telescope Instrumentation and Detectors, ed. M. Iye & A. F. Moorwood, 1305–1316

Barnett, R., Warren, S. J., Banerji, M., et al. 2015, A&A, 575, A31

Barrado y Navascués, D., Zapatero Osorio, M. R., Martín, E. L., et al. 2002, A&A, 393, L85

Beamín, J. C., Minniti, D., Gromadzki, M., et al. 2013, A&A, 557, L8

Becerra, F., Greif, T. H., Springel, V., & Hernquist, L. E. 2015, MNRAS, 446, 2380

Becker, G. D., Bolton, J. S., Madau, P., et al. 2015, MNRAS, 447, 3402

Becker, R. H., White, R. L., & Helfand, D. J. 1995, ApJ, 450, 559

Bennett, C. L. 2006, Nature, 440, 1126

Bennett, C. L., Banday, A. J., Gorski, K. M., et al. 1996, ApJ, 464, L1

Bennett, C. L., Larson, D., Weiland, J. L., et al. 2013, ApJS, 208, 20

Berger, E., Zauderer, B. A., Chary, R.-R., et al. 2014, ApJ, 796, 96

Bertin, E., & Arnouts, S. 1996, A&AS, 117, 393

Bertoldi, F., Carilli, C. L., Cox, P., et al. 2003a, A&A, 406, L55

Bertoldi, F., Cox, P., Neri, R., et al. 2003b, A&A, 409, L47

Best, W. M. J., Liu, M. C., Magnier, E. A., et al. 2013, ApJ, 777, 84

Bialy, S., Sternberg, A., & Loeb, A. 2015, ArXiv e-prints, arXiv:1503.03475

Bihain, G., Scholz, R.-D., Storm, J., & Schnurr, O. 2013, A&A, 557, A43

Bizenberger, P., McCaughrean, M. J., Birk, C., Thompson, D., & Storz, C. 1998, in Society of Photo-Optical Instrumentation Engineers (SPIE) Conference Series, Vol. 3354, Society of Photo-Optical Instrumentation Engineers (SPIE) Conference Series, ed. A. M. Fowler, 825–832

Blain, A. W., Assef, R., Stern, D., et al. 2013, ApJ, 778, 113

Bolton, J. S., Haehnelt, M. G., Warren, S. J., et al. 2011, MNRAS, 416, L70

Boudreault, S., & Lodieu, N. 2013, MNRAS, 434, 142

Bouvier, J., Kendall, T., & Meeus, G. 2009, in American Institute of Physics Conference Series, Vol. 1094, 15th Cambridge Workshop on Cool Stars, Stellar Systems, and the Sun, ed. E. Stempels, 497–500

Bouwens, R. J., Illingworth, G. D., Oesch, P. A., et al. 2015a, ArXiv e-prints, arXiv:1503.08228

—. 2015b, ApJ, 803, 34

Bowler, B. P., Liu, M. C., & Dupuy, T. J. 2010, ApJ, 710, 45

Brisbin, D., Ferkinhoff, C., Nikola, T., et al. 2015, ApJ, 799, 13

Brocklehurst, M. 1971, MNRAS, 153, 471

Bruns, L. R., Wyithe, J. S. B., Bland-Hawthorn, J., & Dijkstra, M. 2012, MNRAS, 421, 2543

Burgasser, A. J., Kirkpatrick, J. D., Brown, M. E., et al. 2002, ApJ, 564, 421

Burningham, B., Pinfield, D. J., Lucas, P. W., et al. 2010, MNRAS, 406, 1885

Burningham, B., Cardoso, C. V., Smith, L., et al. 2013, MNRAS, 433, 457

Buzzoni, B., Delabre, B., Dekker, H., et al. 1984, The Messenger, 38, 9

Calura, F., Gilli, R., Vignali, C., et al. 2014, MNRAS, 438, 2765

Calzetti, D., Armus, L., Bohlin, R. C., et al. 2000, ApJ, 533, 682

Cantalupo, S., Lilly, S. J., & Haehnelt, M. G. 2012, MNRAS, 425, 1992

Cao, H.-M., Frey, S., Gurvits, L. I., et al. 2014, A&A, 563, A111

Capak, P. L., Riechers, D., Scoville, N. Z., et al. 2011, Nature, 470, 233

Carilli, C. L., Furlanetto, S., Briggs, F., et al. 2004a, NewAR, 48, 1029

Carilli, C. L., Gnedin, N. Y., & Owen, F. 2002, ApJ, 577, 22

Carilli, C. L., & Walter, F. 2013, ARA&A, 51, 105

Carilli, C. L., Walter, F., Bertoldi, F., et al. 2004b, AJ, 128, 997

Carilli, C. L., Neri, R., Wang, R., et al. 2007, ApJ, 666, L9

Carilli, C. L., Wang, R., Fan, X., et al. 2010, ApJ, 714, 834

Carnall, A. C., Shanks, T., Chehade, B., et al. 2015, ArXiv e-prints, arXiv:1502.07748

Castro, P. J., Gizis, J. E., Harris, H. C., et al. 2013, ApJ, 776, 126

Chiu, K., Fan, X., Leggett, S. K., et al. 2006, AJ, 131, 2722

Chiu, K., Liu, M. C., Jiang, L., et al. 2008, MNRAS, 385, L53

Chornock, R., Berger, E., Fox, D. B., et al. 2013, ApJ, 774, 26

Cirasuolo, M., Magliocchetti, M., Celotti, A., & Danese, L. 2003, MNRAS, 341, 993

Coe, D., Zitrin, A., Carrasco, M., et al. 2013, ApJ, 762, 32

Combes, F., Rex, M., Rawle, T. D., et al. 2012, A&A, 538, L4

Cool, R. J., Kochanek, C. S., Eisenstein, D. J., et al. 2006, AJ, 132, 823

Costa, T., Sijacki, D., Trenti, M., & Haehnelt, M. G. 2014, MNRAS, 439, 2146

Cruz, K. L., Reid, I. N., Liebert, J., Kirkpatrick, J. D., & Lowrance, P. J. 2003, AJ, 126, 2421

Cruz, K. L., Reid, I. N., Kirkpatrick, J. D., et al. 2007, AJ, 133, 439

Cucchiara, A., Levan, A. J., Fox, D. B., et al. 2011, ApJ, 736, 7

Cushing, M. C., Kirkpatrick, J. D., Gelino, C. R., et al. 2014, AJ, 147, 113

Cutri, R. M., e. 2012, VizieR Online Data Catalog, 2311, 0

—. 2014, VizieR Online Data Catalog, 2328, 0

Day-Jones, A. C., Marocco, F., Pinfield, D. J., et al. 2013, MNRAS, 430, 1171

De Looze, I., Cormier, D., Lebouteiller, V., et al. 2014, A&A, 568, A62

De Lucia, G., & Blaizot, J. 2007, MNRAS, 375, 2

De Rosa, G., Decarli, R., Walter, F., et al. 2011, ApJ, 739, 56

De Rosa, G., Venemans, B. P., Decarli, R., et al. 2014, ApJ, 790, 145

Deacon, N. R., Liu, M. C., Magnier, E. A., et al. 2011, AJ, 142, 77

—. 2012, ApJ, 755, 94

Decarli, R., Falomo, R., Treves, A., et al. 2010, MNRAS, 402, 2441

Decarli, R., Walter, F., Yang, Y., et al. 2012, ApJ, 756, 150

Di Matteo, T., Khandai, N., DeGraf, C., et al. 2012, ApJ, 745, L29

Diamond-Stanic, A. M., Fan, X., Brandt, W. N., et al. 2009, ApJ, 699, 782

Díaz-Santos, T., Armus, L., Charmandaris, V., et al. 2013, ApJ, 774, 68

Donoso, E., Li, C., Kauffmann, G., Best, P. N., & Heckman, T. M. 2010, MNRAS, 407, 1078

Dressler, A., Henry, A., Martin, C. L., et al. 2014, ArXiv e-prints, arXiv:1412.0655

Dunlop, J. S. 2013, in Astrophysics and Space Science Library, Vol. 396, Astrophysics and Space Science Library, ed. T. Wiklind, B. Mobasher, & V. Bromm, 223

Dunlop, J. S., McLure, R. J., Robertson, B. E., et al. 2012, MNRAS, 420, 901

Edge, D. O., Shakeshaft, J. R., McAdam, W. B., Baldwin, J. E., & Archer, S. 1959, MmRAS, 68, 37

Ellis, R. S. 2014, ArXiv e-prints, arXiv:1411.3330

Falcke, H., Sherwood, W., & Patnaik, A. R. 1996, ApJ, 471, 106

Fan, X. 2012, Research in Astronomy and Astrophysics, 12, 865

Fan, X., Carilli, C. L., & Keating, B. 2006a, ARA&A, 44, 415

Fan, X., Knapp, G. R., Strauss, M. A., et al. 2000a, AJ, 119, 928

Fan, X., White, R. L., Davis, M., et al. 2000b, AJ, 120, 1167

Fan, X., Narayanan, V. K., Lupton, R. H., et al. 2001, AJ, 122, 2833

Fan, X., Strauss, M. A., Schneider, D. P., et al. 2003, AJ, 125, 1649

Fan, X., Hennawi, J. F., Richards, G. T., et al. 2004, AJ, 128, 515

Fan, X., Strauss, M. A., Richards, G. T., et al. 2006b, AJ, 131, 1203

Fan, X., Strauss, M. A., Becker, R. H., et al. 2006c, AJ, 132, 117

Fanidakis, N., Baugh, C. M., Benson, A. J., et al. 2011, MNRAS, 410, 53

Fanidakis, N., Macciò, A. V., Baugh, C. M., Lacey, C. G., & Frenk, C. S. 2013a, MNRAS, 436, 315

Fanidakis, N., Baugh, C. M., Benson, A. J., et al. 2012, MNRAS, 419, 2797

Fanidakis, N., Georgakakis, A., Mountrichas, G., et al. 2013b, MNRAS, 435, 679

Fazio, G. G., Hora, J. L., Allen, L. E., et al. 2004, ApJS, 154, 10

Francis, P. J., & Bland-Hawthorn, J. 2004, MNRAS, 353, 301

Francis, P. J., Hewett, P. C., Foltz, C. B., et al. 1991, ApJ, 373, 465

Frey, S., Gurvits, L. I., Paragi, Z., & É. Gabányi, K. 2008, A&A, 484, L39

Frey, S., Paragi, Z., Gurvits, L. I., Gabányi, K. É., & Cseh, D. 2011, A&A, 531, L5

Frey, S., Paragi, Z., Mosoni, L., & Gurvits, L. I. 2005, A&A, 436, L13

Furlanetto, S. R., Oh, S. P., & Briggs, F. H. 2006, Phys. Rep., 433, 181

Geballe, T. R., Knapp, G. R., Leggett, S. K., et al. 2002, ApJ, 564, 466

Geißler, K., Metchev, S., Kirkpatrick, J. D., Berriman, G. B., & Looper, D. 2011, ApJ, 732, 56

George, E. M., Reichardt, C. L., Aird, K. A., et al. 2015, ApJ, 799, 177

Giallongo, E., Grazian, A., Fiore, F., et al. 2015, ArXiv e-prints, arXiv:1502.02562

Gizis, J. E., Burgasser, A. J., Faherty, J. K., Castro, P. J., & Shara, M. M. 2011a, AJ, 142, 171

Gizis, J. E., Kirkpatrick, J. D., & Wilson, J. C. 2001, AJ, 121, 2185

Gizis, J. E., Troup, N. W., & Burgasser, A. J. 2011b, ApJ, 736, L34

Gizis, J. E., Faherty, J. K., Liu, M. C., et al. 2012, AJ, 144, 94

Glikman, E., Djorgovski, S. G., Stern, D., et al. 2011, ApJ, 728, L26

Glover, S. 2015, ArXiv e-prints, arXiv:1501.05960

Goldschmidt, P., Kukula, M. J., Miller, L., & Dunlop, J. S. 1999, ApJ, 511, 612

Gomes, J. I., Pinfield, D. J., Marocco, F., et al. 2013, MNRAS, 431, 2745

González-Alfonso, E., Fischer, J., Aalto, S., & Falstad, N. 2014, A&A, 567, A91

González-López, J., Riechers, D. A., Decarli, R., et al. 2014, ApJ, 784, 99

Goto, T. 2006, MNRAS, 371, 769

Graciá-Carpio, J., Sturm, E., Hailey-Dunsheath, S., et al. 2011, ApJ, 728, L7

Greenstein, J. L., & Matthews, T. A. 1963, AJ, 68, 279

Greenstein, J. L., & Schmidt, M. 1964, ApJ, 140, 1

Greiner, J., Bornemann, W., Clemens, C., et al. 2008, PASP, 120, 405

Guilloteau, S., & Lucas, R. 2000, in Astronomical Society of the Pacific Conference Series, Vol. 217, Imaging at Radio through Submillimeter Wavelengths, ed. J. G. Mangum & S. J. E. Radford, 299

Gunn, J. E., & Peterson, B. A. 1965, ApJ, 142, 1633

Güsten, R., Nyman, L. Å., Schilke, P., et al. 2006, A&A, 454, L13

Haardt, F., & Salvaterra, R. 2015, A&A, 575, L16

Hamuy, M., Suntzeff, N. B., Heathcote, S. R., et al. 1994, PASP, 106, 566

Hamuy, M., Walker, A. R., Suntzeff, N. B., et al. 1992, PASP, 104, 533

Hao, H., Sargent, M. T., Elvis, M., et al. 2014, ArXiv e-prints, arXiv:1408.1090

Hatch, N. A., Wylezalek, D., Kurk, J. D., et al. 2014, MNRAS, 445, 280

Hawley, S. L., Covey, K. R., Knapp, G. R., et al. 2002, AJ, 123, 3409

Hazard, C., Jauncey, D., Goss, W. M., & Herald, D. 2015, in IAU Symposium, Vol. 313, IAU Symposium, ed. F. Massaro, C. C. Cheung, E. Lopez, & A. Siemiginowska, 183–189

Hazard, C., Mackey, M. B., & Shimmins, A. J. 1963, Nature, 197, 1037

Hennawi, J. F., Prochaska, J. X., Burles, S., et al. 2006, ApJ, 651, 61

Hinshaw, G., Larson, D., Komatsu, E., et al. 2013, ApJS, 208, 19

Hodge, J. A., Becker, R. H., White, R. L., Richards, G. T., & Zeimann, G. R. 2011, AJ, 142, 3

Hogg, D. W. 1999, ArXiv Astrophysics e-prints, astro-ph/9905116

Hooper, E. J., Impey, C. D., Foltz, C. B., & Hewett, P. C. 1995, ApJ, 445, 62

Hu, E. M., Cowie, L. L., Barger, A. J., et al. 2010, ApJ, 725, 394

Hu, E. M., Cowie, L. L., McMahon, R. G., et al. 2002, ApJ, 568, L75

Hu, E. M., McMahon, R. G., & Cowie, L. L. 1999, ApJ, 522, L9

Husband, K., Bremer, M. N., Stanway, E. R., et al. 2013, MNRAS, 432, 2869

Ibar, E., Lara-López, M. A., Herrera-Camus, R., et al. 2015, MNRAS, 449, 2498

Ishigaki, M., Kawamata, R., Ouchi, M., et al. 2015, ApJ, 799, 12

Ivezić, Ž., Menou, K., Knapp, G. R., et al. 2002, AJ, 124, 2364

Ivezic, Z., Tyson, J. A., Abel, B., et al. 2008, ArXiv e-prints, arXiv:0805.2366

Jiang, L., Fan, X., Ivezić, Ž., et al. 2007a, ApJ, 656, 680

Jiang, L., Fan, X., Vestergaard, M., et al. 2007b, AJ, 134, 1150

Jiang, L., McGreer, I. D., Fan, X., et al. 2015, ArXiv e-prints, arXiv:1504.01741

Jiang, L., Fan, X., Annis, J., et al. 2008, AJ, 135, 1057

Jiang, L., Fan, X., Bian, F., et al. 2009, AJ, 138, 305

Jiang, L., Egami, E., Kashikawa, N., et al. 2011, ApJ, 743, 65

Jiang, L., Egami, E., Mechtley, M., et al. 2013, ApJ, 772, 99

Kaiser, N., Aussel, H., Burke, B. E., et al. 2002, in Society of Photo-Optical Instrumentation Engineers (SPIE) Conference Series, Vol. 4836, Society of Photo-Optical Instrumentation Engineers (SPIE) Conference Series, ed. J. A. Tyson & S. Wolff, 154–164

Kaiser, N., Burgett, W., Chambers, K., et al. 2010, in Society of Photo-Optical Instrumentation Engineers (SPIE) Conference Series, Vol. 7733, Society of Photo-Optical Instrumentation Engineers (SPIE) Conference Series

Kanekar, N., Wagg, J., Ram Chary, R., & Carilli, C. L. 2013, ApJ, 771, L20

Kaplan, E. L., & Meier, P. 1958, Journal of the American statistical association, 53, 457

Kashikawa, N., Kitayama, T., Doi, M., et al. 2007, ApJ, 663, 765

Kashikawa, N., Shimasaku, K., Yasuda, N., et al. 2004, PASJ, 56, 1011

Kashikawa, N., Ishizaki, Y., Willott, C. J., et al. 2015, ApJ, 798, 28

Kellermann, K. I. 2013, Bulletin of the Astronomical Society of India, 41, 1

Kellermann, K. I. 2015, in IAU Symposium, Vol. 313, IAU Symposium, ed. F. Massaro, C. C. Cheung, E. Lopez, & A. Siemiginowska, 190–195

Kellermann, K. I., Sramek, R., Schmidt, M., Shaffer, D. B., & Green, R. 1989, AJ, 98, 1195

Kendall, T. R., Delfosse, X., Martín, E. L., & Forveille, T. 2004, A&A, 416, L17

Kendall, T. R., Jones, H. R. A., Pinfield, D. J., et al. 2007a, MNRAS, 374, 445

Kendall, T. R., Mauron, N., Azzopardi, M., & Gigoyan, K. 2003, A&A, 403, 929

Kendall, T. R., Tamura, M., Tinney, C. G., et al. 2007b, A&A, 466, 1059

Kennicutt, Jr., R. C. 1998, ApJ, 498, 541

Kim, S., Stiavelli, M., Trenti, M., et al. 2009, ApJ, 695, 809

Kimball, A. E., Knapp, G. R., Ivezić, Ž., et al. 2009, ApJ, 701, 535

Kirkpatrick, J. D., Beichman, C. A., & Skrutskie, M. F. 1997, ApJ, 476, 311

Kirkpatrick, J. D., Reid, I. N., Liebert, J., et al. 1999, ApJ, 519, 802

—. 2000, AJ, 120, 447

Kirkpatrick, J. D., Looper, D. L., Burgasser, A. J., et al. 2010, ApJS, 190, 100

Kirkpatrick, J. D., Cushing, M. C., Gelino, C. R., et al. 2011, ApJS, 197, 19

Kirkpatrick, J. D., Schneider, A., Fajardo-Acosta, S., et al. 2014, ApJ, 783, 122

Knapp, G. R., Leggett, S. K., Fan, X., et al. 2004, AJ, 127, 3553

Konno, A., Ouchi, M., Ono, Y., et al. 2014, ApJ, 797, 16

Kratzer, R. M., & Richards, G. T. 2014, ArXiv e-prints, arXiv:1405.2344

Kurk, J. D., Walter, F., Fan, X., et al. 2009, ApJ, 702, 833

—. 2007, ApJ, 669, 32

La Franca, F., Gregorini, L., Cristiani, S., de Ruiter, H., & Owen, F. 1994, AJ, 108, 1548

Labbé, I., Franx, M., Rudnick, G., et al. 2003, AJ, 125, 1107

Lane, R. A., Shemmer, O., Diamond-Stanic, A. M., et al. 2011, ApJ, 743, 163

Laor, A. 2000, ApJ, 543, L111

Laor, A., & Davis, S. W. 2011, MNRAS, 417, 681

Laureijs, R., Hoar, J., Buenadicha3, G., et al. 2014, in Astronomical Society of the Pacific Conference Series, Vol. 485, Astronomical Data Analysis Software and Systems XXIII, ed. N. Manset & P. Forshay, 495

Laureijs, R., Amiaux, J., Arduini, S., et al. 2011, ArXiv e-prints, arXiv:1110.3193

Lawrence, A., Warren, S. J., Almaini, O., et al. 2007, MNRAS, 379, 1599

Leipski, C., Meisenheimer, K., Walter, F., et al. 2014, ApJ, 785, 154

Lépine, S., Rich, R. M., & Shara, M. M. 2003, ApJ, 591, L49

Liebert, J., & Gizis, J. E. 2006, PASP, 118, 659

Liu, M. C., Wainscoat, R., Martín, E. L., Barris, B., & Tonry, J. 2002, ApJ, 568, L107

Liu, M. C., Magnier, E. A., Deacon, N. R., et al. 2013, ApJ, 777, L20

Lodieu, N., Boudreault, S., & Béjar, V. J. S. 2014, MNRAS, 445, 3908

Lodieu, N., Espinoza Contreras, M., Zapatero Osorio, M. R., et al. 2012a, A&A, 542, A105

Lodieu, N., Pinfield, D. J., Leggett, S. K., et al. 2007, MNRAS, 379, 1423

Lodieu, N., Burningham, B., Day-Jones, A., et al. 2012b, A&A, 548, A53

Loeb, A., & Barkana, R. 2001, ARA&A, 39, 19

LSST Science Collaboration, Abell, P. A., Allison, J., et al. 2009, ArXiv e-prints, arXiv:0912.0201

Lucas, P. W., Tinney, C. G., Burningham, B., et al. 2010, MNRAS, 408, L56

Luhman, K. L., Loutrel, N. P., McCurdy, N. S., et al. 2012, ApJ, 760, 152

Luhman, M. L., Satyapal, S., Fischer, J., et al. 2003, ApJ, 594, 758

Mace, G. N., Kirkpatrick, J. D., Cushing, M. C., et al. 2013, ApJS, 205, 6

Magnier, E. 2006, in The Advanced Maui Optical and Space Surveillance Technologies Conference, ed. S. K. M. E. D. B. Ryan, E50

Magnier, E. 2007, in Astronomical Society of the Pacific Conference Series, Vol. 364, The Future of Photometric, Spectrophotometric and Polarimetric Standardization, ed. C. Sterken, 153

Mahabal, A., Stern, D., Bogosavljević, M., Djorgovski, S. G., & Thompson, D. 2005, ApJ, 634, L9

Mainzer, A., Grav, T., Bauer, J., et al. 2011a, ApJ, 743, 156

Mainzer, A., Cushing, M. C., Skrutskie, M., et al. 2011b, ApJ, 726, 30

Maiolino, R., Cox, P., Caselli, P., et al. 2005, A&A, 440, L51

Maiolino, R., Gallerani, S., Neri, R., et al. 2012, MNRAS, 425, L66

Maiolino, R., Carniani, S., Fontana, A., et al. 2015, ArXiv e-prints, arXiv:1502.06634

Malhotra, S., Kaufman, M. J., Hollenbach, D., et al. 2001, ApJ, 561, 766

Marocco, F., Andrei, A. H., Smart, R. L., et al. 2013, AJ, 146, 161

Marocco, F., Day-Jones, A. C., Lucas, P. W., et al. 2014, MNRAS, 439, 372

Marocco, F., Jones, H. R. A., Day-Jones, A. C., et al. 2015, MNRAS, 449, 3651

Martín, E. L., Basri, G., Zapatero-Osorio, M. R., Rebolo, R., & López, R. J. G. 1998, ApJ, 507, L41

Martín, E. L., Delfosse, X., Basri, G., et al. 1999, AJ, 118, 2466

Martín, E. L., Phan-Bao, N., Bessell, M., et al. 2010, A&A, 517, A53

Massey, P., & Gronwall, C. 1990, ApJ, 358, 344

Matsuoka, Y., Peterson, B. A., Murata, K. L., et al. 2011, AJ, 142, 64

McElwain, M. W., & Burgasser, A. J. 2006, AJ, 132, 2074

McGreer, I. D., Becker, R. H., Helfand, D. J., & White, R. L. 2006, ApJ, 652, 157

McGreer, I. D., Helfand, D. J., & White, R. L. 2009, AJ, 138, 1925

McGreer, I. D., Mesinger, A., & D'Odorico, V. 2015, MNRAS, 447, 499

McGreer, I. D., Jiang, L., Fan, X., et al. 2013, ApJ, 768, 105

McMahon, R. G., Banerji, M., Gonzalez, E., et al. 2013, The Messenger, 154, 35

Mechtley, M., Windhorst, R. A., Ryan, R. E., et al. 2012, ApJ, 756, L38

Meiksin, A. 2006, MNRAS, 365, 807

Metcalfe, N., Farrow, D. J., Cole, S., et al. 2013, MNRAS, 435, 1825

Metchev, S. A., Kirkpatrick, J. D., Berriman, G. B., & Looper, D. 2008, ApJ, 676, 1281

Michałowski, M. J. 2015, ArXiv e-prints, arXiv:1503.08210

Miller, L., Peacock, J. A., & Mead, A. R. G. 1990, MNRAS, 244, 207

Minkowski, R. 1960, ApJ, 132, 908

Momjian, E., Carilli, C. L., Walter, F., & Venemans, B. 2014, AJ, 147, 6

Moorwood, A., Cuby, J.-G., & Lidman, C. 1998, The Messenger, 91, 9

Morganson, E., De Rosa, G., Decarli, R., et al. 2012, AJ, 143, 142

Mortlock, D. J., Patel, M., Warren, S. J., et al. 2009, A&A, 505, 97

Mortlock, D. J., Warren, S. J., Venemans, B. P., et al. 2011, Nature, 474, 616

Nagao, T., Taniguchi, Y., Kashikawa, N., et al. 2004, ApJ, 613, L9

Nagao, T., Kashikawa, N., Malkan, M. A., et al. 2005, ApJ, 634, 142

Nagao, T., Murayama, T., Maiolino, R., et al. 2007, A&A, 468, 877

Oesch, P. A., Bouwens, R. J., Illingworth, G. D., et al. 2014, ApJ, 786, 108

Oesch, P. A., van Dokkum, P. G., Illingworth, G. D., et al. 2015, ArXiv e-prints, arXiv:1502.05399

Oke, J. B. 1990, AJ, 99, 1621

Oke, J. B., & Gunn, J. E. 1982, PASP, 94, 586

Oke, J. B., Cohen, J. G., Carr, M., et al. 1995, PASP, 107, 375

Omont, A., Willott, C. J., Beelen, A., et al. 2013a, A&A, 552, A43

Omont, A., Yang, C., Cox, P., et al. 2013b, A&A, 551, A115

Ota, K., Kashikawa, N., Malkan, M. A., et al. 2008, ArXiv e-prints, arXiv:0804.3448

Ota, K., Walter, F., Ohta, K., et al. 2014, ApJ, 792, 34

Ouchi, M., Shimasaku, K., Akiyama, M., et al. 2005, ApJ, 620, L1

—. 2008, ApJS, 176, 301

Ouchi, M., Ellis, R., Ono, Y., et al. 2013, ApJ, 778, 102

Overzier, R. A., Guo, Q., Kauffmann, G., et al. 2009, MNRAS, 394, 577

Padovani, P. 1993, MNRAS, 263, 461

Peacock, J. A., Miller, L., & Longair, M. S. 1986, MNRAS, 218, 265

Peebles, P. J. E. 1993, Principles of Physical Cosmology

Pentericci, L., Vanzella, E., Fontana, A., et al. 2014, ApJ, 793, 113

Penzias, A. A., & Wilson, R. W. 1965, ApJ, 142, 419

Phan-Bao, N., Bessell, M. S., Martín, E. L., et al. 2008, MNRAS, 383, 831

Pinfield, D. J., Burningham, B., Tamura, M., et al. 2008, MNRAS, 390, 304

Pirzkal, N., Coe, D., Frye, B. L., et al. 2015, ApJ, 804, 11

Planck Collaboration, Ade, P. A. R., Aghanim, N., et al. 2014, A&A, 571, A16

Planck Collaboration, Adam, R., Ade, P. A. R., et al. 2015a, ArXiv e-prints, arXiv:1502.05956

Planck Collaboration, Ade, P. A. R., Aghanim, N., et al. 2015b, ArXiv e-prints, arXiv:1502.01589

Pogge, R. W., Atwood, B., Brewer, D. F., et al. 2010, in Society of Photo-Optical Instrumentation Engineers (SPIE) Conference Series, Vol. 7735, Society of Photo-Optical Instrumentation Engineers (SPIE) Conference Series

Reed, S. L., McMahon, R. G., Banerji, M., et al. 2015, ArXiv e-prints, arXiv:1504.03264

Rees, M. J., Begelman, M. C., Blandford, R. D., & Phinney, E. S. 1982, Nature, 295, 17

Reid, I. N., Cruz, K. L., Kirkpatrick, J. D., et al. 2008, AJ, 136, 1290

Reylé, C., Delorme, P., Artigau, E., et al. 2014, A&A, 561, A66

Richards, G. T., Vanden Berk, D. E., Reichard, T. A., et al. 2002a, AJ, 124, 1

Richards, G. T., Fan, X., Newberg, H. J., et al. 2002b, AJ, 123, 2945

Richards, G. T., Lacy, M., Storrie-Lombardi, L. J., et al. 2006, ApJS, 166, 470

Riechers, D. A. 2013, ApJ, 765, L31

Riechers, D. A., Walter, F., Bertoldi, F., et al. 2009, ApJ, 703, 1338

Robertson, B. E., Ellis, R. S., Dunlop, J. S., McLure, R. J., & Stark, D. P. 2010, Nature, 468, 49

Robertson, B. E., Ellis, R. S., Furlanetto, S. R., & Dunlop, J. S. 2015, ApJ, 802, L19

Rojas-Ayala, B., Iglesias, D., Minniti, D., Saito, R. K., & Surot, F. 2014, A&A, 571, A36

Ross, N. P., Shen, Y., Strauss, M. A., et al. 2009, ApJ, 697, 1634

Ryan-Weber, E. V., Pettini, M., Madau, P., & Zych, B. J. 2009, MNRAS, 395, 1476

Ryden, B. 2003, Introduction to cosmology

Salvaterra, R. 2015, ArXiv e-prints, arXiv:1503.03072

Salvaterra, R., Della Valle, M., Campana, S., et al. 2009, Nature, 461, 1258

Sandage, A. 1965, ApJ, 141, 1560

Sargsyan, L., Samsonyan, A., Lebouteiller, V., et al. 2014, ApJ, 790, 15

Schaerer, D., Boone, F., Zamojski, M., et al. 2015, A&A, 574, A19

Schenker, M. A., Ellis, R. S., Konidaris, N. P., & Stark, D. P. 2014, ApJ, 795, 20

Schlafly, E. F., & Finkbeiner, D. P. 2011, ApJ, 737, 103

Schmidt, K. B., Treu, T., Trenti, M., et al. 2014, ApJ, 786, 57

Schmidt, M. 1963, Nature, 197, 1040

—. 1965, ApJ, 141, 1295

Schmidt, M., & Green, R. F. 1983, ApJ, 269, 352

Schmidt, S. J., West, A. A., Hawley, S. L., & Pineda, J. S. 2010, AJ, 139, 1808

Schneider, D. P., Knapp, G. R., Hawley, S. L., et al. 2002, AJ, 123, 458

Schneider, D. P., Hall, P. B., Richards, G. T., et al. 2007, AJ, 134, 102

Schneider, D. P., Richards, G. T., Hall, P. B., et al. 2010, AJ, 139, 2360

Schneider, P. 2015, Extragalactic Astronomy and Cosmology: An Introduction, doi:10.1007/978-3-642-54083-7

Scholz, R.-D. 2010a, A&A, 515, A92

—. 2010b, A&A, 510, L8

Scholz, R.-D., Bihain, G., Schnurr, O., & Storm, J. 2011, A&A, 532, L5

—. 2012, A&A, 541, A163

Scholz, R.-D., Storm, J., Knapp, G. R., & Zinnecker, H. 2009, A&A, 494, 949

Schuller, F. 2012, in Society of Photo-Optical Instrumentation Engineers (SPIE) Conference Series, Vol. 8452, Society of Photo-Optical Instrumentation Engineers (SPIE) Conference Series

Seifert, W., Appenzeller, I., Baumeister, H., et al. 2003, in Society of Photo-Optical Instrumentation Engineers (SPIE) Conference Series, Vol. 4841, Instrument Design and Performance for Optical/Infrared Ground-based Telescopes, ed. M. Iye & A. F. M. Moorwood, 962–973

Shapiro, S. L. 2005, ApJ, 620, 59

Shemmer, O., & Lieber, S. 2015, ArXiv e-prints, arXiv:1503.07547

Shemmer, O., Trakhtenbrot, B., Anderson, S. F., et al. 2010, ApJ, 722, L152

Sheppard, S. S., & Cushing, M. C. 2009, AJ, 137, 304

Shimasaku, K., Ouchi, M., Okamura, S., et al. 2003, ApJ, 586, L111

Sijacki, D., Springel, V., & Haehnelt, M. G. 2009, MNRAS, 400, 100

Simcoe, R. A., Sullivan, P. W., Cooksey, K. L., et al. 2012, Nature, 492, 79

Simcoe, R. A., Burgasser, A. J., Bernstein, R. A., et al. 2008, in Society of Photo-Optical Instrumentation Engineers (SPIE) Conference Series, Vol. 7014, Society of Photo-Optical Instrumentation Engineers (SPIE) Conference Series

Simcoe, R. A., Burgasser, A. J., Schechter, P. L., et al. 2013, PASP, 125, 270

Simpson, C., Mortlock, D., Warren, S., et al. 2014, MNRAS, 442, 3454

Siringo, G., Kreysa, E., Kovács, A., et al. 2009, A&A, 497, 945

Skrutskie, M. F., Cutri, R. M., Stiening, R., et al. 2006, AJ, 131, 1163

Spergel, D., Gehrels, N., Breckinridge, J., et al. 2013, ArXiv e-prints, arXiv:1305.5422

Spergel, D., Gehrels, N., Baltay, C., et al. 2015, ArXiv e-prints, arXiv:1503.03757

Springel, V., White, S. D. M., Jenkins, A., et al. 2005, Nature, 435, 629

Stacey, G. J., Hailey-Dunsheath, S., Ferkinhoff, C., et al. 2010, ApJ, 724, 957

Steidel, C. C., Giavalisco, M., Pettini, M., Dickinson, M., & Adelberger, K. L. 1996, ApJ, 462, L17

Stern, D., Djorgovski, S. G., Perley, R. A., de Carvalho, R. R., & Wall, J. V. 2000, AJ, 119, 1526

Stern, D., Kirkpatrick, J. D., Allen, L. E., et al. 2007, ApJ, 663, 677

Stiavelli, M., Djorgovski, S. G., Pavlovsky, C., et al. 2005, ApJ, 622, L1

Stubbs, C. W., Doherty, P., Cramer, C., et al. 2010, ApJS, 191, 376

Swinbank, J., Baker, J., Barr, J., Hook, I., & Bland-Hawthorn, J. 2012, MNRAS, 422, 2980

Tanvir, N. R., Fox, D. B., Levan, A. J., et al. 2009, Nature, 461, 1254

Tanvir, N. R., Levan, A. J., Fruchter, A. S., et al. 2012, ApJ, 754, 46

Thompson, M. A., Kirkpatrick, J. D., Mace, G. N., et al. 2013, PASP, 125, 809

Tinney, C. G., Burgasser, A. J., Kirkpatrick, J. D., & McElwain, M. W. 2005, AJ, 130, 2326

Tonry, J. L., Stubbs, C. W., Lykke, K. R., et al. 2012, ApJ, 750, 99

Toshikawa, J., Kashikawa, N., Ota, K., et al. 2012, ApJ, 750, 137

Trainor, R. F., & Steidel, C. C. 2012, ApJ, 752, 39

Trenti, M., Bradley, L. D., Stiavelli, M., et al. 2012, ApJ, 746, 55

Treu, T., Schmidt, K. B., Trenti, M., Bradley, L. D., & Stiavelli, M. 2013, ApJ, 775, L29

Urrutia, T., Becker, R. H., White, R. L., et al. 2009, ApJ, 698, 1095

Utsumi, Y., Goto, T., Kashikawa, N., et al. 2010, ApJ, 721, 1680

Valiante, R., Schneider, R., Salvadori, S., & Gallerani, S. 2014, MNRAS, 444, 2442

van der Werf, P. P., Berciano Alba, A., Spaans, M., et al. 2011, ApJ, 741, L38

Vanden Berk, D. E., Richards, G. T., Bauer, A., et al. 2001, AJ, 122, 549

Vanzella, E., Fontana, A., Pentericci, L., et al. 2014, A&A, 569, A78

Venemans, B. P., McMahon, R. G., Warren, S. J., et al. 2007a, MNRAS, 376, L76

Venemans, B. P., Röttgering, H. J. A., Miley, G. K., et al. 2007b, A&A, 461, 823

Venemans, B. P., McMahon, R. G., Walter, F., et al. 2012, ApJ, 751, L25

Venemans, B. P., Findlay, J. R., Sutherland, W. J., et al. 2013, ApJ, 779, 24

Venemans, B. P., Bañados, E., Decarli, R., et al. 2015, ApJ, 801, L11

Volonteri, M. 2010, A&A Rev., 18, 279

—. 2012, Science, 337, 544

Volonteri, M., & Bellovary, J. 2012, Reports on Progress in Physics, 75, 124901

Volonteri, M., & Rees, M. J. 2005, ApJ, 633, 624

—. 2006, ApJ, 650, 669

Wake, D. A., Whitaker, K. E., Labbé, I., et al. 2011, ApJ, 728, 46

Walter, F., Carilli, C., Bertoldi, F., et al. 2004, ApJ, 615, L17

Walter, F., Riechers, D., Cox, P., et al. 2009a, Nature, 457, 699

Walter, F., Weiß, A., Riechers, D. A., et al. 2009b, ApJ, 691, L1

Walter, F., Bertoldi, F., Carilli, C., et al. 2003, Nature, 424, 406

Walter, F., Decarli, R., Carilli, C., et al. 2012a, ApJ, 752, 93

—. 2012b, Nature, 486, 233

Wang, J.-M., Qiu, J., Du, P., & Ho, L. C. 2014, ApJ, 797, 65

Wang, R., Carilli, C. L., Beelen, A., et al. 2007, AJ, 134, 617

Wang, R., Carilli, C. L., Wagg, J., et al. 2008, ApJ, 687, 848

Wang, R., Carilli, C. L., Neri, R., et al. 2010, ApJ, 714, 699

Wang, R., Wagg, J., Carilli, C. L., et al. 2011a, ApJ, 739, L34

—. 2011b, AJ, 142, 101

—. 2013, ApJ, 773, 44

Watson, D., Christensen, L., Knudsen, K. K., et al. 2015, Nature, 519, 327

West, A. A., Morgan, D. P., Bochanski, J. J., et al. 2011, AJ, 141, 97

Willott, C. J., Bergeron, J., & Omont, A. 2015, ApJ, 801, 123

Willott, C. J., Delfosse, X., Forveille, T., Delorme, P., & Gwyn, S. D. J. 2005a, ApJ, 633, 630

Willott, C. J., McLure, R. J., & Jarvis, M. J. 2003, ApJ, 587, L15

Willott, C. J., Omont, A., & Bergeron, J. 2013, ApJ, 770, 13

Willott, C. J., Percival, W. J., McLure, R. J., et al. 2005b, ApJ, 626, 657

Willott, C. J., Delorme, P., Omont, A., et al. 2007, AJ, 134, 2435

Willott, C. J., Delorme, P., Reylé, C., et al. 2009, AJ, 137, 3541

Willott, C. J., Albert, L., Arzoumanian, D., et al. 2010a, AJ, 140, 546

Willott, C. J., Delorme, P., Reylé, C., et al. 2010b, AJ, 139, 906

Wilson, A. S., & Colbert, E. J. M. 1995, ApJ, 438, 62

Wilson, J. C., Miller, N. A., Gizis, J. E., et al. 2003, in IAU Symposium, Vol. 211, Brown Dwarfs, ed. E. Martín, 197

Woosley, S. E., & Bloom, J. S. 2006, ARA&A, 44, 507

Wright, E. L., Eisenhardt, P. R. M., Mainzer, A. K., et al. 2010, AJ, 140, 1868

Wu, X.-B., Wang, F., Fan, X., et al. 2015, Nature, 518, 512

Wylezalek, D., Galametz, A., Stern, D., et al. 2013, ApJ, 769, 79

York, D. G., Adelman, J., Anderson, Jr., J. E., et al. 2000, AJ, 120, 1579

Zapatero Osorio, M. R., Béjar, V. J. S., Martín, E. L., et al. 2000, Science, 290, 103

Zapatero Osorio, M. R., Béjar, V. J. S., Rebolo, R., Martín, E. L., & Basri, G. 1999, ApJ, 524, L115

Zeimann, G. R., White, R. L., Becker, R. H., et al. 2011, ApJ, 736, 57

Zhang, Z. H., Pokorny, R. S., Jones, H. R. A., et al. 2009, A&A, 497, 619

Zheng, W., Overzier, R. A., Bouwens, R. J., et al. 2006, ApJ, 640, 574

Zheng, W., Postman, M., Zitrin, A., et al. 2012, Nature, 489, 406

Zitrin, A., Zheng, W., Broadhurst, T., et al. 2014, ApJ, 793, L12